INVESTIGATION OF THE SUITABILITY OF WIDE BANDGAP DILUTE MAGNETIC SEMICONDUCTORS FOR SPINTRONICS

A Disseration
Presented to
The Academic Faculty

by

Matthew Hartmann Kane

In Partial Fulfillment
of the Requirements for the Degree
Doctor of Philosophy in the
School of Materials Science and Engineering

Georgia Institute of Technology
August 2007

INVESTIGATION OF THE SUITABILITY OF WIDE BANDGAP DILUTE MAGNETIC SEMICONDUCTORS FOR SPINTRONICS

Approved by:

Dr. Ian Ferguson, Advisor
School of Electrical and Computer Engineering
Georgia Institute of Technology

Dr. Zhong Lin Wang
School of Materials Science and Engineering
Georgia Institute of Technology

Dr. Christopher Summers
School of Materials Science and Engineering
Georgia Institute of Technology

Dr. Nikolaus Dietz
Department of Physics and Astronomy
Georgia State University

Dr. Hamid Garmestani
School of Materials Science and Engineering
Georgia Institute of Technology

Date Approved: June 21, 2007

To the scientists who came before who made this pursuit possible, and to my family, who made this pursuit worthwhile

ACKNOWLEDGEMENTS

I wish to thank my Advisor, Prof. Ian Ferguson, for his guidance during the course of this work. I would also like to thank Prof Chris Summers for his support from the Materials Science department. I thank Angela Yvonne for all of her hard work behind the scenes that made this work possible. I have also had the privilege to work with a number of talented individual in the MOCVD-group at Georgia Tech, including but not limited to: Ali Asghar, Martin Strassburg, Will Fenwick, Shalini Gupta, David Nicol, Paul Helm, Ming Pan, Hun Kang, Omkar Jani, Vincent Woods, James Bain, Dhariya Mehta, Shenjie Wang, Zhe Chuan Feng, Zaili Fang, Tahir Zaidi, Nola Li, Hongbo Yu, and Adam Payne. I would also like to the Prof. Nikolaus Dietz and his group at Georgia State University for performing some of the optical measurements on these sample. In addition, I would like to thank Priv. Doz. Axel Hoffmann, Prof. Wolfgang Gehhoff, Enno Malguth, Rob McKenna, Dmitry Azamat, and Ute Haebock for the EPR measurements and optical measurements on the $Ga_{1-x}Mn_xN$ samples. Additionally, I would like to thank at the group of Dr. John Zhang in the School of Chemistry and Biochemistry at Georgia Tech for the SQUID measurements and Dr. Samuel Graham for use of the Raman spectrometer. TEM measurements were performed by Elizabeth Dickey at Penn State. Additional EPR measurements on the ZnO samples were performed by David Keeble a t the University of Dundee and Graham Smith at the University of St. Andrews. Lastly, I would like to thank my family, especially Laura, Cammi, and Graham, for their unwavering patience and support for the past several years.

TABLE OF CONTENTS

LIST OF TABLES

LIST OF FIGURES

Page

LIST OF SYMBOLS AND ABBREVIATIONS

AFM	Atomic Force Microscopy
BL	Blue Luminescence
CB	Conduction Band
CFSE	Crystal Field Stabilization Energy
CL	Cathodoluminescence
Co	Cobalt
Cp_2Mn	Bis-cyclopentyldienyl Manganese
Cp_2Mg	Bis-cyclopentyldienyl Mangmesium
DBR	Distributed Bragg Reflector
DMS	Dilute Magnetic Semiconductor
emu	Electromagnetic Unit
EPR	Electron Paramagnetic Resonance
eV	Electron volt
FC	Field Cooled
Fe	Iron
FET	Field Effect Transistor
FP	Fabry Perot
FWHM	Full Width Half Maximum
Ga	Gallium
GHz	Gigahertz
GMR	Giant Magnetoresistance
HAADF	High Angle Annular Dark Field
HEMT	High electron mobility transistor

I-V	Current-Voltage
k_B	Boltzmann Contsant
KKR-CPA	Korringa-Kohn-Rostoker-Coherent potential approximation
LDA	Local Density Approximation
LED	Light emitting diode
Li	Lithium
LO	Longitudinal Optical
LT-MBE	Low temperature molecular beam epitaxy
MBE	Molecular Beam Epitaxy
MCD	Magnetic Circular Dichroism
MFA	Mean Field Approximation
Mg	Magnesium
Mn	Manganese
MOCVD	Metalorganic Chemical Vapor Depostion
MRAM	Magnetic Random Access Memory
Oe	Oersted
PEM	Photoeleastic Modulator
PL	Photoluminescence
PSPD	Position-sensitive photodetector
RKKY	Ruderman-Kittel-Kasuya-Yosida
QBits	Quantum Bits
QW	Quantum Well
RF	Radio frequency
RMS	Root Mean Square
RT	Room Temperature

RTA	Rapid Thermal Annealing
Ry	Rydberg
SIMS	Secondary Ion Mass Spectrometry
Sn	Tin
SQUID	Superconducting Quantum Interference Device
STEM	Scanning Transmission Electron Microscopy
T	Tesla
T_C	Curie Temperature
TEM	Transmission Electron Microscopy
TO	Transverse Optical
TMG	Trimethyl Gallium
UV	Ultraviolet
VB	Valence Band
VSM	Vibrating Sample Magnetometry
Wt%	Weight Percent
XRD	X-ray Diffraction
YL	Yellow Luminescence
ZFC	Zero Field Cooled
$\sigma+$	Left-circularly polarized
$\sigma-$	Right-circularly polarized
μ_B	Bohr Magneton

SUMMARY

New semiconductor materials may enable next-generation ‘spintronic’ devices which exploit both the spin and charge of an electron for data processing, storage, and transfer. The realization of such devices would benefit greatly from room temperature ferromagnetic dilute magnetic semiconductors. Theoretical predictions have suggested that room temperature ferromagnetism may be possible in the wide bandgap semiconductors $Ga_{1-x}Mn_xN$ and $Zn_{1-x}Mn_xO$, though the existing models require input from the growth of high-quality materials. This work focuses on an experimental effort to develop high-quality materials in both of these wide bandgap materials systems.

$Zn_{1-x}Mn_xO$ and $Zn_{1-x}Co_xO$ single crystals have been grown by a modified melt growth technique. X-ray diffraction was used to examine the structural quality and demonstrate the single crystal character of these devices. Substitutional transition metal incorporation has been verified by optical transmission and electron paramagnetic resonance measurements. No indications of ferromagnetic hysteresis are observed from the bulk single crystal samples, and temperature dependent magnetization studies demonstrate a dominant antiferromagnetic exchange interaction. Efforts to indroduce ferromagnetic ordering were only successful through processing techniques which significantly degraded the material quality, suggesting a defect-related origin to the observed ferromagnetism.

$Ga_{1-x}Mn_xN$ thin films were grown by metalorganic chemical vapor deposition on two inch sapphire substrates. Good crystalline quality and a consistent growth mode with Mn incorporation were verified by several independent characterization techniques.

Substitutional incorporation of Mn on the Ga lattice site was confirmed by electron paramagnetic resonance. Mn acted as a deep acceptor in GaN, suggesting that hole mediated ferromagnetism in this material is not possible. Nevertheless, ferromagnetic hysteresis was observed in the $Ga_{1-x}Mn_xN$ films. The apparent strength of the magnetization correlated with the relative ratio of Mn^{3+} to Mn^{2+}. Valence state control through codoping with additional donors such as silicon was observed. Additional studies on $Ga_{1-x}Fe_xN$ also showed a magnetic hysteresis. A comparison with implanted samples showed that the common origin to the apparent strong ferromagnetic hysteresis is really a by-product of a change within the paramagnetic ordering from isolated $Mn^{2+/3+}$ substitutional ions. The observed magnetic hysteresis is due to the formation of Mn-rich regions during the growth process, which can be controlled through the use of antisurfactants during growth. Qualitative modeling of the magnetic signature using a combination of Mn-configurations replicated the observed magnetic behavior. Through careful and detailed studies of high-quality materials in the wide bandgap system, it was shown that the original intrinsic models for room temperature ferromagnetism in the wide bandgap semiconductors do not hold and the room temperature ferromagnetism in these materials results from extrinsic contributions.

CHAPTER 1

INTRODUCTION

1.1 Overview

Next generation electronic devices may exploit both the spin and charge of the electron. This combination of properties enables powerful, integrated multifunction computing systems for massively parallel operations in the field know as spintronics. Efforts to develop spin-based electronic devices have been somewhat successful, with the caveat that only low temperature (cryogenic) operation of these devices has been realized. In order for widespread operation of these devices to be realized, it is essential that devices emerge which can operate at room temperature. New materials systems will be crucial towards the development of these room temperature spintronic devices. This dissertation focuses on two potential materials systems for the implementation of room temperature spintronics, transition metal doped GaN and ZnO.

$Ga_{1-x}TM_xN$ and $Zn_{1-x}TM_xO$ (TM = transition metal) are part of a family of compounds know as dilute magnetic semiconductors (DMS). Theoretical predictions suggest that these wide bandgap materials are advantageous for practical spintronic applications relative to their narrow bandgap DMS counterparts. Room temperature ferromagnetism is suggested under several models. However, material of sufficient quality to evaluate these models was not readily available due to complications in the

growth of these materials. The work described herein demonstrates the development of these growth techniques which can be used to evaluate the suitability of these models.

This chapter describes some of the fundamental goals of developing spintronic devices and various potential applications of these devices. The success of many of these spintronic systems requires the development of new materials. In the rest of this dissertation, two unique materials systems for the implementation of spin electronic devices will be investigated. After a review of the basics of magnetic properties and semiconductor growth, a discussion of how these seeming disparate properties can be combined into a single materials system. The prevailing theories of ferromagnetism in semiconductors and the necessary exchange mechanisms will be analyzed. The challenges for the growth and processing of these semiconductors will be discussed. Subsequent chapters will review the results on two such materials systems, taking the approach that in order to elucidate the underlying materials physics necessary for a complete understand of these materials, it will be essential to produce high quality material so that competing effects can be eliminated. This work explores bulk single crystals of ZnO doped with transition metals grown by a modified melt-growth technique, and GaN thin films grown by metalorganic chemical vapor deposition. As was the case with the evolution of traditional semiconductor electronics, materials science and engineering of novel semiconductors will be the enabling element for next-generation electronics.

1.2 The End of Moore's Law

Moore's law [1], which predicts a doubling of the of the transistor density and hence the processing speed of silicon-based electronics every couple of years faces

fundamental size-related obstacles to its continuation over the next several years. New methods and technologies are needed to keep the progress of semiconductor electronics on the semiconductor roadmap which has been driven by Moore's Law over the past half century. As the size of the transistor decreases, classical physics no longer applies. Quantum mechanical effects start to play a role in the performance of these devices. In order to continue the progression of solid state electronic devices, it will be necessary to understand and overcome these quantum mechanical limitations.

An alternate approach to traditional electronics is to exploit these quantum mechanical obstacles advantageously, in order to build a new era of electronic devices based on entirely new paradigms. Some approaches which may form the basis for next generation electronics include semiconductor nanowires or single electron transistors. Another approach which may create next generation devices is the area of spintronics. Spintronics presents a new methodology completely independent of the traditional semiconductor roadmap. It is well known from even the most rudimentary sciences courses that the elementary particle of an electron contains both a charge and a spin. Electronic charge is the baseis for the current system of electronic devices. Spintronic devices seek to exploit this heretofore unused electron spin in order to bring about this next revolution in semiconductor electronics. In order to realize future implementation of these devices, it is imperative to understand the materials properties and processing which can lead to behavior suitable for spin-based electronic devices.

1.3 The Semiconductor Periodic Table

In order to investigate new functionalities in semiconductor devices, it is instructive to look at how the materials evolution of semiconductors has occurred over the past sixty years, and how each advance has been enabled by the inclusion of additonal elements to the semiconductor periodic table, Figure 1.1. The initial point contact transistor developed at Bell Labs was made from germanium, for which Bardeen, Britain,

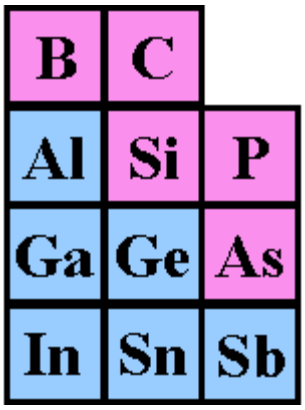

Figure 1.1: The "Semiconductor Periodic Table" of the Early 1980's, summarizing the elements used to make a vast majority of semiconductor electronic devices

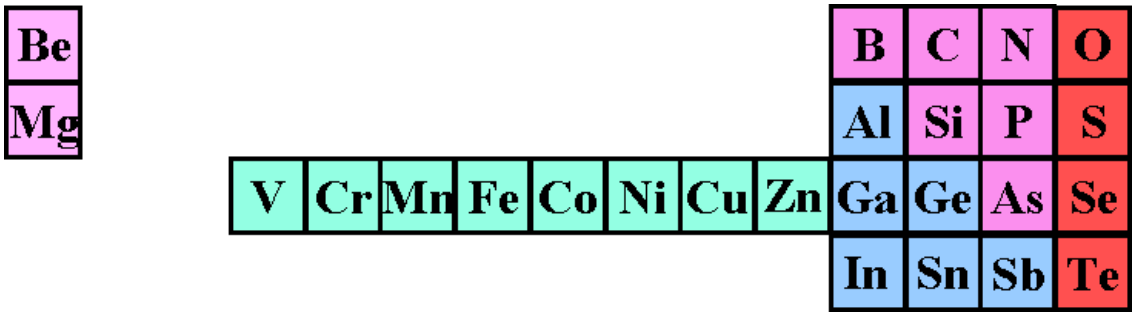

Figure 1.2: Semiconductor periodic table of elements needed for semiconductor spintronics

and Shockley were later awarded the Nobel Prize in Physics for this landmark invention. It was not long before the demand for higher temperature operation, in particular those used in amplifiers for radar applications, necessitated the movement and development of silicon based electronics. These devices were first demonstrated at Texas Instruments by Gordon Teal and coworkers and took advantage of advances in single crystalline technology [2]. The silicon revolution towards faster and smaller electronics continues to this day. However, it was not until the advent of compound III-V semiconductors, which have a direct bandgap instead of the indirect bandgap in Ge and Si, that efficient light emitters in the early 1970's could be produced. Early efforts in semiconductor optoelectronics focused on infrared emitters for data storage and telecommunications based on miniminzing the dispersion in optical fibers. Recent efforts in the 1990's added III-nitrides to the pool of materials available for semiconductor devices. These advances and the corresponding development of blue and ultraviolet emitters have made even higher density data storage and full color display applications possible and potentially widespread application in solid state lighting. This trend of including additional elements in the semiconductor periodic table leading to new functionalities for semiconductors must continue for spintronics, Figure 1.2. Using the magnetic functionality inherent in the unpaired spins in the transition metals may provide further advancement beyond the paradigms of traditional electronics.

1.4 Goals of Spintronics

Spin-based devices offer two routes towards implementation to replace traditional electronic devices [3]. One case suggests that spintronic devices may have an improved performance over traditional electronic devices. The injection of spin polarized currents is predicted to be more efficient that non–spin polarized currents [4]. It is predicted that spintronic devices can be designed that will facilitate higher information storage densities

and higher speeds than today's technology allows [5]. Such improved efficiencies have been already demonstrated in laser-systems [6].

An alternate approach to the implementation of spintronic devices is to take advantage of some of the unique features of the electron spin to introduce entirely new devices within semiconductor electronics. Novel functionalities such as reconfigurable logic, nonvolatile chip-based memory, and solid state quantum computing may be possible magnetic semiconductor systems [7, 8]. For example, nonvolatile Magnetic Random Access Memory (MRAM) has also recently become available commercially [9] and is still an intense topic of research interest for a number of consumer applications. Semiconductor-based spintronic devices such as spin-polarized LEDs and magneto-optical isolators have been demonstrated [10-12]. In addition to these devices in production several theoretical semiconductor-based devices have been proposed including the Spin Field Effect Transistor (Spin-FET) [13]. These devices have not been shown experimentally. In the future, semiconductor spintronics could be used for the implementation of solid state quantum computation. A more detailed description of these novel devices is discussed below.

Spintronic devices have made a significant impact in other areas of device research, but in entirely metallic based systems. The original breakthrough leading to these developments was the discovery of giant magnetoresistance (GMR) in magnetic multilayered materials independently by Gruenberg *et al.*[14] and Fert *et al.*[15] in 1988. The first commercial devices based on spintronic GMR, including GMR sensors and high-capacity hard drives, became available in the late 1990's and are now the prevailing technology. In this layered structure, Figure 1.3, there is a pinned ferromagnetic layer and a free ferromagnetic layer which are separated by a spacer. When the two layers are aligned in a parallel configuration, the resistance is several orders of magnitude lower than when the layers are in the antiparallel configuration. Thus, as the read head glides

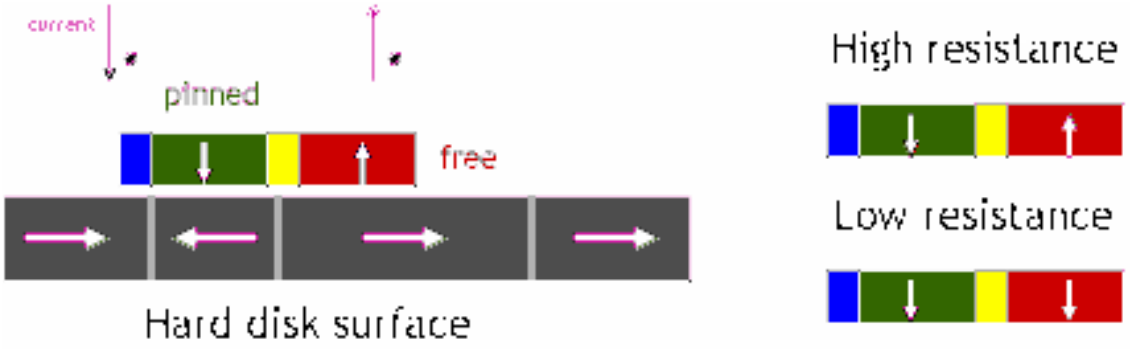

Figure 1.3: Schematic of a giant magneto-resistive read head arrangement, used in modern magnetic data storage applications. This is the most widespread application of a spintronic device to date.

over the surface of the hard disk, the fringing fields from the magnetic domains cause the free layer to switch; the resulting change in the resistance can be used to read the bits. They have led to a vast increase in the storage density of magnetic memories over the past decade because these heads can be made much smaller than the traditional inductive read heads.

1.5 The Need for Magnetic Semiconductors

In order to develop and implement other spintronic devices, several issues must be resolved. For many computing and logic processing information application based on spins at the data carrier, it is essential to have a stable source of spin polarized carriers, and it must also be possible to reliably transport these spin polarized carriers within the device. This would seem to impose two requirements on the system. The first is that the system must have a ferromagnetic element which supports a lengthy storage of the electron spins. The second requirement is that the system should have a semiconducting portion, through which traditional device operation can be performed. At first glance, it may seem possible to construct a heterostructure device, Figure 1.4, with a ferromagnetic

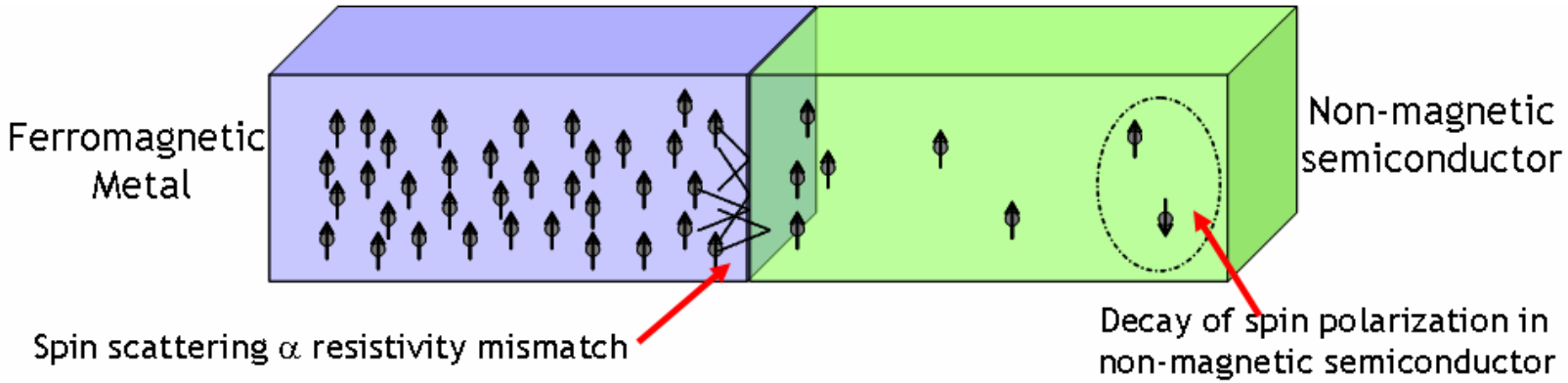

Figure 1.4: The problem with using only ferromagnetic metals and non-magnetic semiconductors is that the resistance scattering at the interface between the two materials can very large. Moreover, the spin polarization in some semiconductors can decay very rapidly away from the interface.

metal element and a semiconductor element. However, the conductivities of the ferromagnetic metal and the semiconductor must be closely matched in order to ensure efficient injection of spin polarized carriers into the semiconductor [16], similar to that previously demonstrated in metal-metal junctions [17]. If there is a large difference between the conductivities of the two materials, then the degree of spin polarization in the semiconductor will be very low. In order to achieve high spin polarization with a ferromagnetic metal source, either the conductivities of the two materials must be closely matched, or the degree of spin polarization in the metal must be 100%. Neither of these solutions is easily attainable in metal-semiconductor devices [18].

Another approach is to create an interface resistance that is much higher than he resistance of either that of the the metal or the semiconductor. This can be accomplished by placing a tunnel barrier – often an oxide – between the two layers, or by doping the semiconductor. A reverse-biased Schottky barrier serves the same purpose as a discrete oxide layer for the tunnel barrier. Heavily doped semiconductors can have a depletion region on the order of ten angstrom increasing the probability of tunneling. This also eliminates the complication of having to add a third layer to the structure. Several groups have reported successful injection of spin-polarized electrons using these structures. Semiconductor spin polarizations exceeding 30% have been reported using both tunnel barrier layers and Schottky barriers to facilitate injection [23-26]. The efficiency of spin injection in these structures is highly dependent on the interfacial quality [27].

Other routes must be developed for room temperature device operation using spin polarized currents in solid state electronics [19-21]. One class of materials that show promise in these areas is dilute magnetic semiconductors (DMS). These are semiconductors doped with rare earth or transition metals to provide magnetic

functionality. This use of ferromagnetic semiconductors as the source of spin-polarized carriers represents another approach to spin injection. This eliminates the problem of conductivity matching at the interface. However, many magnetic semiconductors have Curie temperatures (T_c) that are well below room temperature, making them unsuitable for practical applications. There is still debate over the mechanism of ferromagnetism in these materials, particularly their utility at elevated (non-cryogenic) temperatures. This must be resolved before the potential of spintronics technology is fully realized.

1.6 Novel Semiconductor Spintronic Device Architectures

Dilute magnetic semiconductors have been studied for use in spintronic devices because of their unique electrical and magnetic properties.[22-24] These properties allow control of electron spin as well as charge flow resulting in materials ideal for spintronic applications. Their similarity to existing semiconductors shows promise for monolithic integration with existing semiconductor technology. Possible applications include non-volatile memory, spin-polarized light emitting diodes (Spin-LEDs), electronic devices with faster switching times and lower power consumption, and elements for solid state quantum computing.[25, 26] However, room temperature (RT) operation of spintronic devices, particularly in the all-semiconductor manifestation, has proven difficult to achieve.

1.6.1 Spin Field Effect Transistors

The first proposed semiconductor spintronic device was the Spin Field Effect Transistor, which was first proposed in 1990 by Datta and Das [13], Figure 1.5. Here, a spin-polarized current is injected from source side of the device. The gate voltage is used to control the precession of spins via the Rashba-spin orbit interaction from a ferromagnetic emitted to ferromagnetic collector. Since the degree of spin precession is dependent on the volatage applies, the transport through the device will be affected by the

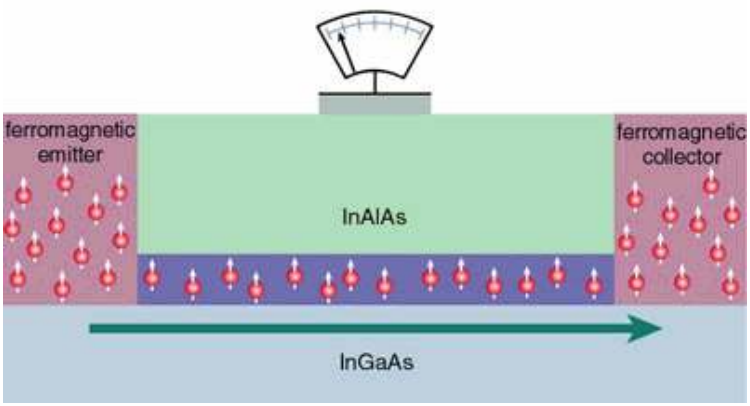

Figure 1.5: A schematic of a Spin Field Effect Transistor (Datta-Das transistor). In this device, the gate voltage is used to control the precession of spins from a ferromagnetic emitted to ferromagnetic collector.After [13].

end of channel spin alignment of the current relative to that of the ferromagnetic collector at the drain end of the device. This control of the drain current through application of a gate voltage is analogous to what is seen in a field effect transistor. The potential benefit of this device is that is conceivably possible to perform this operation at much lower currents and at higher speeds than traditional FETs. This could have a great impact on the overall development of spin-based devices. Implementation of these structures has been slow due to difficulties in the fabrication and operation of these devices. Moreover, there are fundament theoretical disagreements on the ideal device design and, the ultimate practical utility of these spin-based electronic devices is still to be determined.

1.6.2 Spin Light Emitting Diodes

Traditional light emitting diodes (LEDs) rely on the recombination of electrons and holes. The material of choice is a direct bandgap semiconductor for highest efficiency. Usually, the spin effect is taken into account through the use of a spin degeneracy factor of 2 to account for spin-up and spin-down electrons in the device. Normal LEDs emit unpolarized electromagnetic radiation (due to the statistical nature of

the recombination process) over a relatively broad wavelength spectrum as compared to monochromatic laser sources. If it were possible to inject spin polarized carriers into the device, the recombination of these majority-spin electrons would lead to circularly polarized light upon recombination.

In order to understand this phenomenon, it is imperative to look at the quantum mechanical optical selection rules. Figure 1.6 shows a schematic of the conduction band to valence band transitions in a zincblende semiconductor. The matrix elements in a quantum well of a semiconductor are proportional to the net rate of transitions. From the conduction band to the heavy hole band for transverse electrical polarization, this is given by [27]:

$$\left\langle \left| \hat{e} \cdot p_{c-hh} \right|^2 \right\rangle = \frac{3}{4}\left(1+\cos^2\theta\right)M_b^2 \quad \text{(eq. 1.1)}$$

Where M_b is the bulk semiconductor transition matrix element.

Similarly, for transitions from the conduction band to the light hole band [27]:

$$\left\langle \left| \hat{e} \cdot p_{c-lh} \right|^2 \right\rangle = \left(\frac{5}{4}-\frac{3}{4}\cos^2\theta\right)M_b^2 \quad \text{(eq. 1.2)}$$

Assuming a normal incidence electron injection ($\theta=0^o$) and no splitting of the light hole-heavy hole degeneracy, the ratio of heavy hole to light hole transitions will be 3:1. On the other hand, if there were a way to remove the heavy hole-light hole degeneracy, the spin polarization efficiency would equal the optical polarization efficiency. One way to accomplish this is to take advantage of the band alignment and heavy hole-light hole splitting in quantum wells (QWs). Many spin-LEDs have been constructed to take advantage of this feature in QWs, which enables optical and spin injection efficiency ratios nearing unity. Another method for splitting this degeneracy is to use strained quantum wells, which has also been observed to have a marked effect on the transition behaviors.

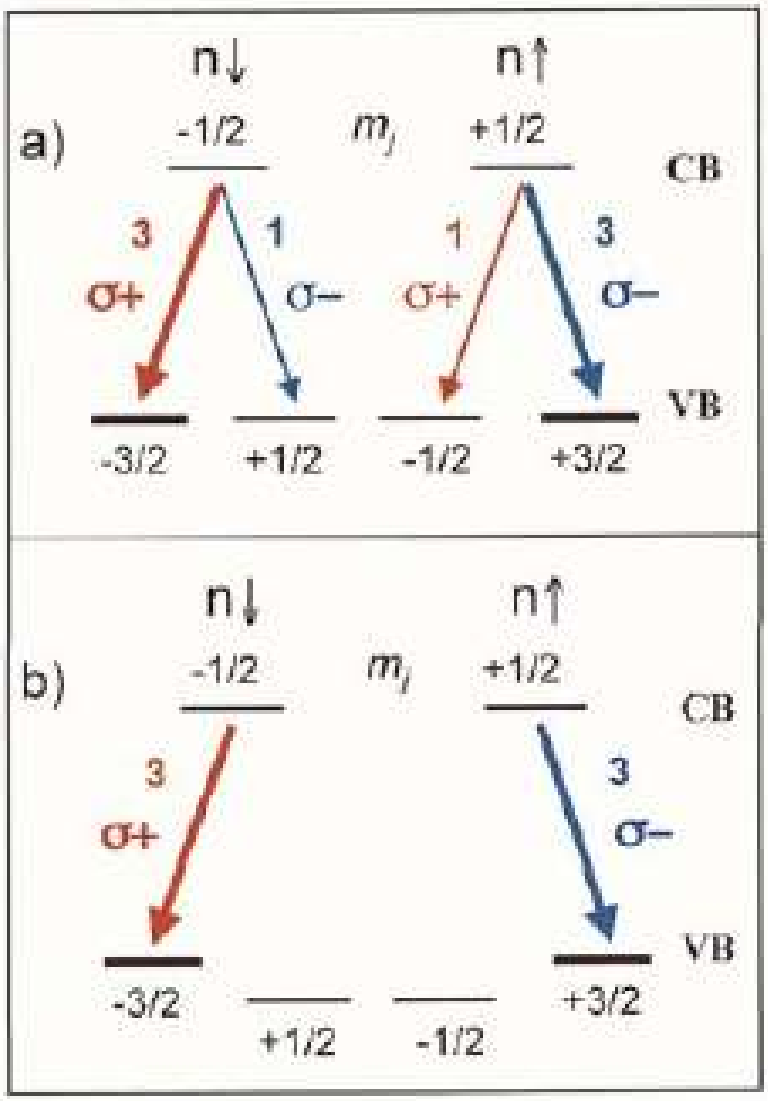

Figure 1.6: Radiative interband transitions and corresponding optical polarizations allowed by the selection rules $\Delta m = m \pm 1$ for (a) bulk material in which the hole bands are degenerate, and (b) a QW in which the reduced symmetry lifts the degeneracy. From [18].

Photons have a net intrinsic angular momentum of +1 for a right circularly polarized photon and -1 for a left circularly polarized photon. Thus, in order to conserve angular momentum, there must be net change in angular momentum from the conduction band to the valence band of J = +/- 1. This leads to the four allowed transitions of the form: $|m_l(\text{electron}) m_l(\text{hole})>$.

Of these four transitions, transitions from excitons with |-1/2 -3/2> and |+1/2 -1/2> emit right circularly polarized photons, whereas the other two transitions, |+1/2 +3/2> and |-1/2 +1/2>, emit left circularly polarized photons. The spin injection efficiency is defined as (where $N_\uparrow$ and $N_\downarrow$ are the concentrations of up (majority) and down (minority) spin electrons:

$$S_{eff} = \frac{\left(N_\uparrow - N_\downarrow\right)}{\left(N_\uparrow + N_\downarrow\right)} \quad \text{(eq. 1.3)}$$

whereas the optical polarization efficiency is described as (with $I(\sigma^+)$ and $I(\sigma^-)$ representing the intensities of right and left circularly polarized light):

$$P_{eff} = \frac{\left[I\left(\sigma^+\right) - I\left(\sigma^-\right)\right]}{\left[I\left(\sigma^+\right) + I\left(\sigma^-\right)\right]} \quad \text{(eq. 1.4)}$$

Thus, if given a completely 100% spin polarized current, the polarization efficiency would only be 50% due to the 3:1 ratio of heavy hole-light hole transitions in the case of degenerate heavy hole-light hole bands.

Ohno and coworkers at Tohuku University demonstrated the first successful spin injection in materials using a ferromagnetic semiconductor as a spin injector [10]. A schematic of their device and the relative spin polarization of the emission is shown in Figure 1.7. For these spin-LEDs, $Ga_{1-x}Mn_xAs$ magnetized in plane (along the easy axis of these films) was regrown on a GaAs/InGaAs quantum well setup. In the electroluminescence measurements, hysteresis is maintained up to 52K; above this temperature, the sample is paramagnetic. Photoluminescence measurements excited through the substrate show no corresponding hysteresis, proving the emitted light

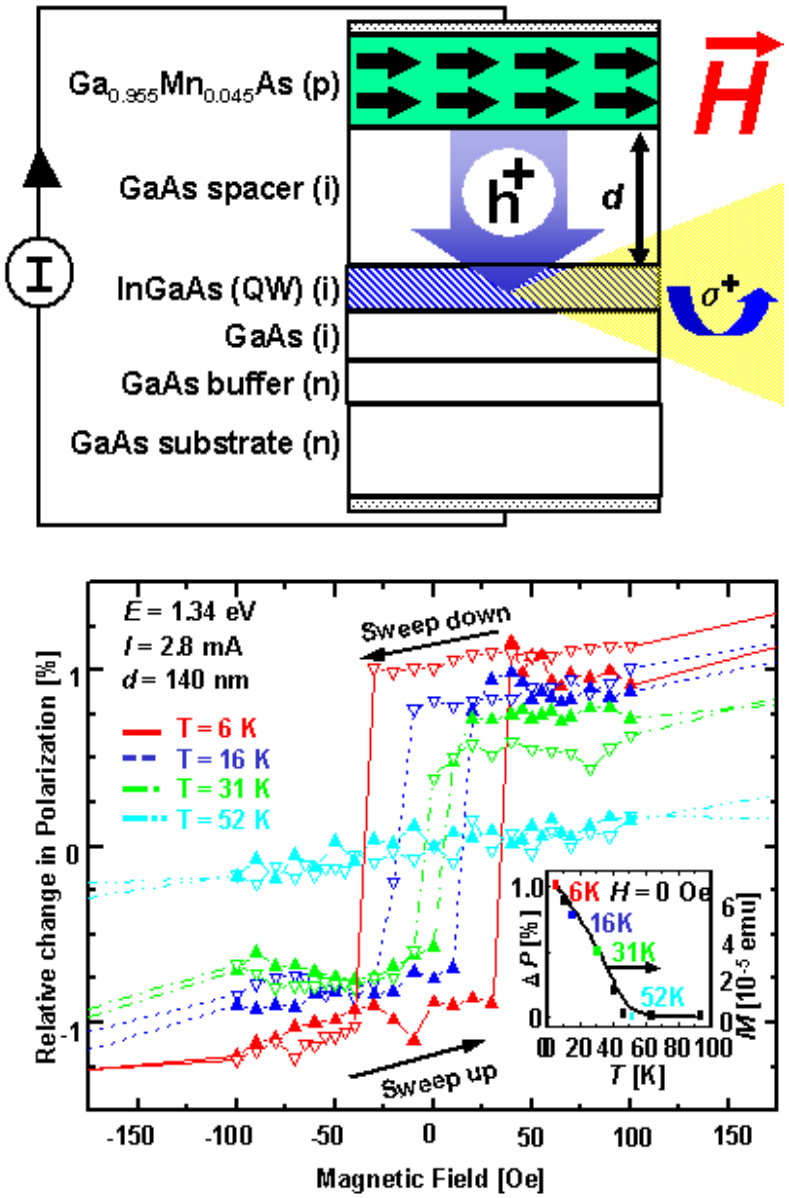

Figure 1.7: Diagram of Spin injector structure used by Ohno *et al.* as well as the hysteresis observed in the spin polarization of the electroluminescence in the GaAs system. From [10].

polarization is indeed due to spin injection from the $Ga_{1-x}Mn_xAs$ layer. Barrier thicknesses of up to 220 nm were used without appreciable loss in the observed spin polarization of the device. Unfortunately, due to the low Curie temperature of the device, spin injection is only observable at cryogenic temperatures. In addition, although there is clear hysteresis observable in these samples, the degree of spin polarization is only 1% at 6K, owing to the fast relaxation times of the holes in the quantum well. However, this work does demonstrate that polarized light emission is possible in the absence of a magnetic field with a suitable magnetic spin injector.

1.6.3 Quantum Dots for Quantum Computation

Quantum wells and dots have been used extensively in traditional semiconductor electronics for improvement of the transport and optical behavior. These quantum structures may also play a key role in the eventual implementation of novel spintronic device architectures. In fact, one of the key drivers in spintronics research has been quantum computing, which would allow for massively parallel algorithms based on the quantum superposition of states [28]. Ferromagnetic semiconductor quantum dots (QDs) are one of the most promising elements proposed for solid state quantum computing, as they meet the fundamental requirements for Quantum Bits (QBits) [28, 29], , the fundamental building block of quantum computers, as outlined by Di Vincenzo [28]. Thus, presuming the size and arrangement of an array of magnetic and non-magnetic quantum dots can be controlled, it may be possible to develop a solid state analog using massively parallel quantum information processing alongside the modern serial computers.

Initial efforts to explore magnetic semiconductor quantum dots are already underway. Spin-LEDs provide a way to study spin injection into quantum dots not just for localized spin- LED emitters, but also for future quantum computation applications. Quantum dots are preferred over quantum wells due to longer spin relaxation times and

lower ground state energies relative to the GaMnAs; this leads to negligible field-induced dichroism in surface emitting structures. Gosh and Bhattacharya [30] have developed a spin-LED using InGaAs/GaAs quantum dots in the active layer. Chye *et al.* [31] have also attempted to exploit the long coherence times in quantum dots in spin-LED structures. In this work, electron spin injection was found not to be sensitive to variation in quantum dot size, whereas hole injection was highly sensitive to quantum dot geometry. In addition, enhancement of the magnetic behavior has been observed in semiconductor quantum dots [49] and quantum wells [50], which might provided another avenue for improving the materials behavior for spintronic applications in these systems in the future.

CHAPTER 2

OVERVIEW OF DILUTE MAGNETIC SEMICONDUCTORS

2.1 Types of Magnetism

2.1.1 Atomistic Origins of Magnetism

In order to understand why semiconductors are traditionally not magnetic and how it is possible to introduce magnetic behavior in these materials, it is first necessary to look at the fundamental origins of magnetic behavior, and then analyze how magnetic behavior can be exploited in the development of dilute magnetic semiconductor compounds. Magnetism in materials arises from the fundamental property of electron spin, which is the intrinsic angular momentum of an electron. This instrinsic spin and the orbital angular momentum of an electron within an atom represent two of the four fundamental quantum numbers of an electron within an atom. An overall net alignment of these electronic spins will manifest itself as a net magnetic dipole moment for the atom.

According to the Pauli Exclusion Principle, no two electrons within an atom may have an identical set of quantum numbers. Thus electrons in an atom will first fill up the lower energy shells (as indicated by the first or principal quantum number). Then they will fill up the individual subshells (s, p, d, f) and orbitals within these subshells according to the lowest energy configuration. Because each orbital can hold one electron of each spin up and spin down, there are two electrons available in each subshell and the spins of a filled shell will cancel each other out such that there is no new magnetic moment for an atom containing entirely filled subshells of electrons. Since covalent and

ionic bonding within solids obey the octet rule, this generally results in entirely filled shells of electrons. The outermost s- and p- subshells (or some hybridization thereof) will be filled with 2 and 6 oppositely spin-paired electrons within the solid; therefore, there is no overall net tendency for a magnetic moment in a solid resulting from the outermost electrons. However, it is possible for a net magnetic moment to result from inner, non-nonbonding d- and f- subshells. They must be only partially filled, as is the case in transition metal and rare earth atoms.

The net magnetic moment arising from the interior shells is again the result of orbital filling rules associated with the Pauli Exclusion Principle, with an additional contribution from Hund's Rules, which dictates how electrons will distribute themselves within a subshell. As electrons are added to the individual subshells of an atom, they will go into the orbital with the lowest energy. In the case of a partially filled subshell, electrons will go into either empty orbitals with the same spin or any previously occupied orbital instead of going into a partially filled orbital and adopting the opposite sign as would be required by the exclusion principle. This predilection towards partially occupied orbitals results from electrostatic repulsion concerns: two like-charged particles occupying the same orbital have a much higher electrostatic energy than two particles spatially separated in different obitals. Meanwhile, the tendency to align with these same spins in different orbitals results from exchange energy concerns: two electrons within a subshell lower their exchange energy by occupying the same spin, such that Hund's Rules dictate that the electrons will fill all orbitals in a subshell with a like spin electron before these orbitals are filled with electrons of opposite spin to complete the shell.

In a transition metal or rare earth compound where these electrons are localized on the interior of an atom and not involved in bonding, it is possible to have large net magnetic moments on an atom even in a crystalline configuration. It is possible to introduce other energetic considerations which will overcome this exchange energy and align in what is deemed a low-spin configuration for the atom when pairing occurs within the orbital of a transition metal. Figure 2.1 shows a comparison of the low spin and high spin configurations. Within a substitutional crystal environment, this energy is known as the crystal field stabilization energy (CFSE). Based on symmetry concerns, different orbitals within a subshell will have their energy lowered in accordance with the external coordination environment – depending on the strength of this crystal field it is possible to overcome the exhange energy, resulting in spin pair above a crossover energy. As it turns out, the nitride materials studied in this work are very close to this cross-over energy; in fact, it may be possible to optically induce a spin-crossover within these systems [32]. Typically, transition metals within a tetrahedrally coordinated lattice are always in a

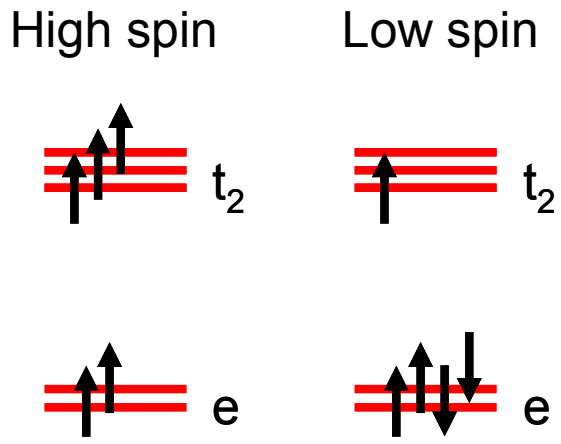

Figure 2.1 Comparison of a d^5 atom in the high spin (S = 5/2) and low spin (S =1/2) under tetrahedral crystal field splitting.

high-spin configuration while a low-spin configuration is seen in octahedral coordination due to the stronger field strength. Only in the reduced bond lengths of these wide bandgap materials is the CFSE possibly large enough to induce this transfer in tetrahedral coordinated material.

Macroscopically, the behavior of a materials system is not determined by individual isolated atoms. The magnetic behavior is determined by the collective behavior of all of the atoms within the system. Depending on the alignment of and interaction between atoms within a material, the observed macroscopic behavior of the system can be very different. The fundamental types of magnetism in a materials system are described below.

2.1.2 Diamagnetism

Most materials exhibit an overall magnetic behavior known as diamagnetism. In the presence of a magnetic field, the material develops an internal magnetization opposite the direction of the applied field. This is a materials analogy to Lenz's Law, where a changing magnetic field induces a current in a coil of wire opposite the direction of the applied field. This type of behavior is prevalent in materials with no unpaired electrons and thus no net magnetic moment internally; adding an additional magnetic field cannot align the electron spins as they are already paired. Using Langevin theory, the magnetic susceptibility of a diamagnetic material is given by the expression:

(eq 2.1) $$\chi = -\frac{Nze^2}{6m_e}\left\langle r^2 \right\rangle_{av}$$

The diamagnetic signal is roughly independent of temperature. Only in the case of superconductors is the diamagnetic field unity; here the magnetic field is completely

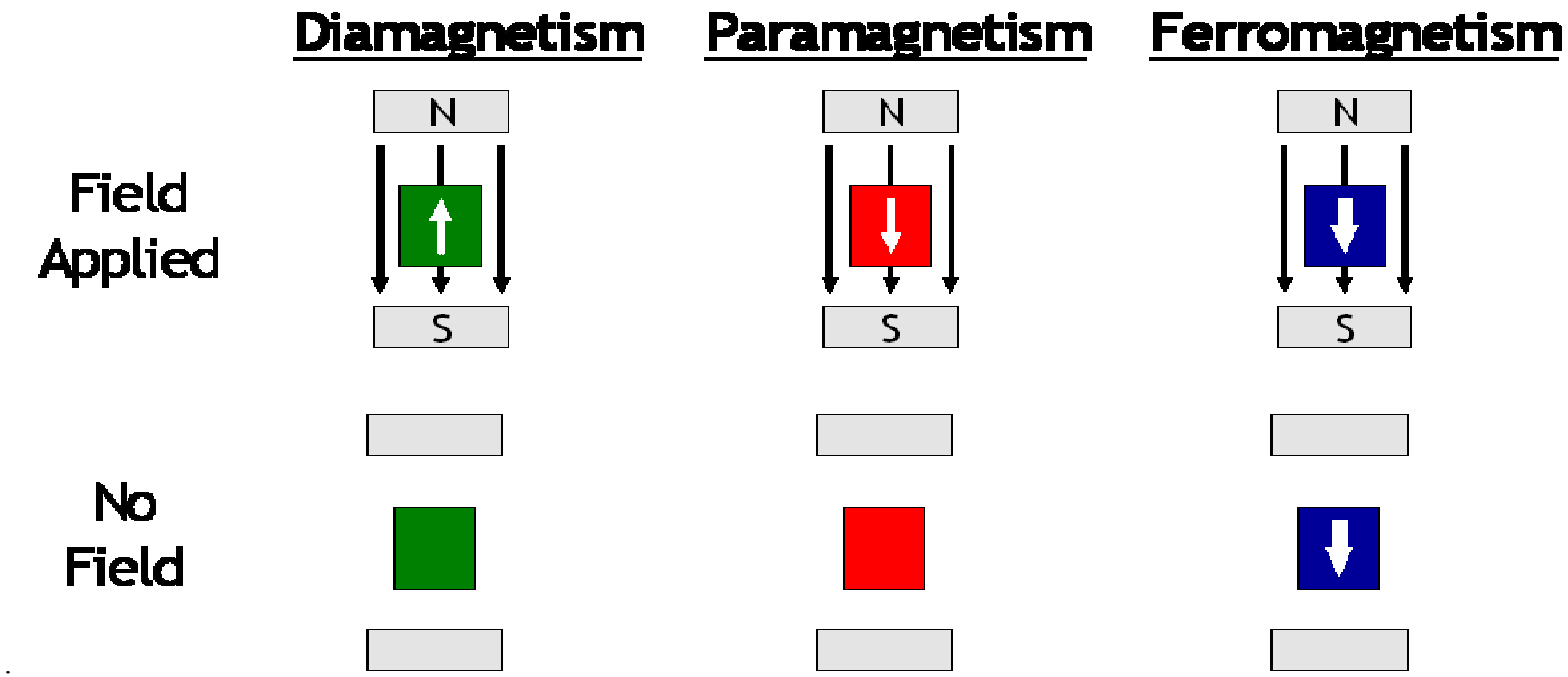

Figure 2.2: Macroscopic behavior observed in diamagnetic, paramagnetic and ferromagnetic materials. In a diamagnetic material, the internal magnetization aligns antiparallel as the material 'rejects' the applied magnetic field. In a paramagnetic material,the internal magnetization aligns weakly with the applied field, but vanished is the magnetic field is removed. In a ferromagnetic material, the magnetization aligns strongly aligns applied magnetic fieldm and maintains this alignment after the field is removed

expelled from the material through a phenomenon known as the Meissner effect. A schematic of the diamagnetic response is shown in Figure 2.2.

2.1.3 Ferromagnetism

Although diamagnetism is present in many materials, due to its weak and transient nature, it is not particularly useful for most applications. In order to have a strong macroscopic signal that is useful, a material must possess not only extra spins on the atoms, but also a mechanism by which the spins collectively align in the same direction. This phenomenon, a diagram of which is shown in Figure 2.3, occurs in materials known as ferromagnetism. Iron is one such material, hence the origin of the name.

With ferromagnetic materials, an external magnetic field can be applied to align the extra spins on the individual atoms in the same direction. Upon removal of this field,

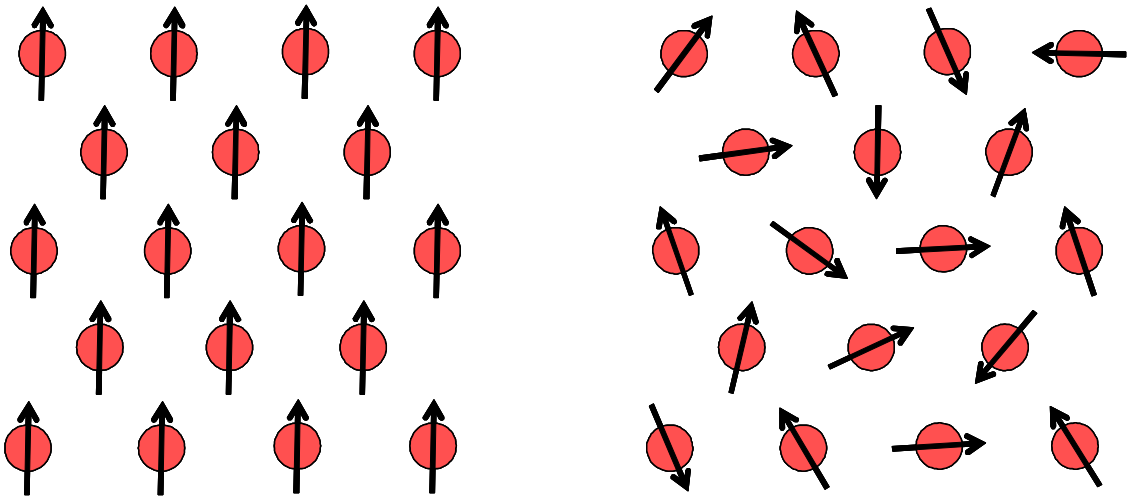

Figure 2.3: Comparison of the spin alignments in a ferromagnetic (left) and paramagnetic (right) material.

a majority of these spins remained aligned in this direction through an energetically favorable exchange mechanism; this will be discussed later in this chapter in relation to magnetic semiconductors. In metals, the ferromagnetism is stabilized by interaction with the free electron carriers in the system; this mechanism is know as the RKKY interaction after the four scientists who proposed it in the late 1950's. In order to align the spins in the opposite direction, an additional field must be applied with an opposite field strength. In general, the strength of a magnetic signature from a concentrated ferromagnet can be roughly 6 orders of magnitude greater than that of a typical diamagnet. Also, because the signal remains after the external field is removed, these materials can be used in applications where non-volatility is required, such as nonvolatile magnetic data storage.

2.1.4 Paramagnetism

Another alternative configuration of spins in materials whose atoms contain unpaired spins is known as paramagnetism. In this case, instead of having a collective alignment of spins on the individual atoms, the atoms are aligned in a random direction; here the material has no overall magnetic moment, since all the spins cancel. This happens in ferromagnetic materials above the ordering temperature (known as the Curie temperature), where the thermal energy of the system is able to overcome the exchange energy and the material loses its magnetic ordering. The overall behavior in the presence of a magnetic field is very similar to that of a diamagnetic material, with the exception that the magnetic susceptibility (χ) is positive rather than negative. Thus, as a field is applied, there is a tendency for unpaired spins to align with the magnetic field; when the field is removed, the atoms resume their random alignment and there is no net magnetic

field. As this is another transient form of magnetism, it is not particularly useful, although paramagnetic semiconductors have been used for spin injection into light emitting devices in the presence of a magnetic field [33].

2.1.4.1 Curie-Weiss Paramagnetism

There are actually two different varieties of paramagnetism that are pertinent in dilute magnetic semiconductors. The most often seen form of paramagnetic transition metals, is known as Curie paramagnetism. In this case, the strength of the magnetic interaction is inversely proportional to the temperature, such that the strength of the magnetization will generally only be significant at very low temperatures. Temperature dependence of the susceptibility to magnetism for a paramagnetic compound of this form is given by the Curie law, which in SI units is:

(eq 2.2) $\chi = \frac{N\mu_o m^2}{3k_B T}$

2.1.4.2 Temperature Independent Paramagnetism

In some cases, the paramagnetic contribution does not obey the Curie law and instead takes on a temperature independent form. One such case, known as Pauli paramagnetism, is seen in some metals with large free electron concentrations, such as Na and Al. The second form of temperature-independent paramagnetism that is sometimes observed is known as Van Vleck paramagnetism. Van Vleck paramagnetism derives from second order perturbation theory constructs in quantum mechanics; it is typically only significant in transition metals having an even number of unpaired electrons, such as Cr^{2+}, Mn^{3+}, and Fe^{2+}. This behavior differs strongly from Pauli paramagnetic materials as a function of temperature; in that Van Vleck paramagnetism, like diamagnetism, has virtually no temperature dependence.

2.1.5 Antiferromagnetism and Ferrimagnetism

Ferromagnetism requires the existence of a strong positive exchange interaction that causes the excess electronic spins to align in the same direction. It is not always the case that the most energetically favorable magnetic alignment of spins will be in the parallel direction. Often, even via the RKKY interaction, the most energetically favorable alignment is to have adjacent spins couple and align in an antiparallel direction. Like ferromagnetism, this will occur below a specific ordering temperature, ;above which the random paramagnetic alignment will prevail; in this case, it is called the Neel temperature. Unlike in the ferromagnetic case, there is no net magnetic moment; the alignment of the various spins will cancel out, as there are equal number of atoms with opposite spin. A schematic of the antiferromagnetic arrangement is shown in Figure 2.4.

An alternate case of antiferromagnetic exchange which leads to a net overall magnetic moment is known as ferrimagnetism. As the name suggests, it is similar, but weaker in magnitude to ferromagnetism. In ferrimagnetism, the net nearest neighbor exchange is antiferromagnetic, such that atoms couple with opposite spins. However, either due to a difference in the either the number of sites with the opposite spins or through engineering of the compound to contain elements with different numbers of unpaired spins on each site, it is possible to have an incomplete cancellation of the unpaired spins and an overall net magnetic moment in the system.

2.1.6 Superparamagnetism

Another form of magnetism which occurs only in nanostructured systems is known as superparamagnetism. Here, the material is not one continuous bulk system, such that the network of magnetic ordering is discontinuous. Rather, the magnetic regions are isolated

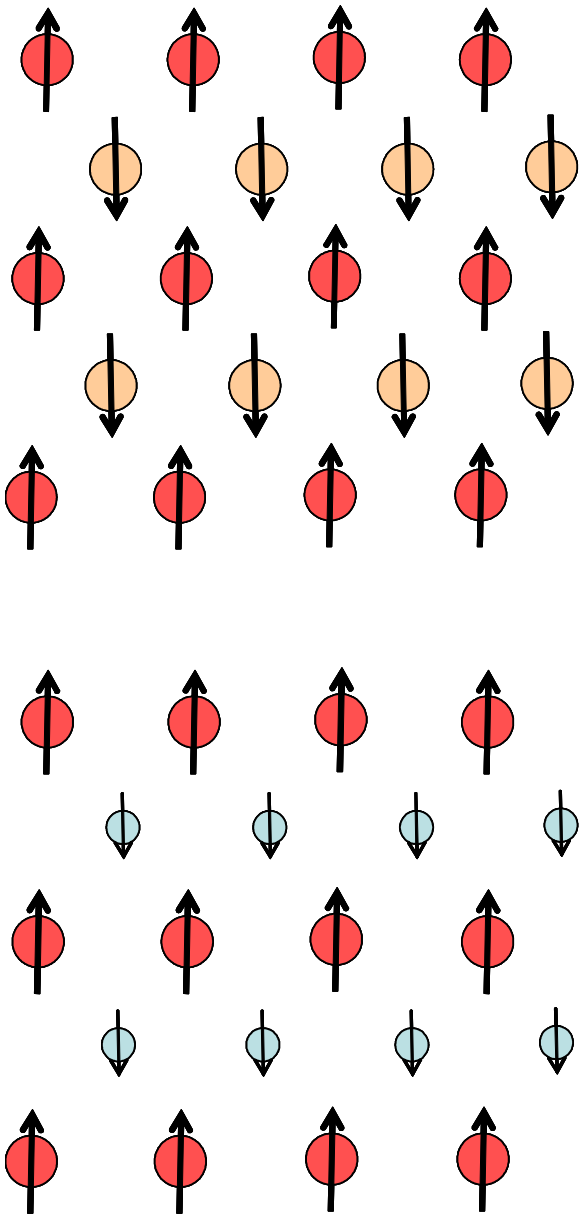

Figure 2.4. Schematic of the atomic configurations in an antiferromagnetic material and ferromagnetic material

into individual nanoscaled regions of ferromagnetic particles. Based on the size, separation, and shape of these particles, it may not be possible for the entire array of particles to switch their orientation simultaneously; as a result, instead of an ordered array of a homogeneous ferromagnetic phase, the system may behave as an array of individual single domain particles rather than atoms and give more of a paramagnetic like behavior. Because it is a collection of atoms, and not single atoms that are acting like single structures, this form of magnetism is known as a superparamagnetism. As a result of this collective behavior, it is possible to observe a blocking behavior, which means that it is possible to freeze this array in a metastable arrangement of spin alignments.

2.1.7 Magnetic hysteresis curves

In order to ascertain what sort of magnetic behavior (or combination of magnetic behaviors) is being observed, magnetization measurement on the samples can be performed by using a form of magnetometry such as superconducting quantum interference device (SQUID) magnetometry or vibrating sample magnetometry (VSM), both of which are described in more detail in the following chapter. These techniques measure the magnetization of a sample, which is then plotted against an applied field. Sample magnetization curves for various types of materials are shown in Figure 2.5. For diamagnetic materials and paramagnetic materials, the observed magnetization, at least at low fields, is linear with the applied field and returns to zero after the field is removed. The slope of a diamagnetic signal is small and negative; for paramagnetic materials it is larger and positive. Ferromagnetic materials are easily identified by their loop-shaped hysteresis magnetization curves. When a magnetic field is applied, the sample rises to its saturation value as the individual domains align with the magnetic field. As the magnetic field is removed, the magnetization does not return to zero. Some remnant magnetization exists from domains which remain aligned with the direction of the applied field. It

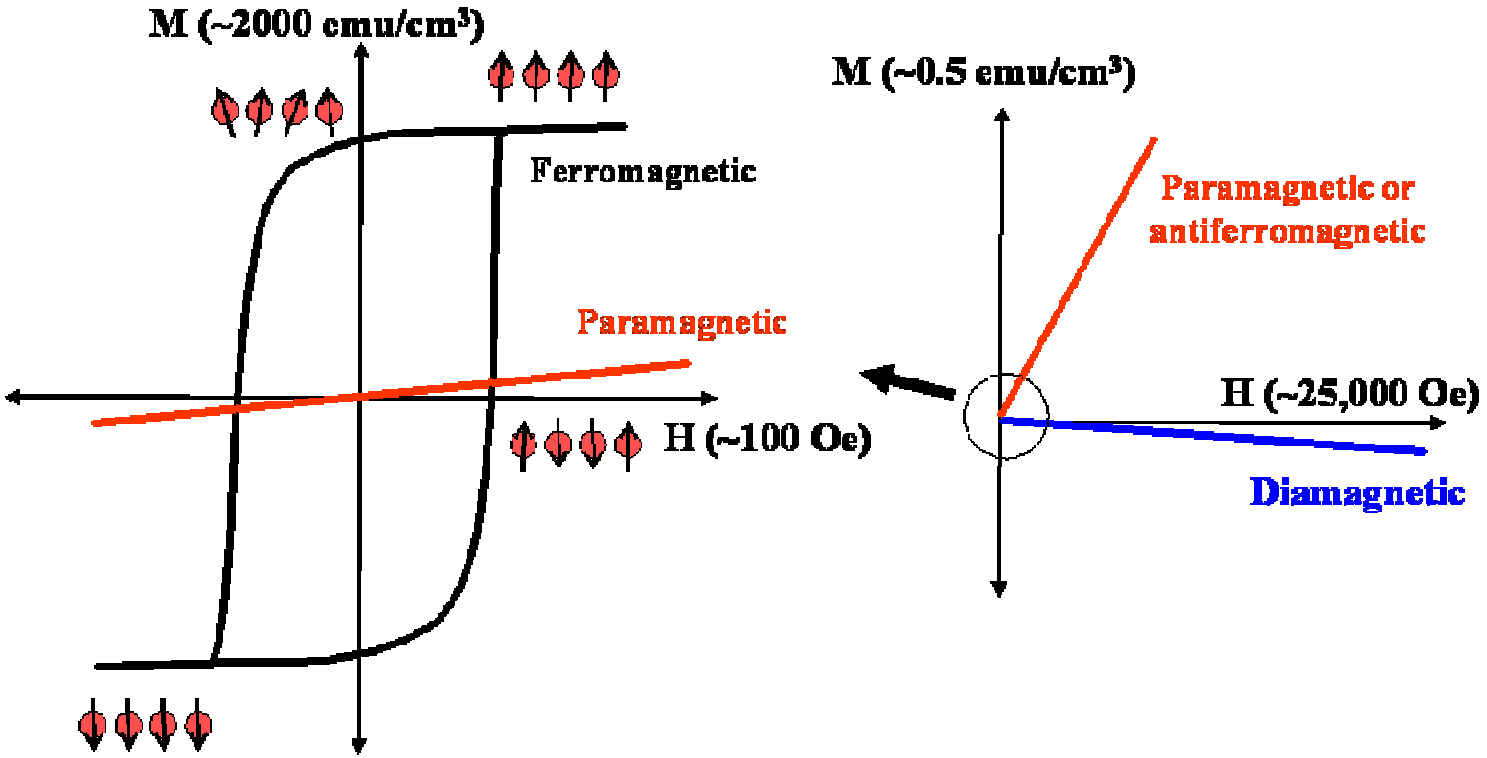

Figure 2.5 A schematic of the magnetization versus field curves expected for ferromagnetic, paramagnetic, and diamagnetic materials.

requires an additional field in the opposite direction, known as the coercive field, to overcome the ferromagnetic exchange interaction between atoms. A similar field is required to saturate the spins in the opposite direction, and if the magnetic field is cycled in the other direction, then the curve will trace out a symmetric loop shape as shown in Figure 2.5. Ferrimagnets exhibit a similar hysteresis behavior. Because an additional field that needs to be applied in order to reverse the domains, additional work is required to overcome the internal magnetic interactions. The area of the hysteresis curve is proportional to the energy expended; hysteresis loops with large areas occur for hard magnetswhile soft magnets produce hysteresis loops with much smaller areas. Materials exhibiting superparamagnetism can also show a loop-shaped hysteresis curve. At low temperatures, because the isolated individual ferromagnetic nanoparticles cannot respond to the field, they are 'blocked', Here, the material will have additional area in the curve like a ferromagnetic hysteresis loop. If the materials stay above the so called blocking temperature, meaning enough thermal energy is provided to prevent freezing in the spin configuration, then the hysteresis curve has no area and a more paramagnetic behavior is observed.

2.1.8 Magnetization versus temperature curves

In order to determine the characteristic magnetic ordering temperatures of a material or ascertain the type of magnetic behavior it exhibits, it is often useful to look at magnetization as a function of temperature. A schematic of the various magnetization versus temperature curves are shown in Figure 2.6. Materials exhibiting diamagnetism show a magnetization which is constant as a function of temperature, and negative due to the internal repulsion of the magnetic field. Van Vleck paramagnets show similar temperature-independent behavior, but their magnetization is positive instead of negative as in diamagnetic materials. For materials exhibiting Pauli paramagnetism, the strength of magnetization is inversely proportional to temperature (α 1/T), such that the signal strength can be large at low temperatures but falls off rapidly. Magnitization curves of

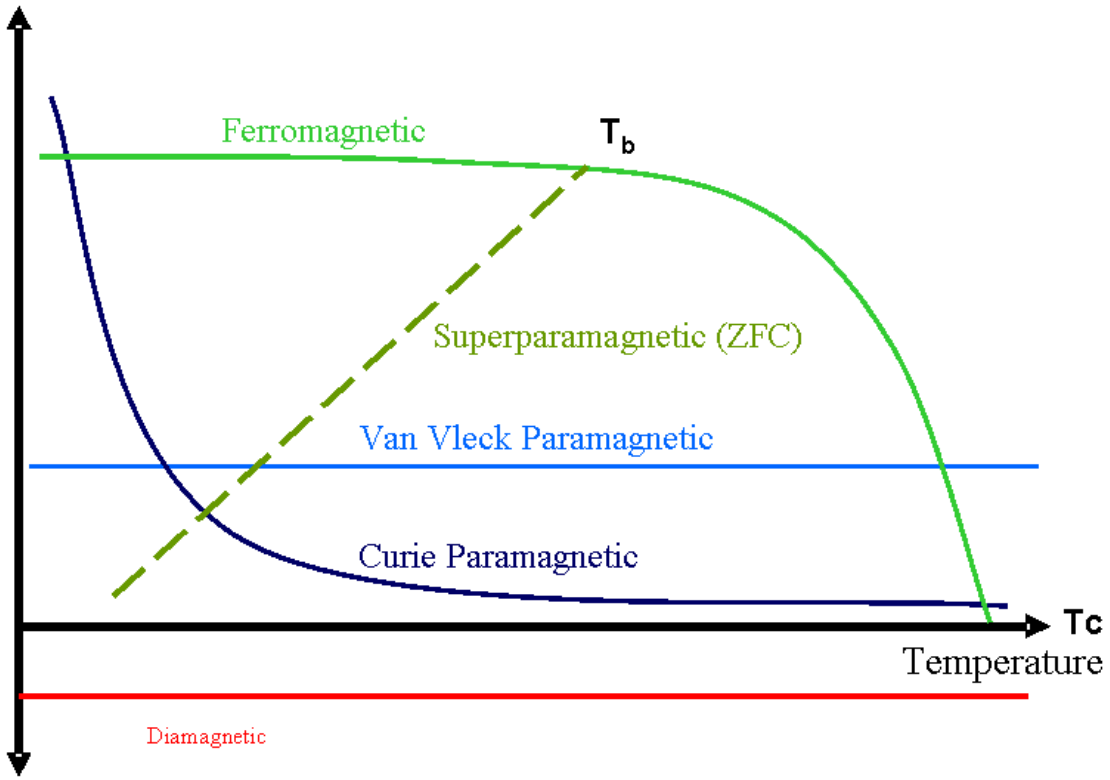

Figure 2.6 Magnetization vs. Temperature curves showing the behavior of different types of magnetic systems.

ferromagnetic materials show a distinctive shape which is nearly temperature independent at room temperature, but as the material approaches the ordering (Curie) temperature, the magnetization drops off to zero at the phase transition where the material goes from ordered to disordered.

Magnetization behavior as a function of temperature is a bit more complicated for nanoclustered materials and depends not only on the magnitude of the applied magnetic field but also on the history of the material. For these materials systems, the typical measurement that is performed involves comparing field cooled and zero field cooled magnetization curves. Under zero field cooling, the sample is taken to cryogenic temperatures without the presence of the magnetizing field. The magnetic field is then applied, and the magnetization is measured as the sample is heated. Since the magnetic field is not applied until the sample is already cooled, some individual nanoparticles are

already frozen into a state of magnetic alignment. There is not sufficient thermal energy at the lower temperatures for them to overcome a metastable energy barrier. Only as the temperature is increased does this agglomeration of particles begin to align with the magnetic field and the magnetization increases, eventually to some value when all of the magnetic particles are aligned. The magnetization of the sample is then measured upon cooling. Because the particles have sufficient thermal energy to realign, they remain at this higher magnetization and the curve does not follow the initial warming magnetization curve. The difference between field cooled and zero-field cooled curves is an irreversibility that is characteristic of spin freezing in materials, either superparamagnetic systems or spin glass; the point at which these two curves converge is known as the blocking temperature.

2.2 $Ga_{1-x}Mn_xAs$ - the prototypical diluted magnetic semiconductor

The search for semiconductor materials with Curie temperatures above room temperature has covered a wide range of elements, compounds, and dopants. In order to make a semiconductor magnetic, the first requirement is that there must be either a transition metal or a rare earth element introduced into the lattice of the semiconductor. This can be done by taking either a rare earth or a transition metal compound that is already a semiconductor. Alternately, in an effort to monolithically integrate magnetic and non-magnetic semiconductors, one can introduce a transition metal into the lattice site as in a traditional semiconductor to form what is known as a dilute magnetic semiconductor. To date, most magnetic semiconductors have T_c much lower than that of ferromagnetic metals such as iron, cobalt, or nickel. One class of materials that has received much attention is concentrated magnetic semiconductors, such as the europium chalcogenides [34]. These materials contain a magnetic rare earth species on each lattice site. For low carrier concentrations, concentrated magnetic semiconductors are 100% spin polarized, which makes it possible to tune the conductivity by means of *n*-type doping to

match the conductivity of the normal semiconductor layer. However, they have extremely low T_c, and are thought to be useful only for research purposes [21]. It has been shown that doping of the insulating layer increases the exchange interaction for some concentrated magnetic semiconductors. This enhances the magnetic properties of the material and increases T_c with increased doping for small changes in carrier concentration [35]. Curie temperatures for these materials may reach as high as 150K with optimum doping and processing [36]. However, this increase in T_c is obviously not substantial enough to permit ferromagnetism at room temperature, though they remain valuable tools for the study of spintronics [21].

The alternate approach of taking dilute magnetic semiconductors (DMS), consisting of III-V or II-VI semiconductor compounds doped with rare earth or transition metals such as Mn, shows some promise for magnetic semiconductor applications. However, most dilute magnetic semiconductors under investigation today also only exhibit ferromagnetism at cryogenic temperatures (<175K). It is imperative that materials be developed with T_c above room temperature so that magnetic semiconductors may be useful in practical spintronics applications. In order to better understand how the Curie temperature might be increased, it is important to examine what is thought to be currently the best understood DMS material, $Ga_{1-x}Mn_xAs$.

2.2.1 Growth of $Ga_{1-x}Mn_xAs$

Due to experimental difficulties relating to the growth of these ferromagnetic semiconductors such as $In_{1-x}Mn_xAs$ [37] and $Ga_{1-x}Mn_xAs$ [38], the development and understanding of these materials was delayed until the beginning of the last decade. . Because of the dissimilarity of gallium to the transition metals, the relative solubility on the gallium sites in these materials is quite low, well below 1% in most cases. Therefore, non-equilibrium growth techniques such as molecular beam epitaxy (MBE) and metalorganic chemical vapor deposition (MOCVD) must be used to produce these

materials. In the arsenides ($Ga_{1-x}Mn_xAs$ and $In_{1-x}Mn_xAs$), this problem is compounded by an extremely stable binary manganese arsenide (MnAs) phase. In order to prevent the formation of this phase, low temperature molecular beam epitaxy or other highly non-equilibrium techniques must be used; Figure 2.7 shows the growth regime where $Ga_{1-x}Mn_xAs$ can be observed during MBE growth [39]. There are reports of room temperature ferromagnetism in MOCVD-grown $In_{1-x}Mn_xAs$ [40] and $In_{1-x}Mn_xAs$ quantum dots[41], but it has yet to be shown that the room temperature ferromagnetism is due to the dilute alloy. One possibility is the presence of coherent zincblende MnAs particles within the lattice which have been observed recently via transmission electron microscopy[42]. These MnAs particles should indeed exhibit the 330 K Curie temperature that has been reported. It is interesting to note that the particles, under certain conditions, can be found with the cubic zincblende instead of the thermodynamically stable hexagonal nickel arsenide structure, which indicates that it may be possible to embed commensurate metastable magnetic phases in the semiconductor lattice.

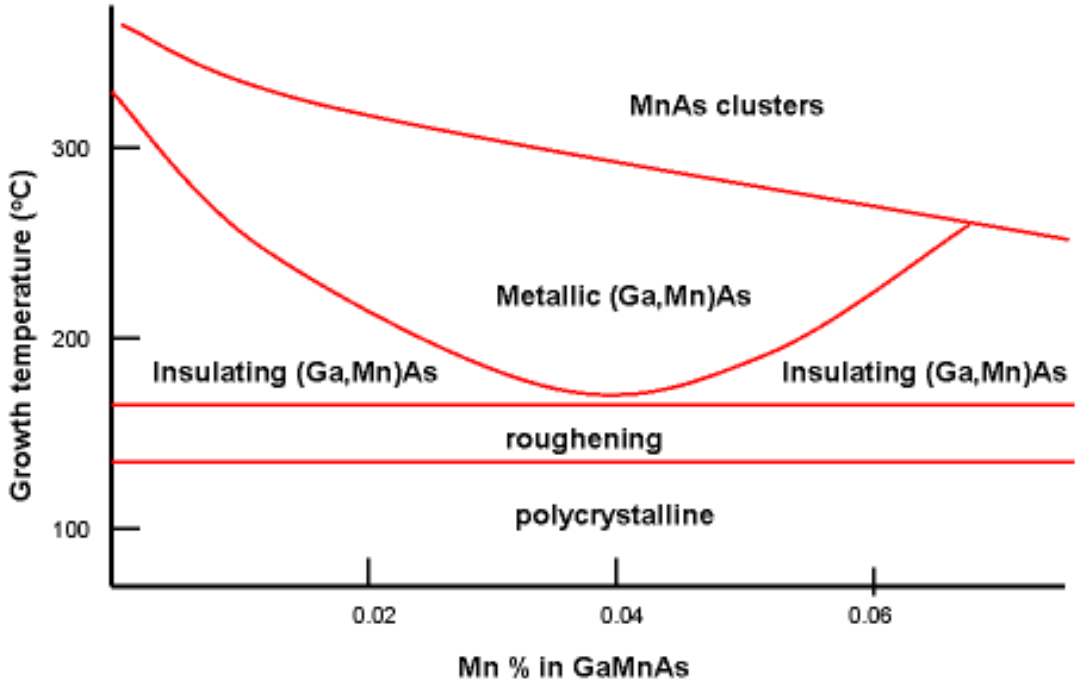

Figure 2.7 Growth parameter window for $Ga_{1-x}Mn_xAs$ when grown by molecular beam epitaxy. From [39].

2.2.2 Role of defects

The low temperature growth techniques typically used lead to a high quantity of native defects within the system. Large quantities of Mn interstitials act as compensating defects and reduce the overall carrier (hole) concentration and ferromagnetic behavior within the arsenides. Through careful low temperature annealing, it is possible to drive out these Mn interstitials, resulting in a reduction of the defect in compensation, an increase in the carrier concentration, and a corresponding increase in the Curie temperature [36] as shown in Figure 2.8. In addition to the Mn interstitials, arsenic antisites are also prevalent and act as double donors within these systems. In $Ga_{1-x}Mn_xAs$ it is fortunate that Mn acts as a relatively shallow acceptor (~100 meV above the GaAs valence band edge), such that even in the case where an enormous amount of defect compensation occurring, it is possible to overcome this compensation and get p-type material. These efforts in $Ga_{1-x}Mn_xAs$ stress an underlying theme in understanding the role of defect compensation, metastable phase segregation, and interface effects in these dilute magnetic semiconductors. Ultimately, for viable room temperature spintronic applications, room temperature dilute magnetic semiconductors are required.

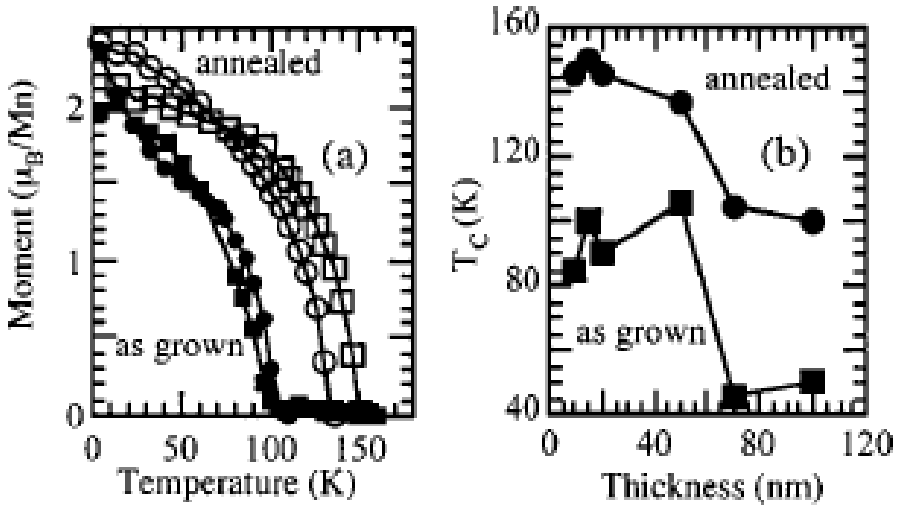

Figure 2.8: Magnetization of $Ga_{1-x}Mn_xAs$ layers before and after a careful low temperature annealing procedure which drives out interstitial Mn and enhances the T_C. From [36]

2.2.3 Device Demonstration in $Ga_{1-x}Mn_xAs$

$Ga_{1-x}Mn_xAs$ has also been of immense importance in the field of spintronics because it is has provided a platform for developing prototype spin based electronic devices within an all-semiconductor system. A number of novel spin based electronic functionalities have been demonstrated in this system, ranging from electrically controlled domain wall motion [43], to optically induced magnetization [44] and spin injection based emitters [45]. A brief summary of these accomplishments is described below.

2.2.3.1 Spin Light Emitting Diodes

As was mentioned in Chapter 1, it has been shown that Mn-doped semiconductors can be used as sources of spin-polarized hole carriers. Original spin injection studies were perfomed using paramagnetic DMS materials. Here, the spin polarization is controlled with an applied magnetic field, allowing for tunable spin polarization up to nearly 100%. $Zn_{1-x}Mn_xSe$ is easily doped *n*-type, and studies have shown that an applied magnetic field allows polarization in excess of 72% [46] when injected from the paramagnetic DMS. Mn is a shallow acceptor in narrow bandgap III-V materials, thus leading to *p*-type material. $Ga_{1-x}Mn_xAs$ is a *p*-type material and is ferromagnetic rather than paramagnetic, so that spin-polarization can be observed even in the absence of an applied field. It has also been shown that Mn-doped ferromagnetic DMS materials can be used effectively as sources of spin-polarized carriers. $Ga_{1-x}Mn_xAs$ injecting contacts have been used in spin-LED structures, with spin polarization of up to 6% reported [47].

2.2.3.2 Esaki Diodes

Most of the proposed spintronic devices such as spin transistors and quantum computation elements are electron vice hole-based devices [46]. In addition, electronic spin injection is anticipated to be more efficient than hole spin injection due to reduced

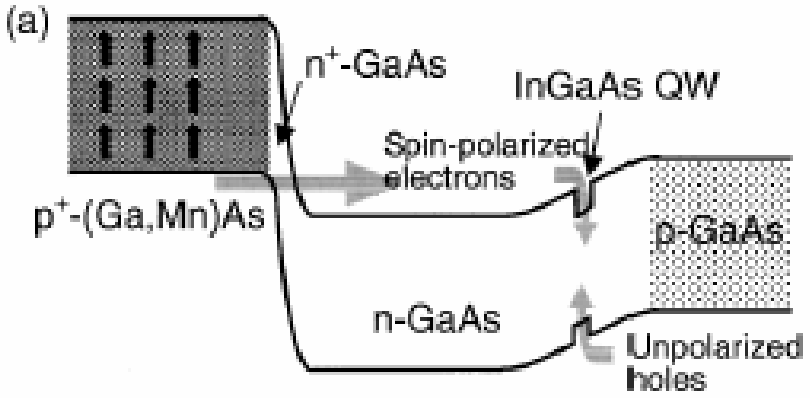

Figure 2.9: Band structure schematic of a $Ga_{1-x}Mn_xAs$ Esaki diode on LED structure which allows for electron spin injection from p-type material. From [47].

spin orbit coupling in the conduction band, which leads to decreased spin decoherence [30]. Unfortunately, most of the confirmed dilute magnetic semiconductors to date are p-type. One way to circumvent this problem and inject a source of spin polarized carriers is to use a spin-Esaki diode-LED arrangement as shown in Figure 2.9. Using this setup, Kohda *et al.* [48] have observed a five-fold increase in the magnitude of the EL polarization. When a magnetic field is applied normal to the easy axis, no spin polarization is observed. This particular arrangement demonstrated that even in p-type DMS, electron spin injection. From a practical standpoint, however, these devices are still limited by small polarization efficiencies (~7%) and the cryogenic temperatures (7 K) characteristic of $Ga_{1-x}Mn_xAs$ based devices. Electron based tunneling spin-LEDs would enable electron based spintronics and a corresponding increase in efficiency and speed [48].

2.2.3.3 Optically Induced Magnetism

One essential feature of magnetism in the band structure of magnetic materials, whether they be metallic ferromagnetic, half metallic materials such as some Heusler

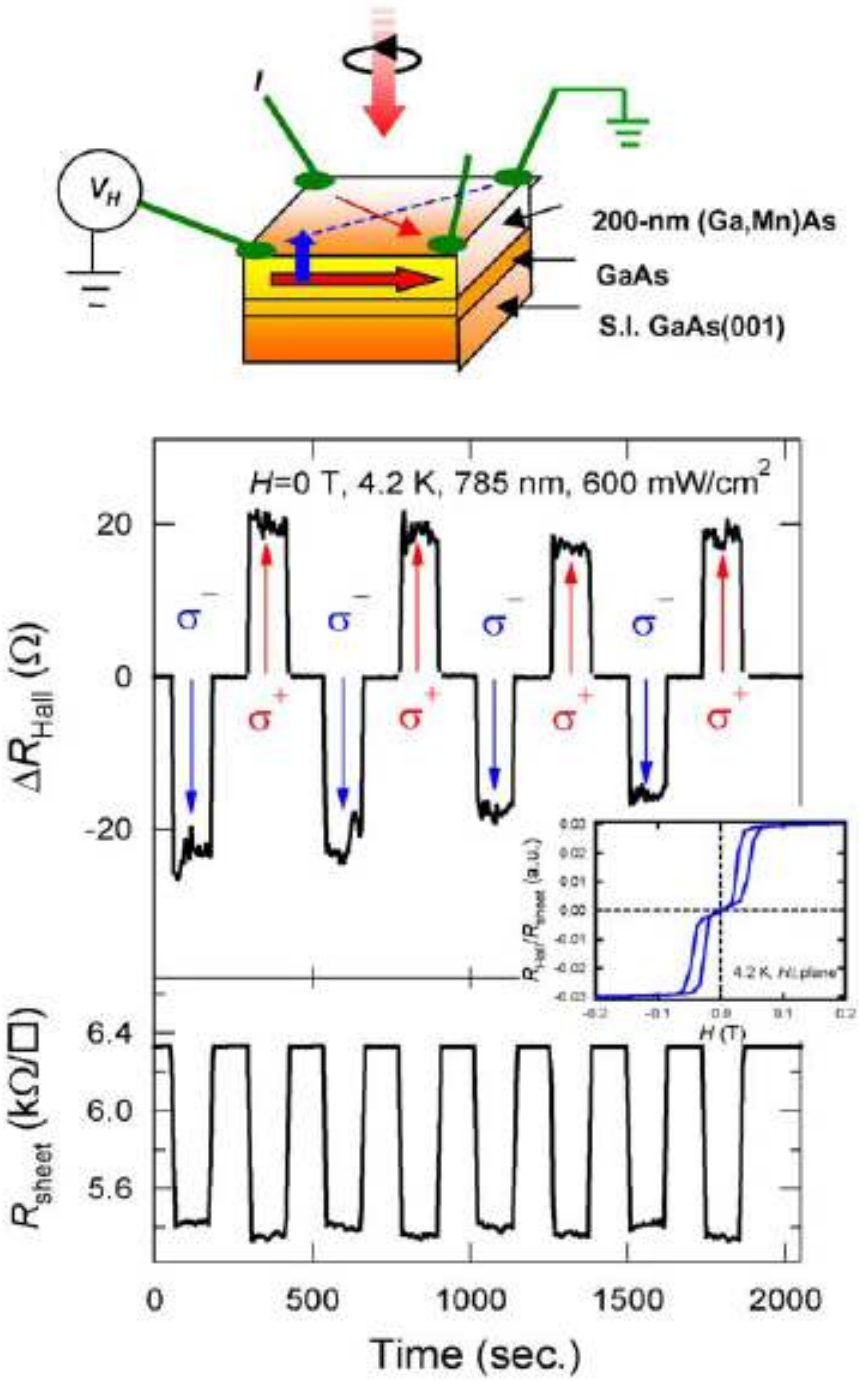

Figure 2.10. Evidence for optically induced magnetization in a $Ga_{1-x}Mn_xAs$ layer. Not the change in Hall coefficient under the influence of circularly polarized light. From [213]

alloys, or magnetic semiconductors, is a spin splitting in the density of states between up and down spins at the Fermi level. In magnetic semiconductors such as $Ga_{1-x}Mn_xAs$, this occurs at the valence band edge. Conceivably, it should be possible to exploit this band splitting in order to develop new devices based on the interplay between polarized light and the magnetization behavior of the material. Munekata et al. have done precisely this in the $Ga_{1-x}Mn_xAs$ system, as shown in Figure 2.10. By using the introduction of polarized light of either right or left circular polarization, they have demonstrated that magnetization of the sample can be induced and controlled in these systems using optical methods. This could serve as a building block for future electronic devices based on the magneto-optical coupling in these systems.

2.3 Magnetic Exchange Mechanisms

Wide bandgap dilute magnetic semiconductors (DMS) show a bit more promise in the search for materials with T_c at or above room temperature. It is predicted that among III-V compounds, nitrides are more likely to exhibit room temperature ferromagnetic behavior than arsenides or phophides [22]. This occurs for two reasons: 1) The smaller lattice constant leads to more spin-dependent interaction between localized spins and holes in the valence band, which in turn leads to larger ferromagnetic coupling. 2) Ferromagnetism in compounds with small anions, such as nitrides, is not detrimentally affected by spin-orbit interactions, which scale as Z^4. For these reasons, III-nitrides, such as $Ga_{1-x}Mn_xN$, are thought to be the best option for ferromagnetic semiconductors and devices to operate at or above room temperature[24]. Transition metal-doped ZnO is another one of two semiconductors predicted by Dietl *et al.*[22] to have a Curie temperature above 300K.

However, the mechanism that produces this ferromagnetism is still under debate. It is often unclear whether the observed ferromagnetism is due to substitutional Mn ions in the semiconductor lattice, unwanted precipitates, or a combination of both. It is

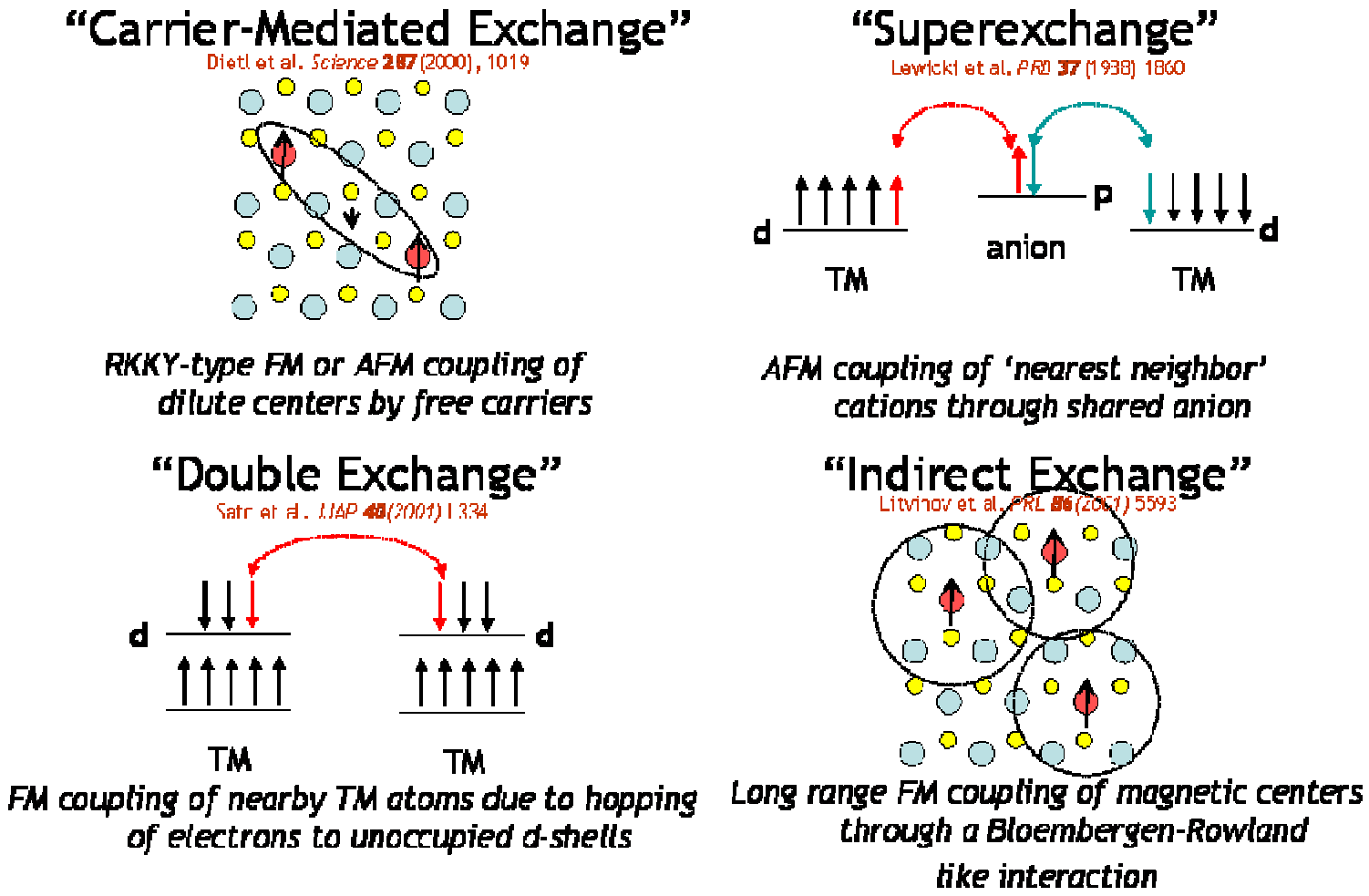

Figure 2.11 Schematic showing some of the competing exchanging mechanisms that will be important in the dilute magnetic semiconductors.

generally thought that the ferromagnetic ordering in DMS, at least in the narrow bandgap DMS, is mediated in some way by the free carriers in the material. The specifics of this exchange mechanism are not clear; several theories have been developed, and these are discussed below. Figure 2.11 summarizes some of the potential exchange mechanisms.

2.3.1 Dietl Free-Carrier Mediated Exchange Model

It has been proposed by Dietl *et al.*[22] that ferromagnetic ordering in Mn-doped dilute magnetic semiconductors is mediated by the charge carriers in the material. This theory is based on earlier work by Zener in the 1950's which was intended to explain ferromagnetism in transition metals [49]. Zener's theory, however, did not take into account the magnetic electron character or the Friedel oscillations around localized spins. However, when the distance between carriers exceeds the distance between spins (carrier concentration is smaller than the concentration of localized spins), the Zener model is equivalent to the Ruderman-Kittel-Kasuya-Yosida (RKKY) model, which takes these effects into account explicitly.

When Mn is incorporated into III-V semiconductors such as GaAs, it contributes a localized spin and acts as an acceptor, thus leading to p-type material. The carrier-mediated exchange theory predicts a Curie temperature that is dependent on the localized spin concentration as well as carrier concentration. Measurements of Curie temperature for various material systems, including $Ga_xMn_{1-x}As$ and $Zn_xMn_{1-x}Te$, match these calculations. Given this evidence, ferromagnetism in III-Mn-V and II-Mn-VI semiconductors is attributed to mediation by the hole concentration in these materials. Using a mean field approximation to this model, the Curie temperature for other semiconductors can be found from the equation:

$$T_C(x) = A_F\left(\frac{x_{eff}}{0.05}\right)\left(\beta N_O[eV]\right)^2\left(\frac{N_O(GaAs)}{N_O}\right)T_F^{nor} - T_{AF}(x)$$

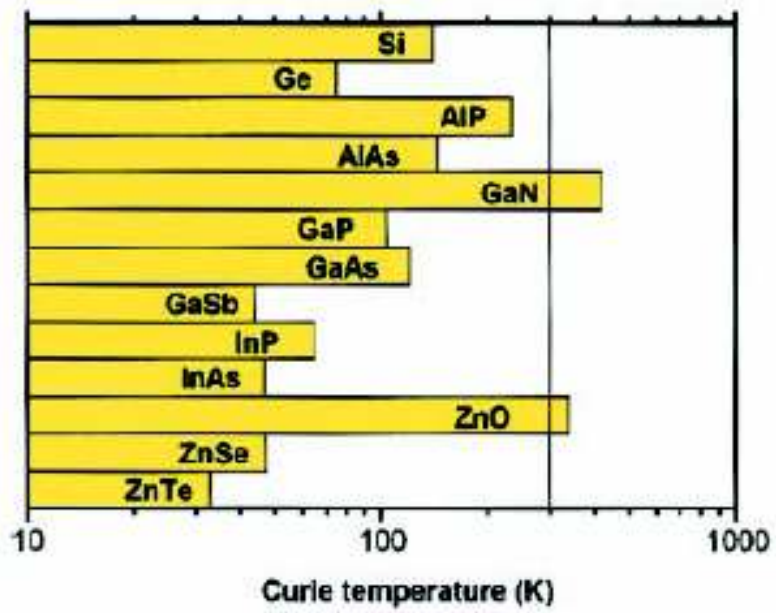

Figure 2.12 Predicted curie temperatures of some group IV, III-V, and II-VI semiconductors using the free carrier exchange model assuming 5% and 3.5×10^{20} holes. From [22].

According to this model, there remains a great deal of room for the increase of Curie temperatures in dilute magnetic semiconductors. In fact, GaN and ZnO are predicted to have T_c above 300K, as shown in Figure 2.12. This shows a tendency for lighter elements to exhibit higher T_c; this tendency arises from the fact that lighter elements have smaller lattice constants, leading to greater p-d hybridization in these materials and less spin-orbit coupling, which has a detrimental effect on T_c. The defect levels in the wide bandgap semiconductors may not be positioned to provide sufficient p-d overlap for this model to be valid.

2.3.2 Sato and Katayamo-Yoshida Model

Others have employed first principles methods in calculations to predict the band structure of ferromagnetic semiconductors [50-53]. In this work, the authors used first principles *ab initio* electronic structure calculations by the Korringa-Kohn-Rostoker coherent-potential approximation (KKR-CPA) method within the local-density

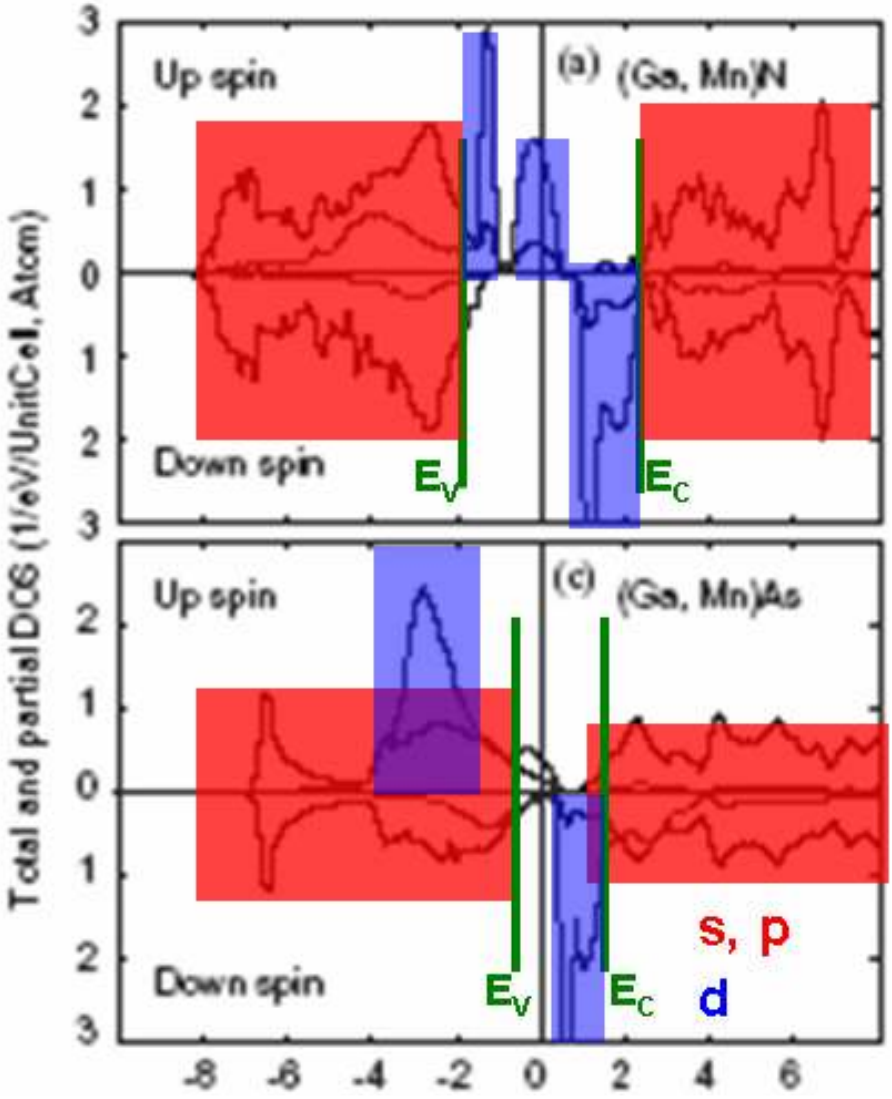

Figure 2.13 Calculated band structures for $Ga_{1-x}Mn_xN$ and $Ga_{1-x}Mn_xAs$ from first principles calculations. The approximate contributions from s,p electrons and d-electrons are highlighted. From [54]

approximation (LDA). Within this framework, it has been shown that the band structure of $Ga_{1-x}Mn_xAs$ exhibits a strong splitting in the density of states function in the valence band. The wide bandgap semiconductors also exhibit a spin-split density of states function; but, unlike the arsenides, in the middle of the energy gap. Sato and Katayama-Yoshida [54] predicted using *ab initio* calculations that there is a ferromagnetic interaction between closely spaced magnetic ions in a semiconductor lattice via shared electrons in their d-orbitals. This exchange mechanism leads to stronger coupling in materials with a smaller lattice constant because the magnetic ions are more closely packed.

Since Mn^{2+} has a d^5 configuration, there are five-fold degenerate states in an isolated atom. Within a tetrahedral crystal field, these states split into doubly degenerate states (e) and three-fold degenerate (t_2) states. The three-fold degenerate states are hybridized with the p-orbitals of nearby anions, while the doubly degenerate states are extended into interstitial areas. If the impurity band forms in the energy band gap, as in the case of $Ga_{1-x}Mn_xN$, this allows for the hopping between d-orbitals of magnetic ions.

This ferromagnetic ordering due to variable range hopping occurs because all ions and conducting electrons prefer a lowest energy configuration. According to Hund's Rules, the lowest energy occurs when all spins in the incomplete d-orbitals are parallel to one another. In this environment, shared electrons can move among ions whose spins are parallel to their own. Thus, a system with the lowest possible energy is one in which all spins are aligned parallel to each other, allowing free movement of conducting electrons among the magnetic ions [55]. This lowest-energy alignment of electron spins in the d-shells of magnetic ions provides the ferromagnetic behavior observed in magnetic semiconductors.

The original model is based on the mean field approximation, similar to what is used for the initial prediction made by the Dietl model. This approximation suggests that

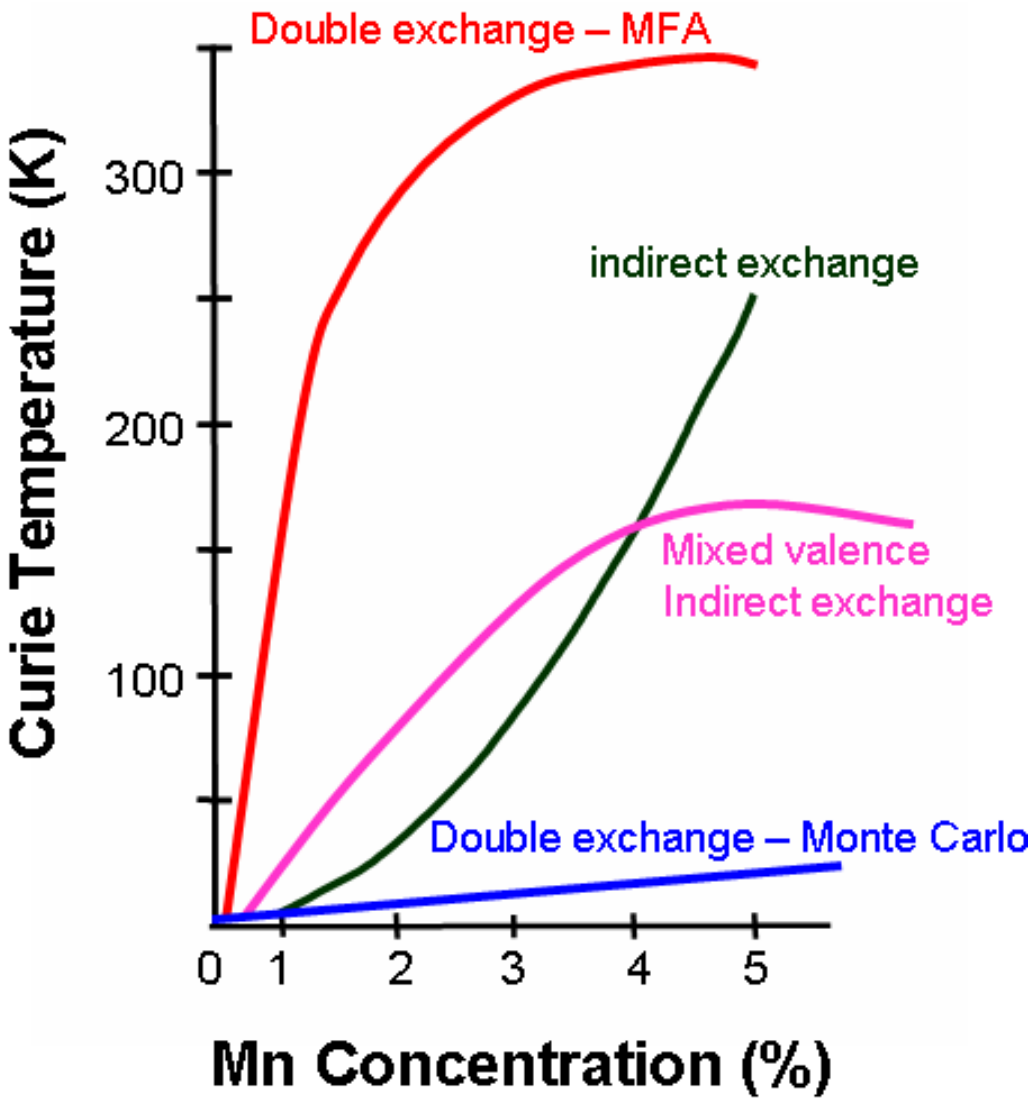

Figure 2.14: Predicted Curie temperature (T_C) versus Mn concentration in GaN using the double exchange model proposed by Sato and Katayamo-Yoshida (after Refs [54,206] and the indirect exchange model proposed by Litvinov et al. (after Refs [60,61]) a similar compositional dependence as the indirect exchange model.

the overall magnetic interaction will be the same on all atoms, assuming a uniform interaction field generated by all of the other atoms. This technique has shown reasonable agreement in the calculated Curie temperature for many semiconductor alloys in the random alloy configuration, including $Ga_{1-x}Mn_xAs$ and $Ga_{1-x}Mn_xP$ [36, 56]. A calculation of predicted Curie temperature using this approximation is shown in Figure 2.14.

First principles calculations suggest that the oxide based materials may also be made ferromagnetic by a similar double exchange mechanism [51, 54]. Figure 2.15 shows a comparison of the exchange energies for the ferromagnetic and antiferromagnetic configuration of various transition metals in ZnO. From this diagram, it is predicted that the majority of transition metal dopants in ZnO should give ferromagnetic arrangements. Mn is different than the other transition metals in this model, as ferromagnetism is predicted only if additional hole doping is present. These

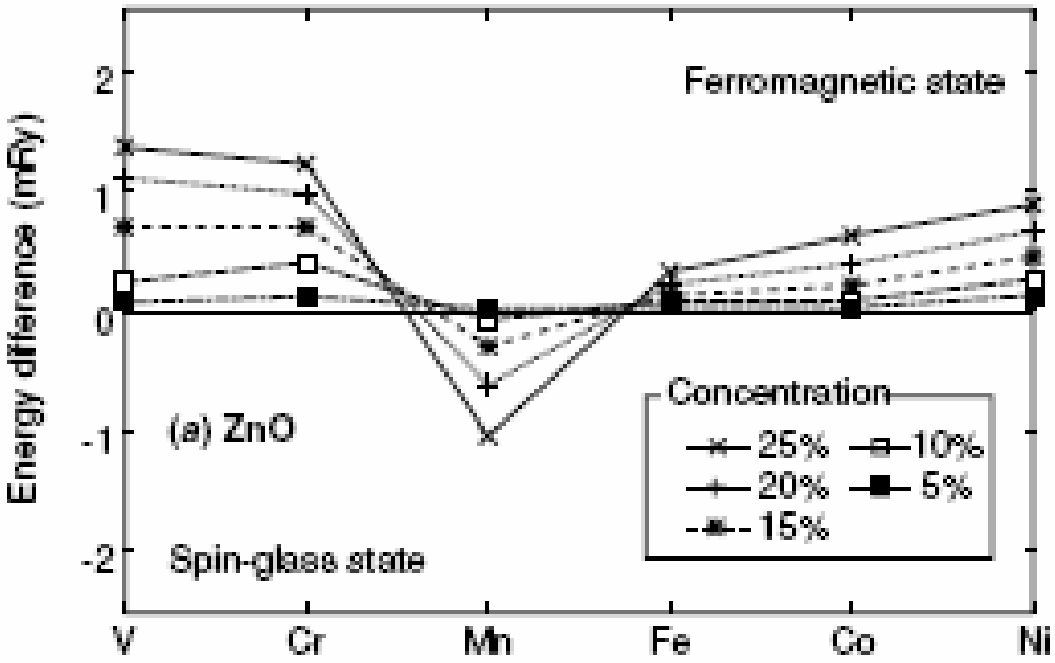

Figure 2.15 Comparison of the energy difference between the ferromagnetic and spin glass states for various transition metals in ZnO from first principles calculations. From [51]

models provide additional design guidance for the dilute magnetic semiconductors, provided that their can be realized a correlation between the theory and experimental data.

In $Ga_{1-x}Mn_xN$, it is predicted that the energy levels for the Mn acceptors lie deep in the gap [57]. This causes the wavefunctions for carriers on the transitional metal sites to be strongly localized, as shown in Figure 2.16. Thus, there is little overlap of the wavefunctions, and long range ferromagnetic exchange between isolated transition metals cannot take place. Disorder effects will be prevalent in the double exchange model. Because Zener double exchange is a short range interaction, it requires that atoms be nearby to have a strong effect. In the dilute case, there is a considerable difference between atoms uniformly spaced about the lattice and randomly spaced atoms. To produce uniform ferromagnetism across the system, there must be a percolative network of ferromagnetically coupled atoms across the lattice. If the interactions are short ranged, in the dilute case, the Curie temperature should be very low since there is a longer range function needed and thus a much weaker coupling strength. In fact, in a comparison of transition temperature versus Mn concentration according to the double exchange model with realistic Monte Carlo simulations of the atomic distribution, the predicted Curie temperature is less that 100K. To contrast, room temperature ferromagnetism is predicted when the mean field approximation is applied to this model, as shown in Figure 2.14. When these factors are taken into account, the simulated Curie temperature of dilute $Ga_{1-x}Mn_xN$ drops to <20 K. Recent reports of low-temperature MBE-grown $Ga_{1-x}Mn_xN$ films do indeed show a Curie temperature of 8 K in dilute $Ga_{1-x}Mn_xN$ with a corresponding X-ray magnetic circular dichroism signal [58, 59].

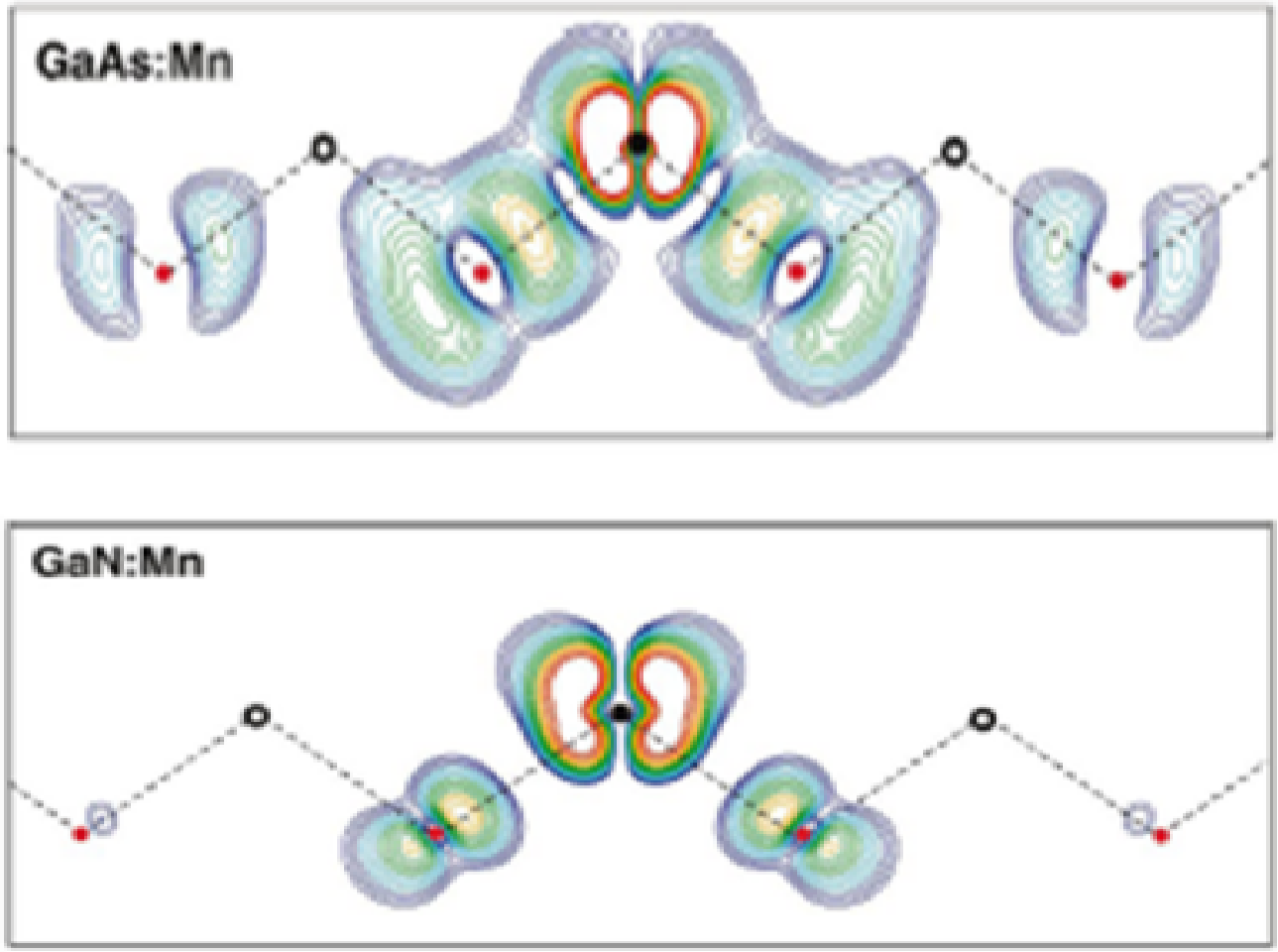

Figure 2.16. Comparison of the extent of the d-electron waverfuntions in $Ga_{1-x}Mn_xAs$ and $Ga_{1-x}Mn_xN$. From [57]

2.3.3 Litvinov Model

2.3.3.1 Basic Model

Though evidence has been shown in favor of carrier-mediated ferromagnetism in dilute magnetic semiconductors, there has been considerable debate as to whether this model is completely accurate. Non-zero T_c has been measured in samples with very low carrier concentrations. Also, as stated earlier, carrier concentration in Mn-doped DMS increases with Mn content, but this increase in Mn content also increases the concentration of localized spins.

In response to these issues, another model has been proposed, with virtual acceptor level-valence band transitions instead of electron-hole pair interactions, as the main mechanism by which ferromagnetism occurs in dilute magnetic semiconductors. In this model, the local magnetic field acting on a magnetic ion is caused by a number of nearest-neighbor magnetic ions, so that the interaction radius is much larger than the average distance between spins [60]. This provides an exchange mechanism that does not depend on carrier concentration, and can explain ferromagnetism in DMS regardless of whether or not they contain degenerate free carriers, as assumed in previous theories.

2.3.3.2 Mixed-valence Model

One major issue with the other theories that have been proposed is that they do not explicitly take into account the mixed valence character of the substitution transition metal ions. Depending on the local coordination environment and nature of the solid, it is possible through various filling of the d-electron levels to have various valences of the transition metal atoms; for example, in Fe_3O_4, both trivalent (Fe^{3+}) and divalent (Fe^{2+}) iron is present. In the transition metal doped tetrahedrally coordinated semiconductors, the valence state of the transition metal can be varied be varied through a number of techniques, as the transition metals introduce midgap states in most semiconductors.

Thus, based on the background compensating defects as well as through the introduction of other dopant species, it is possible to shift the chemical potential in these materials such that the equilibrium atomic configuration shifts. For example, shifts from 3^+ to 2^+ in $Ga_{1-x}Mn_xN$ are possible as is discussed is subsequent chapters of this thesis. Furthermore, although this feature has been observed experimentally, most theories do not directly account for this variability in the valence state of the transition metal. However, recent models using a mean field approximation to this indirect exchange mechanism do show a strong correlation between the Fermi level position relative to the $Mn^{2+/3+}$ acceptor level and the predicted Curie temperature, as shown in Figure 2.17 [61]. In this graph, the position of the Fermi level drops below this level, indicating a transition to the trivalent Mn-condition. Because this uses a mean field approximation, it may not necessarily be quantitatively accurate given the range functions involved with these exchange interactions; but qualitatively there is good agreement between coexistence of the Mn^{3+} state and strong ferromagnetism in the system, as described in more detail later in this thesis.

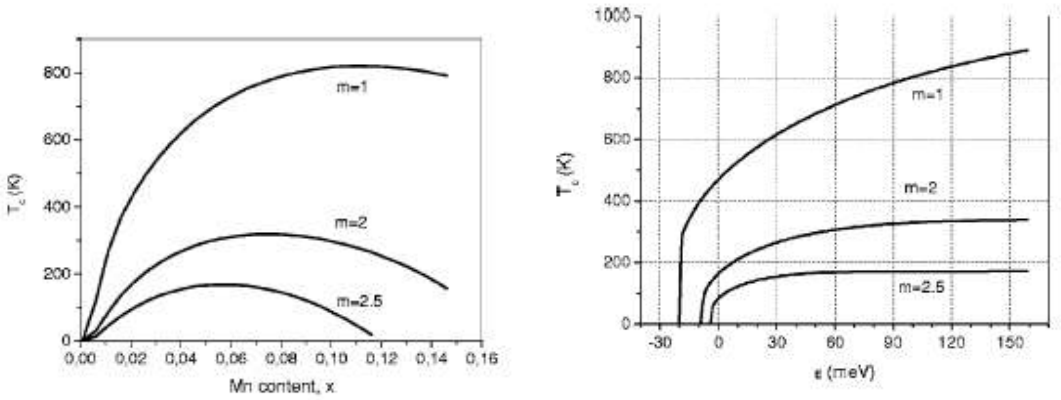

Figure 2.17 a) Percolation critical temperature as a function of different range functions b) Percolation critical temperature for various Fermi level positions for different range functions. From Ref [61]

2.3.4 Bound Magnetic Polaron Model

Though Mn concentration and carrier density appear to play a role in mediation of ferromagnetism in dilute magnetic semiconductors, the randomness of the Mn ion distribution must be taken into account. Berciu and Bhatt [62] have proposed a model that describes hole-mediated exchange in magnetic semiconductors while allowing for this random distribution.

Berciu and Bhatt base their theory on an impurity band of hydrogenic centers with spin –1/2 that are coupled to electrons in their S=5/2 state in the half-filled Mn d-orbital. The theory predicts that for low doping concentrations just above the metal-insulator transition (MIT), randomness of the ion distribution leads to an increase in T_c. This is attributed to the fact that in areas of higher Mn concentration, holes tend to hop between several Mn sites, thus lowering their total energy. This results in close coupling of these closely spaced Mn ions, which in turn leads to spin polarization at higher temperatures and thus higher T_c. However, the reverse also holds true for regions of lower Mn concentration, although simulations show that a random distribution does in fact lead to an increase in T_c [62]. At very high Mn concentrations, Mn-Mn ion interactions become important. Also, at high hole concentrations, it may be necessary to include the band states in addition to the impurity band.

2.3.5 Donor-Impurity Band Exchange Model

Another recently developed theory of ferromagnetism in these suggests that the origins of the magnetic behavior may not be related to interactions between intrinsically pure material. Instead, the defect centers are essential for mediating ferromagnetism in these materials. This observation was based partially on the observation that in ZnO thin films, there was a strong correlation between the magnetic moment and the interfacial area [63]. This work introduces the possibility that it is not the pure bulk material which leads to an overall ferromagnetic behavior, but rather the defects and interfaces play a

crucial role in determining the overall magnetic behavior of the system. In this case, the magnetic interaction is also mediated through the percolation of bound magnetic polarons, which in this case are centered on a donor. For ZnO, this donor has been suggested to be an oxygen vacancy defect, i.e. an f-center. Thus, in order to achieve a strong long-range magnetic interaction, it is essential to have an adequate number of vacancies, as well as a sufficient carrier concentration, such that ferromagnetic percolation may take place. This approach seems to have some evidence in the oxide based materials, and may have some extension to the counterintuitive d^0 ferromagnetism [64] and unusual ferromagnetic interaction observed in copper-containing materials [65]. Recent evidence in solution-grown ZnO nanocrystals suggests that there is evidence for p-type impurity band interaction in $Zn_{1-x}Mn_xO$ and n-type band in $Zn_{1-x}Co_xO$ [66]. However, because the polaronic radius is inversely proportional interaction to the depth of the impurity level within the band, it is unlikely that percolation would be achievable at low concentrations with a deep donor or acceptor center, as is the case in nitrides. Figure 2.18 shows a schematic of the band splitting induced by this model.

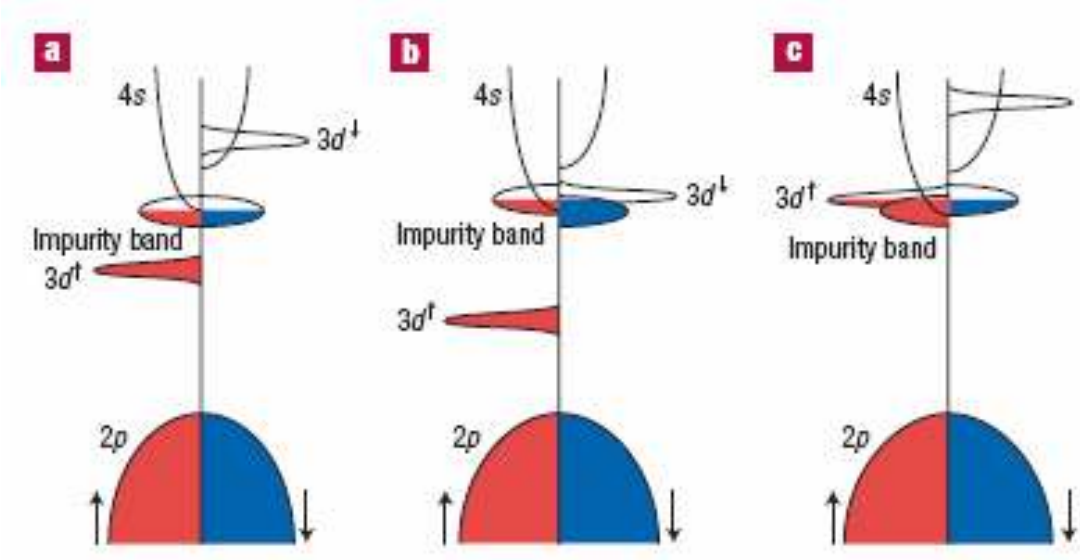

Figure 2.18 Comparison of three different possible impurity band alignment. The first would lead to comparatively low temperature ferromagnetism, whereas the latter two would result in high temperature ferromagnetism. From [63]

2.3.6 Transition Metal Clustering Models

It is imperative to note that the well-accepted arsenide DMS are grown by techniques such as low-temperature molecular beam epitaxy (LT-MBE) in order to avoid phase segregation. As this technique uses a non-equilibrium growth method at a temperature that minimizes diffusion during growth, it can be termed 'far-from-equilibrium'. On the other hand, the nitride materials to date have not necessarily been produced by such far-from-equilibrium techniques, but instead are produced using methods which require either elevated temperature or post-growth elevated temperature processing. Figure 2.19 shows some potential atomic distributions of transition metal atoms within a dilute magnetic semiconductor lattice. The degree to which the transition metals exhibit a completely random distribution, a completely phase-separated distribution, or some sort of intermediate phase where the Mn atoms are embedded in clusters within the material, will have a profound impact on the observed magnetic behavior, at least according to some first principles calculations.

2.3.6.1 Van Schilfgaarde Model

In order to determine the ultimate origin of ferromagnetic behavior in the diluted magnetic semiconductors, it is essential to analyze the local arrangement of Mn atoms within the semiconductor lattice, and also to look at the variation in exchange energies of the system according to the relative orientation and coupling between nearby Mn atoms, in particular in dimer and trimer configurations. Upon performing an analysis using first principle local spin-density approximation density functional theory calculations, Van Schilfgaarde and Myrasov found that relative to isolated Mn atoms, the formation of dimers and trimers is energetically favorable in the MnAs system. Moreover, comparison

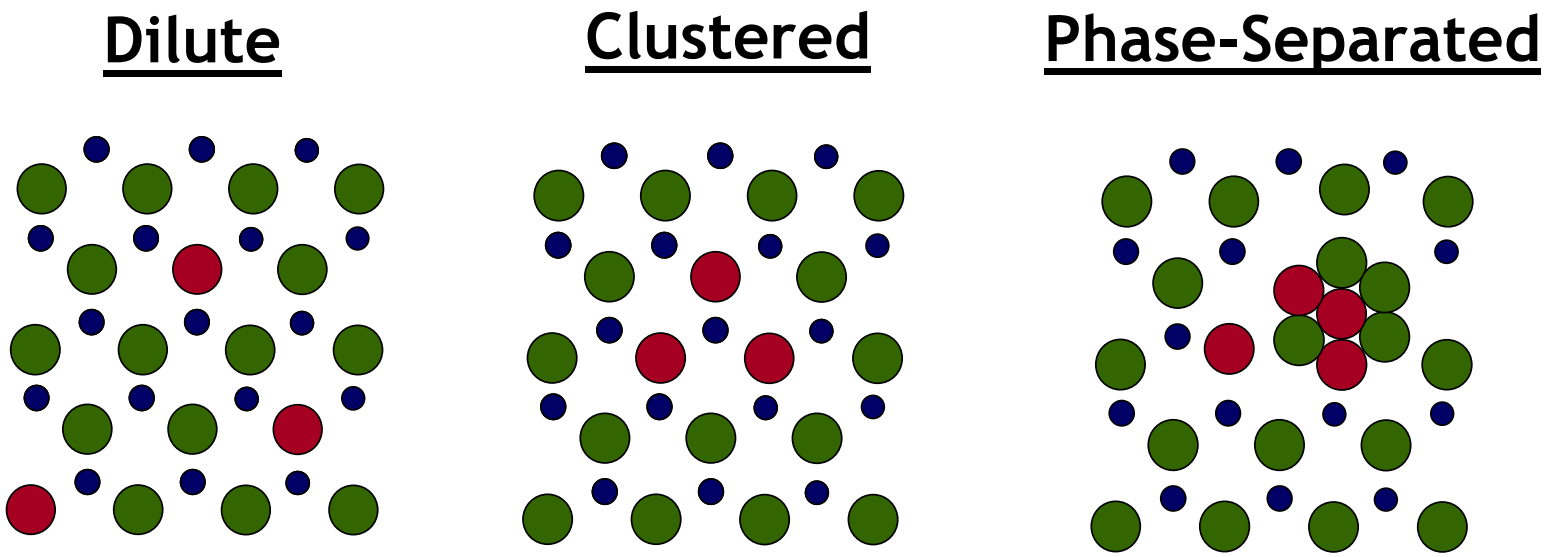

Figure 2.19: Schematic showing some potential atomic configurations that can be present when a transition metal is doped into a semiconductor lattice.

of the interaction energy between the ferromagnetic double exchange and antiferromagnetic superexchange, predicts that the ferromagnetic arrangement is thermodynamically stable. Thus, as the Mn arrangement shifts from random to dimer- and trimer-like, there is a predicted thermodynamic tendency towards the formation of high Tc ferromagnetic clusters within the system. Cr shows similar behavior and a similar tendency towards strong ferromagnetism, whereas Fe shows a strong predilection for antiferromagnetic ordering. This would provide a method for elucidating this model through the variation of the incorporated transition metal within the lattice. Based on a change in growth conditions in the $Ga_{1-x}Mn_xAs$ system, with a transition to higher temperature and chemical vapor deposition environment, it has been suggested that this model adequately describes the anomalously high Tc in MOCVD-grown $In_{1-x}Mn_xAs$. Whether MOCVD-grown $Ga_{1-x}Mn_xN$ will exhibit a similar clustering tendency as in $In_{1-x}Mn_xAs$ is still yet to be determined.

2.3.6.2 Rao and Jena Model

Other models using first principles calculations have extended the theoretical analysis into clusters in the $Ga_{1-x}Mn_xN$ system. In particular, Rao and Jena [67] have used a molecular orbital theory and a generalized gradient approximation for the exchange-correlation energy to show that the presence of nitrogen stabilizes the formation of Mn-rich clusters, and also tends to result in a ferromagnetic arrangement of Mn atoms in these small nanoclusters. Anomalously high magnetic moments can be observed from these clusters, to a value of roughly 17 μ_B for a Mn_4N cluster. Rao and Jena have theorized that this may be the origin of the high Tc ferromagnetism which is often seen in the literature, but this is extremely difficult to verify experimentally due to the small size of the clusters involved.

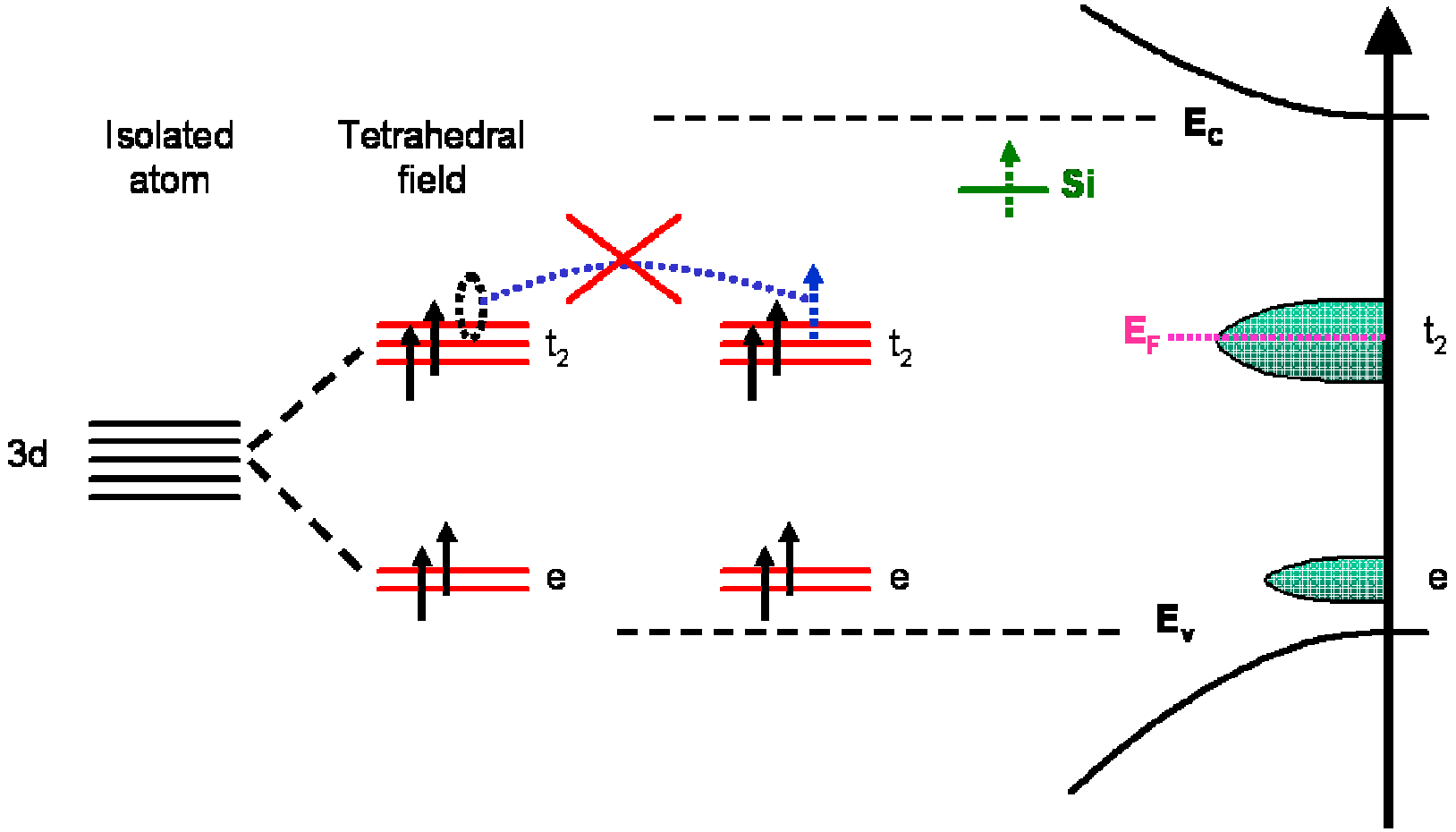

Figure 2.20: Phenomenological model and band filling as a route towards room temperature ferromagnetism in the GaN based dilute magnetic semiconductors.*

2.3.7 Phenomenological Models for Ferromagnetism in $Ga_{1-x}Mn_xN$

In spite of considerable theoretical efforts to develop an underlying theory of ferromagnetism in $Ga_{1-x}Mn_xN$, there are several experimental observations that are difficult to reconcile with the prevailing theories of ferromagnetism [68]. In order to reconcile this disparity, some experimentalists have sought to explain the observed experimental observations [69]. One such model states that the ferromagnetism in the wide bandgap nitrides is mediated by hopping conduction of carriers in a mid-gap spin polarized impurity band, as shown in Figure 2.20. This mechanism, at least on the surface, is similar to a de Gennes-type double exchange mechanism [70], which is observed in some transition metal perovskite compounds. This is consistent with experimental observations of a midgap absorption feature as well as experimental evidence of hopping conduction in these materials. Moreover, recent results, as shown in Figure 2.21, exhibit a decrease in magnetization with decreasing temperature, which has been attributed to carrier freezeout within the system [71]. This approach seems to phenomenologically describe the observed results; however, the localized nature of the midgap d-electron states [57] precludes the overlap of the electron wavefunctions, which is essential for the formation of such an impurity band. Thus, in order to understand or

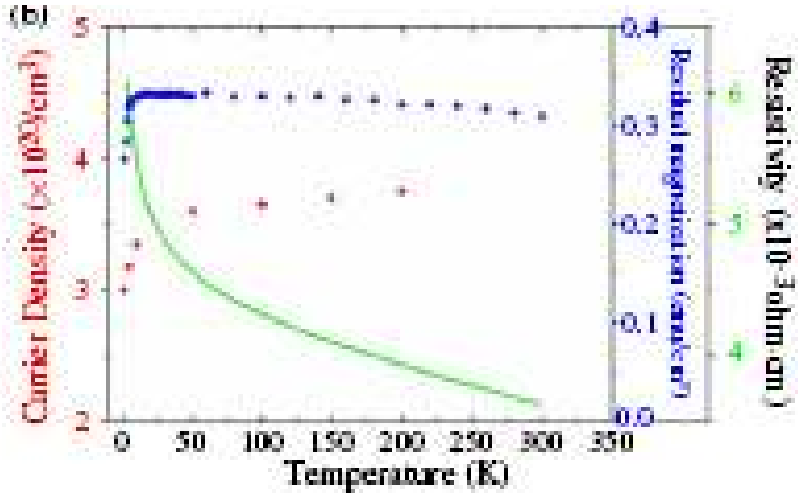

Figure 2.21: Temperature dependence of M vs T curve and its relation to carrier density and resistivity in MBE-grown $Ga_{1-x}Mn_xN$ with a Tc > 400 K. From Ref [70].

prove the validity of this model, it will be necessary to understand how such a robust and long range ordering can be achieved with what is typically a short-ranged interaction.

The rare earth-doped nitrides show a different trend and different phenomenon which appears to be at work in these systems, at least according to a another experimentally developed phenomenological model. In contrast to the observation of ferromagnetism in the transition metals, which obeys typical expectation values for the magnetization strength relative to the concentration, giant magnetic moments have been reported in $Ga_{1-x}Gd_xN$ [72]. Because there is no way to wholly attribute the reported magnetic moments to the rare earth concentration, it has been suggested that the Gd atoms polarize the spins within the GaN lattice and contribute to the overall magnetization in the sample. It is unclear which free spins become polarized, whether they are associated with carriers, point defects, or surface atoms. Such giant magnetization has also been reported for other materials systems; but if this mechanism holds, it is unclear why it sometimes appears in GaN, but does not appear in other materials systems. In addition, there are other reports of magnetization in the normal (on the order of one Bohr magneton per atom) regime [73] in grown samples of the same material system. Whatever the mechanism for high temperature ferromagnetism, particularly if it is due to one of these phenomenological models, at some point there must be a convergence of the solid state physics and the observed materials behavior.

2.3.8 Superexchange Interactions

Another omnipresent exchange interaction in these materials is the coupling of nearest neighbor transition metals through the shared anion. This mechanism was demonstrated by Lewicki *et al.*[74] as the major mechanism in effect for the II-VI dilute magnetic semiconductors. Magnetic ordering in Mn-doped dilute magnetic semiconductors stems from interaction of magnetic cations via a shared anion. This mechanism, known as superexchange, involves the virtual hopping of carriers between

completely filled p-orbitals of anions and half-filled d-shells of the magnetic Mn^{2+} cations. In order for electrons from both adjacent atoms to occupy the same p-level, they must be opposite in spin based on Pauli Exclusion Principle considerations. This leads to an antiferromagnetic coupling of nearest-neighbor cations through a shared anion. Magnetic susceptibility measurements of Mn-containing ternary and quaternary semiconductor compounds with varying energy gaps show that susceptibility is independent of energy gap, but not independent of Mn mole fraction [74]. Also, estimations for second-nearest-neighbor interactions show that they are much smaller than nearest-neighbor interactions, which supports the superexchange theory [51].

The magnetic moment of Mn in II-VI materials was found to be S~5/2, which is expected for the $3d^5$ high-spin configuration for Mn^{2+}. This indicates that Hund's Rules are fulilled in the high spin configuration and that the interaction results in hybridization of the p-orbital in the anions and the d-orbital in the magnetic cations. The crystal field stabilization energy, at least in the narrow bandgap materials, is insufficient to induce a transition into the low spin configuration. Superexchange is also present in the nitrides, although the strength of the exchange integral is roughly one order of magnitude less than in the oxide-based materials [75].

2.4 Obstacles to the Growth of Wide Bandgap Diluted Magnetic Semiconductors

Despite the considerable interest in these novel materials systems, there are several challenges to the development of both GaN and ZnO-based wide bandgap dilute magnetic semiconductors. Just as these materials were developed later for typical electronic applications, the challenges in the production of GaN and ZnO for spintronic applications have also caused the study of the wide bandgap materials to lag behind their other III-V and II-VI counterparts. Any discussion of the relative difficulties must address issues in creating lattice-site incorporation of a phase pure semiconductor; these are discussed in more detail below.

2.4.1 Phase Segregation

As mentioned before, the relative solubility on the gallium sites in these III-V materials is quite low, well less than 1% in most cases. Therefore, non-equilibrium growth techniques such as molecular beam epitaxy (MBE) and metalorganic chemical vapor deposition (MOCVD) must be used. In the arsenides ($Ga_{1-x}Mn_xAs$ and $In_{1-x}Mn_xAs$), this problem is compounded by an extremely stable hexagonal binary manganese arsenide (MnAs) phase. In order to prevent the formation of this phase, low temperature molecular beam epitaxy or other highly non-equilibrium techniques must be used.

The nitride-based ferromagnetic semiconductors will have considerable obstacles to their fabrication as well. In particular, the roles of phase separation and magnetic atom clustering have not been well investigated in the nitrides. A number of phases have been reported to form under non-optimal growth and annealing conditions, including Ga_xMn_y intermetallics, $Mn_6N_{2.58}$, Mn_3N_2, and Mn_4N [76-78]. Note that none of these are 1:1 binary compounds, and thus they may have very different nucleation and growth behavior than in the arsenides. The $Mn_{4-x}Ga_xN_{1-y}$ series is of considerable interest regarding the ferromagnetic behavior of these materials. This materials system has been shown to be one of the key decomposition products under annealing or non-optimal growth of these compounds [79, 80]. Due to Ga-Mn site disorder, it can result in a ferrimagnetic metallic perovskite phase with Curie temperatures ranging from 270 K to 743 K [81]. Similar Curie temperatures have been reported in the literature, and this phase does have structural properties where it is commensurate with the wurtzite lattice [82]. In addition, the growth temperatures used in the preparation of the nitride-based materials are often much closer to normal processing temperatures that what is reported for $Ga_{1-x}Mn_xAs$. Methods such as ion implantation, which are not suitable growth techniques for DMS behavior in the arsenides, have been reported to produce

ferromagnetic $Ga_{1-x}Mn_xN$. All of these behaviors point to a very different mechanism in the production of the nitride based materials relative to the arsenides.

The use of II-VI compounds such as ZnO and II-IV-V chalcopyrites presents an attractive alternative for achieving high transition metal concentrations within the lattice. Based on simple Hume-Rothery considerations, the transition metal solubility on the group II site should be much higher. In fact, at temperatures of 700^{o}C, the solubility limit has been established to be greater than 10% in ZnO [83]. However, this comes at the expense of a major problem with respect to the second criteria. Specifically, p-type doping in ZnO is difficult, and it is unrealistic to assume that such high hole doping levels will be possible in this II-VI system.

2.4.2 Lattice Incorporation and Carrier Concentrations

In the arsenide-based dilute magnetic semiconductors, Mn is incorporated on the group III lattice site. Based on the electron affinity of the transition metal, this compound acts as a shallow acceptor, roughly 100 meV above the valence band edge of the GaAs system [57]. As such, the introduction of Mn has the simultaneous beneficial effect of introducing free carriers as well as the residual d-spins necessary for magnetic behavior. This lattice site incorporation is essential, as non-lattice site occupancy would produce a neutral or donor impurity state. In addition, the presence of Mn and the low growth temperatures used promote the formation of other defects, including Mn interstitials and arsenic antisites, both of which act as donor species and compensate for the free electron concentrations imparted to these materials. Thus, for the development of future electronics based on the wide bandgap materials, it will be essential to understand how the processing conditions affect the defect structure of the systems, though nitrogen antisites are highly energetically unfavorable in the nitride system [84].

Another controversial aspect of ferromagnetism in the nitrides compared to the arsenides is carrier concentrations within the material. According to the original mean

field theory, the carrier concentrations to observe ferromagnetism are typically about 10^{20} cm^{-3} with Mn concentrations of 5%. Similarly, in ferromagnetic II-VI DMS, the carrier concentration can be controlled through external dopants, and with an increase in carrier concentration, an increase in the magnetic ordering temperature is observed. Such high hole concentrations are unlikely in the nitrides and oxides, as typical p-type carrier concentrations are roughly two orders of magnitude lower in the nitrides and nearly non-existent in the oxides. Moreover, the observed background carrier type in $Ga_{1-x}Mn_xN$ is usually n-type [85]; otherwise, the material is highly resistive. Temperature dependent resistivity measurements have indicated that activated variable range hopping is the key transport mechanism within these materials [71]. In addition, strong ferromagnetism is observed at Mn concentrations well below 5%. These observations are inconsistent with validity of any sort of free carrier mediated mechanism for the nitrides.

2.5 Current Experimental Status of Wide Bandgap DMS

2.5.1 Current Experimental Status of Transition Metal Doped ZnO

Since the prediction of room temperature ferromagnetism within the wide bandgap semiconductors, numerous attempts have been made to produce these materials. This has resulted in a number of reports of ferromagnetism in the $Zn_{1-x}Mn_xO$ and $Zn_{1-x}Co_xO$ materials systems by numerous production methods, including pulsed laser deposition [86-88], ion implantation [89, 90], molecular beam epitaxy [91], and solid state reaction [92, 93]. The results to date are still somewhat controversial, and so far there is not a convergent picture of the processing techniques and criteria to routinely and reliably obtain room temperature ferromagnetism. In spite of this, there are several reports of ferromagnetic behavior in the $Zn_{1-x}TM_xO$ systems for TM=Mn, Co, and Fe[89, 90, 92, 94, 95]. Figure 2.22 shows the diversity and disparity of the reported magnetic behavior for the $Zn_{1-x}Mn_xO$ system.[90-92, 96-100].

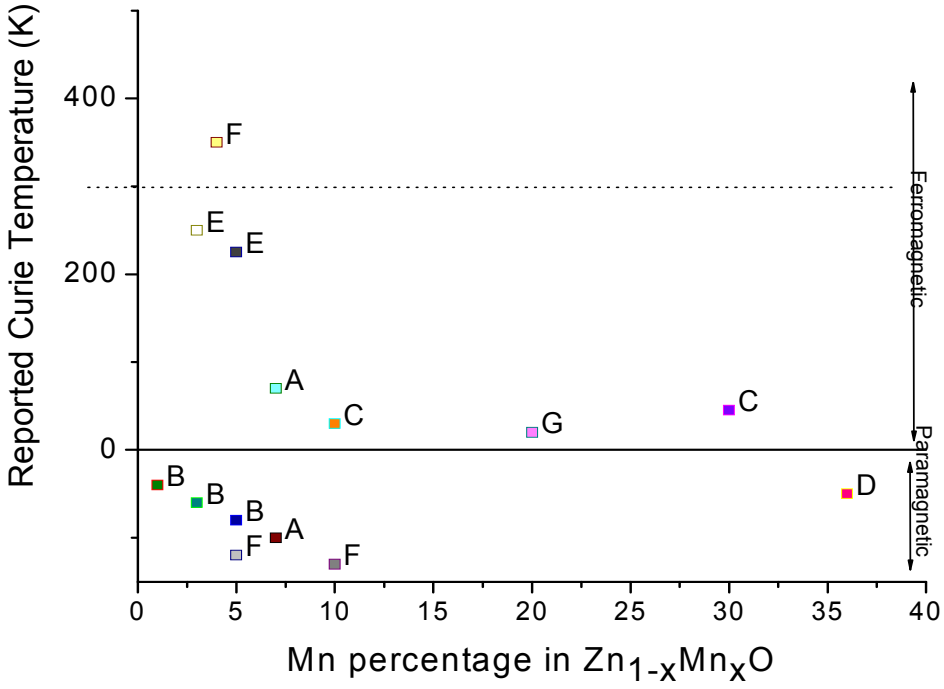

Figure 2.22 Experimental results in the $Zn_{1-x}Mn_xO$ system for samples grown by a number of different methods. Depending on the growth technique, behavior ranging from paramagnetic dominated by antiferromagnetic superexchange interactions to room temperature ferromagnetism at dilute concentrations has been observed. Growth methods are labeled as A- magnetron sputtering, B- modified melt growth, C- molecular beam epitaxy, D- pulsed laser deposition, E-ion implantation , F-solid state reaction, G-sol-gel

ferromagnetic behavior is largely a function of the processing conditions; often, highly non-equilibrium methods are still needed to produce ferromagnetic material, including low temperature solid state reaction methods[92] or post-process vacuum annealing of thin films grown by pulsed laser deposition[101]. It should be noted that neither of the two routes for observed ferromagnetic behavior is consistent with standard 'high quality' semiconductor material. Moreover, these experiments have been plagued by highly process-dependent properties, very often with minimal reproducibility [86].There are also several reports for $Zn_{1-x}Mn_xO$ and $Zn_{1-x}Co_xO$ that do not exhibit ferromagnetic behavior[98, 99], and recent results have provided evidence that ferromagnetism in $Zn_{1-x}Mn_xO$ is not an inherent property of the system but could be due to secondary phases or clusters[102]. To date, it has been difficult to ascertain whether this ferromagnetism is an intrinsic property of the material or an artifact of certain production methods. This problem is further complicated in thin film measurements, as any magnetic signature from the substrate can significantly contribute to the measured signal.

2.5.2 Transition Metal Doped GaN

The search for $Ga_{1-x}Mn_xN$ films that exhibit ferromagnetism above room temperature has been facilitated by recent developments in the growth of DMS. A summary of sample data of the reported magnetic data in the literature for $Ga_{1-x}Mn_xN$ is shown in Figure 2.23 [75, 77, 79, 82, 103-112]. Room temperature ferromagnetism has been reported in $Ga_{1-x}Mn_xN$ films grown by molecular beam epitaxy (MBE)[85], post-growth diffusion [82], and in Mn-implanted GaN epilayers[113, 114]. Ferromagnetic behavior is still highly controversial, as there are several competing theoretical approaches to explain the origin of room temperature ferromagnetism in group III nitrides [22, 54, 62, 63]. The thermodynamic tendency towards forming ferromagnetic second phases and/or nanoclusters leads to an increase in the complexity of this field.

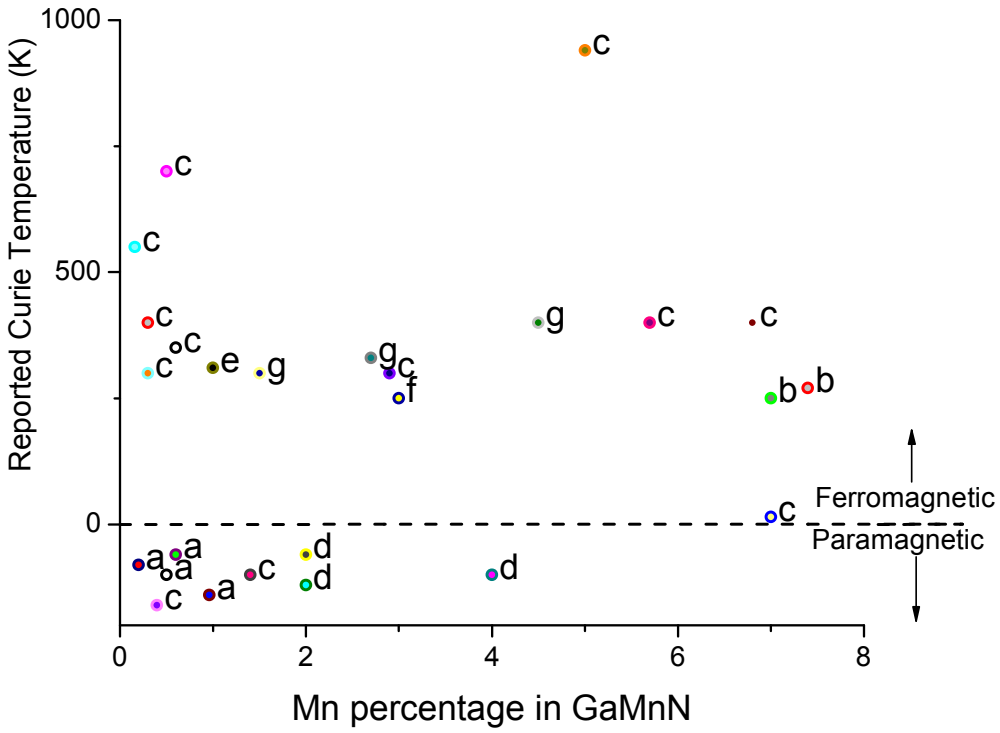

Figure 2.23 Summary of some of the reported experimental results in the $Ga_{1-x}Mn_xN$ system for samples grown by a number of different methods. Ferromagnetic behavior near or above room temperature has been observed for thin film samples prepared by several non-equilibrium growth techniques. Data points below the horizontal dashed line have other than ferromagnetic behavior. Growth techniques are abbreviated as follows :MBE – molecular beam epitaxy, MOCVD – metalorganic chemical vapor deposition, a – ammonothermal growth, b – ion implantation , c– molecular beam epitaxy, d- gas phase reaction, e – post growth diffusion, f – nebulized spray pyrolysis, g – metalorganic chemical vapor deposition

Ferromagnetism which is closely coupled with the free carriers in the system would be ideal for a majority of room temperature spintronic devices[22, 54, 62, 74]. Curie temperatures (T_C) of up to 940 K [109] have been reported, depending on growth conditions.

There are limited reports involving Mn-incorporation into GaN films grown by metalorganic chemical vapor deposition (MOCVD) at dopant concentration levels [115]. The magnetic properties of MOCVD-grown $Ga_{1-x}Mn_xN$ with requisite manganese concentrations for DMS behavior are largely unexplored in the literature. RT ferromagnetism in $Ga_{1-x}Mn_xN$ is also still controversial; the materials are insulating and do not exhibit band edge magnetic circular dichroism [116], which is an indicator of mean-field DMS behavior in $Ga_{1-x}Mn_xAs$. Additionally, second phases such as GaMn or Mn_4N have been observed through transmission electron microscopy (TEM) and x-ray diffraction (XRD) in heavily-doped samples produced by MBE [76, 78]. These phases are sometimes attributed as the sole source of ferromagnetism in these materials. Furthermore, there is little evidence at this time to support the conclusion that the currently produced RT ferromagnetic films of $Ga_{1-x}Mn_xN$ have any coupling between the free carrier concentration (either in the valence or in the conduction band) and the magnetic centers, which would be required for practical spintronic applications.

2.5.3 Discussion

Several features of the reported ferromagnetism in these materials are not well-understood in light of the cluster and phase separation based models. In addition, the high Curie temperatures reported are not completely consistent with any of the prevailing theories of ferromagnetism. Presumably, if the ferromagnetic behavior were due to phase separation or clustering, then increasing the transition metal concentration or clustering

should increase the formation of these magnetic phases and the magnetic signature. In fact, the opposite is observed in both $Ga_{1-x}Mn_xN$ and $Zn_{1-x}Mn_xO$:Sn[90, 112]; increasing the Mn concentration reduces the magnetic contribution per atom due to increasing superexchange, and the ferromagnetic behavior can even be destroyed upon heavy alloying.

It has been suggested that clustering leads to the observed hysteresis, though these clusters have yet to be observed in ferromagnetic samples via electron paramagnetic resonance[117], extended x-ray absorption fine structure measurements[79], and/or transmission electron microscopy[118]. In fact, it has been demonstrated that an overwhelming percentage of atoms will reside on the lattice sites in $Al_{1-x}Cr_xN$ [119]. Clustering cannot explain the strength per magnetic atom observed in optimized $Ga_{1-x}Mn_xN$ growth either, since almost all of the Mn atoms must be involved with clustering to achieve the measure magnetization values. When clustering and second phases do become visible via x-ray diffraction, there is the similar expected superparamagnetic cusp in the zero field cooled magnetization behavior that is not observed in phase-pure ferromagnetic samples.

Some irreversibility is commonly observed in the published ZFC/FC curves of homogeneous thin films. The double exchange model looks promising as an explanation for the ferromagnetic behavior, but this interaction is typically short range. At dilute concentrations, it would require third or fourth nearest neighbor interactions to be ferromagnetic in order to form a percolation network resulting in ferromagnetic behavior. First principles calculations do suggest that up to fourth nearest neighbor interactions may couple ferromagnetically along certain directions, but at energies far less than would be needed for room temperature ferromagnetism[57]. If indeed the double exchange model holds, it must be demonstrated why this typically weak and short-ranged interaction can result in robust ferromagnetism in these materials.

Much of the confusion regarding the nature of ferromagnetism in dilute magnetic semiconductors results from the difference in growth methods used to produce these materials. This can result in material of widely varying quality. Though all of these reported samples may nominally be termed $Ga_{1-x}Mn_xN$ or $Zn_{1-x}Mn_xO$, these samples can exhibit vastly different observed materials properties due to the dissimilar nature of the structural and electronic defects within the material. Thus, in order to separate out intrinsic properties of the material from those that could be caused by artifacts of the growth technique used, it is imperative to be able to grow high-quality material. This study focuses on two such techniques in the wide bandgap materials system: melt growth and metalorganic chemical vapor deposition (MOCVD). For ZnO, it is possible to grow high quality single crystals using modified melt growth techniques [120]. Because the predicted solubility limit of transition metals in ZnO can be high, these carriers can be introduced in the melt phase of growth at dilute concentrations. For GaN-based materials, metalorganic chemical vapor deposition is regarded as the choice for producing high quality material for electronic and optoelectronic devices. This technique has overcome the limitation of not having lacking a lattice-matched substrate and has also circumvented the p-type doping issues, without some of the polarity and inversion domain problems that plagued the early years of MBE GaN seen in other growth techniques. It remains to be shown whether or not these two growth routes are suitable for producing high-quality ferromagnetic $Zn_{1-x}Mn_xO$ and $Ga_{1-x}Mn_xN$.

CHAPTER 3

EXPERIMENTAL PROCEDURE

3.1 Bulk Single Crystal Growth of ZnO

3.1.1 Overview of Bulk growth methods

One of the key features in the rapid development of semiconductor electronics over the past several decades was the realization and implementation of high quality, ultra-pure single crystals [2]. In addition, the ability to produce single crystals of ZnO is one of the drivers for investigating this materials system as a competitor to GaN for lighting applications, as homoepitaxy naturally leads to higher quality material and enhanced device performance [121] III-nitrides are generally limited to heteroepitaxial growth, as high quality GaN substrates require an excessive pressure to produce and cannot be done in large wafer form. Recent efforts to grow these substrates through hydride vapor phase epitaxy have shown some success in reducing the defect densities [122, 123].

Single crystal growth techniques generally fall into one of three categories: growth from a melt, growth from solution, or vapor phase deposition growth. The most commonly used method for the growth of silicon single crystals is the Czocralski technique, where a seed crystal is used to pull a larger crystal from a melt of the sample to be grown. This technique works well for Si and other materials such as sapphire, but its use for ZnO is less well-established. Another technique that is suitable for high-

volume synthesis of ZnO single crystals is hydrothermal growth [124, 125]. In this technique, ZnO crystals are growth through precipitation onto single crystal seeds in an autoclave. Though this process can produce nominally large single crystals, the process requires the use of mineralizers such as lithium in order to control the growth of these crystals. These additives can be problematic, as they often are incorporated and diffuse into the single crystals and lead to electronic compensation of carriers found within the materials or lead to complications in the formation of electronic devices based on these materials.

3.1.2 Cermet Melt Growth method

This work focus on single crystals grown by another technique performed in collaboration with Cermet Inc. The high quality melt grown crystals were produced using a proprietary pressured melt growth process[120, 126]. This approach exploits a patented method of melting and crystallizing materials that have volatile components or have thermodynamic instabilities at or near the melting point of a material. A schematic of the growth apparatus is shown in Figure 3.1. The system used an RF induction melting process. Eddy currents developed in the material result in joule heating of the system. Reaction with the crucible is prevented through water cooling. This process has several advantages over other growth techniques; issues with crucible reactivity, crystal contamination and decomposition have been minimized sing a high pressure variation of the established induction melting technique. Using this technique, both undoped crystals and crystals doped at various levels of up to 5% Mn and Co were produced. In order to introduce the alloying element, stoichiometric amounts of the powders of a cobalt or

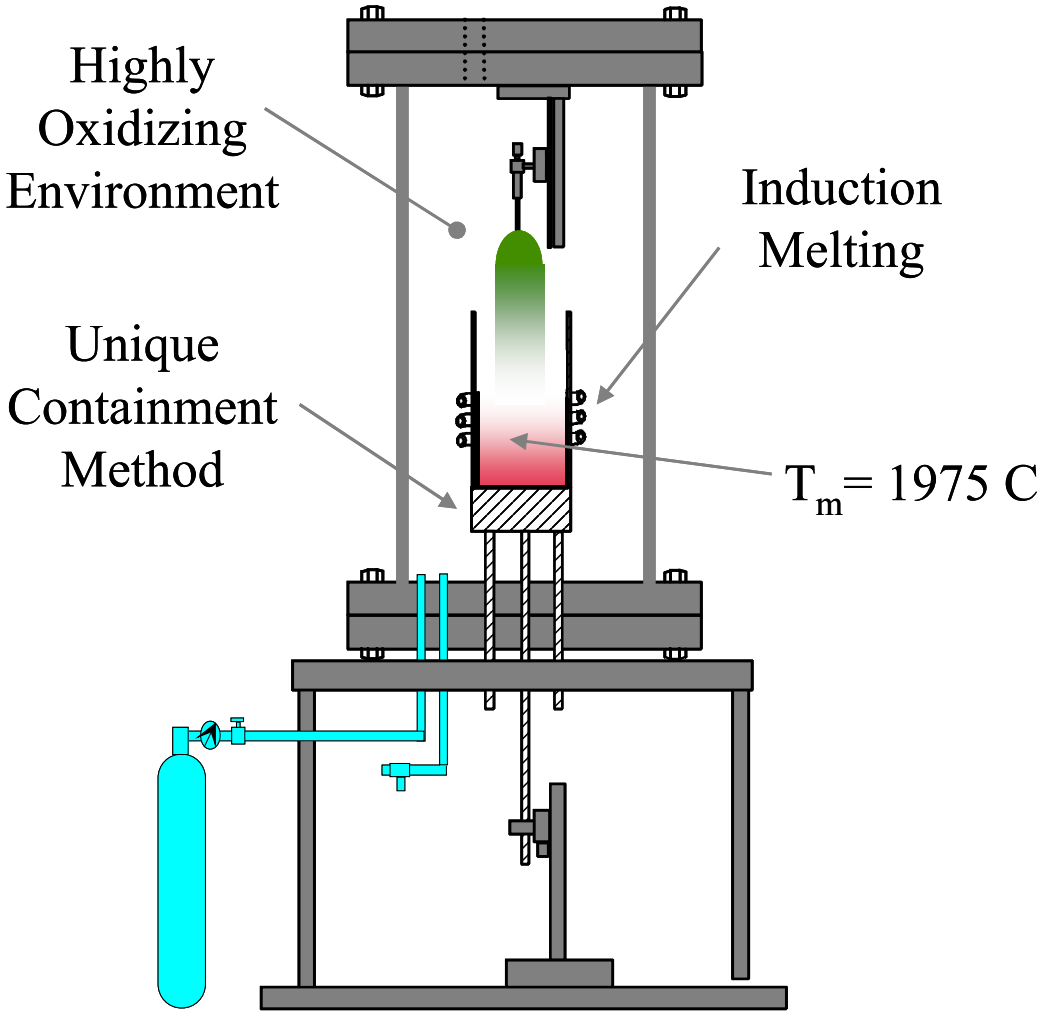

Figure 3.1 Schematic of the growth setup used for the growth of the bulk single crystals used in this study.

manganese precursor were introduced to the ZnO precursor powder prior to start of the melt growth process.

3.2 MOCVD growth of GaN

3.2.1 Challenges to GaN crystal growth

The development of GaN based semiconductors occurred much later than other group III-V and group IV semiconductors, primarily because a number of materials related challenges for the growth of these materials. For example, whereas silicon devices were developed in the mid-1950s and GaAs-based devices appeared in the 1970s, it was not until the early 1990s that gallium nitride based devices began to appear. The challenge that exist with the MOCVD growth of GaN still persist to this day and are an intense area of both academic and industrial research.

The first major problem that needs to be overcome for the growth of gallium nitride is the lack of a suitable lattice matched substrate for GaN. Ideally, for the growth of high quality material with a low dislocation density, homoepitaxial growth is preferred. However, because GaN is a refractory material with a melting temperature in excess of 1800 K, it is very difficult to produce single crystals of GaN by the standard single crystal growth techniques. An alternate approach is to use heteroepitaxial growth techniques ideally with a lattice matched substrate, as this can also lead to a low epitaxial strain and a lower critical thickness before the appearance of misfit dislocations. However, even the identification of latticed matched substrates in GaN is problematic. Instead of being the cubic zincblende structure as is common in most III-V semiconductors, the equilibrium phase of GaN is the hexagonal wurtzite phase. Thus, there are fewer substrates available simply because of the lower relative number of

hexagonal compounds to cubic compunds. Figure 3.2 shows a plot of the bandgap energy and lattice parameter diagram of GaN and some heteroepitaxial substrate materials. The most widely used candidates are the 6-H polytype of SiC, which has a lattice mismatch of 3.6%, and sapphire (corundum), which through a 30° rotation to a [1-100]GaN||[11-20]Al_2O_3 epitaxial arrangement has a 16% lattice mismatch.

The second major obstacle to the growth of GaN-based devices lies in the difficulty in p-doping the material. Both n- and p-doping are essential elements of heterostructure based devices including heterojunction bipolar junction transistors and light emitting diodes. The background intrinsic defects in GaN are almost universally n-type because the valence band minimum is far from the vacuum level [127]. Moreover, no shallow acceptors are known for this material. Thus, it is difficult to overcompensate the intrinsic defects and introduce sufficient hole carriers in III-nitride devices in order to produce heavy p-type doping in these materials. In fact, it was the simple realization of p-type material that was one of the key advances for mainstream introduction of the III-nitrides, as described below.

3.2.2 Historical perspective

The development of GaN based electronic and optoelectronic devices required new paradigms and advances in the growth processes used in order to overcome the obstacles described above. It was recognized very early on, in the 1970's, that GaN had the potential as a wide bandgap direct emitter to push technology towards the blue end of the spectrum, but the materials issue were never resolved as material of sufficient crystalline quality could be produced. In was the groundbreaking work of Akasaki through the development of AlN buffer layers that enabled the growth of high quality

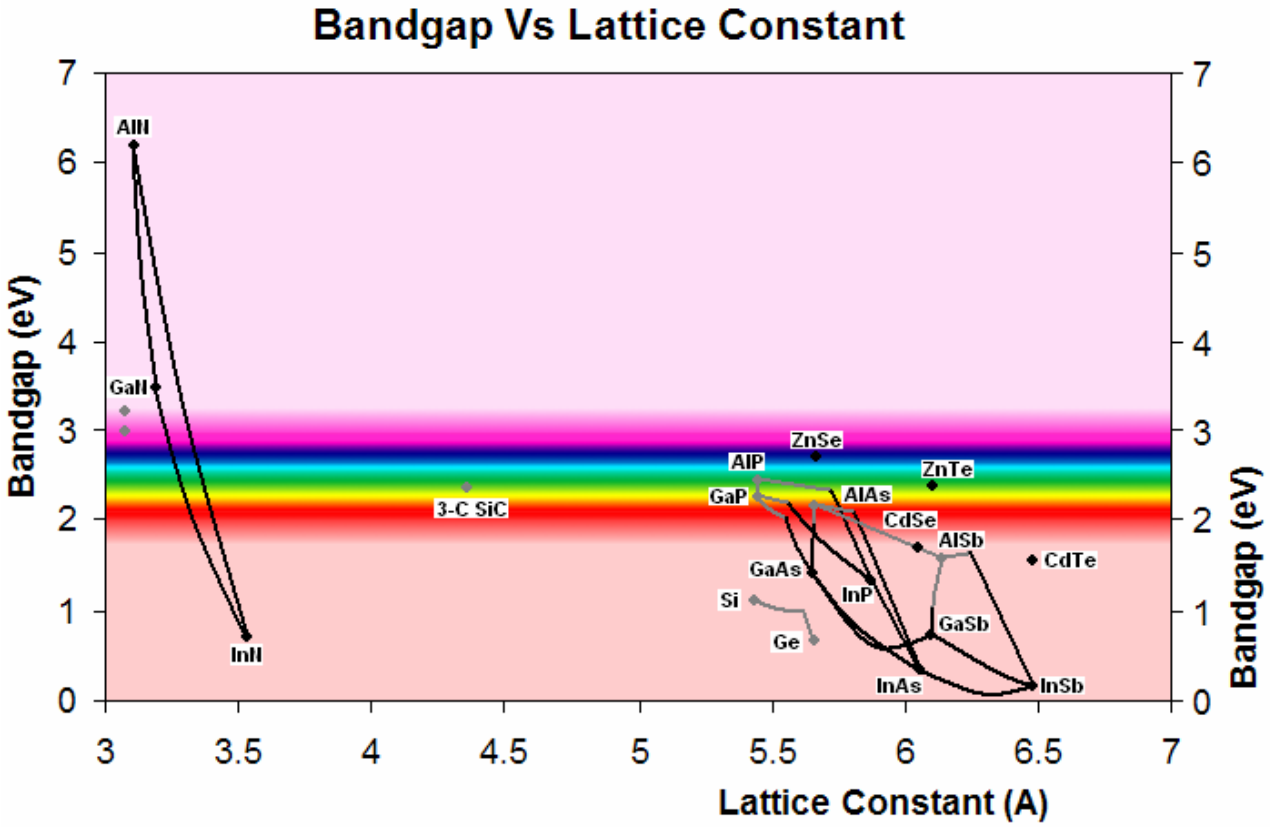

Figure 3.2 Bandgap versus lattice constant diagram for various III-V and II-V semiconductors

epitaxial layers [128]. The layers act to buffer and relax the strain between the sapphire substrates and the epitaxial layers. Once these layers are recrystallized at a high temperature, they provide a suitable template for the growth of high quality epitaxial layers on top, though with dislocation densities several orders of magnitude greater than what is found in other III-V semiconductors. Later work by Nakamura *et al.* allowed for the development of GaN buffer layers [129]. The other major issue with respect to GaN materials, p-doping, was also solved by Akasaki in the late 1980's [130]. Though Mg is not a shallow dopant in GaN as the acceptor level is roughly 200 meV above the valence band edge, it can still provide a suitable level of p-doping. The problem in early studies is that the MOCVD growth process is performed in a hydrogen atmosphere. When Mg is introduced, it forms a neutral Mg-H complex which substituted in the lattice. No p-type conductivity is observed in the as-grown material as all of the acceptors are passivated. It is only through careful annealing procedures which disassociate the Mg and H that the Mg acceptor becomes activated and contributes to observable p-type conductivity.

3.2.3 Overview of GaN growth

After these major issues were resolved, there was a rapid upshoot and development of reactor technology and commercialization of III-nitride based devices, and the growth of GaN has become widespread in industry and academic laboratories. The principle of metalorganic chemical vapor deposition is relatively simple. Precursors of the compound to be deposited are introduces into a heated reactor vessel. The precursors for the Group III compound is often a metalorganic, which is transported to the reactor via a carrier gas which bubbles through the liquid source. The group V precursor is often a hydride, such as arsine, phosphine, or ammonia. Near the substrate

surface, these precursors will pyrolyze, or disassociate with heat. The atomic species then adsorb to the surface and diffuse until they assemble it the form of a crystalline compound semiconductor thin film.

A convenient method for monitoring the growth of GaN is through *in situ* reflectance. GaN is transparent in the visible spectrum, so a light beam passed perpendicular to the same will not be significantly absorbed. Based on differences in the refractive indices of the substrate and epilayer, reflections will occur at the interface of the materials, as well as at the epilayer-atmosphere interfaces. Because of constructive and destructive interference depending on the thickness of the film, it is possible to measure the growth of the film through the use of Fabry-Perot oscillations in the reflectance spectra. In addition, the reflectance spectrum also provides a way to monitor the various steps which are occurring during the growth process. Figure 3.3 shows a typical *in situ* reflectance spectrum for a GaN layer growth.

The first step taken during GaN MOCVD growth on a sapphire substrate is to anneal the substrate is a nitrogen atmosphere. This helps to clean the sapphire substrate and nitride the surface; the increase in reflectivity at this time is due to a change in refractive index with temperature. The sample is subsequently ramped down to a lower temperature, around 530°C, and a low temperature buffer layer is deposited. The sample is then ramped back up to the growth temperature (>1000°C), and the 3-D low dimensional growth is allowed to recover, and subsequent coalescence of the islands leads to an increase in the reflectance signal. Once the islands have coalesced, the growth mode transforms from 3-D to 2-D layer-by-layer growth, and Fabry-Perot oscillations are visible for the remainder of the growth, provided the surface remains specular.

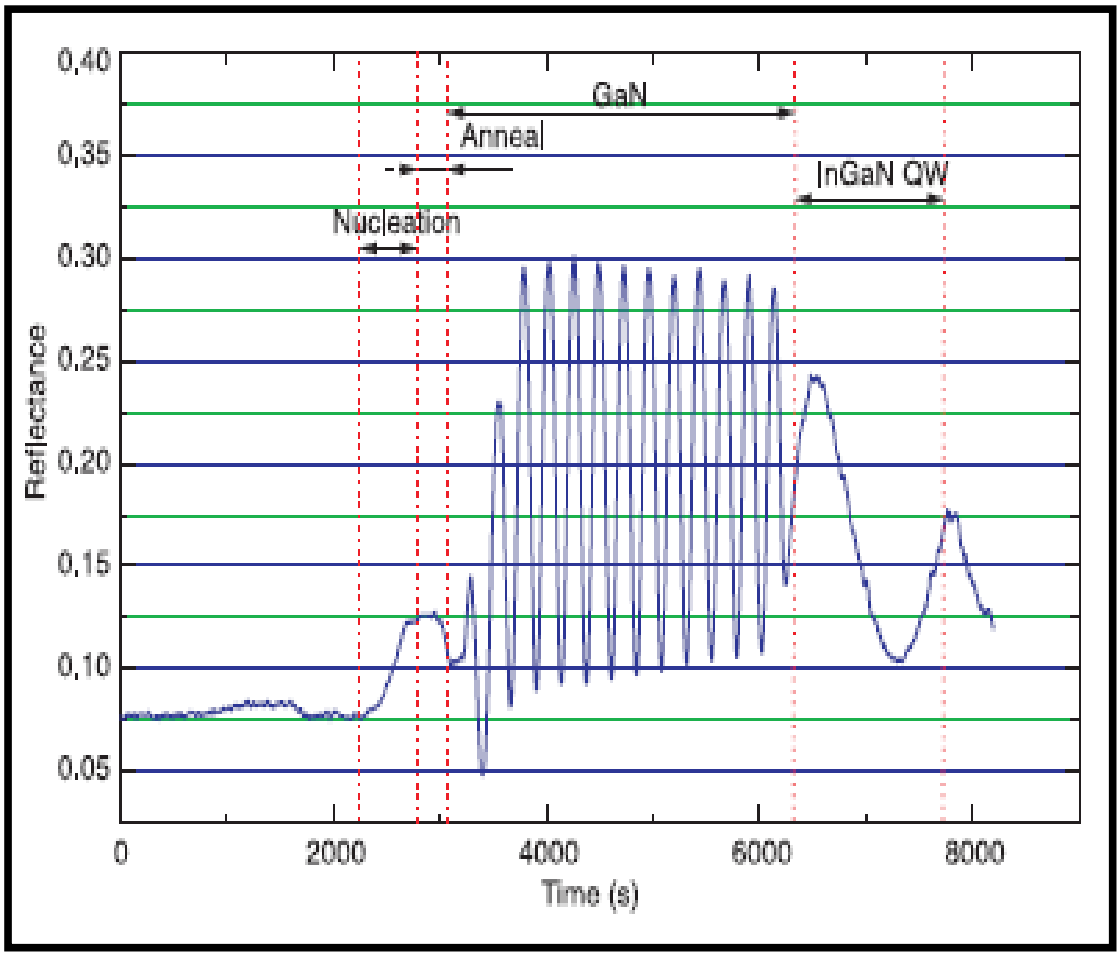

Figure 3.3 A typical in situ reflectance curve for a GaN device structure

In order to grow a high quality GaN films, it is essential to optimize the gas flow conditions and V-III ratio. Trimethyl gallium (TMG) is often used as the metalorganic gallium source as it has a high vapor pressure, is relatively stable in liquid form, readily disassociates at the growth temperature, and is commercially available in ultrapure quality. The nitrogen source is more problematic, as there are no good organic nitrogen sources which disassociate at low enough temperature and crack cleanly so that they do not result in carbon contamination of the as-grown films. Ammonia (NH_3) is usually used as the nitrogen source and undergoes pyrolysis at a temperature in excess of 800°C. Efficient cracking of ammonia is difficult to achieve, such that the V-III ratio during the

growth of typical GaN films is near 2000-3000 in order to ensure that there is sufficient nitrogen available to be incorporated into a stoichiometric film.

3.2.4 Modified GaN growth capability at Georgia Tech

The GaN growth system at Georgia Tech used in this study is based on a commercial system but has been specially modified to account for some of the challenges that will be faced in the development of the transition metal doped III-nitride dilute magnetic semiconductors. A photograph of the growth tool is shown in Figure 3.4; the reactor is on the left in this image and the load lock used to transfer the wafer carrier into the reactor is shown in the right hand side.. The system is designed to accommodate growth temperatures ranging up to over 1200^{o}C. Moreover the system has been designed

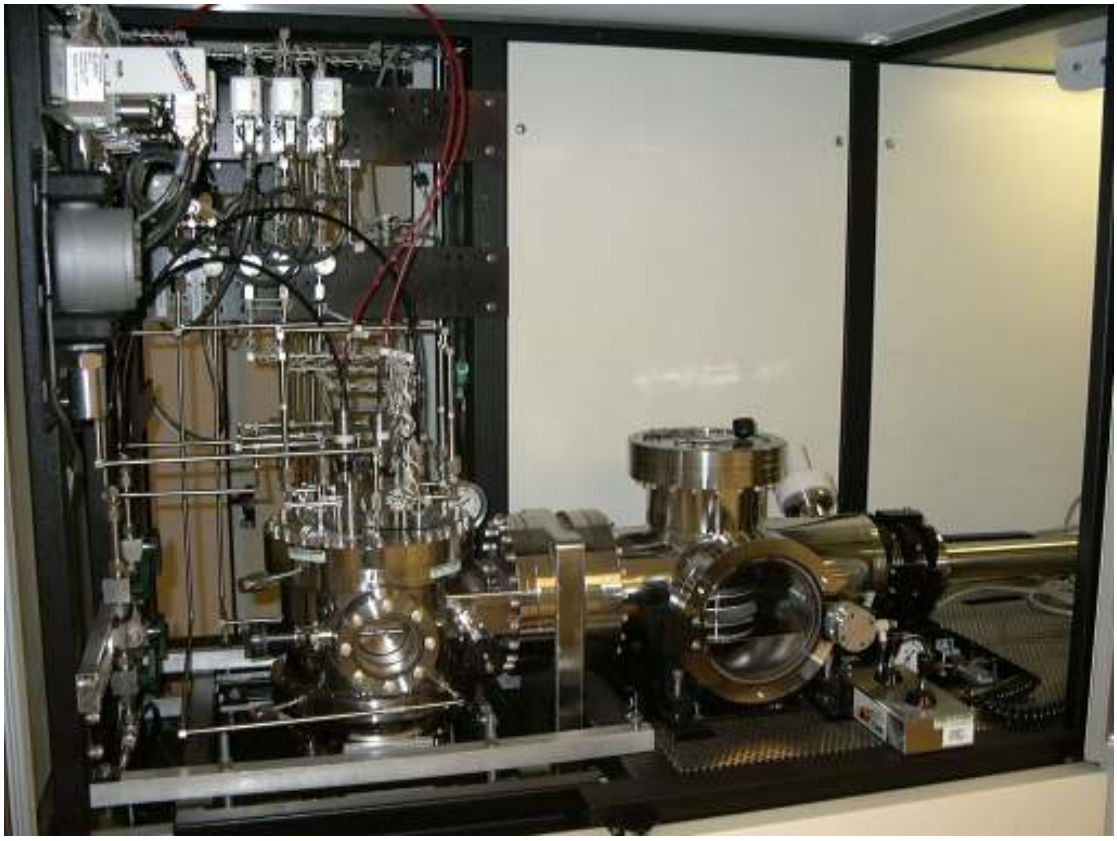

Figure 3.4 Photograph of the MOCVD Growth tool used in this study.

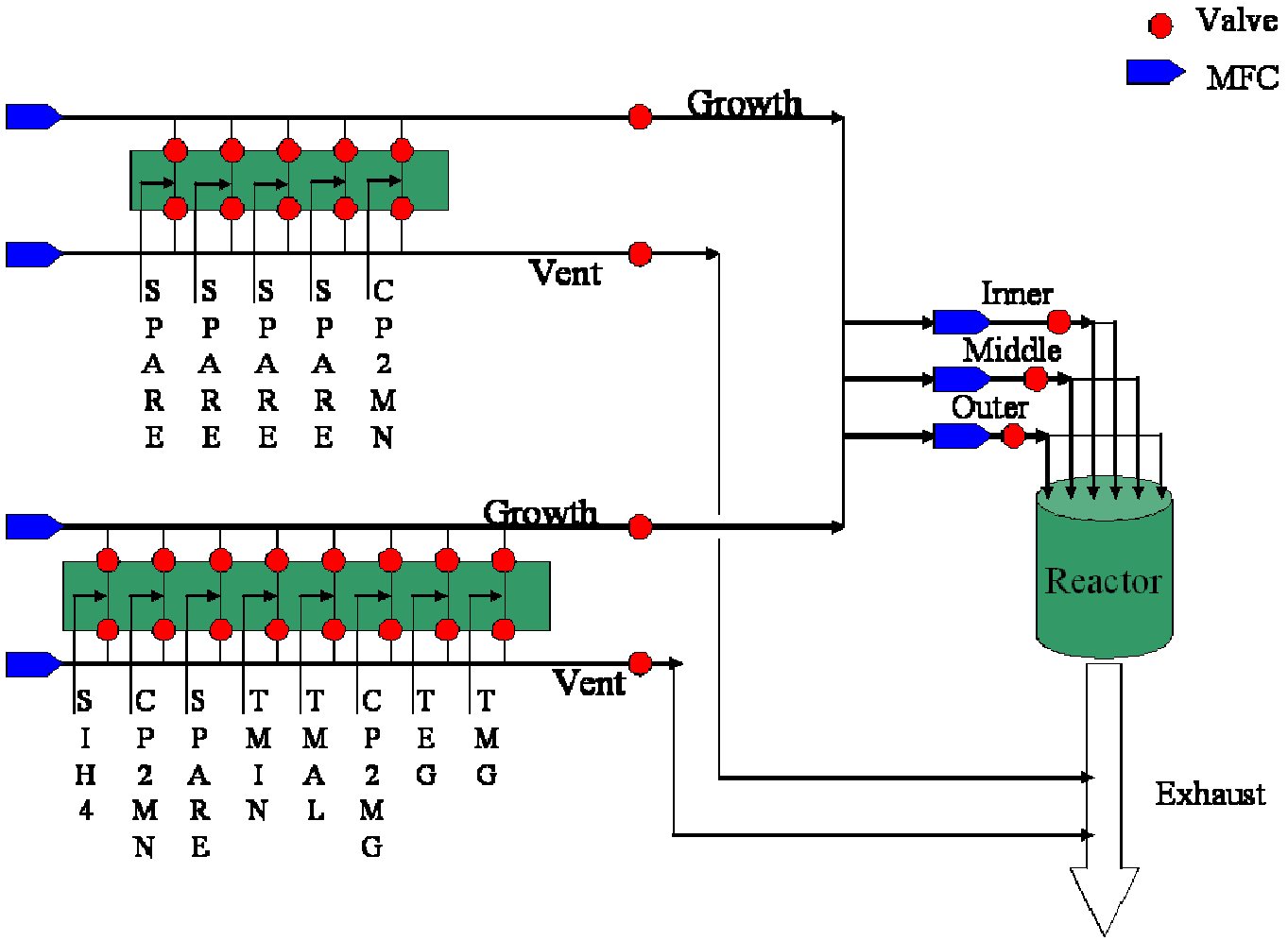

Figure 3.5 Schematic of the flowpaths used for the transition metal and other alkyl sources prior to their introduction to the reactor.

to be able to rapidly switch between two carrier gases, such that depending on the environment and chemistry, either nitrogen or hydrogen can be used as the carrier gas. Another potentially significant modification to this reactor system is shown in Figure 3.5. In this schematic, a diagram of the dual injector blocks used in the system, which allows for the segregation of the Mn precursor from the rest of the precursors used in the process up until the point that they are introduced into the reactor. This could be significant, as very little is known about the use of Mn during the MOCVD process, and is essential to avoid gas phase prereactions or precipitation in the lines if high quality material is going to be grown with Mn incorporated into the GaN layers.

3.2.5 Transition metal precursor selection

One particular concern is the compatibility Mn precursors with the current GaN growth chemistry. The growth conditions must be selected such that the transition metal incorporates substitutionally on the gallium sub-lattice and will not segregate or form precipitates. Mn sources have not been specifically developed for compound semiconductor growth and are not be available in a sufficient quality to allow the growth of high quality $Ga_{1-x}Mn_xN$. Moreover, most transition metal sources, particularly those used to produce semi-insulating templates of $Ga_{1-x}Fe_xN$ for HEMTs have very low vapor pressures compared with the traditional GaN precursors, and as such it will be difficult to observe lattice levels of incorporation on the Ga site. Figure 3.6 shows a comparison of the vapor pressures of a typical transition metal sources based on the bis-cyclopentadienyl sources used in this study compared with that used for the other group III sources such as trimethyl gallium. Note that the difference between these vapor pressures is roughly three orders of magnitude at a given temperature. Under some

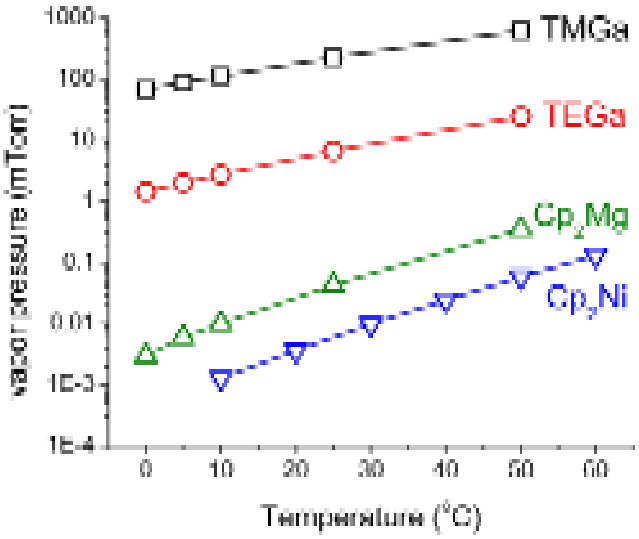

Figure 3.6 Vapor pressure versus temperature graph for the standard MOCVD gallium sources and some p-type and transition metal dopant sources

growth conditions, some percentage of the Mn (or Fe) may also reside in interstitial sites resulting in the compensation Mn on the Ga sub-lattice. If this occurs it is likely that the concentration of interstitial sites will vary depending on the stoichiometric conditions for nitrogen incorporation. Another concern is the development of a growth process for $Ga_1.Mn_xN$ that is compatible with GaN. In particular, the efficient incorporation of Mn may require growth temperatures below those normally used for GaN, i.e. < 1000°C. It is critically important that the Mn does not react with other metalorganic sources or nitrogen source gas such that it polymerizes and then does not incorporate into the growing layer. In order to address these issues, the selection of the bis-cyclopentyldielnyl manganese and iron precursors (Cp_2Mn) were used. Though these materials have a low vapor pressure, they are similar to the know chemistry for the p-type dopant, and should thus be more straightforward to introduce into the growth process.

3.3 Characterization Techniques

In order to understand the physics behind what is occurring in these dilute magnetic semiconductor materials, it will be essential to perform detailed characterization studies to first understand exactly what sort of material has been grown, and secondly to use a combination of these various techniques in order to correlate the materials properties in an attempt to understand the underlying physics. A brief overview of the characterization techniques used in this study is provided below.

3.3.1 X-ray diffraction

One of the most fundamental studies used to characterize the structure of materials is X-ray diffraction. This technique uses the principle that waves interacting with atomic planes in a material will exhibit the phenomenon of diffraction. A schematic of the diffraction process is shown in Figure 3.7. X-rays incident on a sample are scattered off at an equal angle. At certain angles of incidence, x-rays scattering off of neighboring parallel planes of atoms will inteferere destructively. At other angles, these waves will interefere constructively and result in a large output signal at those angles. These constructive interferences occur when the path length difference is an integer multiple of the X-ray wavelength, or when the Bragg condition is met for these X-rays, given by the famous expression:

$$n\lambda = 2d \sin\theta$$

For powder diffraction, this technique is useful for determining lattice parameters and the composition of substances, as there will be a large number of planes of various orientations, all of which contribute to the generation of the x-ray diffraction patterns. In epitaxial single crystal thin films, however, the situation is different, as there is only one

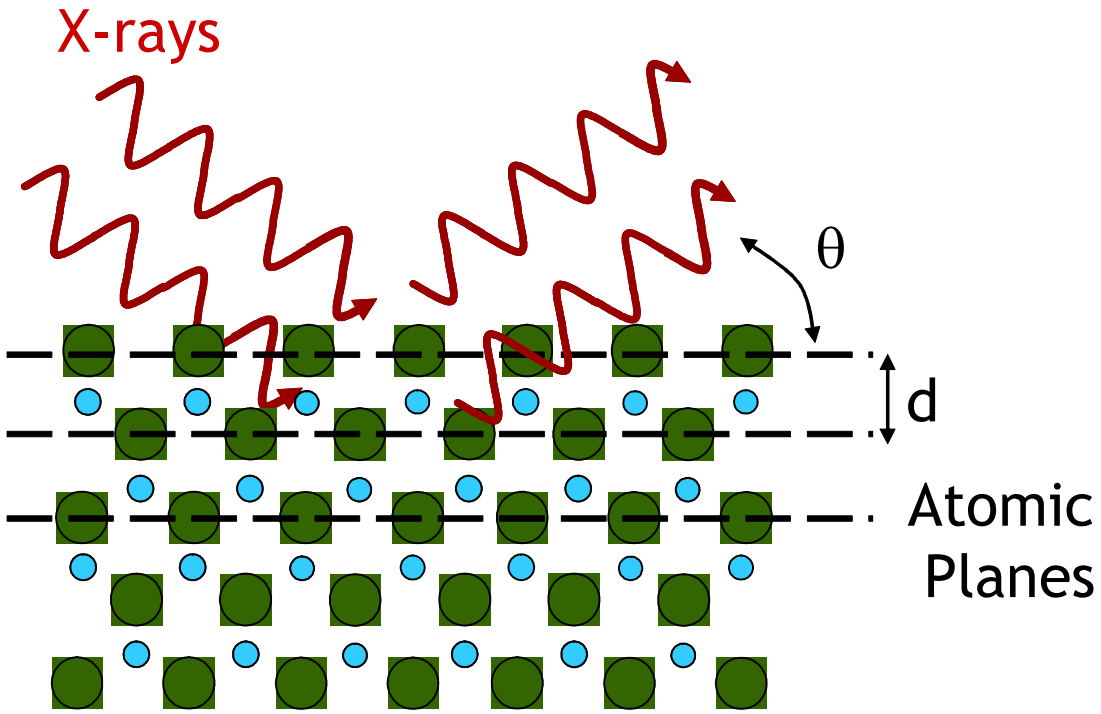

Figure 3.7. Diagram of the experimental geometry for X-ray diffraction

family of planes parallel to the growth axis. Thus other information related to the crystalline quality and strain in the thin films can be ascertained from diffraction data through other X-ray measurements, such as rocking curves (ω scans), reciprocal space maps, superrlattice peaks, and x-ray reflectivity. Moreover, if one wants to examine the crystalline quality of off-axis reflections, it is important the goniometer have a full range of motion such that it can tilt the diffraction planes of interest into a position perpendicular to the beam of the diffractometer. Studies used in this work were performed using a Philips X'pert MRD-pro 4-circle diffractometer using a monochromatized CuKα as an x-ray source.

3.3.2 Optical Techniques

Other approaches that provide information related to the electronic structure of the material also involve the interaction of the material with electromagnetic radiation, this time near the visible regime where bandedge and defect related transitions are known to occur.

3.3.2.1 Transmission

Optical transmission consists of shining a lighnt source through a sample and observing the spectrum of transmitted light on the other side. This technique is useful absorption related features that may or may not show up during luminescence measurements. It can provide an indication of the optical bandedge within a semiconductor material, and for the dilute magnetic semiconductors in this study, be used to observe transitions related to internal d-shell transmissions, which very often end up in the ultraviolet or the infrared. Transmission measurements for this work used two different setups. UV-Visible transmission was performed on bulk ZnO samples using a Varian–Cary 500 UV-Vis spectrometer. In addition, transmission measurements were performed in the infrared portion of the spectrum using an XBO lamp. Transmission

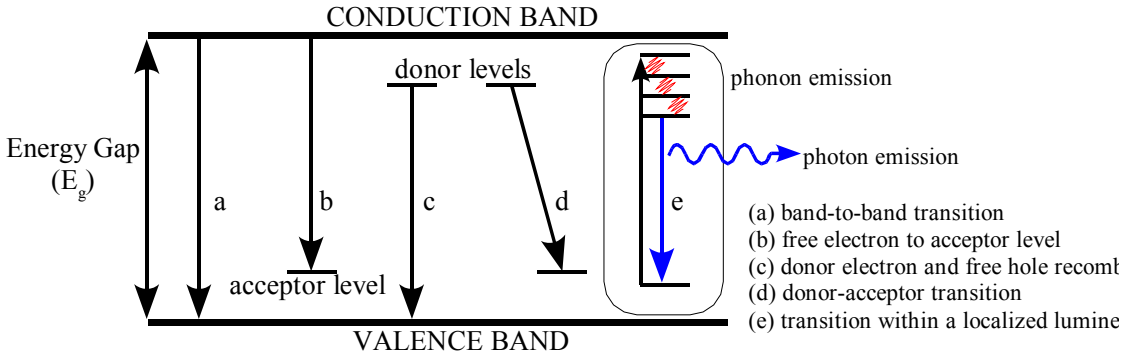

Figure 3.8 Schematic of possible optical transitions that can be observed via photoluminescence

measurements were performed using the red and infrared spectrum of a halogen lamp. The transmitted light was detected by a photomultiplier attached to a 0.24 m monochrometer with a spectral resolution of better than 1 nm for emission and better than 6 nm for transmission.

3.3.2.2 Photoluminescence

Another technique for determining information about the band structure, and more importantly the defects within the sample, is photoluminescence. In this technique, electron-hole pairs are generated by the application of an incident laser beam on the surface of a sample. These electrons-hole pairs will recombine, often through radiative transition back to the ground state of the atom. Some of the observed recombination

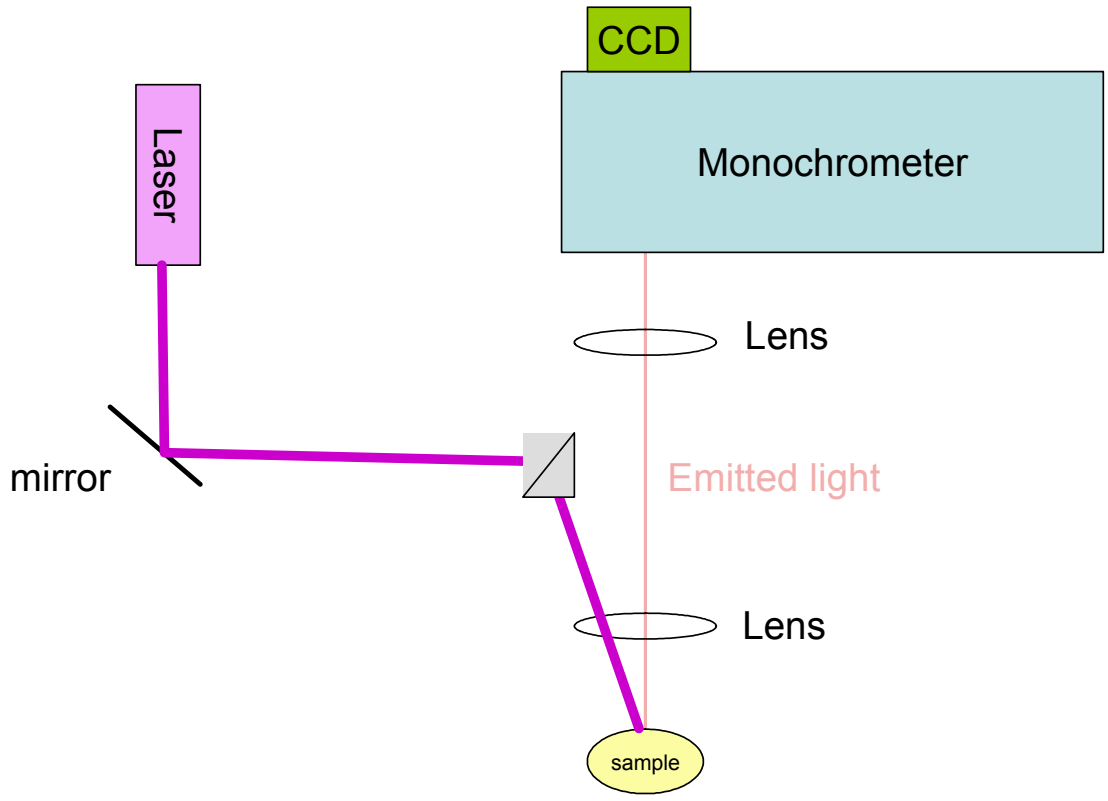

Figure 3.9 Diagram of a typical photoluminescence setup

pathways are shown in Figure 3.8. By measuring the wavelength of the emitted photon from the observed recombination, information can be derived about the band structure, donor and acceptor levels, defect types, impurities, crystalline quality, and defect densities with the materials system. Figure 3.9 shows a schematic of the experimental setup used in a photoluminescence study. In studies of these materials, various excitation sources were used including a frequency-doubled Ti:sapphire laser, a He-Cd 325nm laser, or Ne-Cu 248 Nm laser system. The detected light was passed through a monochrometer and detected using either a IXIS100 CCD camera or photomultiplier tube.

3.3.3 Atomic Force Microscopy

Atomic force microscopy is a useful technique for deriving atomic-resolution information about the surface morphology in these samples. Figure 3.10 shows a schematic of the atomic force microscopy setup. In this technique, an atomically sharp tip mounted at the end of a cantilever is scanned across the surface of the sample. A laser light is reflected off of the top of the cantilever, and the position of the reflected laser spot on a position sensitive photo detector (PSPD) can be used to very precisely measure the amount of deflection in the cantilever and thus the contours of the surface.This can either be done at a constant height above the sample and the force is measured, as is the case of non-contact mode, or using a fixed force measuring the deflection of the cantilever. Other scanning probe microscopes extend the utility of this technique to include the interaction with other forces. For example, magnetic force microscopy is useful for imaging the domain structure of magnetic materials using the deflection based on the strength of a magnetic force. The surface morphology of the $Ga_{1-x}Mn_xN$ layers in this work was

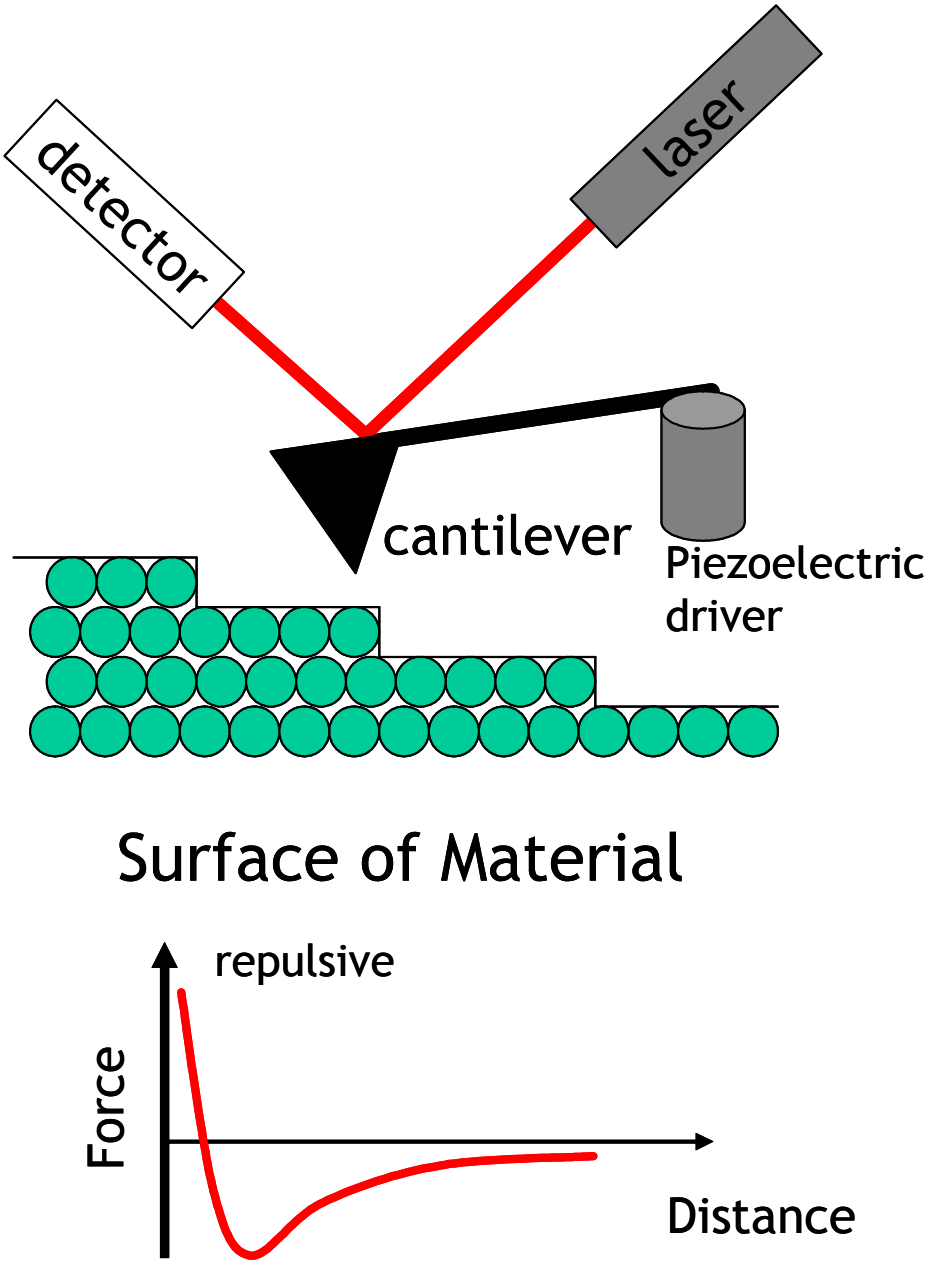

Figure 3.10 Diagram of an atomic force microcopy setup

analyzed using *ex-situ* experimental AFM in a PSIA XE 100 in both contact and non-contact mode.

3.3.4 Electron Paramagnetic Resonance

Electron paramagnetic resonance (EPR) is a technique which allows for the analysis of the nature of point defects as well as their localized atomic environment. It provides distinct chemical state information as well as a positive indication of the local atomic environment. A schematic of the principles of EPR are shown in Figure 3.11 [131]. In the presence of a magnetic field, the energies of the ground state of an ion will undergo a Zeeman splitting, which increases as the strength of the magnetic field. At nominal magnetic fields, the magnitude of this splitting is comparable to the energy of a photon in the GHz range. Thus, it is possible, under the influence of a magnetic field, to

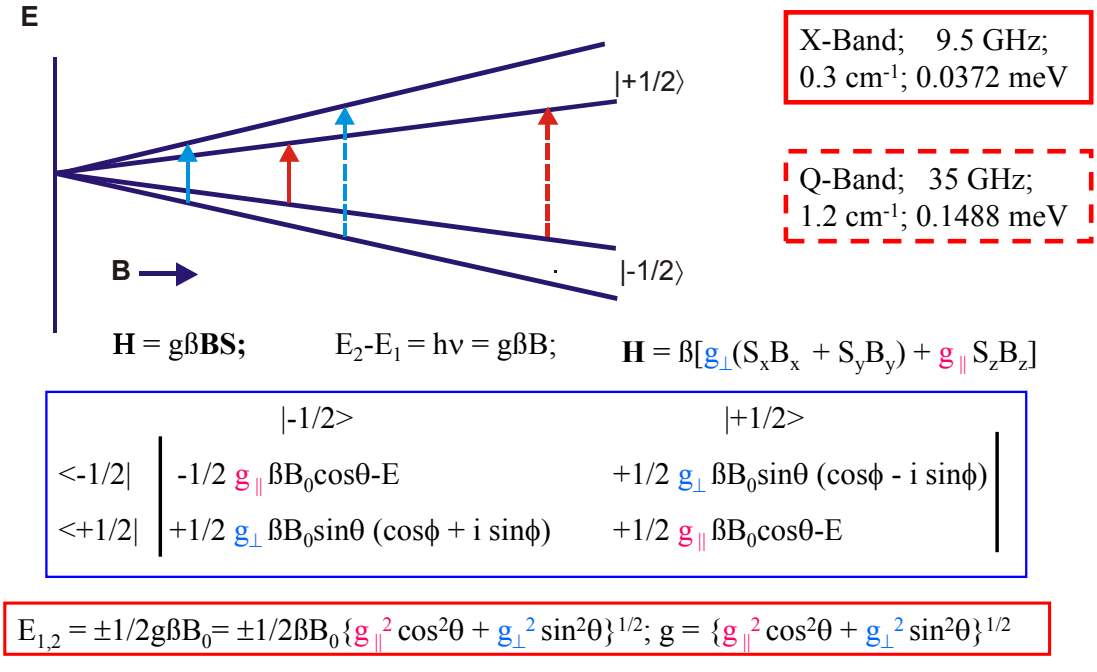

Figure 3.11 Fundamentals of electron paramagnetic resonance. From [130]

induce transitions from the ground state to an excited state of the ion through the application of radiation in the microwave range. By varying the magnetic field, there will be a resonant absorption feature when the energy of the Zeeman splitting is precisely equal to that of the incident radiation.

The calculation of where these expected resonance features are expected to occur can be calculated through a detailed analysis of the Spin Hamiltonian for a particular ion and localized environment. Moreover, it is possible for EPR spectra to provide more detailed information about the localized atomic structure through observation of hyperfine lins from the interaction of the electron and nuclear spins. Because the ground state and degree of splitting of these atoms is dependent on the local symmetry of the ion and direction of the applied magnetic field, through a comparison of the predicted curve over a range of applied magnetic field and angles, it is possible using this spectroscopy to get detailed information on the local atomic environment.

3.3.5 Secondary Ion Mass Spectrometry

In dilute magnetic semiconductors, as is the case in most other semiconductor devices, it is important to be able to figure out the atomic concentration of different alloying elements within the lattice. One way to perform this measurement is to use secondary ion mass spectrometry. In this destructive technique, ionized particles of are accelerated towards the materials to be measured. The sputtered particles are then captured via a mass spectrometer, which counts the amount of particles of a given mass. Through comparison with a standardized sample to account for the differing sputter yields of the sample, it is possible to back out the concentration of an element within the host materials. This method can be very sensitive and depending on the particle and

source ion, measure concentrations of an element on the order of 10^{17} cm^{-3}. However, some resolution and accuracy is lost at alloying concentrations because of changes in the secondary ion yields. In this work, SIMS depth profiles were performed using an Atomika Instruments Ionmicroprobe A-DIDA 3000.

3.3.6 Raman Spectroscopy

Raman scattering spectroscopy is another technique which employ light wave-matter interaction to probe certain materials properties. Specifically, Raman scattering measures the interaction of light via ineleastic scattering from an incident laser beam off of a material. One method for inelastic scattering is to transfer this energy into lattice vibrations or phonons. The energy of these lattice vibrations is quantized and a function

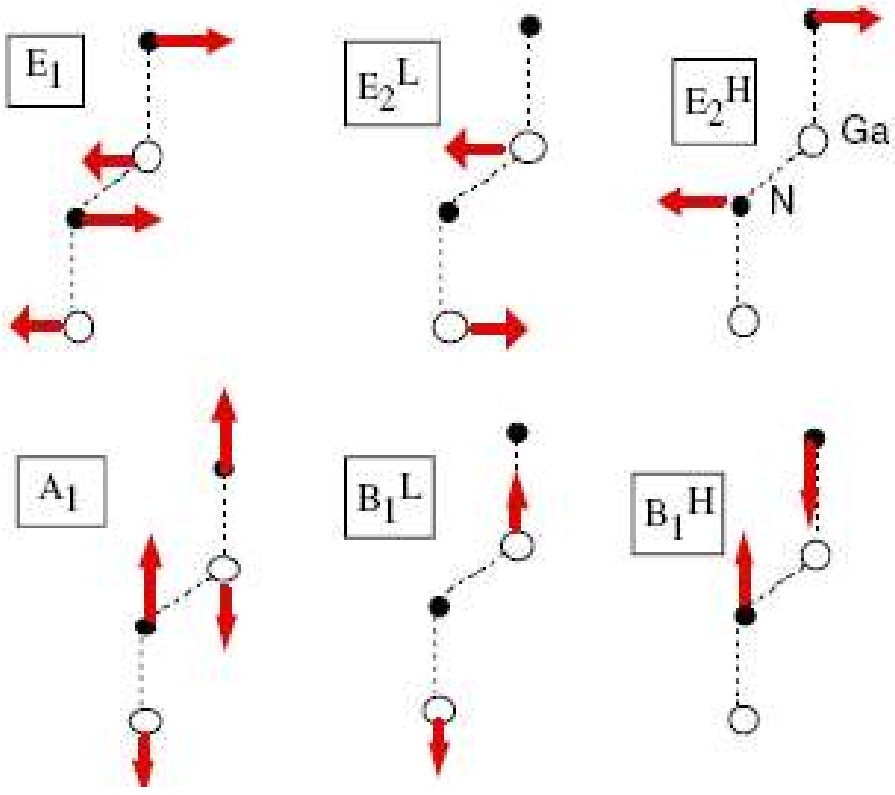

Figure 3.12 Optical phonon modes in the wurtzite GaN structure. From [131]

of the local bonding and atoms involved in the structure. Thus, by measuring the energy transferred to or from phonons to photons, which is manifested as a Stokes or Anti-stokes shift in the inelastically scattered light source, valuable information regarding the quality of the thin films can be gained. These generally appear as a weak peak, several orders of magnitude weaker than the laser line, which must be filtered out in order to observe the Raman signal. Figure 3.12 shows the optical phonon modes and their vibrational direction in the wurtzite lattice.

The modes that can be observed are highly sensitive to the polarization of the

Table 3.1. Porto notation for the active optical Raman modes in wurtzite GaN. From [131]

Configuration	Mode
$x(y,y)\bar{x}$	A_1(TO), E_2
$x(z,z)\bar{x}$	A_1(TO)
$x(z,y)\bar{x}$	E_1(TO)
$x(y,z)y$	E_1(TO), E_1(LO)
$x(y,y)z$	E_2
$z(y,x)\bar{z}$	E_2
$z(y,y)\bar{z}$	A_1(LO), E_2

incident light and the orientation of the crystal upon which the laser light is incident. Porto notation is a convenient method for identifying the direction that the laser light is incident on a crystal, observed, and the polarization of the light in each case. The form of this notation is a(b,c)d, where a is the direction of the incident beam, b the polarization direction of the incident beam, c is the polarization direction of the scattered beam, and d is the direction the scattered light is observed. Table 3.1 lists the modes for the wurtize lattice, and the corresponding Porto notation for the scattering geometries for which these modes are active [132]. Raman spectroscopy measurements in this work were performed to determine the crystalline quality using a Renishaw micro-Raman system with a 488 nm excitation source.

3.3.7 Hall Effect Measurements

The electrical carrier concentration and carrier type are a critical element in many of the prevailing theories of ferromagnetism in these materials. In order to get more detailed information on the carrier concetration and carrier type, Hall effect measurements are a standard characterization technique which can be performed. A schematic of the Hall effect is shown in Figure 3.13. This technique takes advantage of the fact that moving charged particles in an electric field are subject to a force perpendicular to their direction of motion, the Lorentz force given by:

$$\vec{F} = q\left(\vec{v} \times \vec{B}\right)$$

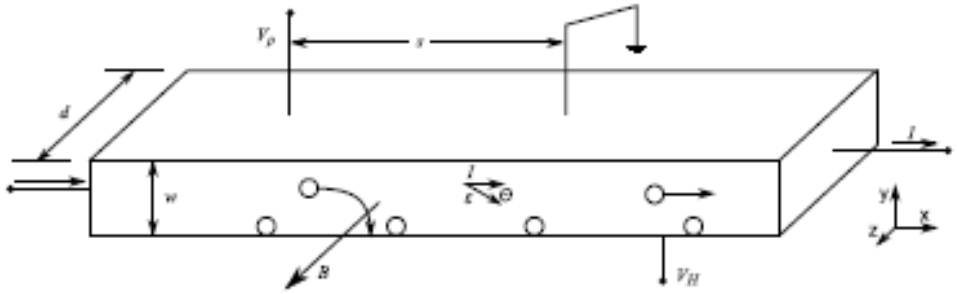

Figure 3.13 Schematic of the Hall effect measurement in a p-type sample.

Thus, a continuous electrical current in a magnetic field will deflect electrons and holes to opposite sides of the sample, setting up an internal electric field which introduces a electrostatic force opposing the Lorentz force. Through a measurement and the sign of this Hall voltage, the carrier type and concentration can be extracted, if the conductivity is known.

In thin film samples, two-dimensional transport dominates and it is not practical to construct thin film samples of the geometry shown in Figure 3.13. This can be mitigated by measuring samples in the Van Der Pauw geometry. In this experimental setup, ohmic contacts are mounted at the corners of a convex quadrilateral or circular sample. Through cycling of the currents and voltages through the four contacts and varying the sign of the magnetic field, the carrier concentration in these samples can be extracted. In this work, Hall effect measurements were performed on $Ga_{1-x}Mn_xN$ and $Ga_{1-x}Fe_xN$ layers using indium alloy contacts. An Ecopia EKS Hall effect measurement system with 0.51 T magnet was used in order to perform these measurements.

3.3.8 Magnetometry

In order to determine the macroscopic magnetic properties of the two materials in question, two forms of magnetometry were performed. Measurements were taken between 5 K and 300 K on these samples using these two techniques.

3.3.8.1 SQUID magmetometry

Superconducting interference device (SQUID) magnetometry is the standard measurement technique for highly sensitive magnetization studies. In this form of magnetometry, a magnetic sample is drawn through a coil of superconducting wire in the presence of a magnetic field. The moving magnetic field from the sample induces a current in the wire, which through signal processing can be analyzed and converted to a signal proportional to the magnetization of the sample. The noise floor on this technique can be as low a 10^{-8} emu, which would make it ideal for studies of dilute magnetic systems. In addition, the superconducting magnet and coil must be cooled to cryogenic temperatures, as the critical temperature for the superconducting wire coil is 20 K. Thus, for the measurement of low Curie temperature materials this technique is ideal because this apparatus already requires liquid helium. Moreover, it is easy sing this setup to perform high sensity field cooling and zero field cooling experiments without a need for an additional oven or cryostat which degrades the sensitivity. In these experiments, SQUID measurements were performed using Quantum Design MPMS-5 magnetic property measurement system. In a majority of experiements, the magnetic field of the sample was applied in the plane of the sample.

3.3.8.2 Vibrating Sample Magnetometry

Another form of magnetometey that was used in these studies was vibrating sample magnetometry (VSM). In this setup, the sample is mounted on a sample tail and

placed between the coils of an electromagnet. The magnet supplies a field, which the sample is oscillated at a known, low frequency. The moving magnetic field from the sample induces a current in the pick up coils, which is sent, amplified, and converted to a known magnetic signal. This technique is nice because it is inexpensive and fast for routine measurements. However, it is much more difficult to perform low temperature studies, as it needs an additional cryostat. In addition, with these dilute samples, the magnetization of the sample is very often much less than that of the sample holder, such that the data must be background corrected in order to pull out the data from the sample from the measurement noise. In addition, the noise floor on this measurement technique is two orders of magnitude greater than what it is for the SQUID measurement technique, so it is difficult to measure very weakly magnetic samples. In this work, measurements were performed using a Lakeshore 7404 Vibrating Sample Magnetometer, with the magnetic field applied in both parallel and perpendicular to the plane of the thin film.

CHAPTER 4

BULK SINGLE CRYSTALS OF TRANSITION METAL DOPED ZINC OXIDE

4.1 Overview

In the study of dilute magnetic semiconductors, II-VI compounds enjoy several advantages. Relative to the III-V compounds such as $Ga_{1-x}Mn_xAs$ and $In_{1-x}Mn_xAs$, there is a longer history of development for these materials. This is primarily due to solubility concerns, as the transitional metals are more chemically similar to group II compounds (such as zinc) than the group III compounds. As such, the chemical solubility on the lattice site is much greater in the II-VI materials, and it is much more straightforward to dope Mn at high concentrations into these compounds. However, the chemical solubility is concomitant with an isovalent doping process; thus, transition metals in the II-VI compounds do not generally contribute carriers on their own, as required by many of the ferromagnetic models. Moreover, II-VI devices have a number of inherent materials instabilities which render them more difficult to employ in traditional electronic devices. These problems also influence their implementation in spintronic devices

Another problem regarding the origin of ferromagnetism in the II-VI compounds is the dichotomy that between bulk versus thin films. In the III-V systems, all of the reports of ferromagnetism are for thin films. Because of the high tendency for phase

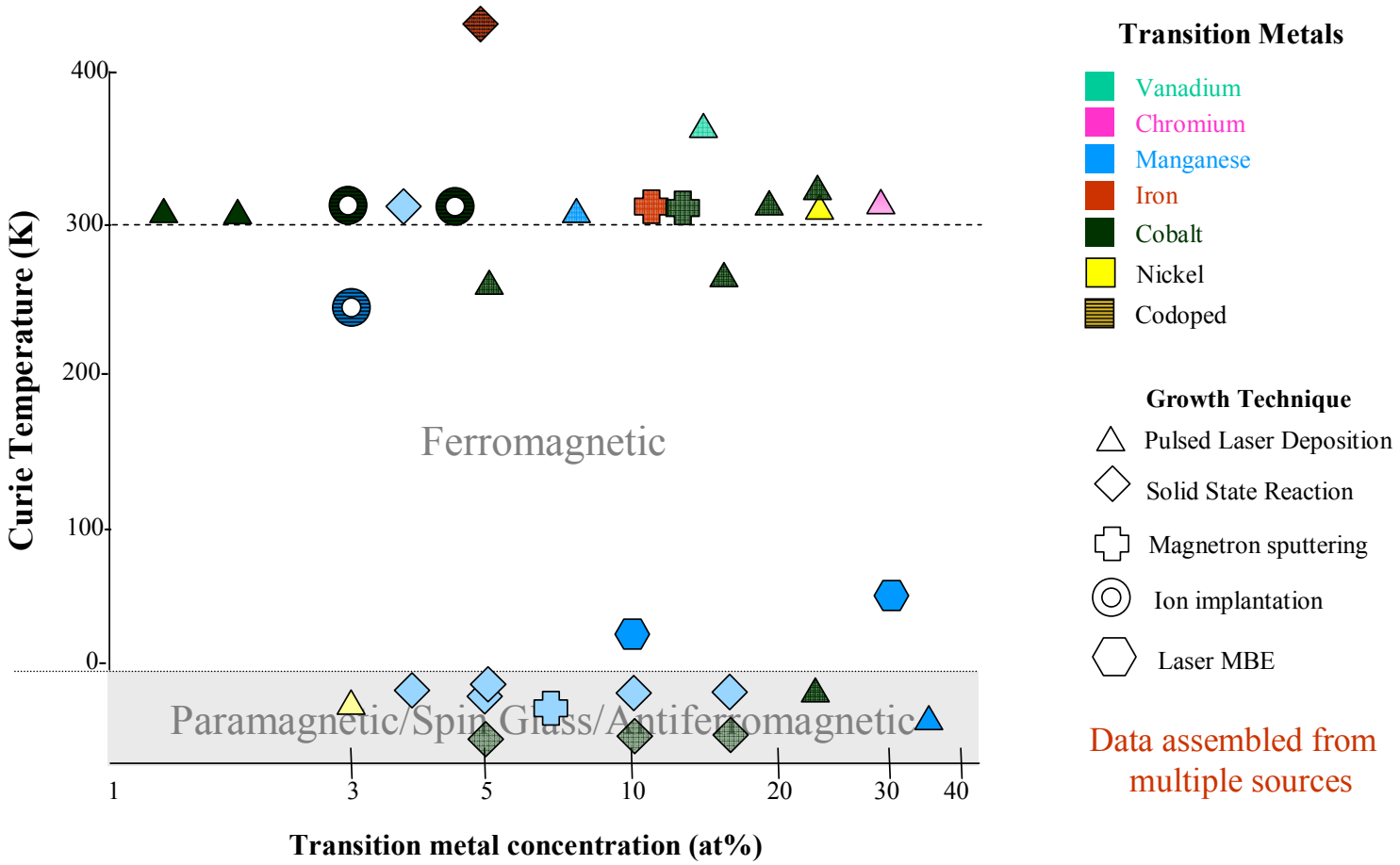

Figure 4.1 Schematic summarizing some of the experimental reports of ferromagnetism in the literature

segregation, non-equilibrium techniques must be used, which eliminates the possibility of bulk growth techniques. In the nitride system, bulk crystallites have been produced; but without significant acceptor codoping, these crystallites exhibit high background donor defect concentrations. This drives the Fermi level towards the conduction band and the substitutional Mn into a paramagnetic d^5 state [75]. In zinc oxide, the reports of ferromagnetism are vastly disparate, and ferromagnetism has been reported in thin film and nanostructured form [90-92, 96-100]. Figure 4.1 summarizes the reports of ferromagnetism and the growth techniques used from a sampling of the current literature. The background intrinsic defects in ZnO will also be mostly of donor character. If the free carrier (hole) mediated mechanism holds for these compounds, this may be prohibitive to the observation of ferromagnetism in these materials, but this is yet to be determined.

Nevertheless, bulk crystals have a number of advantages over thin films for the analysis of these materials. One problem with the analysis of thin films is the background magnetic signal from the substrate, which is often much larger than that of the thin film. Also, defects associated with the growth mechanism have been observed to result in clustering of the magnetic impurity atoms or clusters near the substrate-film interface [133]; this could significantly complicate the magnetic analysis of these systems. It has also been suggested that the defects themselves associated with the interface have an inherent magnetic moment themselves [63]. The use of bulk crystals eliminates these complications. Moreover, these bulk single crystals can then be employed as homoepitaxial substrates or latticed matched substrates for the growth of ZnO- or GaN-based ferromagnetic semiconductors by thin film growth techniques, such as

metalorganic chemical vapor deposition (MOCVD) or molecular beam epitaxy (MBE) [112]. This could potentially enable control of spin injection and coherence times in these materials relative to the dislocation densities in future studies.

4.2 X-ray Diffraction of $Zn_{1-x}TM_xO$

The most prevalent feature of individual transparent crystals of transition metal-doped ZnO is their distinct color with varying transition metal doping. The cobalt doped samples show a striking green color, which deepens with increasing cobalt incorporation. Similarly, the Mn-doped samples possess a range of reddish colors, from a pale orange for the samples doped at <0.1% Mn, to a deep red for the samples doped at closer to 5% alloying content. Iron doped single crystals exhibit a yellow color. Photographs of the as-grown crystals are shown in Figure 4.2. UV-visible transition measurements taken from these samples confirm that the color trends are caused by interatomic transitions within the divalent transition metal dopant atoms, as reported elsewhere [97] and discussed in more detail below.

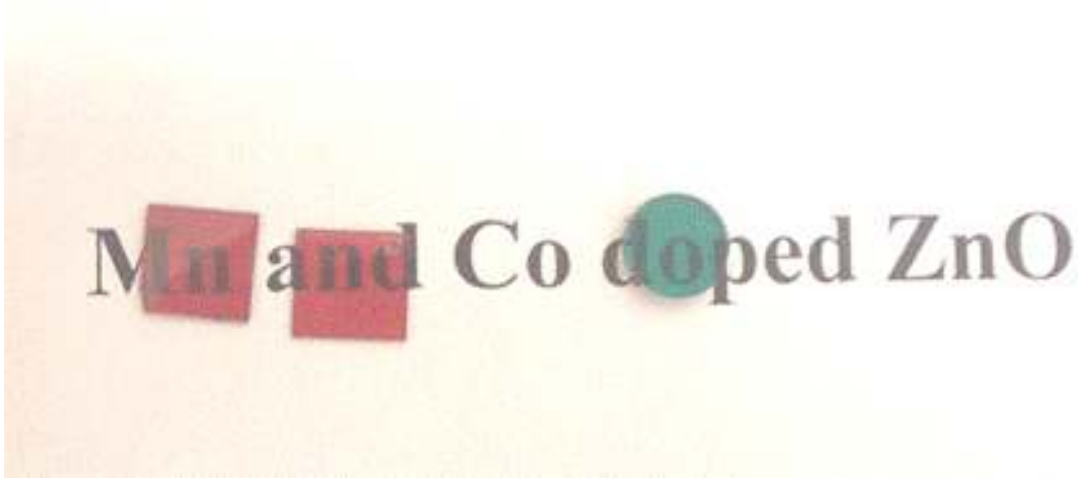

Figure 4.2 Photographs of Mn- and Co-alloyed melt grown single crystals.

High-resolution x-ray diffraction shows no evidence of secondary phases in either the $Zn_{1-x}Mn_xO$ or the $Zn_{1-x}Co_xO$ samples at concentrations up to 5%. The as-grown material in the x-ray diffraction scans appears to be completely-oriented single crystals. No peaks are attributable to second phase formation. Pole figure analysis is consistent with the assertion that these are single crystals. In some cases, particularly with heavy transition metal doping, indications of small angle grain boundaries within the nominal single crystal are visible in the scans of the sample. Only c-axis (0002) and (0004) peaks were visible in the ω–2θ scans at doping levels up to 5% Mn and 3% Co, as shown in Figure 4.3. Phi scans from the asymmetric (102) reflections clearly revealed the 6-fold symmetry of the wurtzite structure. The measured c-axis lattice parameter was 5.207Å in

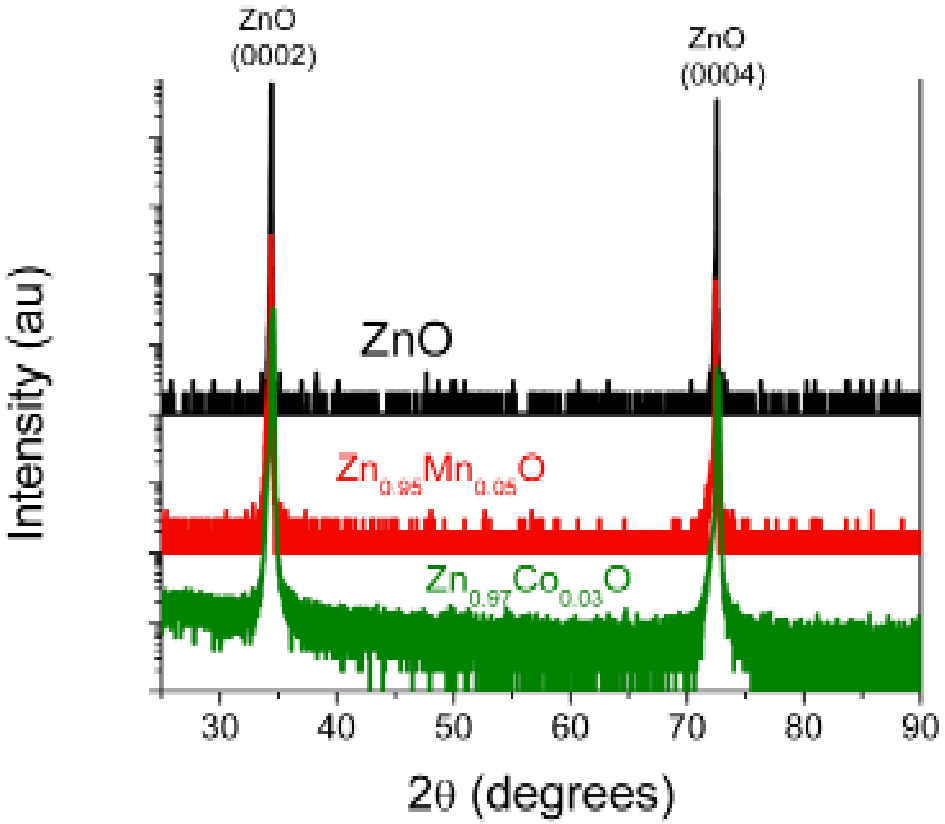

Figure 4.3 High resolution x-ray diffraction scans of various ZnO crystals. Only the basal plane reflections are present, and there is no indication of secondary phases.

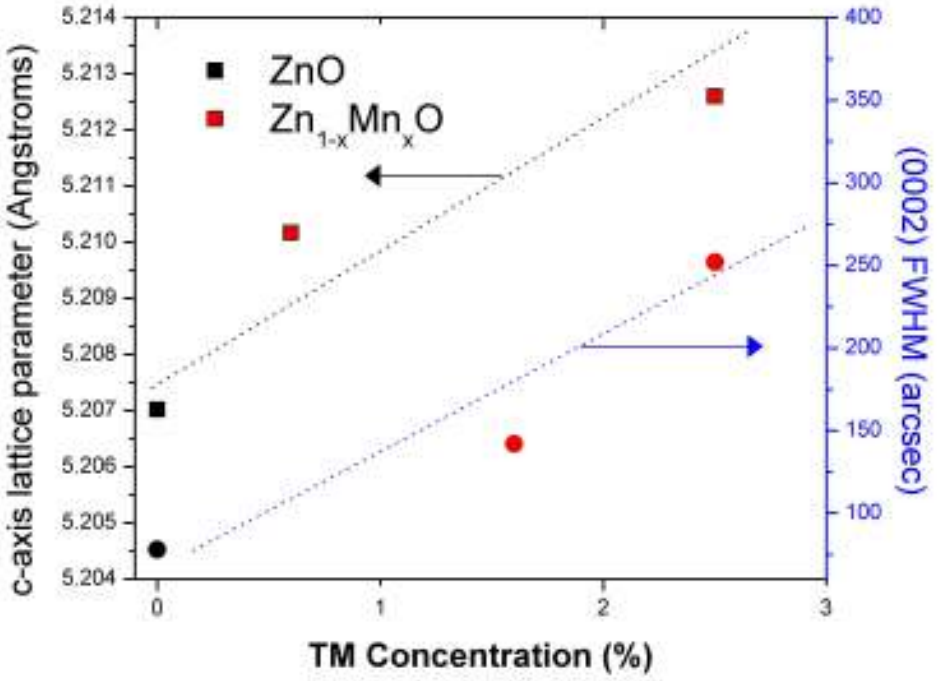

Figure 4.4 Increase in lattice parameter and full width half maximum (FWHM) of the line scans observed in the Mn-doped zinc oxide single crystals

the undoped sample, but increased with Mn incorporation to a value of 5.211Å at the 5% Mn-doping level, as measured from the growth conditions. The difference in these values is close to the experimental error in the measurement,; however, using multiple c-axis reflections through the (0006) reflection and a Bradley-Jay extrapolation function, a larger c-axis lattice parameter was observed for all of the Mn-doped samples.

An increase in lattice parameter was not conclusively demonstrated in the Co-doped sample, owing to the more similar more similar tetrahedral ionic radii of Zn^{2+} and Co^{2+}. The tetrahedral ionic radius of Zn^{2+} is 0.074 nm, compared to 0.072 nm for Co^{2+} and 0.080 nm for Mn^{2+}. Crystal quality was observed to decrease with increasing transition metal concentration as evidenced by $2\theta-\omega$ scan linewidths, increasing from 78 arcsec in the undoped sample to 252 arcsec at 5% Mn. A plot of the measured linewidth

and full width at half maximum (FWHM) of the $2\theta-\omega$ scans are shown in Figure 4.4. In addition, peak asymmetry increased on the low angle side as the transition metal elements were added, indicating the likely incorporation of Mn/Co interstitial atoms into the crystal lattice with increasing doping concentration.

4.3 Secondary Ion Mass Spectrometry results for ZnO:TM

Secondary Ion Mass Spectrometry (SIMS) has been performed on the samples as shown in Figure 4.5. The peaked curve in Figure 4.5 is a reference sample implanted with $3x10^{16}$ Mn ions at 200 keV. In comparison to the ion implanted sample which shows a peaked distribution, the as-grown crystals show a uniform dopant distribution throughout the $Zn_{1-x}Mn_xO$ crystal. The Mn concentrations of the samples were calculated to be 0.2%, 0.6%, and 1.6% from these curves. These values are slightly different from those expected from the growth conditions due to the limitations of SIMS for quantization at

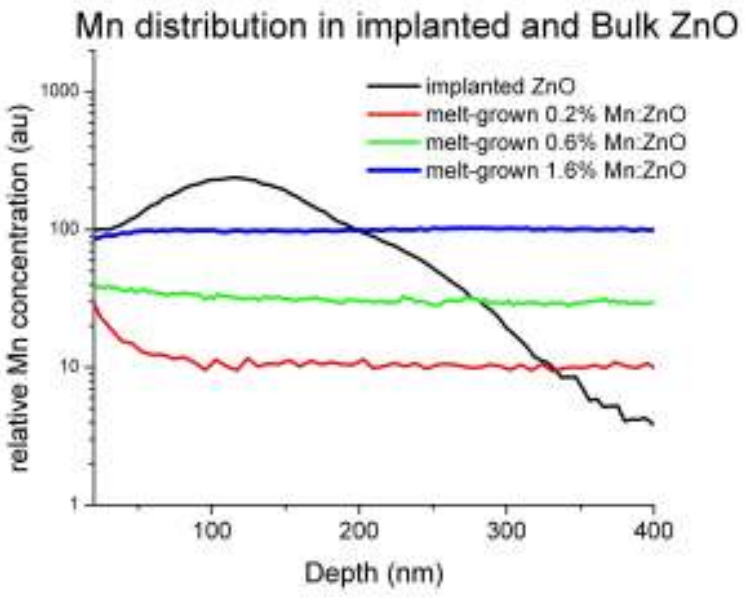

Figure 4.5 SIMS depth profiles of implanted and bulk melt grown samples.

alloying concentrations. These results demonstrate the utility of this modified melt growth technique for producing high-quality, uniformly-alloyed, single crystals of ZnO.

4.4 UV Visible Transmission

4.4.1 Line splitting and internal transitions

The UV-visible transmission of these materials is shown in Figure 4.7. Assignment of the absorption transitions reveals that interatomic d-shell Mn^{2+} transitions are responsible for the absorptions leading to the characteristic color within these materials[97]. UV-visible transition measurements taken from these samples confirm that these trends are attributed to interatomic transitions within the divalent transition metal dopant atoms. The undoped ZnO crystal shows a sharp absorption edge at 391.4 nm (3.17 eV) at room temperature. Note that this differs from the expected room temperature band edge of ZnO at ~360nm (3.4 eV), which is due to both thermal broadening of the edge, and likely also cause by a large concentration of intrinsic donor impurity states as a function of the growth process. The absorption edge shifts nonlinearly from 500 nm at 0.04% to 552.7 nm at 1% to 607.5 nm at 5% with increasing Mn concentration, as shown in Figure 4.. This absorption can be attributed to the overlapping Mn^{2+} d^5 crystal field transitions from the ground state $^6A_1(S)$ to $^4T_1(G)$, $^4T_2(G)$, $^4A_1(G)$, and $^4E(G)$. These transitions have been seen in thin film and bulk absorption and cathodoluminescence measurements [134]. Similar transition lead to the red color of the widely used ZnS:Mn phosphor. The nonlinear nature of this shift is a combination of both the doping density and the thickness of the as-cut crystals, which was not consistent for the samples analyzed in this study. The $Zn_{1-x}Co_xO$ sample also shows distinctive character with doping of the transition metal element that; this differs from the $Zn_{1\ x}Mn_xO$, due to the

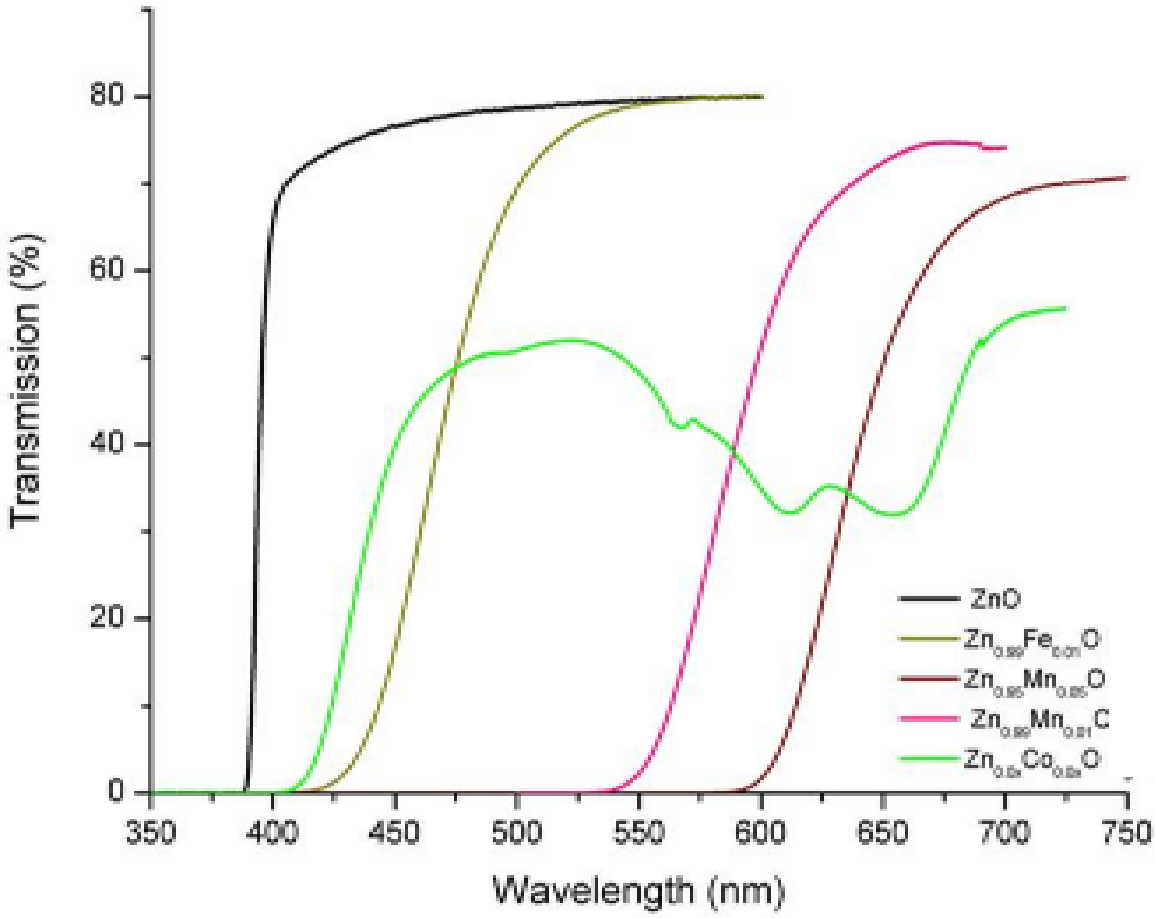

Figure 4.6 Optical transmission scans through Mn, Fe, and Co doped single crystals of varying doping levels and thickness

partially full nature of the d-orbitals in the high spin d^7 state. The Co-doped sample shows an absorption cutoff at 415.3 nm, near a CL peak in previously grown ZnO which was attributed to the $^6A_1(S) \rightarrow {}^4T_1(G)$ transition [83]. However, this assignment may not be correct in these bunk samples, as the as $^6A_1$ is not the ground state of the divalent cobalt ion. Other reports suggest that this is a slight bandedge shift with transition metal doping [135]. Also prevalent are two absorption maxima centered at 605 nm and 655 nm, which are due to the d-d transitions in the high-spin d^7 state of the Co^{2+} ions, as has been previously observed in thin film samples and attributed to the $^4A_2(F) \rightarrow {}^2E(G)$, $^4A_2(F) \rightarrow {}^4T_1(P)$ transitions [83]. These two transitions lead to stronger absorption in the red at 605 nm and 655 nm. Combined with the violet region absorption cutoff at 415 nm, this explains the deep green color in these samples.

4.4.2 Tanabe-Sugano diagrams for Co^{2+} and Mn^{2+}

In order to investigate and confirm the assignment of the optical transitions as a verification of the valence state in the transition metal doped ZnO crystals, it is instructive to look at the Tanabe-Sugano diagrams for the d^5 and d^7 atomic configurations within a tetrahedral crystal field. These diagrams, originally developed by the two scientists from whom they derive their name, plot the energies of the ground and various excited states within an ion as a function of the crystal field stabilization energy (Δ). Figure 4.7 shows a schematic of the splitting in the d^5 and d^7 levels,expected for divalent Mn and Co substitutional on a tetrahedrally-coordinated lattice site. These have previously been derived [136], and the amount of the splitting is a function of the interaction of the orbitals and their symmetry with that of the tetrahedral crystal field. Because the atomic spacing within ZnO is expected to be smaller than that for the other Zn-VI compounds, the strength of the tetrahedral field is expected to be stronger for these

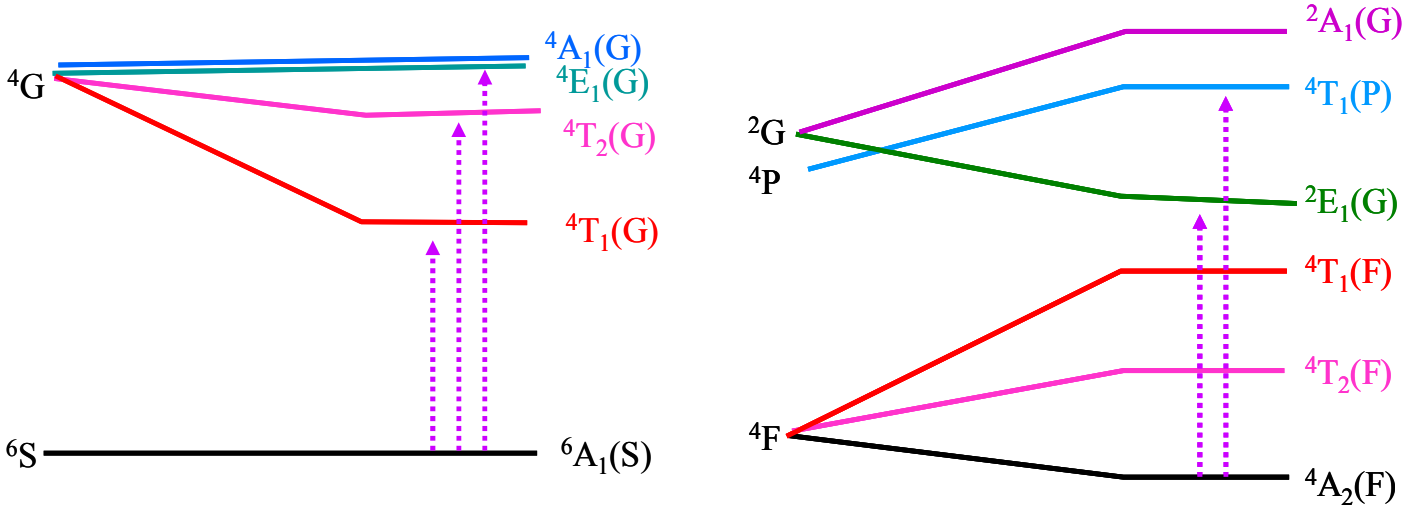

Figure 4.7 Tanabe-Sugano diagrams from d^5 and d^7 ions in the presences of a tetrahedral crystal field

ions in ZnO. This is indeed observed in the single crystals, and further confirms the assignment of the distinctive color within these crystals as transitions from ground to excited states of the d-shell substitutional atoms.

4.5 Electron Paramagnetic Resonance

In order to confirm the lattice site occupancy of the transition metal atoms on the lattice site as well as to verify the valence state of the individual transition metals, electron paramagnetic resonance spectroscopy was performed on these samples. In the case of both Mn and Co, the divalent state (Mn^{2+} and Co^{2+}) on the lattice site is observed, as evidenced from a comparison of the measures spectrum with those predicted from the published spin Hamiltonian from $Zn_{1-x}Mn_xO$ [137] and $Zn_{1-x}Co_xO$ [138]. Figure 4.8 and Figure 4.9 show the predicted and measured curves for the Mn and Co doped samples respectively.

It should be noted that the agreement between the measured and experimental curves is not ideal, and does suggest some crystalline or compositional imperfection in the as-grown bulk crystals. In particular, there appears to be a broad underlying signal in the measured region when taken using a 9.5 GHz excitation source. If the frequency is increased to 94 GHz with B||c taken at 5 K, this additional signal becomes more pronounced, as shown in Figure 4.9. Additionally, if a plot is made of the measured EPR intensity versus the temperature, the measured signal deviates from the expected decrease in intensity via the Curie law. This sharp deviation from the Curie law above 50 K is likely due to an increase in the free carrier concentration, which in turn results in a decrease in the resonator cavity Q. A similar degradation in quality, due to the free carrier concentration is observed in the $Zn_{1-x}Co_xO$ samples. Hall Effect measurements of both

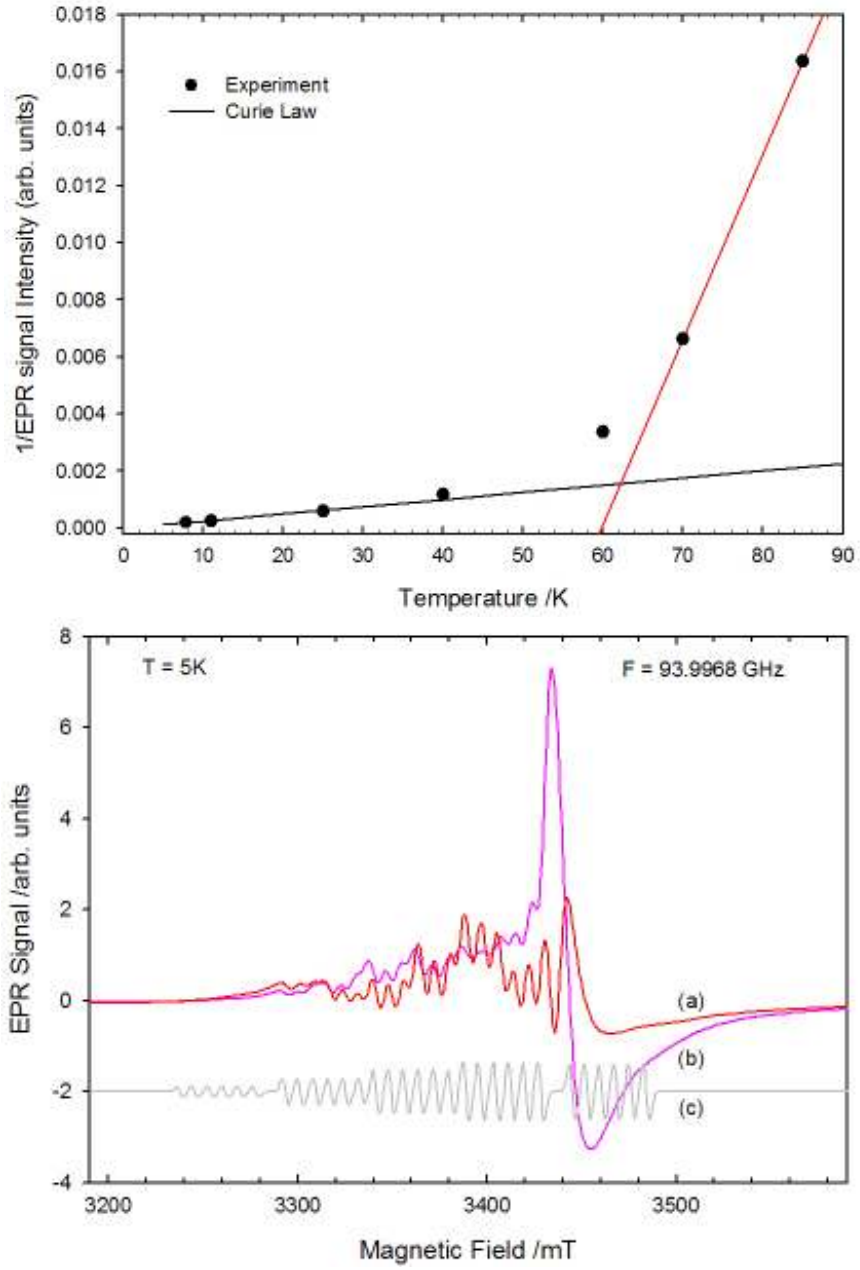

Figure 4.8 Curie law dependence of the EPR signal from $Zn_{1-x}Mn_xO$ single crystal and the influence of excitation power (low (a), high (b)) on the EPR spectrum at 94 GHz.

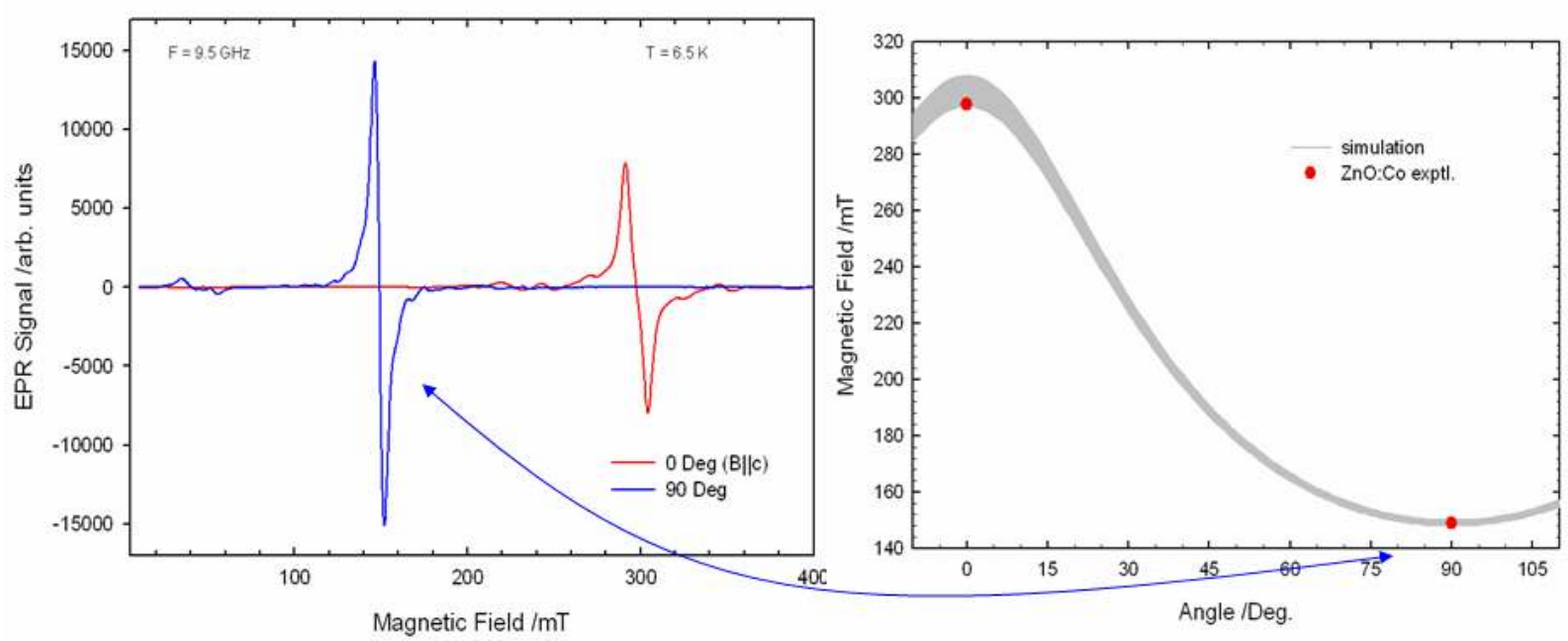

Figure 4.9 Comparison of the predicted and measured EPR signal parallel and perpendicular to the c-axis.

the Mn- and Co-alloyed ZnO samples show a strong n-type conductivity (~10^{19} cm^{-3}) resulting from the intrinsic defects in the system.

4.6 Raman Results

Raman spectra for varying concentrations of transition metal dopants in the $Zn_{1-x}Mn_xO$ and $Zn_{1-x}Co_xO$ are shown in Figure 4.10 and Figure 4.11. The scans for the undoped crystal are shown at the bottom of the graph; the other curves are shifted vertically for clarity. All samples were taken in the back scattering geometry using a 488 nm Ar laser. In the undoped sample, the most prevalent features are the lines at 437 cm^{-1}, which corresponds to the E_2(high) mode, and a mode at 332 cm^{-1}, which correspond to a 2-phonon line. There is also a shoulder on the E_2(high) peak at 407 cm^{-1}, which has been previously indexed as the E_1(LO) mode, and a smaller peak at 202 cm^{-1} corresponding to twice the E_2(low) mode [139]. Upon Mn doping, the overall shape of the Raman spectrum changes, due to loss of symmetry conservation; this leads to the appearance of 'silent' and mixed Raman modes from points off the center of the Brillouin zone [140]. In $Zn_{1-x}Mn_xO$, these modes are particularly prevalent at 522 cm^{-1} and 580 cm^{-1}. The major peaks of the undoped ZnO lattice are still also visible, indicating that the structural quality is only slightly degraded. $Zn_{1-x}Co_xO$ shows a similar behavior, though the silent modes are less enhanced, and there is still a strong contribution from the 437 and 332 cm^{-1} modes of the host lattice. Also, the dominant mode in the disordered region appears to be closer to 550 cm^{-1} instead of 522 or 580 cm^{-1}. These findings are quite similar to reports of Raman spectra in $Zn_{1-x}Co_xO$ which does exhibit the ferromagnetic behavior reported from other researchers [141]. Additionally, in both cases there appears to be a broad line near 487 cm^{-1}. This mode is not attributed to any of the expected Raman

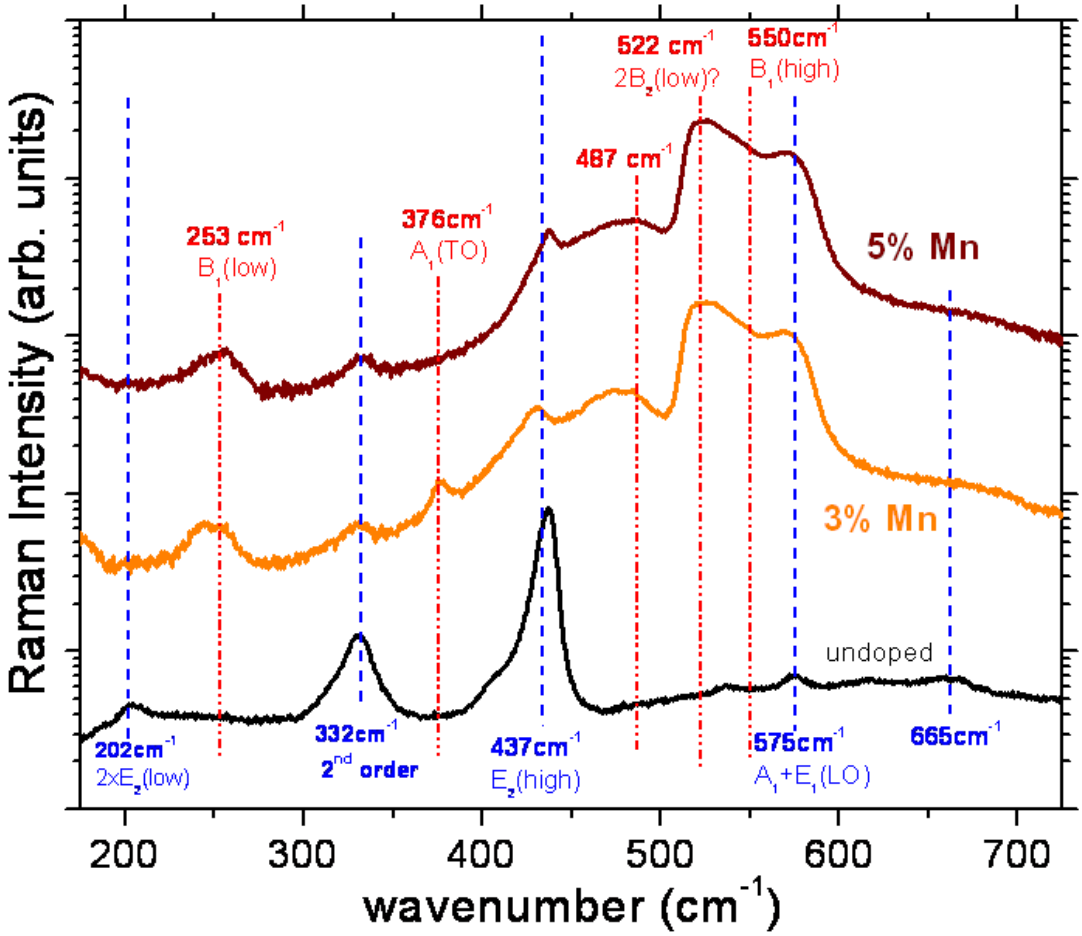

Figure 4.10 Raman spectra of undoped and Mn-doped ZnO single crystals with increasing alloying content

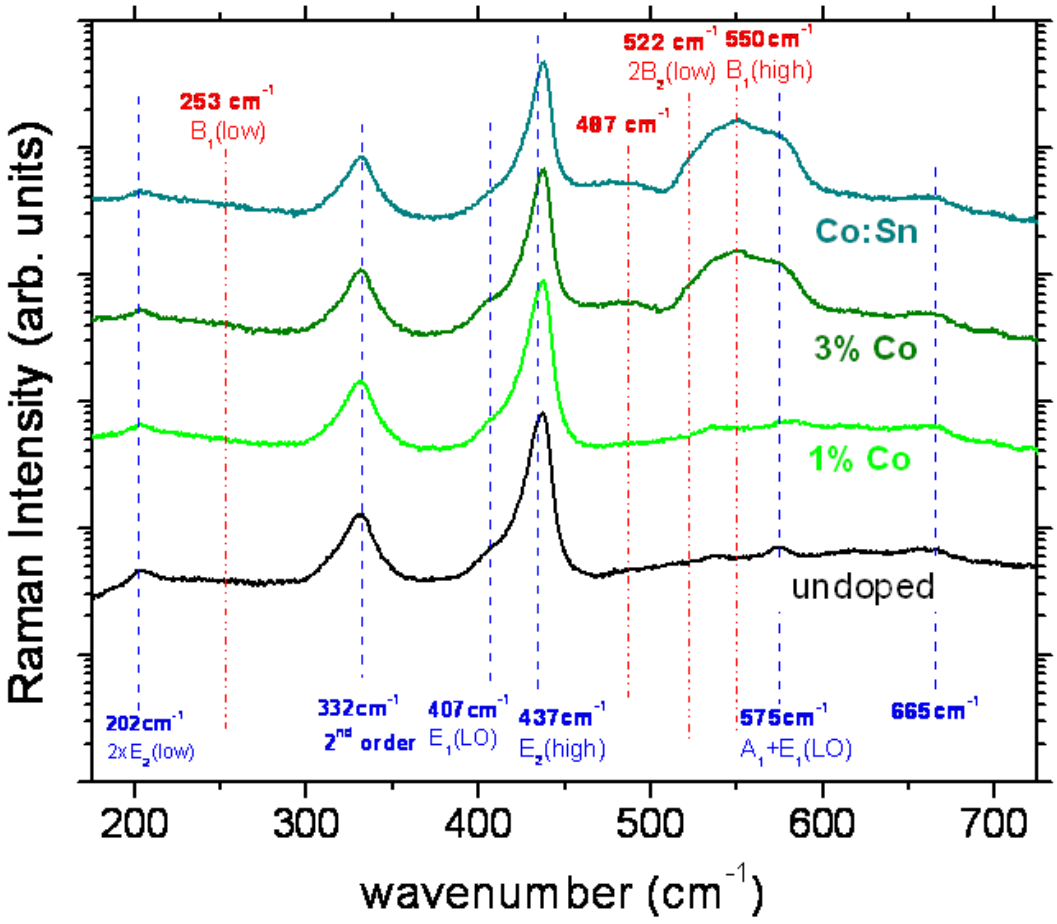

Figure 4.11 Raman spectra of $Zn_{1-x}Co_xO$ single crystals as a function of the transition metal alloying content.

modes for the wurtzite structure. There is, however, a mode in the spinel (TM_3O_4) structure to which this mode may be linked, as has been previously suggested and observed via detailed Raman studies [142]. Given the breadth of this mode, it may be a product of the surface decomposition and, given the critical temperature of the typical spinels (T_C = 43 K for Mn_3O_4 and T_N = 40 K for Co_3O_4), should not lead to a competitive ferromagnetic phase complication of the magnetic data.

4.7 Magnetization Studies of $Zn_{1-x}TM_xO$ results

4.7.1 Magnetization studies in $Zn_{1-x}Mn_xO$ and $Zn_{1-x}Co_xO$

The magnetic behavior of these materials is of critical importance for spintronic applications. Figure 4.12 shows the magnetization vs. temperature plot for three samples with increasing Mn doping concentration (0.2%, 0.6%, and 1.6% composition by SIMS for samples A, B, and C respectively) taken at 100 K. Also included in these figures, to give an estimate of the magnetization involved in the system, are lines indicating the expected magnetization behavior based on the diamagnetic volume susceptibility of ZnO, the paramagnetic susceptibility of MnO, and non-interacting mixture of 99 wt% ZnO – 1 wt% MnO. The 100 K temperature is above the most likely ferrimagnetic oxide contaminant, the spinel Mn_3O_4, which has a Curie temperature of 46 K. Linear, paramagnetic behavior is observed for samples B and C, due to the incorporation of the Mn atoms. In Sampl A, the most lightly doped, the 100 K and 300 K curves show diamagnetic behavior, due to the nominally temperature independent diamagnetic contribution from ZnO becoming dominant over the smaller temperature-dependent paramagnetic Mn^{2+} contribution. At 5 K, the most lightly doped sample shows

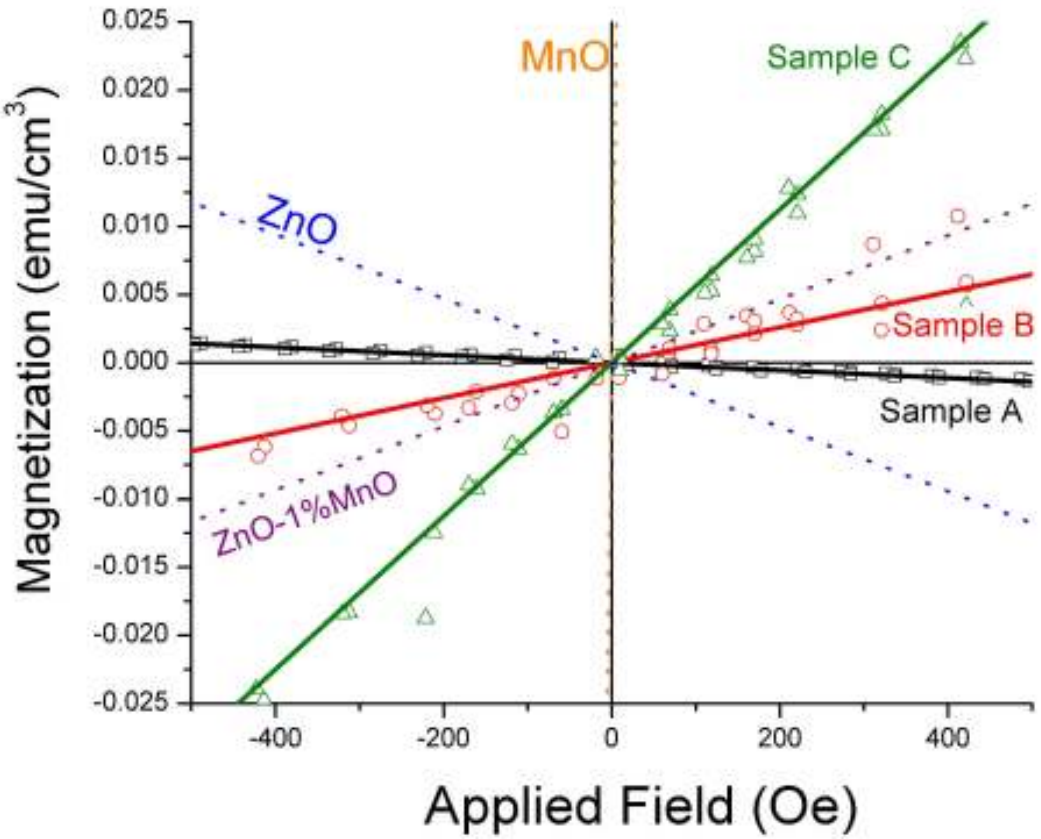

Figure 4.12 100K magnetization plot for $Zn_{1-x}Mn_xO$ for samples A x=0.0004, B x=.01, and C x=.03. The dotted lines show the expected behavior for ZnO, MnO, and a linear mixture of ZnO–1% MnO for comparison.

macroscopically paramagnetic behavior because of the 1/T dependence of the paramagnetic signal becomes a larger influence than the temperature independent diamagnetic ZnO signal. In addition, no hysteresis is observed at 5 K, indicating the exclusion of any ferrimagnetic oxide second phase.

Magnetization versus applied field curves for $Zn_{1-x}Mn_xO$ and $Zn_{1-x}Co_xO$ at room temperature are shown in Figure 4.13. It is readily apparent that neither of the as-grown crystals exhibits ferromagnetism; the plots are linear and reflective of the superposition of the diamagnetic ZnO signal and the paramagnetic signal from the individual isolated transition metal ions. These curves show the magnetization vs. applied field plot for

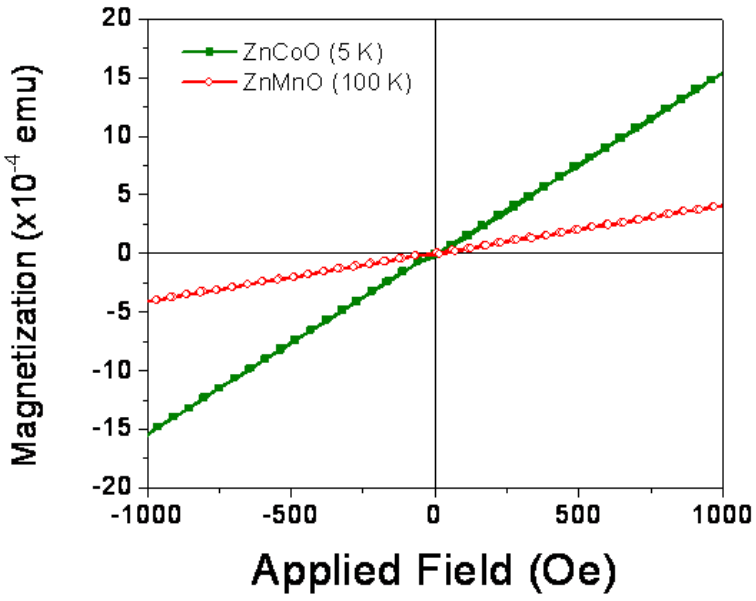

Figure 4.13 Magnetization curve for 3% Mn- and Co-doped samples

samples doped at 3% Mn and Co concentration. Linear, paramagnetic behavior is observed for almost all samples at temperatures ranging from 5 K to 300 K. No ferromagnetic or ferrimagnetic oxide contaminants, such as Mn_3O_4 (T_c = 46 K), were present. The curves are of the expected slopes due to a contribution from predominantly isolated d^5 or d^7 atoms in a diamagnetic, noninteracting ZnO matrix. This is completely consistent with many theoretical predictions as well as earlier reports of Mn in other II-VI compounds [74, 143, 144]. Such a magnetization behavior is also expected from Mn^{2+} in the ZnO lattice via the double exchange mechanism [54].

4.7.2 Curie-Weiss Behavior of $Zn_{1-x}Mn_xO$

The inverse magnetic susceptibility of $Zn_{1-x}Mn_xO$ is shown in Figure 4.14. It is clear from this Curie-Weiss plot that a linear behavior is observed at elevated temperature. There is a slight deviation from linear behavior at low temperatures, due to

the antiferromagnetic Mn-Mn exchange interactions. After performing the required correction [74] for the diamagnetic background, the extrapolated intercept with the x-axis gives Θ=-33.6 K. Assuming only nearest-neighbor interactions, Mn in the 5/2 spin state, and fitting to a Curie-Weiss type function, the exchange integral can be calculated to be:

(eq. 4.1) $$J_1 = \frac{3k_B\theta_o}{2z(S)(S+1)}$$

The exchange integral J_1/k_B is calculated to be -17.2 K when using z=12 as the number of nearest neighbors in the wurtzite lattice and correcting for the atomic fraction of Mn. This calculated value is similar to the 15K observed with Mn-Mn in heavily alloyed (x=0.36) $Zn_{1-x}Mn_xO$ grown by pulsed laser deposition [98]. The less-pronounced deviation from linearity and smaller magnitude of the temperature intercept are indicative of the dilute

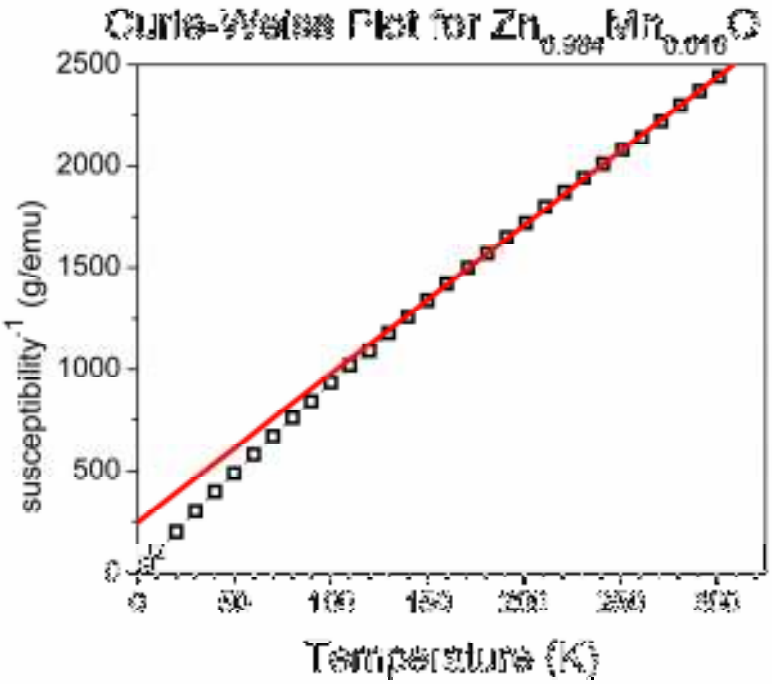

Figure 4.14 Curie–Weiss plot of $Zn_{1-x}Mn_xO$ showing a deviation from nominal paramagnetic behavior is observed at low temperatures. The extrapolated intercept of the linear high-temperature region is at Θ=−33.6 K.

nature of the Mn atoms, such that the average distance between Mn is large and fewer atoms participate in the superexchange process. If the Mn atoms were distributed randomly on Zn sites, at this concentration only one sixth of the Mn-atoms would have a single nearest-neighbor Mn atom on an adjacent Zn-site for a 1.5% doping level. For a randomly distributed alloy where all transition metals are on substitutional sites, the expectation value for nearest neighbor occupancy is only $\langle z \rangle = 0.36$. For $x=0.36$, $\langle z \rangle$ is 4.32, which is 12 times that of the dilute case. Thus, the lower observed temperature intercept would be expected for the dilute case and is consistent in magnitude with previously grown thin film samples.

These results indicate that the dominant exchange mechanism is Heisenberg exchange, which is consistent with samples grown by other high-temperature techniques and with other Mn-doped II-VI compounds [74]. For comparison, the J_1/k_B for the other II VI compounds are -13.7/K and -11.8/K for $Zn_{1-x}Mn_xSe$ and $Zn_{1-x}Mn_xTe$ [74]. The larger exchange integral would be expected based on the reduced interatomic distances in ZnO relative to the other II-VI materials, which results in a stronger antiferromagnetic coupling among Mn atoms in nearest neighbor sites.

The high-spin (S=5/2) Mn^{2+} spin state configuration is observed in other tetrahedrally coordinated Mn in II-VI semiconductors [74], and can be verified in ZnO using the Curie-Weiss law, $\chi = X/T-\Theta$. The Curie constant is related to the Bohr magnetons per Mn ion through the relation:

(eq. 4.2) $$C = p_{eff}^2 \mu_B^2 N_{avo} x / 3k_B$$

where p_{eff} is the Bohr Magneton number. From the calculation of the Curie constant, the estimated Bohr Magneton number for Mn is 5.4 μ_b/Mn atom, which indicates that the Mn is in the high spin state (S=5/2) as expected.

4.7.3 Unusual hysteretic behavior in $Zn_{1-x}Co_xO$

The magnetic behavior of the some of the cobalt-doped samples is considerably different than in the Mn-doped crystals, as seen in Figure 4.15. In this curve, clear evidence of hysteresis is observed in this loop for $Zn_{1-x}Co_xO$. The curve is reminiscent of uncorrected curves reported for thin film DMS, where the diamagnetic contribution of the substrate is significantly larger than the film and is usually subtracted out. In this case, there is no substrate contribution. The ZnO background does lead to a large diamagnetic

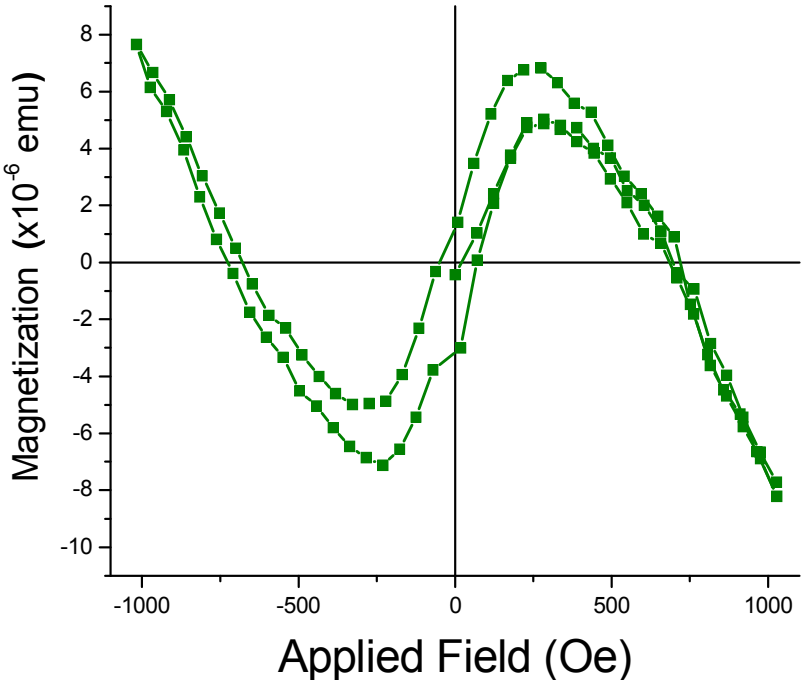

Figure 4.15 Hysteresis curve observed from a lightly doped (x=0.01) $Zn_{1-x}Co_xO$ samples showing a superposition of ferromagnetic and diamagnetic behavior.

contribution, but if the entire material consisted of a ferromagnetically coupled Co-based dilute magnetic semiconductor, the expected magnetization should be significantly larger than the ~10^{-4} emu/g (less than 0.01 μ_B/Co) observed in the $Zn_{1-x}Co_xO$ crystal. The negative slope in the diamagnetic region is less than that anticipated from pure ZnO, indicating a paramagnetic contribution from the remaining cobalt atoms. Closer examination of the field cooled and zero field cooled magnetization curves in Figure 4.16 taken at 100 Oe shows a superparamagnetic-cluster type behavior of these two curves. The extrapolated lopes vs. temperature are of opposite sign in the ZFC and FC curves and there is a significant deviation in these two values. Similar behavior has been reported previously in suspended Co particles in ZnO [102] as well as MnAs nanoparticles in $(Zn_{1-x}Mn_x)_3As_2$ [145]. Thus, the observed hysteresis is most likely due to nanoscale paramagnetic Co-clusters below the blocking temperature or surface magnetic phases, with the remaining dissolved isolated Co^{2+} atoms providing a paramagnetic contribution. Though it is difficult to extract due to the masking effects of the Co clusters, it is reasonable to assume that the dominant exchange mechanism here is also antiferromagnetic superexchange, similar to that found above in $Zn_{1-x}Mn_xO$, and that observed in $Zn_{1\ x}Co_xS$ and $Zn_{1\ x}Co_xSe$.[146]. Recent analysis of single crystalline $Zn_{1-x}Co_xO$ confirms this prediction [147]. These findings would also be consistent with recent density functional calculations for dilute, intrinsic $Zn_{1-x}Co_xO$ [148]. A slight hysteresis likely due to Co precipitates was observed in the 1% samples, but the low Bohr magneton contribution per Co (<0.01 μ_B/Co) and the strong splitting in the zero field cooled/field cooled magnetization curves preclude this from being a bulk alloy effect.

4.8 Efforts to introduce ferromagnetic behavior

The absence of ferromagnetism in the as grown crystals may be caused by intrinsic defects if the ferromagnetism within the transition metal spectra is indeed due to an impurity band, as has been recently suggested [149]. Though the high temperature

melt growth method does promote uniform mixing of the transition metal substituents, it also allows for equilibrium concentrations of intrinsic defects to form. These intrinsic defects are overwhelmingly n-type in the as grown material, which drive the Fermi level towards the valence band and outside of any impurity band which may stabilize ferromagnetism in the material. Hall measurements confirmed an overall n-type behavior in the as grown crystals. Ferromagnetism is not anticipated in either the mean-field or double-exchange model without additional p-type doping in this system. There is no intentional carrier doping in these samples, although a background n-type electrical conductivity typical of ZnO has been confirmed through electrical property measurements. Photoluminescence in these samples exhibited a broad greenband emission centered around 550 nm, which is typically attributed to intrinsic defect transitions in the doped material. The large doping levels, however, quenched any cathodoluminescence in these samples. These findings do not preclude double exchange at higher doping levels and/or indirect exchange becoming dominant in the presence of free carriers, which could lead to ferromagnetism in these samples. Additional efforts were made to introduce an observed ferromagnetic behavior into these single crystals, as described in more detail below.

4.8.1 Sn co-doping

One method for introducing carriers within the system that may stabilize a carrier mediated exchange is the use of additional donors to the system. In the literature, Sn has shown some promise in controlling the ferromagnetic behavior of manganese-doped ZnO when produced via molecular beam epitaxy [90]. In this study, a single crystal sample of cobalt doped ZnO was produced and co-doped with 10^{18} cm^{-3} Sn atoms by adding a

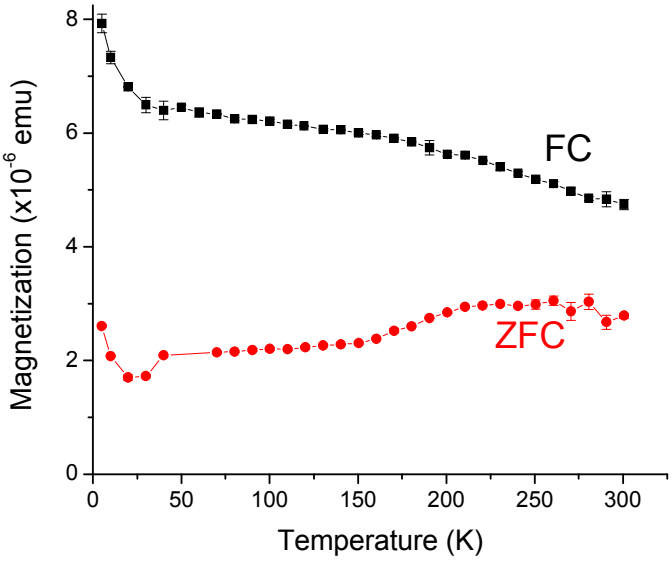

Figure 4.16 Zero Field Cooled and Field Cooled plots from a $Zn_{1-x}Co_xO$ (x=0.01) sample at 100 Oe.

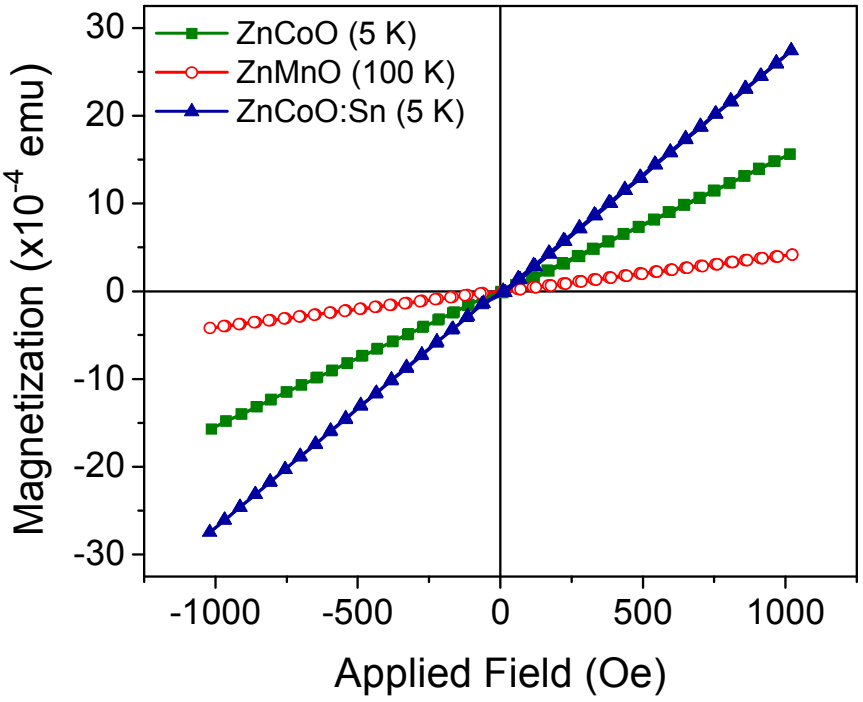

Figure 4.17 Comparison of magnetization curves for $Zn_{1-x}Mn_xO$ and $Zn_{1-x}Co_xO$ with and without tin codoping. Paramagnetic behavior is observed in all cases.

stoichiometric amount of Sn precursor to the melt powder. Figure 4.17 magnetization data grown on Sn-doped ZnO samples. A similar linear behavior in the magnetization versus field curves for $Zn_{1-x}Co_xO$ and $Zn_{1-x}Co_xO$:Sn indicates that n-type carrier conduction or ferromagnetic superexchange (which is possible in d^7 ions) are not sufficient to stabilize ferromagnetism in this compound. Moreover, the contribution from cobalt metal precipitates which has been observed previously is not present in these samples. The dominant exchange mechanism here is also antiferromagnetic superexchange, as confirmed by an evaluation of the negative linear intercept of the inverse susceptibility vs. temperature plot. Like $Zn_{1-x}Mn_xO$, the results show that $Zn_{1-x}Co_xO$ is an extension of the II-VI family of materials.

4.8.2 Li co-doping

As both the carrier concentration and carrier type are controversial variables in the study of introduction of ferromagnetism into semiconductor materials, it is also instructive to look at attempts to dope this material p-type, or to try to introduce some acceptor dopants into this materials system. One such dopant that could be used would be Li, which could act as an acceptor in ZnO provided it substitutes on the Zn lattice site. For this study, Li metal was deposited on the surface of a ZnO crystal and, using diffusion, driven into the crystal. Figure 4.18 shows the resulting hysteresis curve from the Li-doped $Zn_{1-x}Co_xO$ sample. No change is observed with the lithium doping. A possible explanation is that the reported ferromagnetism is a result of some mechanism not related to the origin p-type doping model. However, there is no guarantee that the diffusion process causes the lithium atoms to be substitutionally incorporated on the ZnO site. Lithium is a particularly tiny ion and often ends in interstial sites rather than substitional sites, where it does not act as an acceptor. Given that attempts to p-dope ZnO using lithium have largely been unsuccessful, this explanation seems plausible.

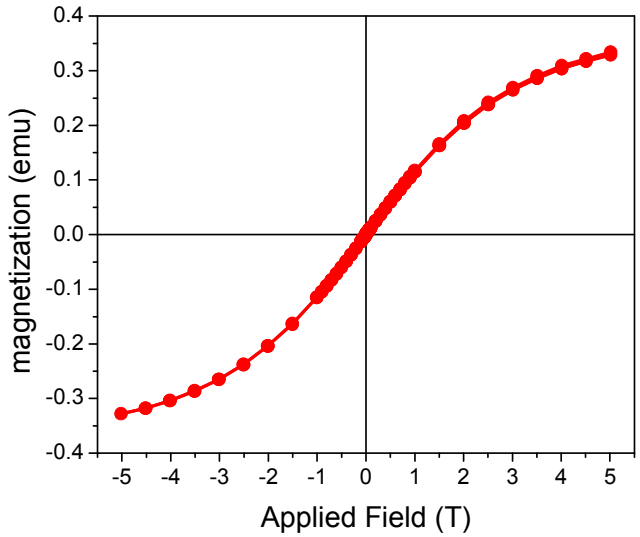

Figure 4.18 Magnetization curve for vacuum annealed $Zn_{1-x}Mn_xO$ sample showing no indication of ferromagnetic behavior.

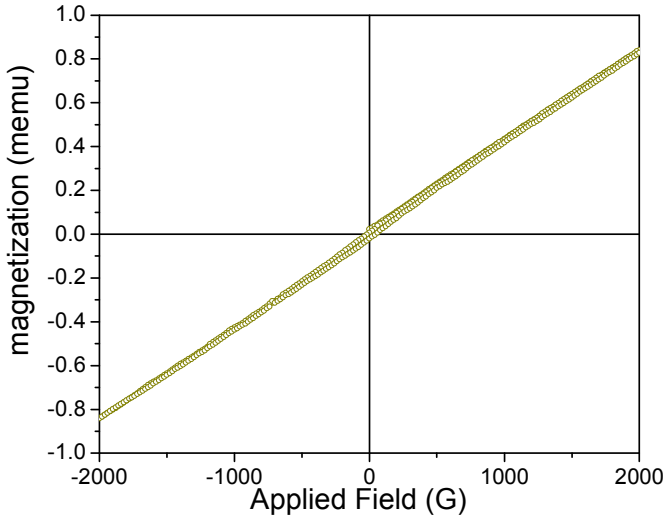

Figure 4.19 Room temperature vibrating sample magnetometry scan from a $Zn_{1-x}Co_xO$ following lithium diffusion.

4.8.3 Vacuum Annealing

Another method that has been used to induce the observed ferromagnetic behavior in $Zn_{1-x}Mn_xO$ is the use of vacuum annealing [150, 151]. The exact reason why this procedure results in an observed ferromagnetic ordering is not clear at this time, but is thought either that carrier introduction compensates the formation of oxygen vacancies, or else that these vacancies themselves help to mediate the ferromagnetic interaction. A $Zn_{1-x}Mn_xO$ sample was placed inside a glass ampoule, which was then evacuated. The evacuated ampoule was then baked in a furnace at a temperature of 900^oC for 24 hours, conditions which had been reported to result in the formation of a ferromagnetic alignment in thin films. Figure 4.19 shows the magnetization at 5 K up to a field of 5 T; a Brillouin-shaped function confirms the paramagnetic nature of the isolated Mn d^5 centers in ZnO. No hysteresis was observed in this sample. This may indicate that either the annealing conditions were insufficient to induce a sufficient quantity of vacancies in the crystal, or that some sort of grain boundary vacancy formation or secondary phase formation is the cause of the magnetic hysteresis in the previous reports.

4.8.4 Ion implantation

Another method that has been frequently suggested to be a valid means for producing homogeneous and ferromagnetic transition metal doped nitrides is ion implantation. For this work, samples implanted at $3x10^{16}/cm^2$ Mn ions at 200 keV were examined via SQUID magnetometry. The resulting magnetization curve is shown in Figure 4.20. In contrast to the other methods that were attempted to induce ferromagnetism in these materials, the ion implanted sample did have an indication of

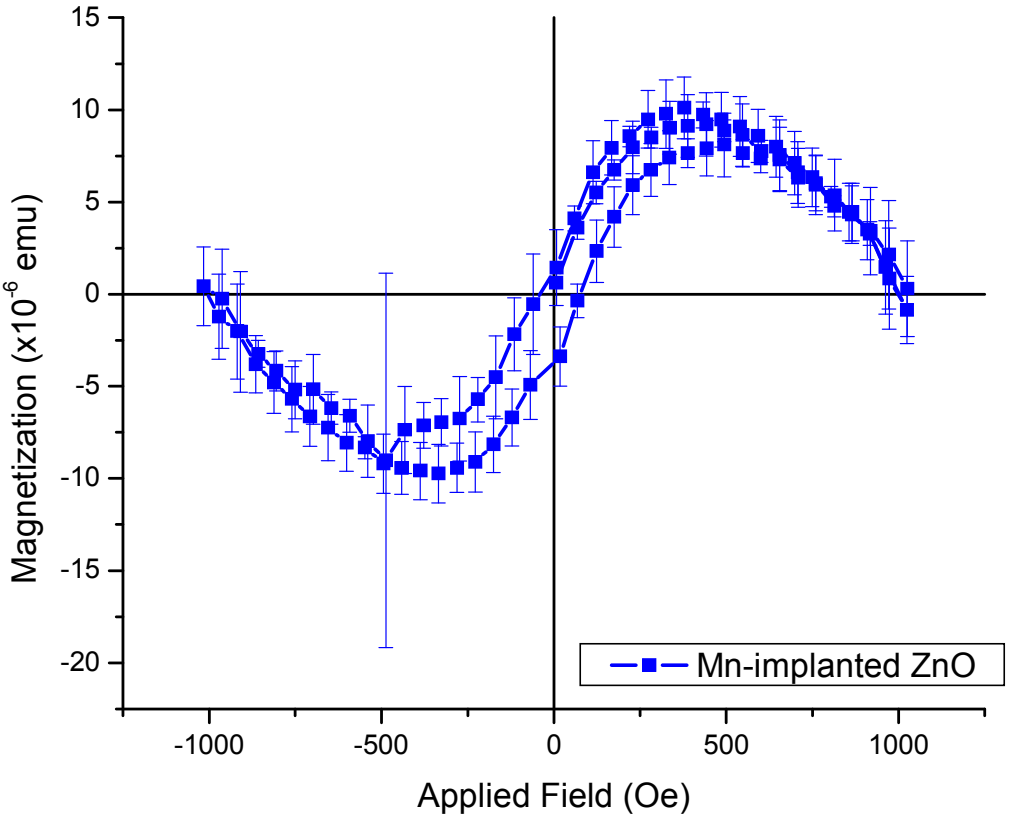

Figure 4.20 Hysteresis curve from bulk ZnO single crystal which has been implated with 3 x 10^{16} cm^{-2} Mn ions

magnetic hysteresis. Given the large excess of Mn ions which were introduced and the large amount of lattice damage that resulted, it is unlikely that the resulting hysteresis signal is from isolated and substitutional Mn atoms. Only the method which should produce the most defective material resulted in the observation of ferromagnetism in these samples. Thus, the FM may be dependent on the formation of defects that are not accessible through the melt processing route.

4.9 Discussion

In order to understand these results within the overall framework of the literature on transition metal doped zinc oxide, it is imperative to examine how these results

compare with other reported results. As mentioned before, there is still a large amount of published data suggesting that the ferromagnetic ordering is due to an intrinsic mechanism related to either carrier mediation or magnetic polaron interaction. Moreover, the reproducibility of the ferromagnetic ordering data is still highly questionable; though this is not unusual for the ZnO system, where even seeming simple goals such as p-type doping suffer from problems in both the stability and reproducibility [152]. Moreover, the observation of reversible ferromagnetism in polycrystalline thin films that can be tailored with either zinc- or oxygen-atmospheric annealing is an interesting result which is difficult to reconcile with a phase segregation model [153].

It is interesting to compare the methods of growth across the spectrum with the various magnetic properties and fit the results of this work into the rest of the literature. Of particular interest are some studies performed on $Zn_{1-x}Mn_xO$ and $Zn_{1-x}Co_xO$ nanocrystals produced by solution synthesis. This is another route by which near equilibrium growth techniques can form these compounds. When producing thin films of the material, ferromagnetism was found to be strongly dependent on the rate at which the films were coalesced [154]. Conditions which led to the formation of grain boundaries were essential to the observation of room temperature ferromagnetism in these materials. Another study which explored in detail the processing conditions necessary for the realization of room temperature ferromagnetism via the equilibrium solid state reaction route also pointes to a processing-related origin of the ferromagnetism [92]. This study emphasizes the need to do extensive ball milling on the sample prior to the reaction. It was suggested that ball milling is necessary because this eliminated the formation of any trace amounts of antiferromagnetic Mn-O compounds which quench the ferromagnetism. In reality, aggressive ball milling within the sample introduces large amounts of vacancy-related defects in the system. These may be related to formation of a defect-related pathway for ferromagnetism as has been suggested in some of the models. Additionally, the observation of antiferromagnetic interactions in this work on single crystals and in

studies on single crystalline thin films, the observation of low temperature ferromagnetism and x-ray magnetic circular dichroism in hydrogen-rich ZnO films [155], and the experimental observation of grain boundary clusters or Cu-O plates in ferromagnetic samples [156] suggest that experimental ferromagnetism diverges from the originally suggested model. Moreover, only low temperature magnetotransport effects have been observed [157]. Defects play an essential role in the mediation of ferromagnetism in these materials, and further work must be performed to understand the role of grain boundaries in the macroscopic behavior of the materials explored in this system. Further studies using systems with high surface area to bulk ratios may help in exploring the ultimate origin of the ferromagnetism in transition metal doped ZnO systems.

CHAPTER 5

ION IMPLANTATION AND MOCVD GROWTH OF GALLIUM MANGANESE NITRIDE

5.1 Introduction

Though the initial results in the ZnO crystals are not promising for the development of room temperature ferromagnetic semiconductors, these results should not be surprising considering the development of ferromagnetic dilute magnetic semiconductor materials in the 1990's. Earlier results had shown the II-VI compounds to be largely paramagnetic; it was only through the introduction of large alloying concentrations, on the order of 20% Cr in $Zn_{1-x}Cr_xTe$ [158], that true dilute magnetic semiconductor behavior was ultimately observed.

In the III-V materials, particularly $Ga_{1-x}Mn_xAs$ and $In_{1-x}Mn_xAs$, the situation is somewhat different. Through the introduction of Mn, ferromagnetism can be stabilized through a carrier mediated mechanism as described in more detail in Chapter 2. The question remains: is the situation in the wide bandgap materials relative to the III-V and II-VI compounds the same? Namely, are the III-V compounds more suitable for spintronic applications than their II-VI wide bandgap counterparts?

If this question is to be resolved, a detailed study must be performed on these materials. In order to ultimately determine what is going on in this materials system, it is essential to use optimal growth techniques and use characterization techniques to examine the materials properties. In this chapter, methods to study and optimize the

growth of $Ga_{1-x}Mn_xN$ are explored. Magnetic optical and structural studies have been used to investigate the origin of the room temperature (RT) ferromagnetism (FM) observed in $Ga_{1-x}Mn_xN$ epilayers. In general, RT ferromagnetism scales with the Mn concentration. RT FM was also observed, but significantly weaker, in MOCVD-grown semi-insulating and n-type epilayers. This indicates that the RT FM is very sensitive to the position of the Fermi level, requiring that the Mn ion is in the Mn^{3+} state. However, the magnetization data alone do not provide enough information to reveal the actual origin of the RT ferromagnetism. More detailed magnetic studies suggest that based on a splitting of the curves, the room temperature magnetic signal may indeed originate from clustering behavior in this system.

5.2 Implantation Studies

Ion implantation is an efficient technique for introducing additional elements into a semiconductor system after the growth of the materials has been completed. It was used extensively for dopant introduction; for example, in the development in silicon-based materials. In particular, because of masking techniques, it is possible to implant different regions of the material with different dopant types and thus get a lateral spread of dopants within the materials. Implantation may also be useful for the introduction of dopants into dilute magnetic semiconductor materials. In particular, it is attractive because the method is extremely straightforward. It is possible to implant almost any ionic species into a host material, and all that is needed is an implantation tool and an elemental source. Through control of the accelerating voltage, a known profile of dopant atoms can be introduced into the system. Moreover, control of the dopant density is merely a function of the dose applied to the system. This method also eliminates challenges with *in situ* doping

techniques, including optimization of growth conditions or and the need to locate a suitable chemical precursor for chemical vapor deposition processes.

It is essential to note that this method is not without its problems for DMS materials. In particular, large dopant densities required need huge (i.e. lattice) concentration of atoms to be introduced, and to introduce them uniformly at a sufficient depth requires large energies. This results in significant lattice damage within the system, which must be annealed out and may be impossible to be completely recovered. In addition, if only transition metal atoms are implanted, the implantation process results in the introduction of a disparate proportion of atoms, such that the cation/anion stoichiometry is not maintained. This could result in the formation of metal rich regions in the lattice. Note, however, that much of the initial work reported in the literature suggests that ion implantation is a valid way of producing transition metal-doped GaN. This work can investigate these claims and, using comparisons with existing literature, can serve as a good baseline for our measurements and development of MOCVD-grown $Ga_{1-x}Mn_xN$.

5.2.1 Implantation procedure

In this work, Mn^+ ions were implanted into MOCVD-grown GaN layers. The doping concentration was $3x10^{16}/cm^2$ at an energy of 200 keV and a substrate temperature of 400^oC; these characteristics were chosen based on a similarity to previously reported conditions [159]. The elevated temperature stage may promote dynamic annealing during the growth process and was intended to mitigate the amount of lattice damage in the system [160]. In order to compare the role of carrier concentrations on possible magnetic behavior in the system, different GaN templates were used,

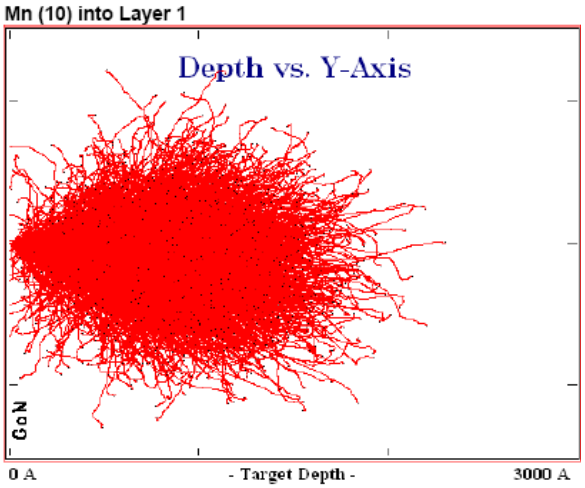

Figure 5.1 Monte Carlo simulation of the atomic distribution of implanted Mn ions under the conditions used in this study.

including material that was originally intrinsic (unintentionally doped), p-type ($p=2x10^{16}/cm^3$), and n-type ($n=6x10^{17}/cm^3$). In order to remove the implantation damage, samples were subsequently annealed face-down on GaN templates in a flowing nitrogen ambient at temperatures ranging from 700°C to 900°C.

5.2.2 SRIM calculations

Calculations of the expected doping profile were performed using a publicly available *Stopping Ranges of Ions in Materials* (SRIM) program [161]. This program takes inputs of a materials density and atomic makeup, and then uses Monte Carlo simulations to determine the expected range and distribution of implanted atoms within the system. Figure 5.1 shows the ion profile of a sample calculation using this program. Moreover, this method can also calculate the amount of vacancies and backscattered atoms within this configuration. A plot of a sample expected ion distribution is shown for the implantation conditions used in this study. From these results, the expected implantation range is 910 Å, with a straggling of 380 Å and a radial range of 431 Å. It is

imperative to note that the particular model used in this study does not take into account any self-healing which may be occurring in this material. Self-healing behavior has been reported previously in the GaN system [104] and seems to mitigate, at least somewhat, the lattice damage which occurs through the implantation process.

5.2.3 X-ray diffraction studies

XRD 2θ−ω scans for the ion implanted samples before and after annealing are shown in Figure 5.3, along with the 2θ−ω scan for an undoped GaN layer on c-sapphire. The annealing conditions used to recover the implantation damage in the sample are shown to the right in this figure. The scans are similar for the undoped and as-implanted samples, with the exception of a distinct elbow and tail on the low angle side of the peak due to the large local Mn concentration and predominantly interstitial defects in the implanted samples. Because the low-angle side represents material with a larger lattice parameter, the lower angle tail indicates damage which increases the lattice parameter. Since Mn and Ga have similar tetrahedral atomic radii, the introduction of lattice site Mn cannot be the sole cause of this shift in lattice parameter. Thus, this is likely due to the presence of interstitial Mn or knock-on Ga atoms. No additional phases are observed in the as grown samples.

5.2.4 Annealing and damage recovery

In order to minimize the damage to the lattice, as would ultimately be necessary for spintronic devices, annealing studies were performed on the implanted samples. High-resolution XRD 2θ−ω scans for the ion implanted samples before and after annealing are shown in Figure 5.2, along with the scan for an undoped GaN layer on c-sapphire. The scans are similar for the undoped and as-implanted samples, with the exception of a

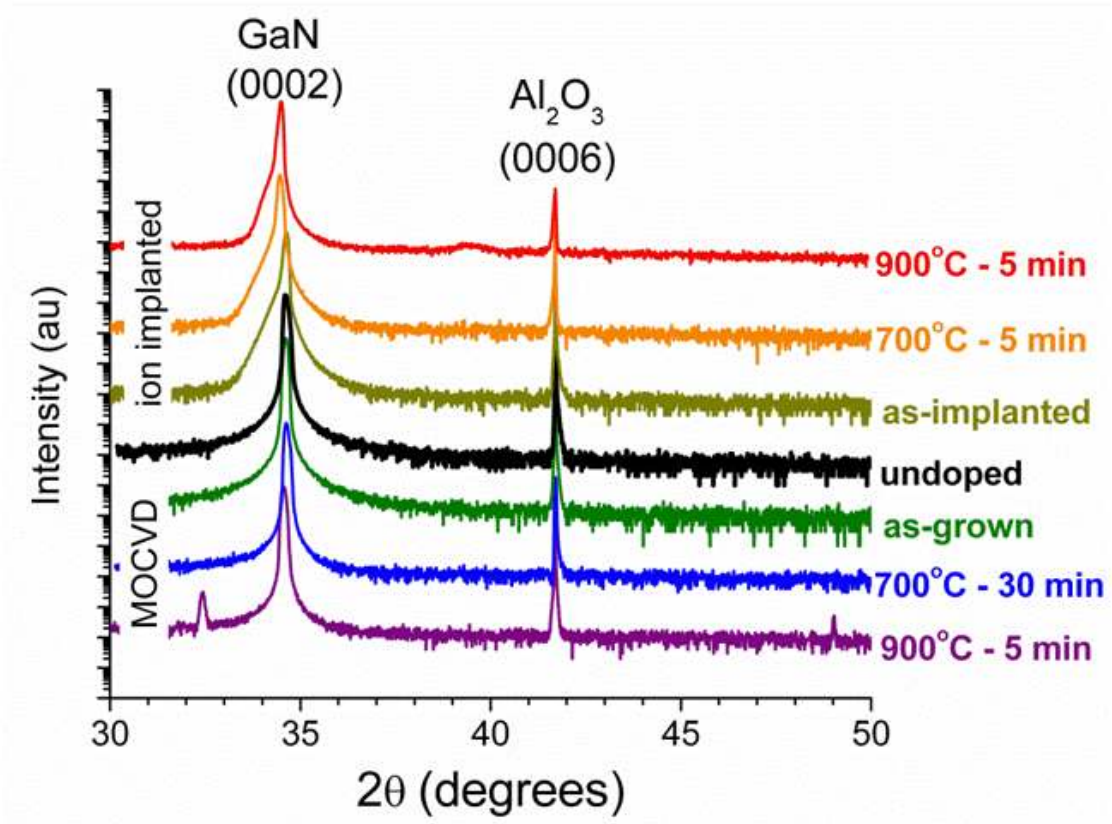

Figure 5.2 High resolution X-ray diffraction scans for implanted and as-grown layers before and after annealing

distinct elbow and tail on the low angle side of the peak due to the large local Mn concentration and predominantly interstitial defects in the implanted samples. After annealing, this low-angle peak shelf is still visible, indicating that the damage is not fully recovered. Furthermore, additional XRD peaks are observed in the annealed samples. Figure 5.3. The peak at 32.4° corresponds most closely to either the metallic perovskite phase $Mn_{4-x}Ga_xN_{1-y}$ or the intermetallic Mn_8Ga_5. Also visible in some scans are peaks from the antiferromagnetic compounds $Mn_6N_{2.58}$ and Mn_3N_2. Similar non-stoichiometric phases have been observed previously in MBE grown [76] and heavily-annealed implanted samples [162]. Ion implantation introduces an excess of gallium site cations; the annealing conditions are not suitable for the replenishment of nitrogen and subsequent rearrangement of a 1:1 stoichiometric crystal. Thus, the end result of the annealing process is a mixture of Mn on lattice sites and regions of a Mn rich phase, plus a high quantity of interstitials and vacancies leftover from the implantation process. It will be difficult to ascertain the exact magnetic contribution from each of these sources. The other important feature to note is that phase separation can occur even at temperatures that are standard for activation of GaN materials and that have also been reported as suitable for $Ga_{1-x}Mn_xN$ annealing [162]; this observation would significantly complicate the processing conditions for the production of implantation-based dilute magnetic semiconductor devices.

5.2.5 Magnetization studies

SQUID magnetometry was used to examine the Mn-implanted GaN samples. The magnetization vs. field results are shown for an implanted intrinsic, p-type, and n-type GaN sample in Figure 5.4. In this diagram, it is clear that for the p-type, n-type and

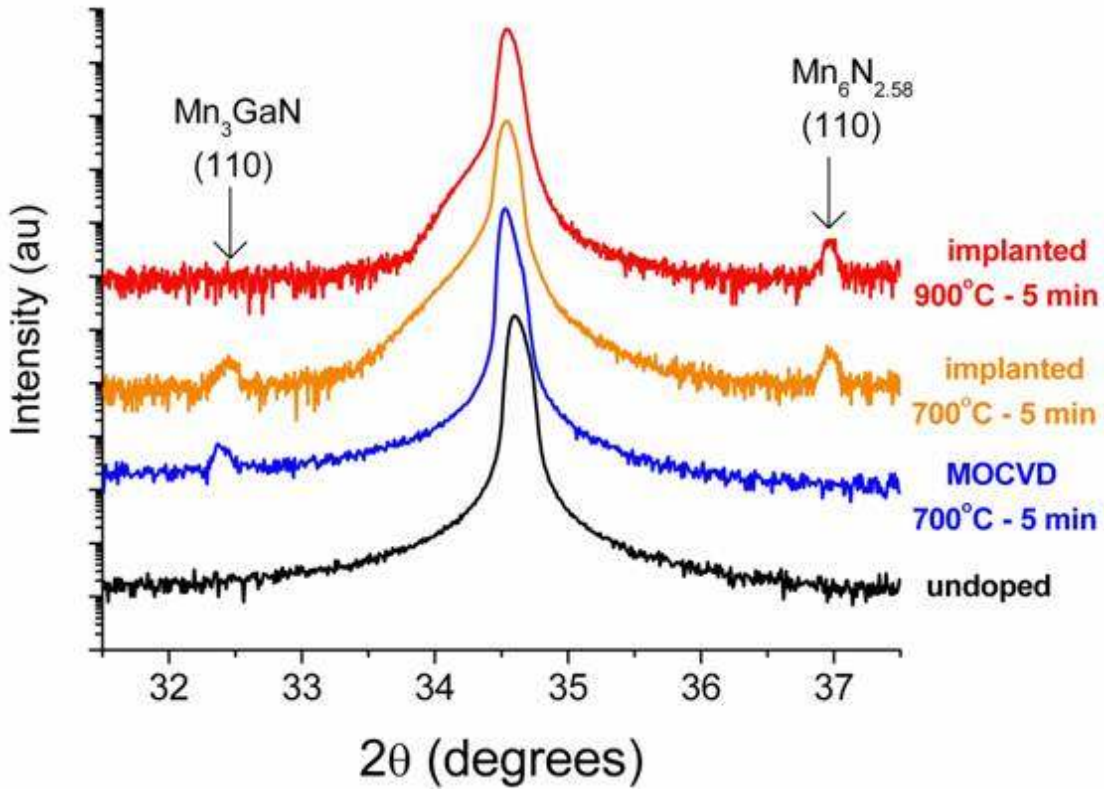

Figure 5.3 Close up of XRD scans showing the formation of Mn-rich secondary phases upon annealing.

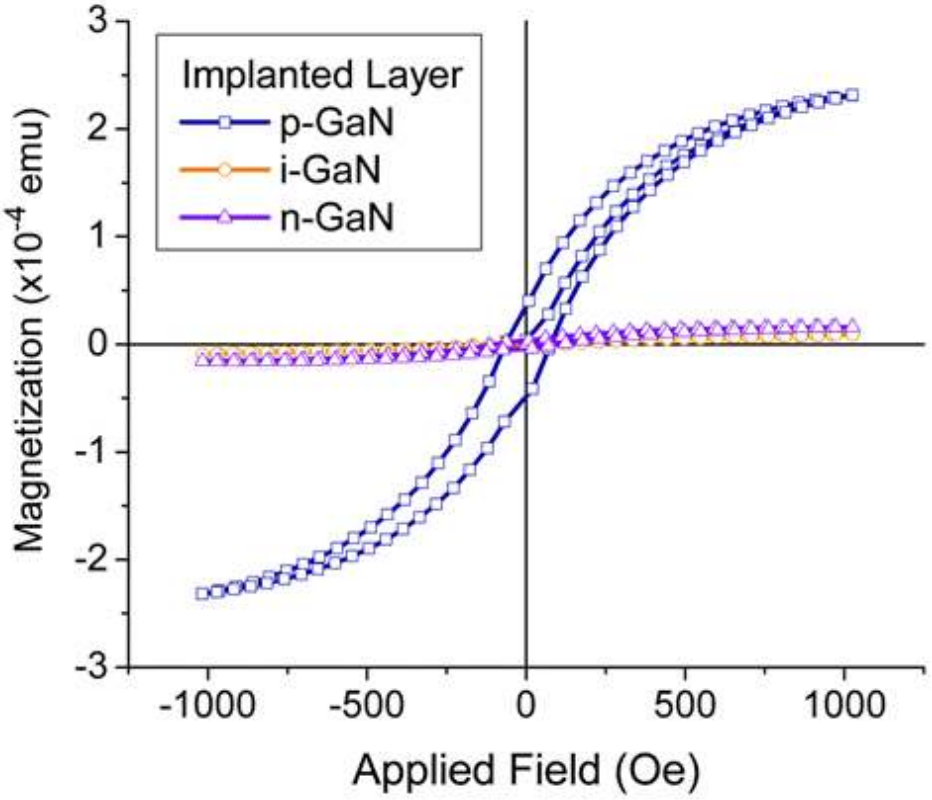

Figure 5.4 Hysteresis curved for p-GaN, intrinsic GaN, and n-GaN samples following implantation with $3x10^{16}$ cm^{-2} of 200 keV Mn^{+} ions

nominally intrinsic implanted samples, clear hysteresis is visible in the curves at room temperature. The Curie temperature in both cases is well above RT, as observed by M vs. T curves. All of the implanted samples are of roughly the same size, but due to the inherent asymmetry in the doping profiles achieved via implantation, the curves have not been volume corrected. The SQUID signal from the p-type $Ga_{1-x}Mn_xN$ is a factor of ten higher than that from the other samples All three samples (p-type, intrinsic, and n-type) exhibit coercivities of around 50 Oe and remnant to saturation magnetization ratios of 0.1-0.2. Ferromagnetism in the intrinsic and n-type samples may not necessarily be due to the macroscopic alloy, but instead may be due to unobserved second phases or to Mn-rich clusters in the as-grown system. The magnetic signal decreases as doping goes from p- to

n-, with the largest signal observed in the p-type sample, as would be expected from the original models for ferromagnetism in the III-nitrides.

5.3 Structural Studies of MOCVD-grown $Ga_{1-x}Mn_xN$

5.3.1 Overview

The as-grown $Ga_{1-x}Mn_xN$ films were specular and had a reddish hue that increases with increasing thickness and Mn incorporation. Figure 5.5 shows a photograph of two wafers: the first is a 2-inch sapphire with an intrinsic GaN layer grown, and the second has a $Ga_{1-x}Mn_xN$ layer. The reddish color is distinctly evident even at low doping levels. The origin of this coloring is the same as in the ZnO:Mn samples, where the crystal field parameters for GaN should be similar in strength to those in the ZnO system, and thus intrashell d-d absorptions lead to the color variation. Varying the temperature outside the optimal growth band resulted either in the appearance of hexagonal GaN growth temperature defects which were visible via optical microscopy, or in the loss of film integrity as evidenced by *in-situ* reflectometry. Secondary ion mass spectrometry (SIMS)

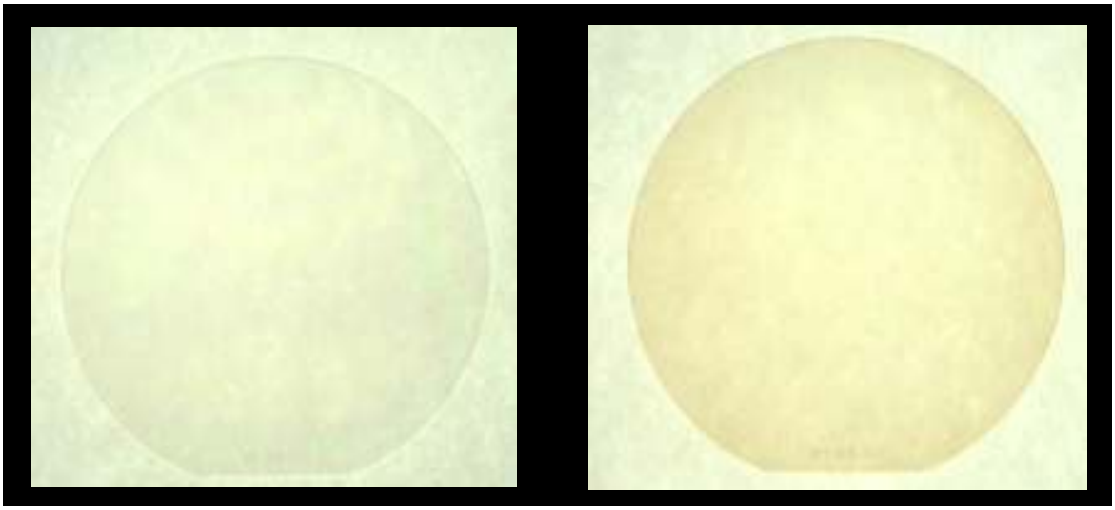

Figure 5.5 Photographs of undoped GaN compared with $Ga_{1-x}Mn_xN$ (x=0.5) layers on 2-inch sapphire substrates

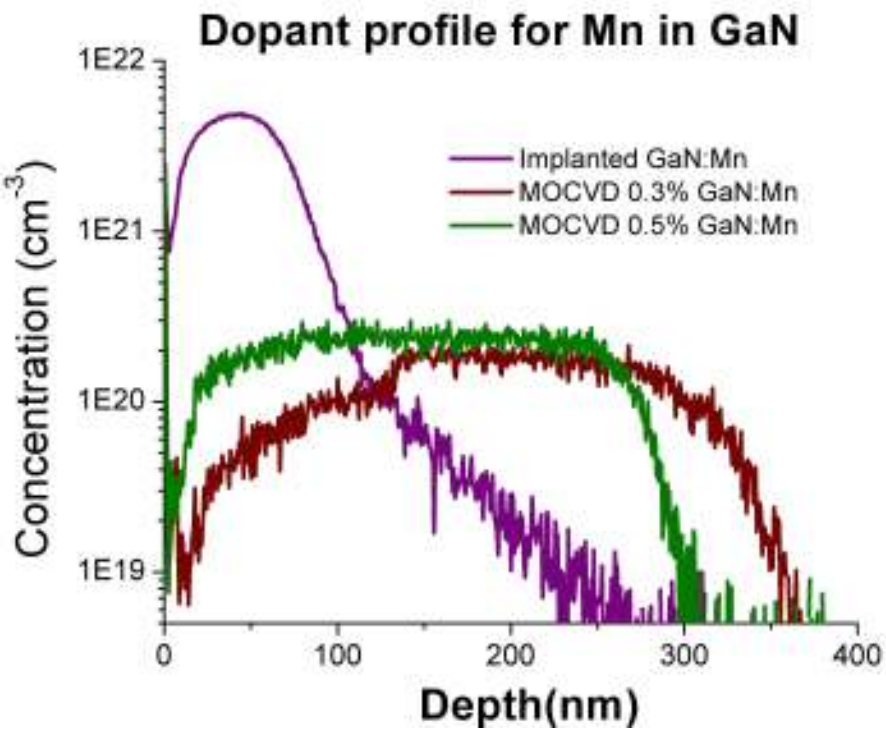

Figure 5.6 SIMS profile showing the dopant distribution in implanted vs. MOCVD-grown $Ga_{1-x}Mn_xN$

verified the uniform incorporation of manganese within the layers. Figure 5.6 showed calibrated SIMS measurements taken from two $Ga_{1-x}Mn_xN$ layers of varying thickness grown on GaN-on-sapphire templates. It is clear from these scans that it is possible to not only introduce Mn through the MOCVD-growth process, but to control the doping level and the layer thickness without significant interdiffusion within the layers.

5.3.2 X-ray diffraction

High resolution x-ray diffraction (HRXRD) was performed in order to examine the phase purity and the crystalline quality of the MOCVD grown films. X-ray diffraction scans on the MOCVD-grown GaMnN samples are depicted in Figure 5.7 In these scans, no second phases are observable. The $Mn_6N_{2.58}$ and Mn_3N_2 phases were not observed via XRD in the annealed MOCVD grown samples as has been previously reported in

implanted samples [163].The position of the $Ga_{1-x}Mn_xN$ peaks did not shift relative to the GaN at low doping levels, indicating a lattice parameter similar to that of GaN. Moreover, the peak shapes are very similar to those for the undoped GaN sample In contrast to the Mn-ion implanted samples, the GaN (0002) peak is symmetric, indicating little macroscopic strain with Mn incorporation and a considerable improvement in the crystalline quality when compared to the implanted samples. No statistically significant deviation in the lattice parameter was observed, even for Mn concentrations on the order of ~2% (as estimated from the growth conditions), although this may have been influenced by the underlying template layers in some of the films. The linewidths of the scans were all within a few hundred arcsec of each other, showing no significant increase

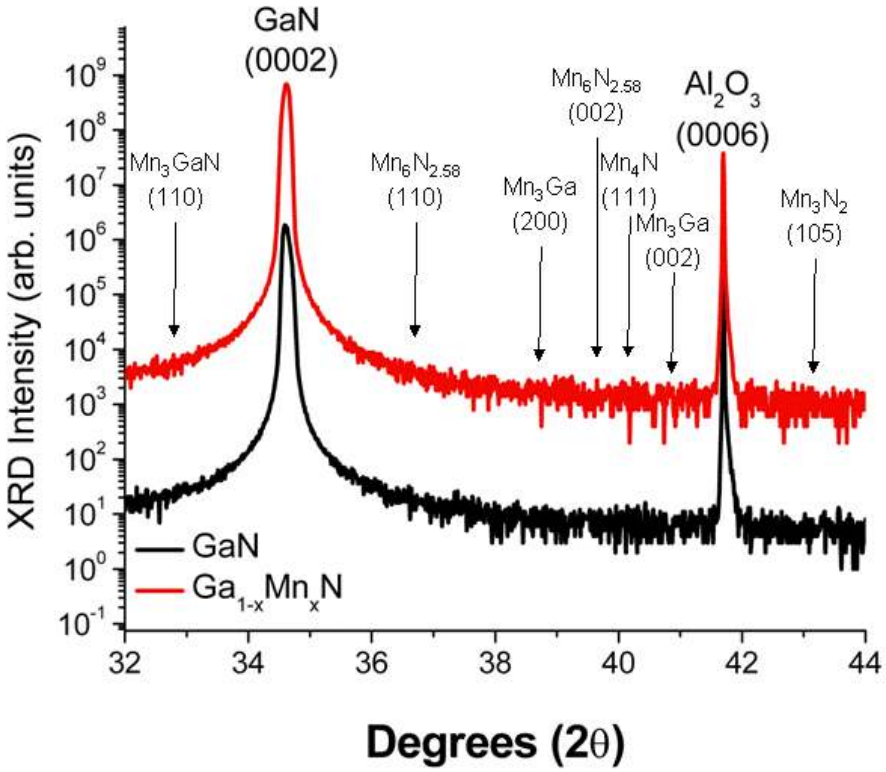

Figure 5.7 High resolution XRD scan showing the absence of secondary phases in the $Ga_{1-x}Mn_xN$ layers.

compared to width of the template; there is similarly little change in the rocking curve widths of the symmetric and asymmetric reflections: Thee 2θ–ω scan linewidths (179, 196, and 251 arcsec for the undoped, 0.3%, and 2.25% Mn 2θ–ω scans respectively). This is compared with 179 and 518 arcsec for the underlying template layer. Some scans indicate the presence of the forbidden (0001) and (0003) peaks in the doped Mn-layers; these have been previously observed in diffusion-grown $Ga_{1-x}Mn_xN$ [2]. These additional reflections are only seen in the Mn-doped samples and may be caused by local structural imperfections due to compensation effects from the heavy Mn doping. Alternately, these may be simply be due to diffraction from λ/2 monochrometer pass-through of the Brehmstrallung radiation.

5.3.3 Transmission electron microscopy

X-ray diffraction is a suitable technique for measuring the overall crystalline behavior of the samples, though it suffers from some severe limitations in analyzing the crystalline structure from local areas of the sample. A more precise determination of the crystalline quality of the samples and nature of any secondary phases which might be present can be performed via high resolution cross section transmission electron microscopy (TEM). High resolution cross sectional transmission electron microscopy was performed on a two-micron thick sample containing Mn all the way from the buffer layer through the $Ga_{1-x}Mn_xN$ layer. The TEM images are shown in Figures 5.8 and 5.9. In the first figure, a clear homogeneous epitaxial layer on a sapphire is substrate. Threading dislocations are clearly evident in these images, as would be expected from the large lattice mismatch between the sapphire substrate and GaN layers. In addition, some areas of the sample posses basal plane stacking faults. These have been observed in reports of

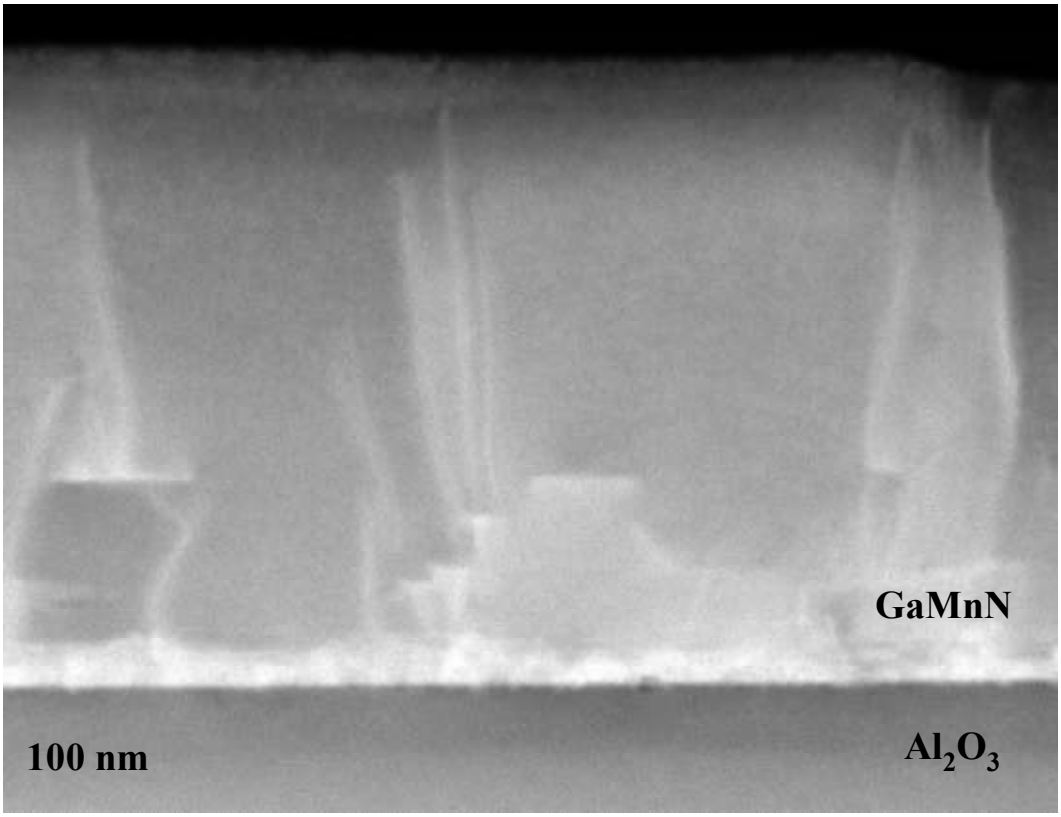

Figure 5.8 HAADF STEM image of the heterostructure. The contrast appears homogenous in regions without dislocations and stacking faults. Second phases or precipitates were not observed.

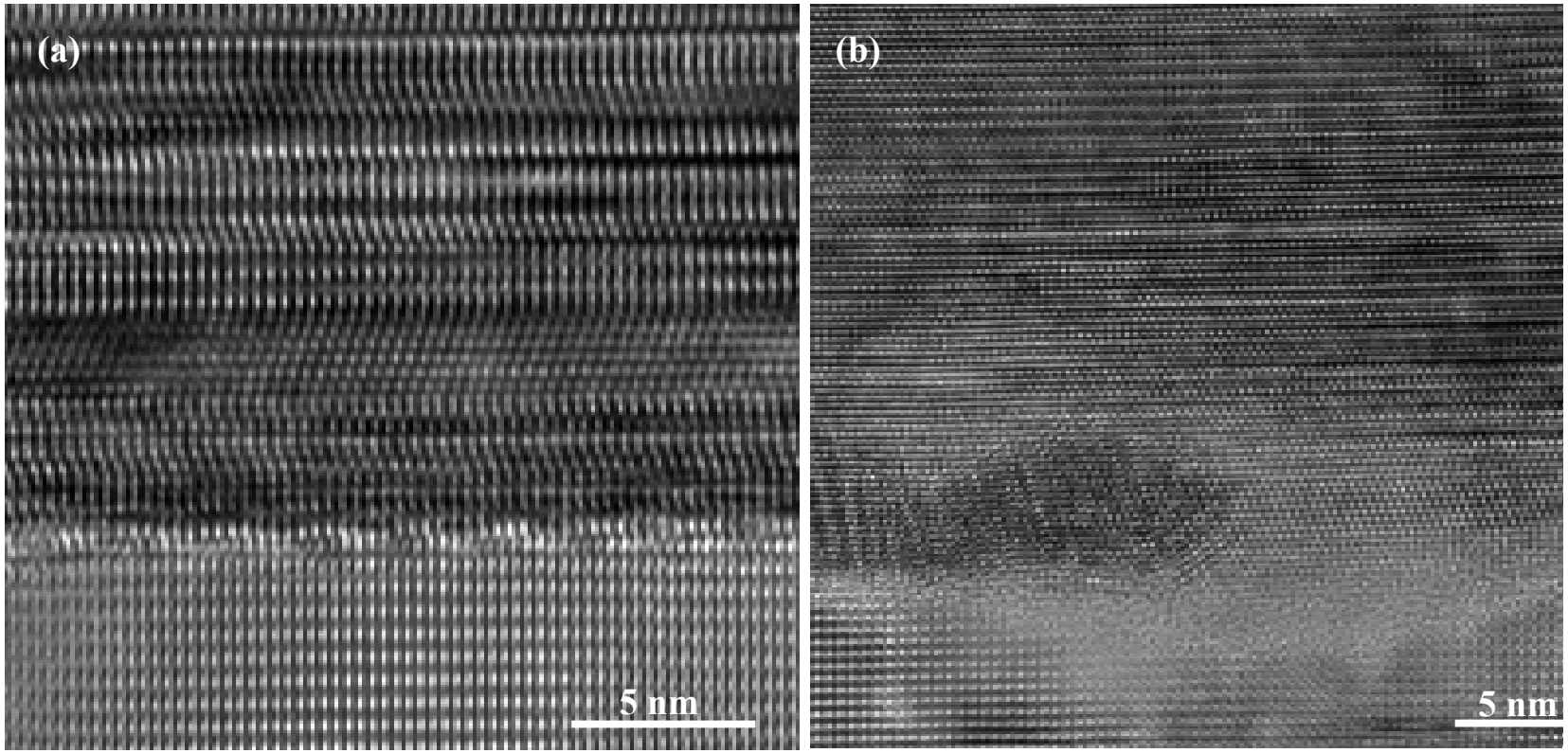

Figure 5.9 (a) HRTEM image collected near the interface between the GaMnN buffer layer and the sapphire substrate. A high density of stacking faults in the buffer is evident. Small amorphous phases, secondary particles, and cavities also exist in some regions, an example of which is shown in (b).

$Ga_{1-x}Cr_xN$ samples by MBE [164], so their presence is not surprising. Selected area diffraction patterns only show patterns characteristic of the wurtzite GaN structure. No additional secondary phases are observed in any portion of the sample.

In both of the images there is indication of secondary phase formation either embedded within the lattice, as has been previously reported in MBE-grown samples [165], or segregated into surface regions. Note that this does not preclude the existence of secondary phases whose major axis is perpendicular to the growth direction; some calculations have suggested that this would be the preferred orientation within these GaN system, as discussed in more detail later. The transmission electron microscopy results indicate that the behavior of the system will be determined in large part by the behavior of a bulk, dilute magnetic semiconductor alloy.

5.3.4 Atomic Force Microscopy

An important feature to understand about the growth process of the GMN alloy is how the incorporation of this new precursor and element affects the surface quality of the films. Atomic force microscopy (AFM) was used to derive information about the growth mechanism of $Ga_{1-x}Mn_xN$ and surface morphology of the $Ga_{1-x}Mn_xN$ layers. Figure 5.10 shows images of a typical as-grown layer. The overall film quality is smooth with atomic layer surface steps. The root mean square (RMS) surface roughnesses are between 3 and 11Å depending on the film and underlying template layer. Clear step flow growth patterns are seen in the as-grown MOCVD sample scans, which are typical of two-dimensional growth modes seen in GaN MOCVD. This mode does not change with the introduction of Mn into the growth process. Films grown outside the optimal temperature

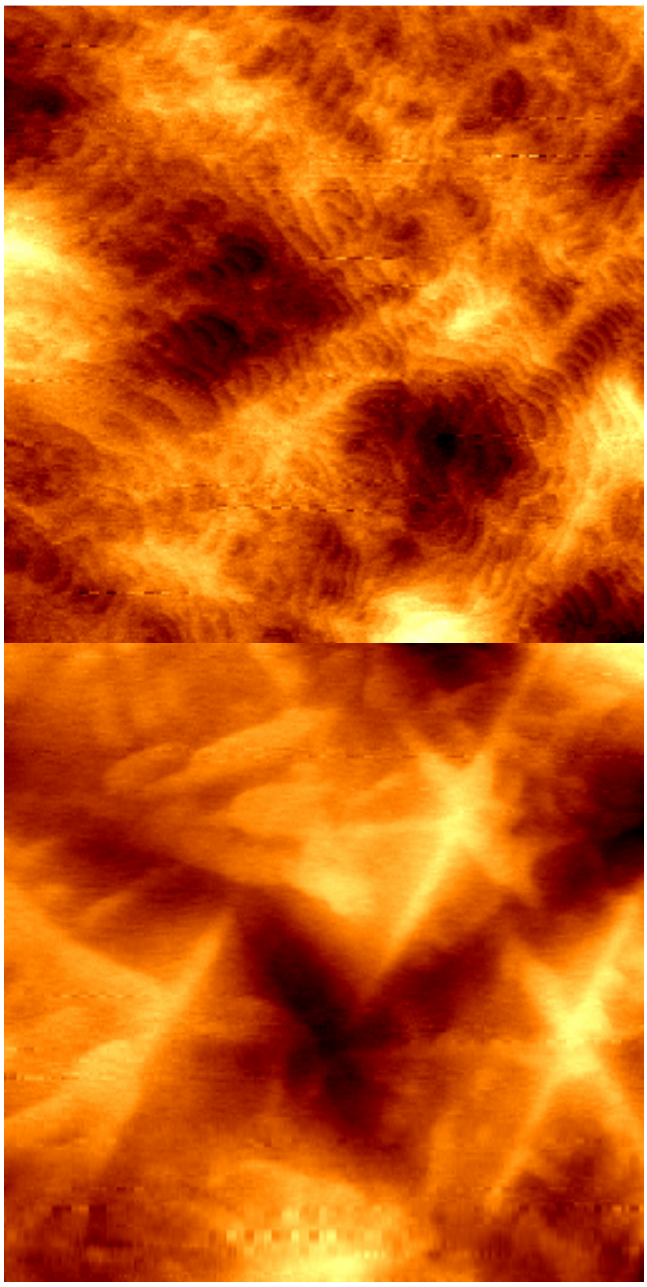

Figure 5.10 Atomic force microscopy images of $Ga_{1-x}Mn_xN$ grown at 1000^{o}C and 900^{o}C showing a transition from step flow growth to hexagonal growth defects.

bands exhibit hexagonal GaN temperature defects, which can be seen in both the AFM and optical microscopy.

5.4 Magnetization studies of MOCVD-grown $Ga_{1-x}Mn_xN$

5.4.1 Hysteresis curves

SQUID magnetometry was performed to determine the overall magnetic behavior of the MOCVD grown $Ga_{1-x}Mn_xN$ films. Ferromagnetic hysteresis was recorded in the as-grown $Ga_{1-x}Mn_xN$ films The macroscopic magnetization behavior of the films was determined by temperature-dependent SQUID magnetometry on undoped and Mn-doped samples from 5 K to 300 K. The curves are shown at 300K. In general, there is little deviation for these curves at 5K, indicating that the hysteresis is due to a phase with a high Curie temperature (T_C>400K). A perspicuous magnetic hysteresis was obtained in samples at doping levels from 0.3% to 1.5%, providing a clear evidence for a room temperature ferromagnetic contribution, Figure 5.11. A coercivity of 70 Oe and saturation

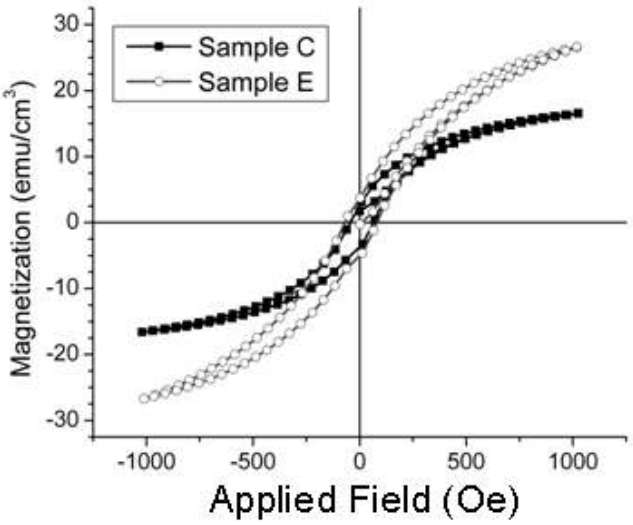

Figure 5.11 Magnetization vs. field scans for $Ga_{1-x}Mn_xN$ with x=0.01 (sample C) and x=0.015 (sample E)

magnetization of 11.6 emu/cm^3 is observed in sample C (1% Mn doping) at 300 K. The magnetization shows anisotropic behavior relative to the growth axis of the film; the magnetization is significantly stronger in the place of the film, as would be expected from the magnetic shape anisotropy of the film. Etching the sample in hydrogen peroxide or aqua regia does not eliminate the magnetic hysteresis as was previously observed in bulk crystallites [166].

To check whether the magnetic behavior is due to second phases or clusters, the concentration per magnetic element was calculated. Assuming a uniform growth rate and Mn concentration as measured by SIMS across the wafer, the measured saturation magnetization corresponds to a contribution of 2.9 μ_B/Mn for the 1% doped sample and 1.2 μ_B/Mn for the 1.5% doped sample. This is similar to values observed in high-quality lightly doped $Ga_{1-x}Mn_xN$ produced by other methods [79, 167]. As doping increases, the calculated magnetic contribution per Mn atom decreases. This may be due to the formation of Mn-related compensating defects, as has been previously observed in $Ga_{1-x}Mn_xAs$ [168], or the introduction of antiferromagnetic coupling via superexchange as is observed in the ZnO:TM materials. Note that ferromagnetism was achieved despite both the Mn and free hole concentration being far lower than that required by the mean field theory [22].

It should be noted that if this model holds, the predicted contribution based on first principles band structure calculations of 4 μ_B/Mn when the Fermi level is located in the center of the Mn impurity band. The predicted contributions for the mean field model are also around 4 μ_B/Mn for hole mediated ferromagnetism, though experimental values in $Ga_{1-x}Mn_xAs$ are often much lower than anticipated - especially at high doping levels -

due to defect cluster and/or defect compensation [168]. Though the deep nature of the Mn acceptor in GaN [169] results in carrier concentrations lower than required by the mean-field mode for RT ferromagnetism, the as-grown $Ga_{1-x}Mn_xN$ layers, the films still exhibit room temperature magnetic hysteresis at concentrations of ~0.8% Mn, as shown in Figure 5.11. For comparison, the predicted magnetic moment per Mn_4N cluster is 17 μ_B/Mn [67]. Thus, if the ferromagnetism were due only to this atomic configuration, greater than half of the Mn would have be tied up in these clusters; this should be observable through the structural characterization techniques. However, since phase-separation based FM has been observed in ferromagnetic chalcopyrite materials with similar magnetization strength, further work is required to unambiguously rule out clusters as the origin of FM

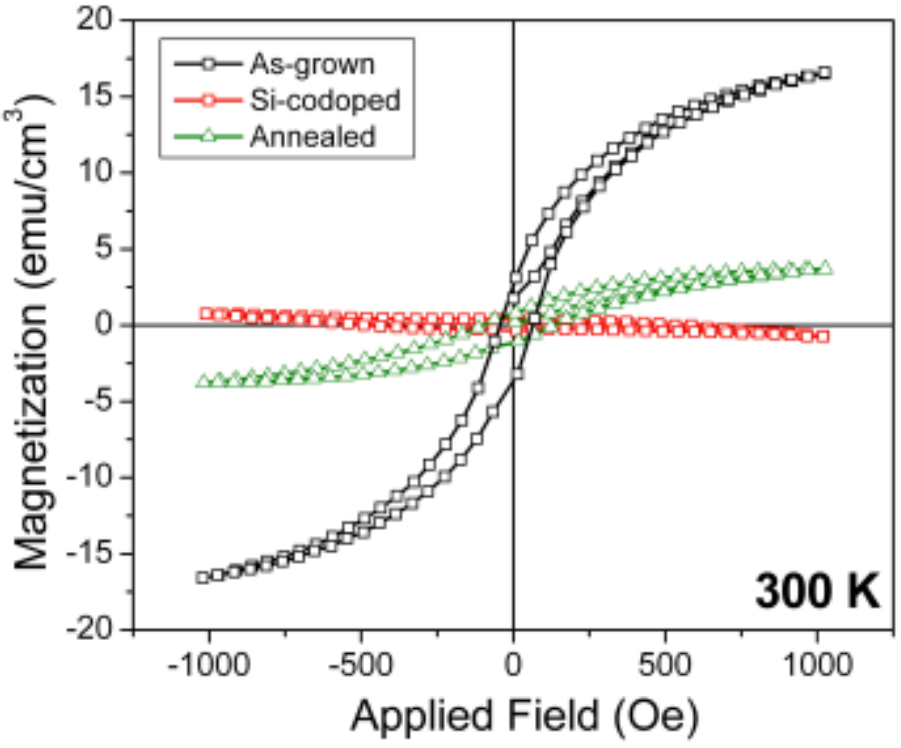

Figure 5.12 Magnetization versus field curves showing a decrease in the observed magnetization strength upon annealing or Si-codoping

in MOCVD-grown $Ga_{1-x}Mn_xN$ [170, 171].

5.4.2 Annealing effects

5.4.2.1 Magnetization strength

One challenge in achieving p-type doping in GaN was understanding how to properly process and anneal the samples such that acceptor doping could be observed [130]. The precursor used in this study is almost identical to that used for magnesium codoping, so it is possible, particularly if some sort of carrier mediation is responsible for the observed ferromagnetic behavior, for there to be an activation step necessary to realize or optimize ferromagnetism in $Ga_{1-x}Mn_xN$. Significant changes are indeed observed in the magnetic behavior with annealing of the layers. Upon annealing, the magnetic signature decreases [163], Figure 5.12; similarly, a stark difference in magnetic signature is also seen between p-type and intrinsic GaN layers under the same implanting and annealing conditions, as reported elsewhere [163].

5.4.2.2 Surface structure

In order to determine the cause of the magnetic signature degradation, it is possible to correlate the magnetic properties with surface-sensitive structural characterization techniques. There is little change in the morphology of the layer with low temperature annealing (700°C). However, there is a significant difference in the AFM images with annealing at higher temperatures. The AFM image of the uncapped sample annealed at 900°C shows clear areas of what are likely second-phase precipitates on the surface, Figure 5.13. Close inspection of the 800°C image reveals smaller spots of these second phases which are likely at nucleation sites,. X-ray diffraction scans can attribute this to either Mn_4N or Mn_3GaN-type phase, as shown in Figure 5.14. These most

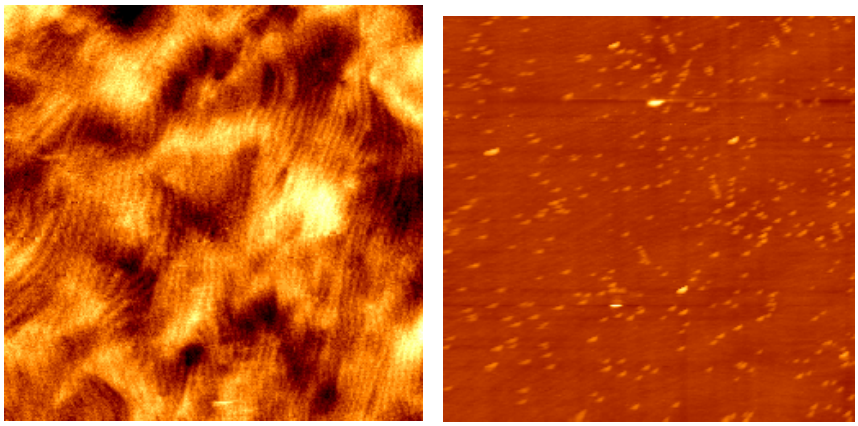

a) As grown b) 900°C 5 min

Figure5.13 Atomic force microscopy images of $Ga_{1-x}Mn_xN$ (x=0.015) terminated MOCVD grown $Ga_{1-x}Mn_xN$ samples, as-grown and annealed at 900°C for 5 minutes. All scans are 10μm x 10μm. RMS roughness values from left to right are 5.68Å and 7.71Å.

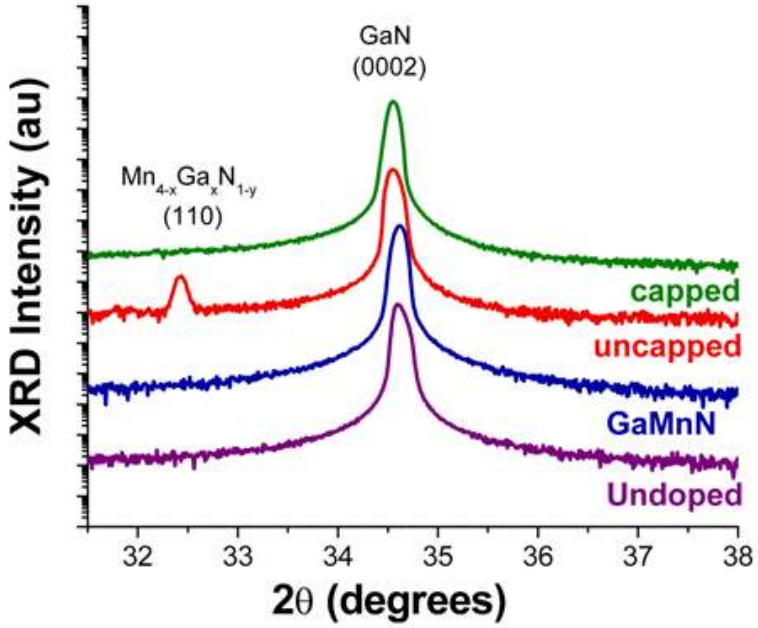

Figure 5.14 XRD scans of $Ga_{1-x}Mn_xN$ following annealing with and without a capping layer. Second phase formation is only seen in the uncapped sample

closely index to the (110) reflections of the Mn_3GaN phase. This phase has been observed previously, as noted above, though the peak position is quite close to a GaMn intermetallic phase which has been reported to be present in MBE-grown $Ga_{1-x}Mn_xN$ [76]. On the other hand, the annealed GaN-capped samples show no change in surface morphology even at the elevated temperature. This is not unexpected, as GaN under the same annealing conditions does not exhibit a surface morphological change. However, it is not possible to completely eliminate the possibility of second phases solely on the x-ray diffraction results. This suggests a possible mechanism for the decay of the thermodynamically unstable $Ga_{1-x}Mn_xN$ compound: in the absence of a reactive nitrogen environment that is present during MBE or MOCVD growth, nitrogen desorption and phase rearrangement of the surface may occur at the $Ga_{1-x}Mn_xN$-to-atmosphere interface. This second phase is not observed in the samples capped with a thin GaN layer, even at annealing temperatures as high as 900°C. Infrared Raman spectroscopy measurements do indicate that there may be a weakening of the GaN lattice through Mn introductions; these results would be consistent with that analysis.

5.4.3 Si-effects on magnetization strength

The magnetisim exhibits a similar behavior in the MOCVD-grown samples co-doped with silicon, where prior to co-doping, a large magnetic moment per atom can be seen. As the Si doping concentration increases, the magnetic moment decreases and is nearly destroyed upon a target doping concentration greater than $10^{19}/cm^3$ Si, Figure 5.15. Secondary ion mass spectrometry of the samples confirms that there is no systematic decrease in the manganese doping level with increasing silane flow. In all cases, a weak hysteresis is still observed in the sample, though in the most heavily doped sample, an overall negative slope and diamagnetic signal is observed. This residual

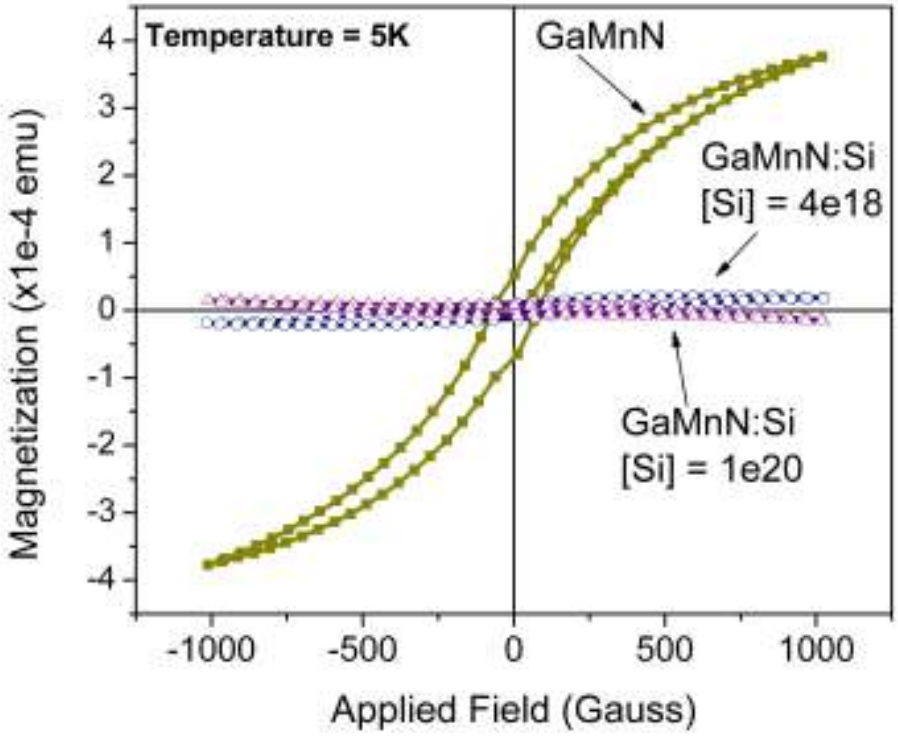

Figure 5.15 Magnetization versus field as a function of intended Si-doping concentration.

hysteresis may be the result of magnetic impurities within the substrate, where Cr^{3+} is known to be a major impurity in the sample. It is somewhat interesting to note that even though the overall saturation magnetization contribution is significantly affected, there does not seem to be a corresponding change in the coercivity of the samples.

5.4.4 Mg-codoping effects

5.4.4.1 Magnetization strength

A decrease in the magnetic signature is also observed with Mg codoping, as shown in the VSM data in Figure 5.16. In the case of the most heavily doped p-type $Ga_{1-x}Mn_xN$:Mg, almost no hysteresis is observed. This is in direct contrast with the implanted p-type sample, which showed a much more prominent hysteresis loop than the

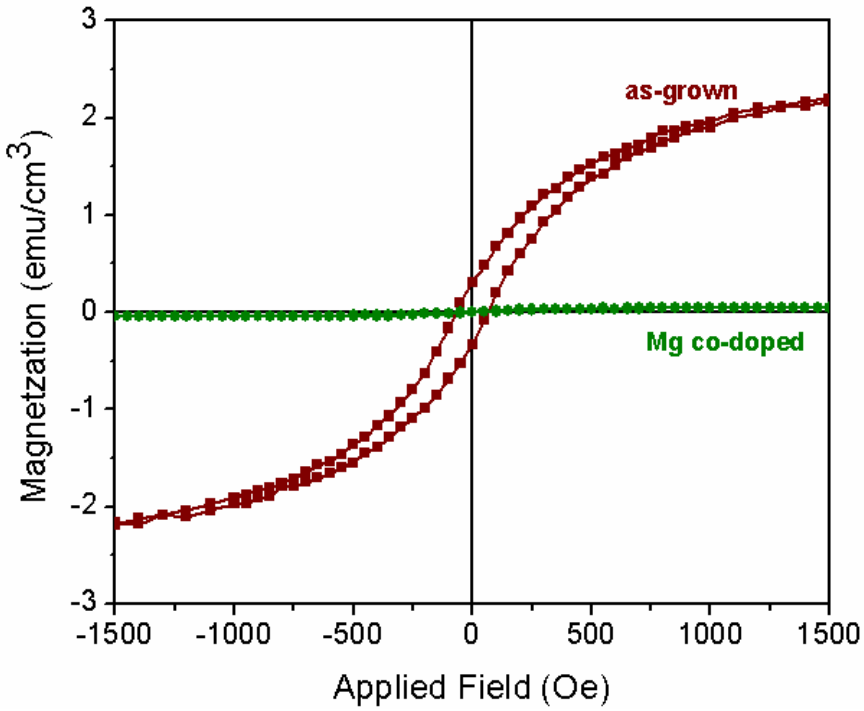

Figure 5.16 Vibrating sample magnetometry scans for as-grown and Mg-codoped $Ga_{1-x}Mn_xN$ samples

intrinsic and n-type samples. Mg introduction requires annealing to activate the acceptors. However, at the elevated temperatures required for activation, strong surface decomposition through the creation of nitrogen vacancies or secondary phases is known to occur [80], as described above. Almost no change in the magnetization is observed after annealing, indicating that acceptor activation is not strong enough to overcome self-compensation that occurs during the growth process.

5.4.4.2 SIMS behavior

Secondary ion mass spectrometry was used to investigate the effects of the growth process and doping on the incorporation of Mn and other elements into the lattice. Compositional and thickness fluctuations are observed over the area of the wafer, due to local variations in the temperature and flow patterns of the inlet precursor gases. Fig. 5.17

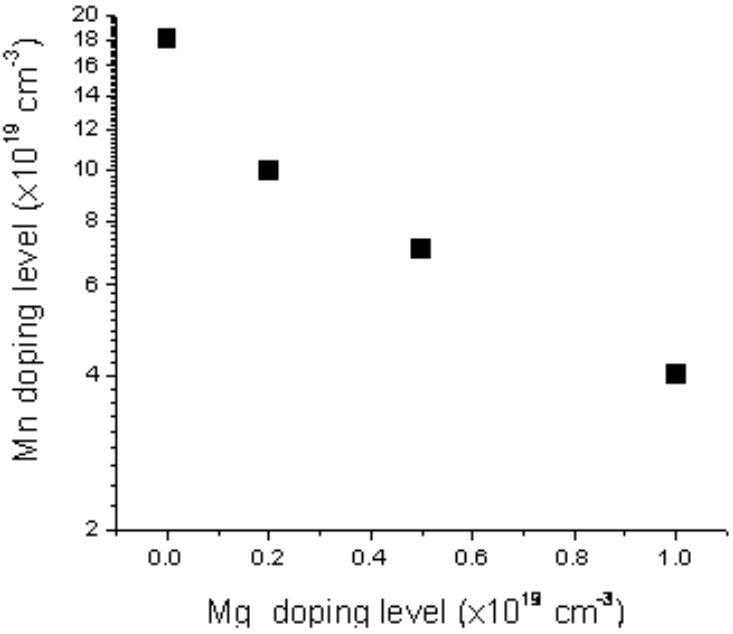

Figure 5.17 Calibrated SIMS results for the measures SIMS Mn concentration as a function of the Mg doping concentration.

shows the measured Mn concentration as a function of Mg concentration in the films for a constant flow of Mn gas. The values for the concentrations were calculated using a known ion implantation standard which was measured in parallel to these samples. As the Mg flow rate is increased, there is a large decrease in the measured Mn concentration. This is not altogether unexpected, as the precursors for Mn and Mg are identical except for the metal within the metalorganic source.

The reduced Mn concentration should lead to a corresponding decrease in the overall magnetization, but in this case the magnetization completely disappears. The concentration of Mg is an order of magnitude lower than for the concentration of Mn; so it is impossible for this concentration of acceptors to completely depopulate the Mn impurity levels, and there should not be a significant lowering of the Fermi energy. This

suggests that the reduced magnetization does not originate from this drifting outside the band on the low side or the formation of Mn^{4+}, which has been previously reported. A similar SIMS profile for the Si co-doped samples does not show the same systematic drop in Mn concentration with increasing n-type doping.

5.4.5 Growth rate dependence

Another possible variable that may control the magnetization is the growth rate. This would be particularly true if clustering were involved, though the role of the incorporated compensating defects in this material may also be a function of the growth rate. Due to the low vapor pressure of the transition metal sources, this is somewhat problematic for transition metal-doped GaN, as discussed about previously in Chapter 3. Based on flow considerations in the reactor, it is not possible to maintain a normal high growth rate (~2 μm/hr) for GaN and introduce sufficient precursor for alloying concentrations using the metallocenes. Figure 5.18 shows the magnetization behavior of two samples grown at difference growth rates. The Mn:Ga precursor ratio was held constant in these two samples based upon the anticipated vapor pressures at the growth temperature. It is evident in this diagram that the samples grown at a slower rate tended to have a higher magnetic signal strength. This may be solely due to fluctuation in concentration across the wafer, though even lightly doped samples grown slowly tended to have larger magnetization strengths. This may also be a result of incorporation limits of the transition metal atoms into the lattice. Some reports of Fe doping into GaN suggest that the transition metal ions "float", or segregate to the surface during the growth process [172]. If this were saturated at the surface, then an increase in the growth rate would lead to a decreased incorporation of Mn.

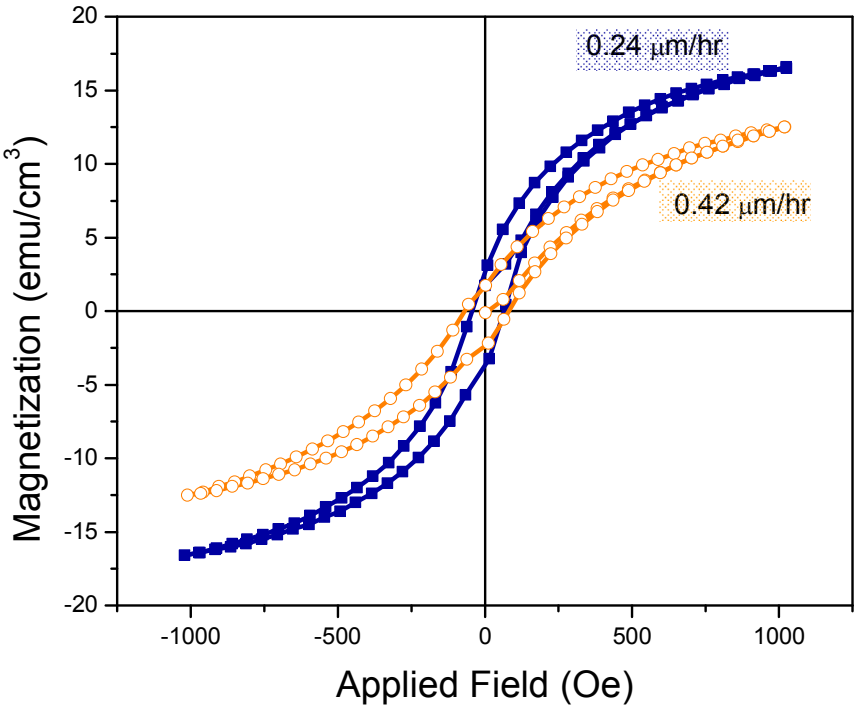

Figure 5.18 Hysteresis curves for a constant Mn/(Mn+Ga) ratio at two different growth rates

Another possible cause for the increased magnetization strength with reduced doping is the role of surface diffusion and its relation to clustering. With slower growth rates, there is more time for transition metal atoms to diffuse on the surface and they are more likely to interact with other transition metal atoms. If there is a strong free energy benefit to staying in this clustered configuration, then this could also lead to an increase in the contribution to the magnetic signal from secondary magnetic phases. Future studies focus on understanding this phenomenon.

5.4.6 Magnetic property discussion

Although no direct evidence of metallic GaMn- or MnN- clusters was observed in high-resolution XRD, the presence of small ferromagnetic clusters or additional phases could not be completely ruled out. Small size, small volume fraction, or an orientation

along non c-axis directions would suppress the respective signals. Hence, the experimental findings do not fully preclude the existence of these second phases below the resolution limit of the XRD instrument. Based on the contribution per Mn atom, however, this is unlikely to be the sole source of FM. In addition, the cluster model cannot explain differences in the strength of the magnetization with annealing or in the p-type and n-type implanted samples. Formation of manganese nitride compounds has also been seen in bulk crystals of $Ga_{1-x}Mn_xN$ [103] and annealed samples of Mn-implanted GaN [173]. Theoretical predictions anticipate large T_C values for MnN clusters in the nitride-based materials [67], which could play at least a small role in these samples. The elevated growth temperatures in MOCVD promote enhanced surface and bulk diffusion, and hence may lead to more Mn-Mn and Mn-N interactions than in samples produced by lower growth-temperature methods.

The origin of the variation in magnetization strength with varying doping level and p-type and n-type doping is still under debate. The large decrease in magnetization with co-doping and annealing suggests a common origin to the deterioration of the magnetic properties of $Ga_{1-x}Mn_xN$ in annealed and as-grown samples. The initial theory that drove people to study these materials relied on the presence of a large quantity of free carriers – specifically hole free carriers – to stabilize the ferromagnetism. Hall measurements indicated that the as-grown $Ga_{1-x}Mn_xN$ is semi-insulating, as described elsewhere in this chapter. Co-doping with other shallow dopants or acceptors does not improve the conductivity significantly, which is consistent with the report of Mn as a deep trap [169]. No p-type conductivity was observed, in contradiction to predictions of prevailing mean field DMS theories; thus a different origin of the ferromagnetism must

be considered. This lack of agreement with the DMS mean field theories is often reported for ferromagnetism in the III-nitrides.

Alternately, the ferromagnetism may be tied to a Mn-related impurity band within the bandgap resulting from double exchange, as also suggested via density functional theory calculations [53]. A similar school of thought suggests that this variation is due to the depopulation of an impurity band [69]; the location of this band relative to the conduction and valence band may be anywhere between 1.4 eV [50] and 1.8 eV [169] above the valence band.. This model does not require additional carriers, and predicts elevated (above RT) Curie temperatures for even low (2%) Mn concentrations [54] when using a mean field approximation to this model. The reasons for the drastic difference in the magnetic behavior in these samples may be understood within the framework of filled and un-filled Mn impurity band states. In order to be able to support ferromagnetism, the Fermi level of the system must be in the spin split DOS Mn-impurity band, which is essentially midgap. The Fermi level must lie below the $Mn^{2+/3+}$ acceptor level so that the t_2 band is only partially filled, allowing it to support hopping and double exchange that stabilize the ferromagnetism. Increasing the Fermi level by introducing donor states above this level results in trapping of donor electrons filling the t_2 band. This leads to a conversion from the Mn^{3+} (d^4) to the Mn^{2+} (d^5) configuration, thus eliminating the hopping pathway necessary for ferromagnetic ordering. These donor states may be introduced either by intentional co-doping, as in the case of Si co-doping, or by the introduction of vacancies and other shallow donor defects during the annealing process. Data reported below for these same samples showed a close correlation between the optical properties and electron paramagnetic spectrum with the valence state variation

and magnetic properties in this system. This model does have some difficulty in explaining why band type conductivity would be observed with essentially no overlap in the electron wavefunctions.

Based on the double exchange model, an increase in the hole concentration is predicted to lead to an increase in the Curie temperature and magnetization [174], as should light p-type doping in the cases of an impurity band.This is clearly not the case in these films, and may be a result of overcompensation and structure degradation at the high doping level in the growth process.

A similar observation can be made for the decrease in magnetization in the annealed samples. For both the mean field and double exchange mechanisms to be valid, Mn must be in the 3^+ valence state [24], either as d^4 or d^5 + hole; Mn^{2+} in GaN has been observed to lead to paramagnetism. Several mechanisms could lead to the decrease in ferromagnetism in these samples with annealing, in addition to outdiffusion of Mn. Increased antiferromagnetic Mn-Mn superexchange interactions would result from Mn atom nearest-neighbor clustering. Additionally, secondary phases - including the antiferromagnetic Mn_xN_y compounds - are known to form at elevated temperature annealing [162].

Annealing in a nitrogen atmosphere also drives out any residual hydrogen from the layers; hydrogen has been shown to aid magnetic behavior by passivation of defect states [175]. Similarly, annealing can introduce nitrogen vacancies which act as shallow donors, driving the Fermi level towards the valence band. Given that strong ferromagnetism is seen in the p-type implanted sample and the as-grown MOCVD sample, it is proposed that controlling the Fermi level by keeping E_F less than the

$Mn^{2+/3+}$–acceptor level can lead to enhanced ferromagnetic behavior in the $Ga_{1-x}Mn_xN$ dilute magnetic semiconductor system.

Another suggestion regarding the effects of the various dopants is that they cause Fermi level-dependent changes in the diffusion of the material [24]. This would foster different diffusion rates in the material and result in enhanced clustering and/or ferromagnetic second phase formation. Diffusion studies performed on these materials in this work are inconclusive regarding the differences in Mn diffusion in n-type and undoped GaN via bulk diffusion. An analogous surface diffusion-related effect may be observed during the growth process, due to anti-surfactant effects. Si is a well-known antisurfactant in GaN growth; it reduces the overall diffusion lengths by providing additional nucleation sites for film growth. Under sufficient flows of silane, the MOCVD growth mode has been reported to shift from a 2-dimensional to 3-dimensional growth [176]. The ZFC/FC splitting observed in some magnetization studies may be related to this transition in the growth scheme and reduced Mn cluster size or Mn-Mn interactions owing to the Si anti-surfactant effect; this hypothesis will be discussed in more detail in the next chapter. As reported elsewhere, nucleation studies for $Ga_{1-x}Mn_xN$ suggest that Mn may also have an antisurfactant effect [177].

5.5 Hall Effect measurements

In order to investigate the role of carriers on the magnetic coupling in these materials, it is first essential to investigate their electrical properties. This can be done using Hall Effect measurements. Through extrapolation of this method in magnetic fields, some dilute magnetic semiconductors are known to exhibit a large anomalous Hall contribution, which can indicate magnetic ordering in the system. The measured carrier

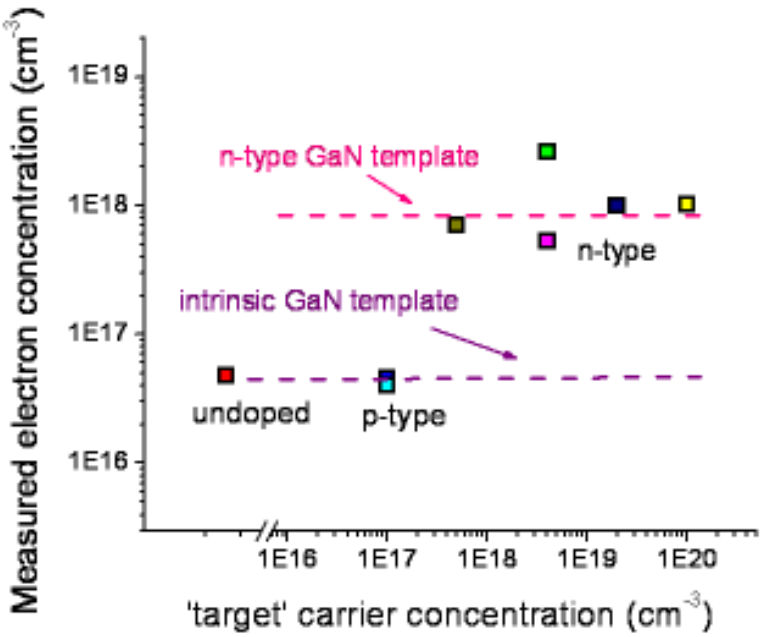

Figure 5.19 Measured Hall concentration in n-GaN and GaN with Mn doping. No systematic deviation in carrier concentration is observed due to parallel conduction through the templates

type in these samples is n-type in all cases, similar to what has been reported for ferromagnetic $Ga_{1-x}Mn_xN$ in the literature [85]. However, it is likely that this is merely a function of the template layer used to grow the samples, especially in the samples without Si codoping. To achieve high structural quality for the $Ga_{1-x}Mn_xN$ layer, these epilayers were grown on 1 micron thick GaN template layers; for the Si codoped samples, these layers were doped n-type. The measured Hall concentrations of the as-grown, unintentionally doped $Ga_{1-x}Mn_xN$ films were around $n=5x10^{16}/cm^3$, which is very close to the measured background carrier concentration of the unintentionally doped template layer. Similarly, increasing the Si doping within the $Ga_{1-x}Mn_xN$ layer does not result in an increase in measured carrier concentration: the value observed was $n=8x10^{17}/cm^3$, almost exactly the measured carrier concentration in the n-type template layer on which these samples were grown. Thus, all of the measured n-type behavior is due to parallel

conduction through the virtual template, and the observed 'n-type' character that is often reported in these systems may be solely due to the template. In order to clarify this point, layers were grown from the substrate up with Mn in the virtual template layers. For these samples, the resistivity was too high to measure and the contact resistance increased by several orders of magnitude, consistent with predictions and other observations of Mn as a deep impurity level. It should be noted that the layer grown on the Mn-containing template has a reduced quality and does not exhibit strong ferromagnetism,, even though it exhibit the strong reddish tint indicative of Mn^{2+} incorporation.

5.6 Electron Paramagnetic Resonance in $Ga_{1-x}Mn_xN$

Electron paramagnetic resonance (EPR) in the X-band was used to study the incorporation and electronic structure of the manganese ions in GaN. This technique is particularly useful because it provides an indication of the local environment of a particular atom within the lattice. Moreover, this technique also allows for the investigation of Mn-Mn interactions, which are also reflected in the EPR signal.

Applying this technique in the thin films, particularly $Ga_{1-x}Mn_xN$ thin films, is not without its challenges. EPR is usually a bulk technique, so the signal is much weaker in thin films simply because the sample volume of the sample is lower. The dilute nature of the substituent transition metal atoms also gives a lower signal to work with in the analysis of these samples. The mixed-valence character of transition metals adds another complication to the EPR analysis. Only ions with half-integral unpaired spins, such as Mn^{2+}, give a strong signal. The signal from a trivalent Mn ion would be a couple of orders magnitude weaker. Another issue that hinders the complete analysis of the Mn-doped samples is a large effect from the relatively thick substrate. One of the primary impurities found in Czocralski-grown sapphire crystals is the Cr^{3+} ion. This ion gives a

strong signal in the same region of the EPR spectrum as the desired Mn^{2+} signal, as is seen near 250 mT in Figure 5.20.

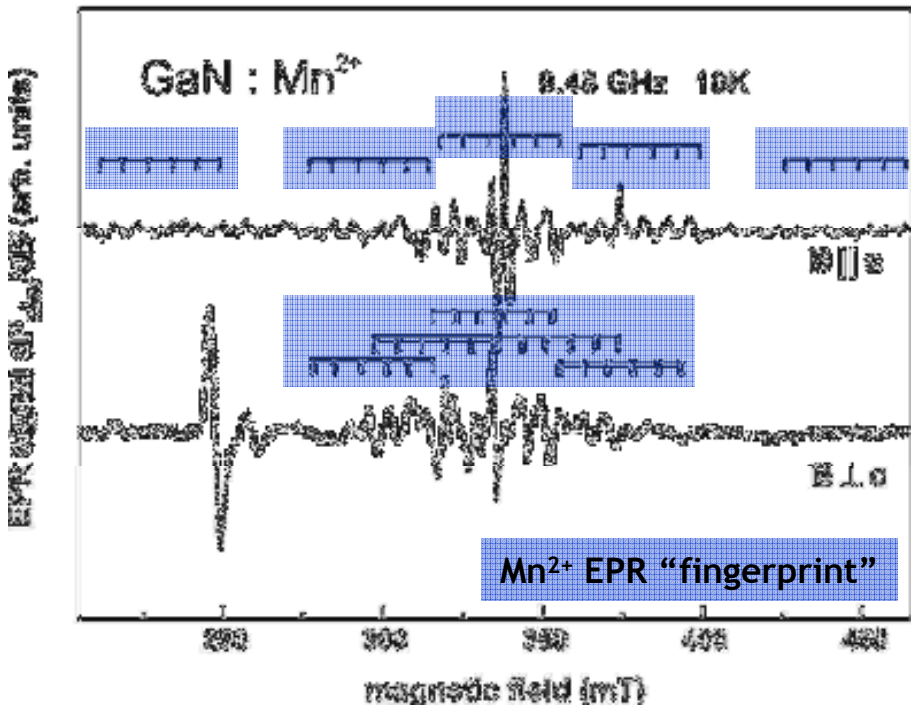

Figure 5.20 X-band EPR spectra of $Ga_{1-x}Mn_xN$ thin film following annealing at 800°C for 5 min.

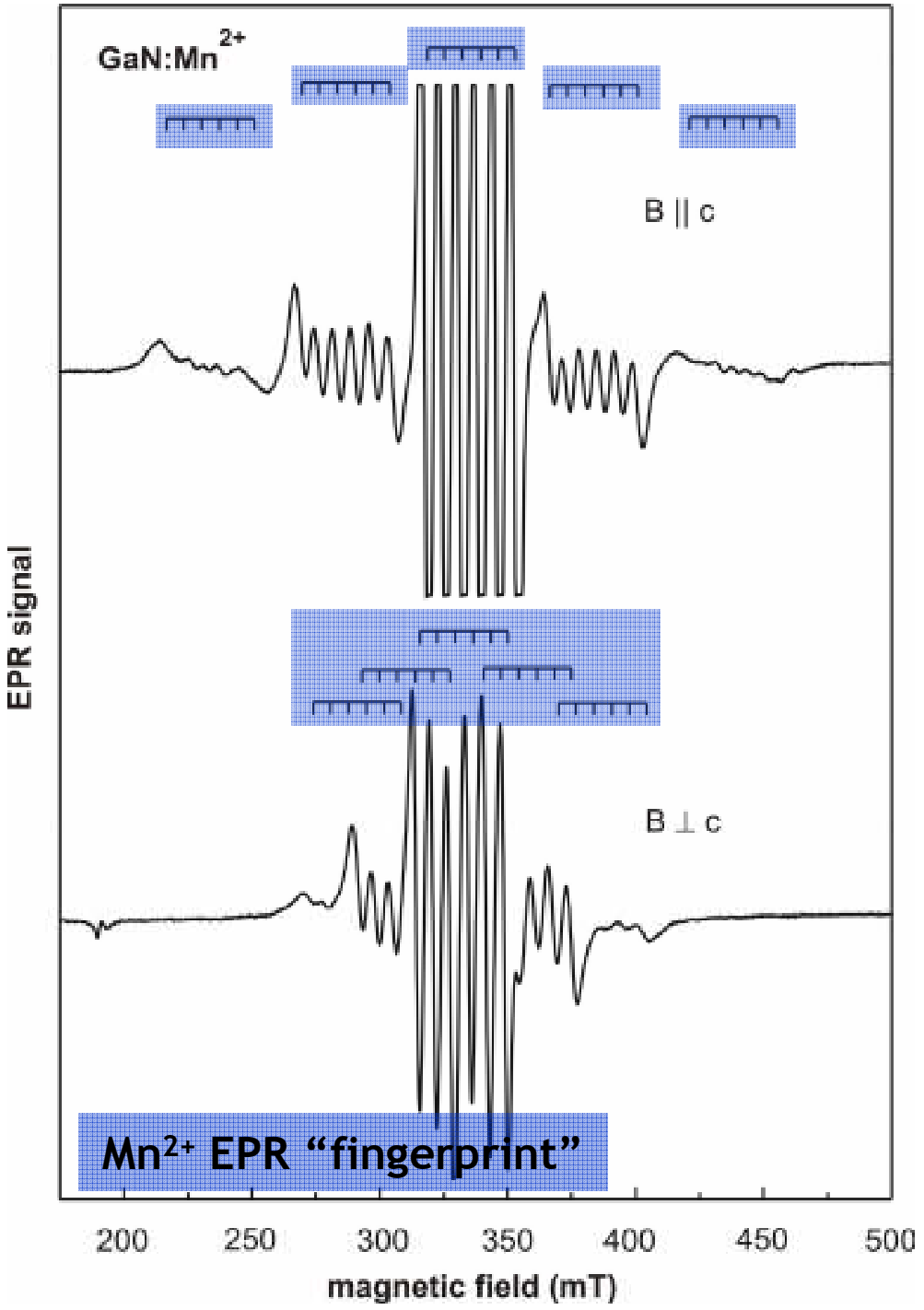

Figure 520 EPR spectrum showing Mn^{2+} character in an intentionally codoped $Ga_{1-x}Mn_xN$:Si samples

Figures 5.20 and 5.21 show measured X-band EPR spectra from annealed and Si-codoped MOCVD grown samples, with the magnetic field applied parallel and perpendicular to the c-axis of the crystal. For reference and comparison, the figures also show the expected positions of the hyperfine lines based on calculation using the spin Hamiltonian for Mn in the GaN lattice. The predicted spectra of isolated Mn^{2+} were observed in the X -band, but only in annealed and Si co-doped $Ga_{1-x}Mn_xN$. The as-grown samples did not show a measurable Mn^{2+} signal, presumably because a majority of the transition metal is in the Mn^{3+} state. The characteristic EPR spectra of a 1μm thick $Ga_{0.985}Mn_{0.015}N$ epilayer for the magnetic field directions (B)parallel and perpendicular to the hexagonal crystal c-axis are shown in Figures 5.19 and 5.20 together with the corresponding stick spectra. The allowed five fine structure lines generated by the electron spin transitions with $\Delta M = \pm 1$ are resolved, each six fold split by the ^{55}Mn hyperfine interaction due to the coupling of the $^6A_1$ ground state of Mn^{2+} to the nuclear spin I=5/2 of the natural isotope ^{55}Mn. No allowed EPR transition within the Mn^{3+} ground state manifold with S=2 could be observed in the X-band with the available magnetic field, since this signal is expected to be much weaker due to the non-Kramers character of the Mn^{3+} ion. It is also interesting to note that nn the Si-codoped samples, no indications of Mn-Mn interactions are observed. Previously, Mn-Mn interactions have been observed in MnP compounds [178], so their absence in these samples may be significant and an indication of reduced interactions based on Si-codoping in these materials.

5.7 Raman spectroscopy

5.7.1 Mn doping series

A more detailed study of the local and long-range lattice properties was performed by Raman spectroscopy. Micro-Raman spectroscopy was performed to determine the influence of Mn incorporation on the vibrational properties of MOCVD-

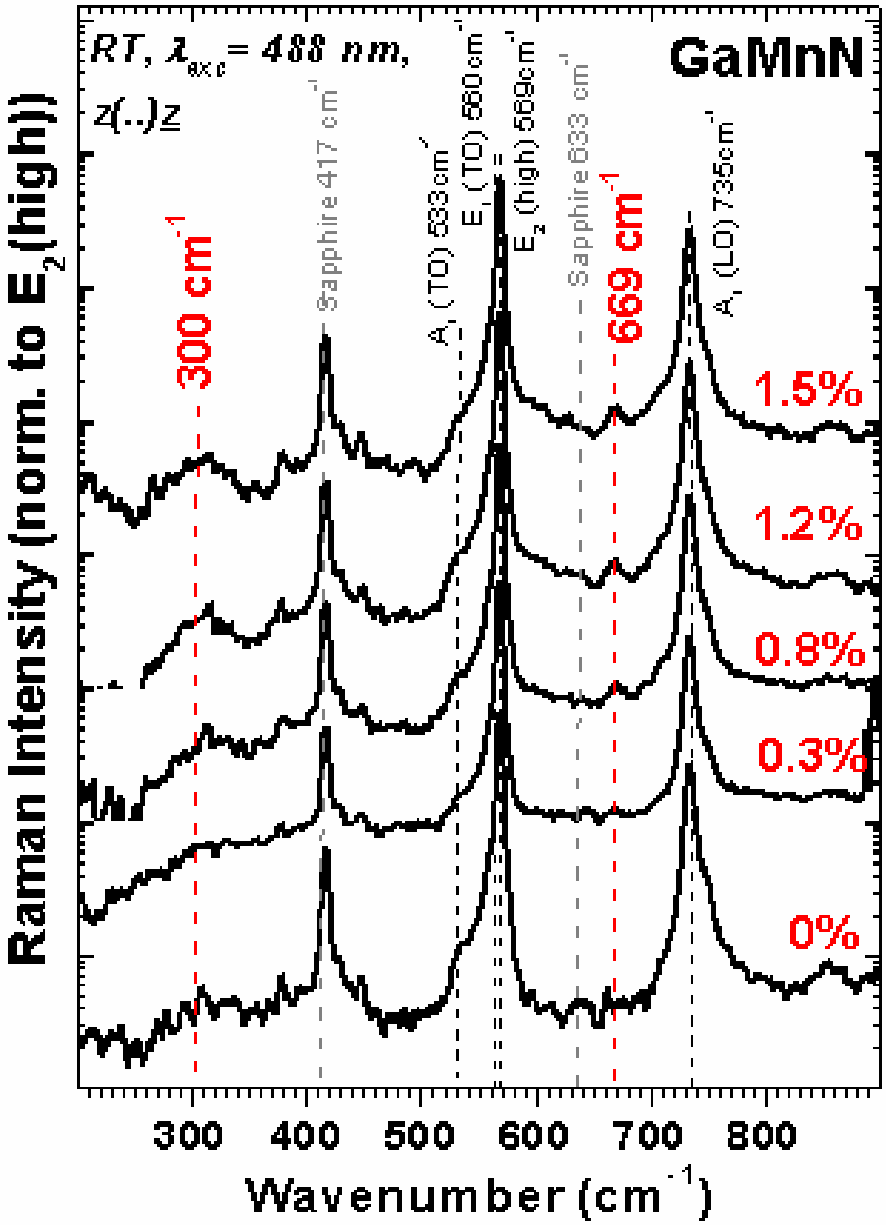

Figure 5.22 Raman spectra of MOCVD-grown $Ga_{1-x}Mn_xN$ epilayers as a function of alloying concentration. The spectrum is dominated by the GaN E_2(high) mode. The modes around 160, 300, and 670 cm−1 are disorder activated

grown $Ga_{1-x}Mn_xN$, in an effort to explore the effects of Mn introduction on the crystalline quality of the nitride system. Raman spectra were recorded at room temperature in back scattering geometry for GaN epilayers varying in Mn concentration from 0.0 to 1.5%. Figure 5.22 shows Raman spectra for the as-grown $Ga_{1-x}Mn_xN$ samples.

All of the spectra are dominated by the GaN E_2(high) mode at 569 cm^{-1}. This peak is shifted by 2 cm^{-1} from the relaxed GaN value of 567 cm^{-1} due to tensile strain as a result of the growth on sapphire substrates. Other Raman modes detected at 735 cm^{-1}, 560 cm^{-1}, and 533 cm^{-1} (A_1(LO), E_2(TO) and A_1(TO), respectively) are consistent with those of the GaN host lattice. The presence of sapphire modes at 417 cm^{-1} and 633 cm^{-1} could not be completely eliminated based on the wavelength of the laser used (488 nm), which penetrates through the transparent layers to the sapphire substrate. No correlation of these modes to the Mn concentration was observed by Raman studies. The observations also confirm the absence of Mn-induced strain. In the case of the $Ga_{1-x}Mn_xN$ layers, even at the highest doping levels, the primary modes in the $Ga_{1-x}Mn_xN$ layers track almost identically with GaN epilayers grown on sapphire. This is in direct contrast to GaN layers on silicon, which exhibit a shift in Raman modes to lower energies [179]. Thus, even though a high concentration of Mn ions (~10^{20} cm^{-3}) was incorporated in the GaN, no significant contribution to the strain in the sample could be observed. However, far infrared reflection studies revealed that the E_2(TO) phonon shifts slightly to higher energies with Mn concentration [180], which was attributed to a weakening of the bonding within the GaN lattice.

The presence of a strong A_1(LO) mode at 735 cm^{-1} confirms the absence of free carriers within this system due to the large binding energy of the Mn acceptors. A high

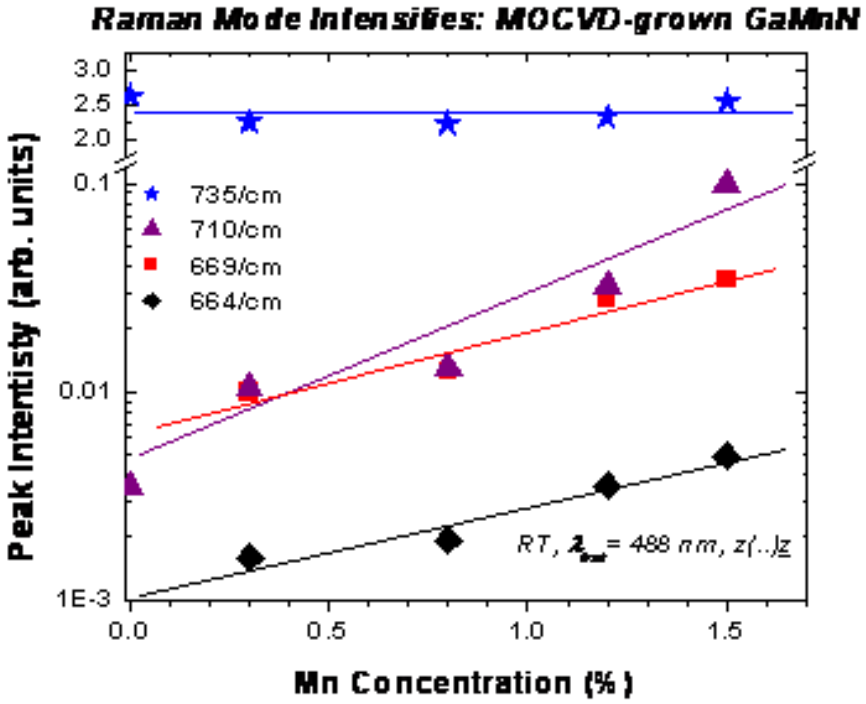

Figure 5.23 The intensity of the vacancy-induced LVMs and the disorder-activated mode near 670 and at 710 cm^{-1} are shown as a function of the Mn concentration in the inset. The intensity of the A_1(LO) mode does not depend on the Mn concentration and is shown for comparison. Note the semilogarithmical plot for the modes at 664, 669, and 710 cm−1. The lines are guide to the eye only.

carrier concentration (above 10^{18} cm^{-3}) was ruled out since no broadening of the A_1 (LO) mode occured. In heavily doped samples, this mode is well-known to broaden and wash out in samples with large carrier concentrations [132, 179]. Additional Raman evidence of the absence of significant carrier concentrations can be seen in the region of the GaN E_2(high) mode. In all of these samples, even those under the highest Mn ad Mg- and Si-codoping levels, no local phonon-plasmon coupled modes were detected. These modes are an indicator of high carrier concentrations [179].

Mn doping during the MOCVD growth of GaN caused the appearance of modes in the Raman spectra not typically observed for the GaN epilayers or the sapphire

substrate. Specifically, Raman modes around 160 cm^{-1} 300 cm^{-1}, and 669 cm^{-1} appeared to be more sensitive to Mn incorporation. Figure 5.23 shows a comparison of the intensity of these modes as a function of Mn incorporation, demonstrating a direct relationship. The intensities of these modes increased with Mn concentration, but no significant shift in their mode energies was observed. In comparison, the intensity of the A_1(LO) mode does not change with Mn concentration. Similar behavior was detected for a shoulder near 610 cm^{-1}, though low intensity prevented a deeper insight into the nature of this band. While the 710 cm^{-1} mode scales even more with the Mn concentration, a direct assignment to a Mn-related vibrational mode is not likely since this mode is also observed in, for example, Cu-doped GaN [181].

Comparison of the measured Raman spectra with phonon-dispersion curves for hexagonal GaN shows that the broad peak at 300 cm^{-1} is a disorder-activated mode attributed to the highest acoustic phonon branch [103, 182, 183]. This activated mode did not show a systematic dependence on the Mn concentration, but instead correlated more strongly with the crystalline quality determined by XRD, EPR and AFM [112, 117]. It should be noted that in this study the intensity of these modes is significantly lower (normalized to the E_2(high) mode) compared to other reports, suggesting that MOCVD growth results in the generation of less lattice disorder due to Mn incorporation [103, 111, 182, 183].

A closer inspection of the mode near 669 cm^{-1} reveals an asymmetric broadening of this mode. This substructure can be fitted with an additional mode at 664 cm^{-1}. The intensity of both the mode at ~669 cm^{-1} and a shoulder at 664cm^{-1} were found to strongly correlate to the Mn concentration, however, the linewidth of this mode did not show a

significant dependence on the Mn concentration. These modes have previously been attributed to local vibrational modes (LVM) due to vacancies [103, 111, 182, 183]. In this spectral range, a mode was found in GaN microcrystals at 670cm^{-1}, and it was assigned to a disorder-activated vibrational mode [182]. A more general study Limmer *et al.* reported on such a mode caused by vacancies in ion-implanted GaN epilayers [183]. In a more recent work based on MBE-grown $Ga_{1-x}Mn_xN$ [111], this line was attributed to a local vibrational mode of the GaN host lattice caused by a vacancy. The data obtained from MOCVD-grown GaN and presented in this work appear to support the conclusions drawn by Harima[111]. The MOCVD growth conditions preferentially support the generation of nitrogen vacancies and Mn interstitials in the epilayers. In addition, the lower intensity of the 669cm^{-1} mode compared to that reported elsewhere [111] could be explained as a consequence of the MOCVD growth, where the elevated growth temperatures and more efficient cracking of ammonia lead to lower vacancy concentrations. Other work on defect modeling in $Ga_{1-x}Mn_xN$ suggests that a Mn-nitrogen double vacancy pair may as a primary compensating defect [184]; this may be the source of the 669 cm^{-1} mode.

Based on the GaN E_2 (high) LO mode with respect to the difference in the reduced masses, local vibrational modes (LVMs) of Mn ions on Ga site might be expected around 580cm^{-1}. However, no such mode was found in the $Ga_{1-x}Mn_xN$ epilayers, and no phase separation was detected [80]. Unambiguous detection was prevented by the dominance of the GaN E_2 (high) LO mode and a mode near 576cm^{-1} that was also seen in bare Sapphire substrate. In the future, resonant Raman experiments may reduce the influence of the sapphire. Unlike the report by Harima et al.[111], no

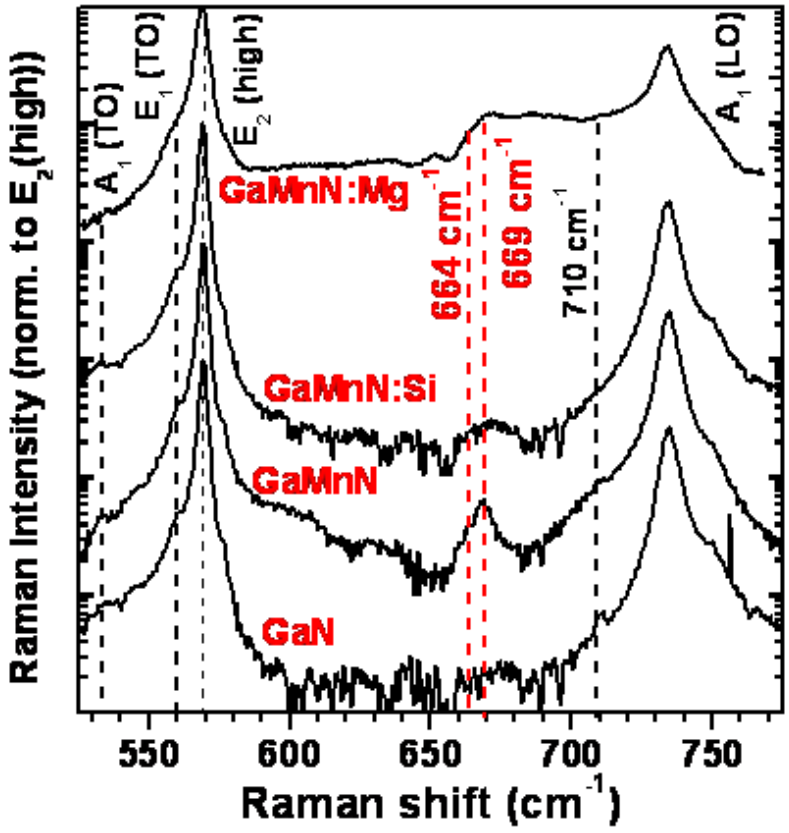

Figure 5.24 Sensitivity of the vacancy-induced local vibrational mode LVM at 669 cm^{-1} on codoping. Magnesium was used for acceptor codoping, and silicon was applied to create shallow donors in $Ga_{1-x}Mn_xN$.

feature around 580 cm^{-1} was observed in the Raman spectra that could be assigned to Mn substitution in GaN. However, substitutional Mn incorporation has been confirmed by other studies on these samples [112, 185-187].

5.7.2 Effects with and without Si-codoping

An interesting behavior is observed in the samples co-doped with silicon. Silicon was originally added to investigate the role of carrier concentration on the magnetism in these samples. However, it also plays a role in the underlying defect structure of the material. For example, the incorporation of Si as a donor on Ga sites is known to reduce

the amount of nitrogen vacancies in GaN since the formation energy for nitrogen vacancies in n-type GaN is significantly higher than in p-type GaN [84].

Si co-doping, providing shallow donor states in GaN, can be applied to suppress the intensity of the formation of nitrogen vacancies. In this Raman investigation, the Mn concentration was held constant at the "heavily doped" level of 1.5 % and the nominal Si concentration was ~10^{20} cm^{-3}. Raman spectra of two $Ga_{0.985}Mn_{0.015}N$ epilayers are shown in Figure 5.24. For comparison, Raman spectra of samples co-doped with Mg are also shown. The intensity of the 669cm^{-1} mode increases with increasing Mn concentration, though the line width does not change. Upon Si co-doping, the intensity of the 669cm^{-1} mode is strongly reduced. Moreover, the lack of plasmon-phonon coupled modes even with heavy Si-codoping indicates that Mn was incorporated as a deep acceptor, leading to the trapping of the electrons provided by the Si donors. Doping considerations, specifically a change in the free energy for vacancy formation [127], provide a further argument for this mode to be related to nitrogen vacancies or complexes. Polarized Raman spectroscopy performed on these samples confirms that this mode is point defect related, Figure 5.25. Vacancy formation is also suggested by the infrared reflection data which shows a weakening of the GaN lattice with heavy Mn incorporation [180], and has been suggested as the predominant decay mechanism in ion implanted p-GaN [77]. A high vacancy concentration could also result in the observed decrease in lattice parameter with Mn-doping via MBE [167], whereas based on strictly atomic radii considerations an increase in lattice parameter would be expected.

5.7.3 Comparison with implanted samples

Raman spectroscopy was also used to compare the structural quality of the ion implanted samples with that o the samples grown by MOCVD. Figure 5.26 shows Raman

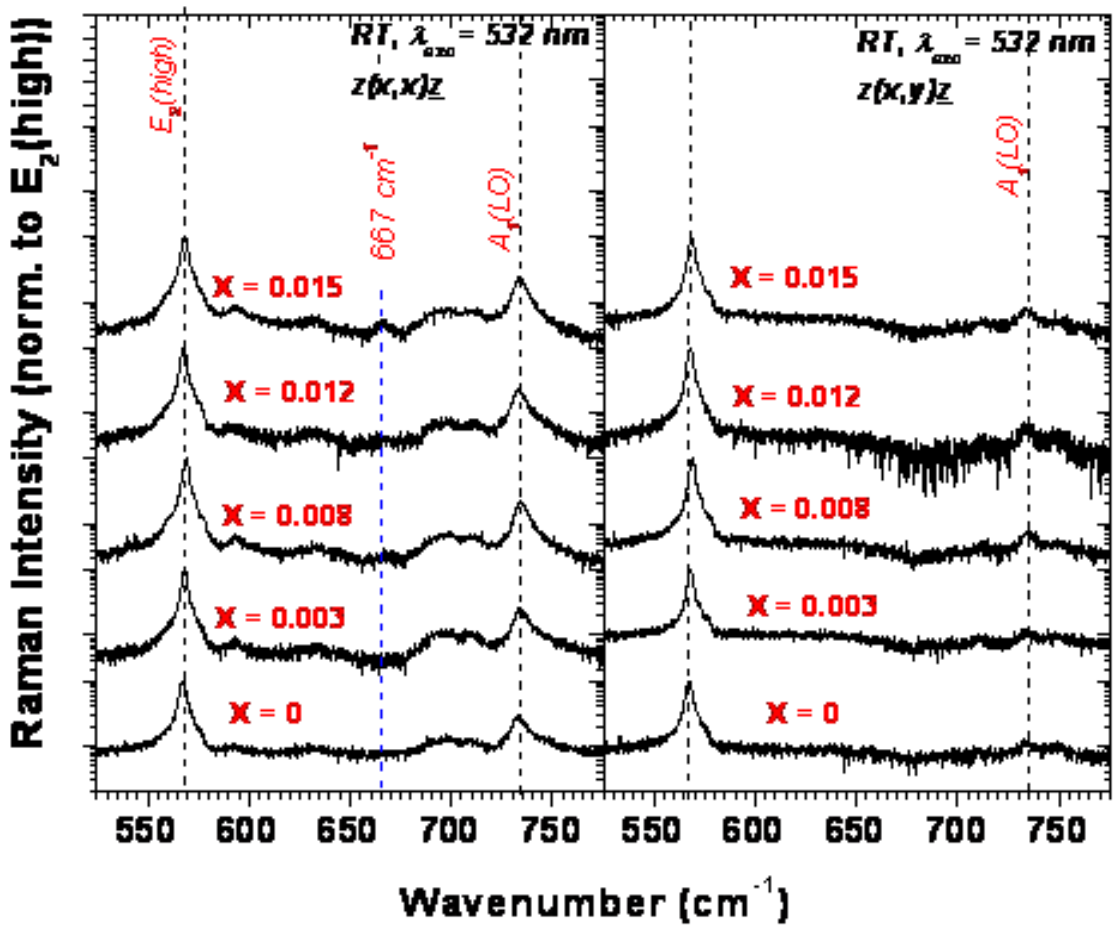

Figure 5.25 Polarized raman spectroscopy of $Ga_{1-x}Mn_xN$ as a function of doping, showing that the mode near 670 cm^{-1} is point defect related.

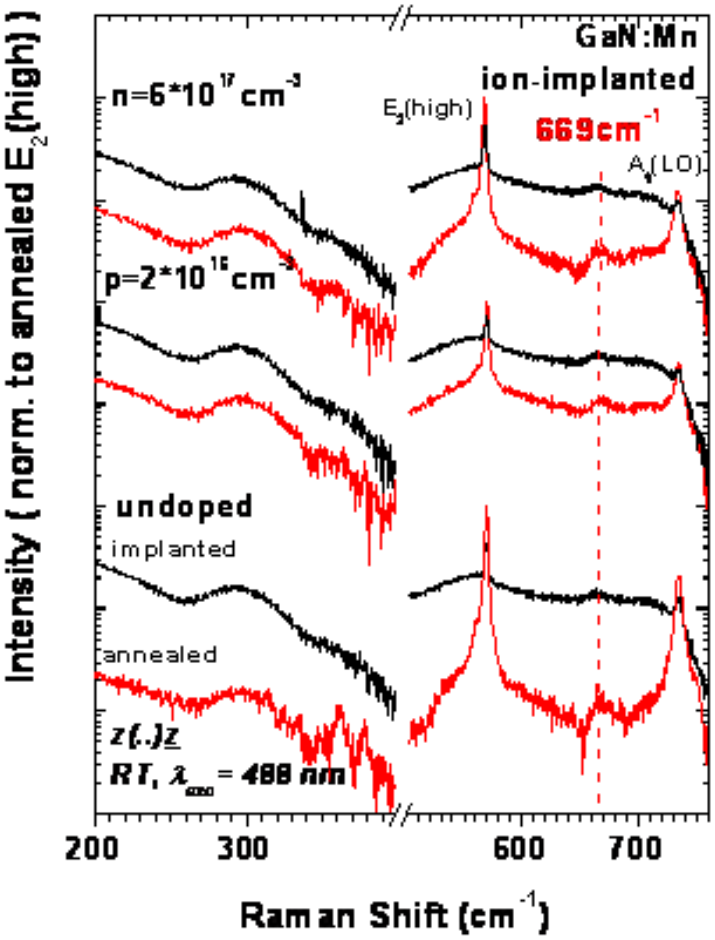

Figure 5.26 Raman spectra of ion-implanted GaN:Mn epilayers Raman spectra were also recorded after a 5 min RTA treatment at 700 °C in nitrogen atmosphere. The same base lines were chosen for the spectra of the asi-mplanted and the annealed samples

spectra for the as-grown $Ga_{1-x}Mn_xN$ samples and the ion-implanted samples. The most prevalent feature in these samples is the much higher background signals and presence of a strong disorder mode around 300 cm^{-1}. These low-energy Mn disorder-activated modes result from defect densities that cause a loss of wave vector conservation in the scattering process [103, 182]. Both the 160 $cm^{-1}$and 300 cm^{-1} modes were also observed with a higher intensity in the ion-implanted GaN epilayers. Annealing at 700 °C reduced their intensity, and the Raman spectra became similar to those of the MOCVD-grown $Ga_{1-x}Mn_xN$ epilayers. However, annealing could not completely remove the lattice disorder, a result which is consistent with the previously mentioned x-ray diffraction data. In addition, in the GaN:Si implanted samples there is still a mode at 669 cm^{-1}. This suggests that is important to have the donors present during the growth process. This vacancy-related mode, which is also observed in samples implanted with other elements, can also be formed through implantation damages. Thus, no suppression of the vacancy-induced LVM was observed for the n-type sample.

5.8 Optical properties of $Ga_{1-x}Mn_xN$ films

Optical studies are an essential tool for examining the crystalline quality, defect states, and formation of impurity bands from the introduction of manganese or other transition metals into the lattice. In the following section the effect of substitutional lattice-site incorporation of Mn on the optical properties of these materials is discussed in comparison with the extensive studies in the literature.

5.8.1 Photoluminescence

Photoluminescence (PL) studies were performed in the visible and ultraviolet spectral range in order to further understand the role of Mn-introduction in MOCVD-grown and implanted $Ga_{1-x}Mn_xN$ epilayers. PL measurements were performed on implanted layers,

for as-grown, co-doped and annealed epilayers. Additional PL studies were performed in the visible spectral range in order to derive more information about the ferromagnetic nature and Mn-induced disorder of $Ga_{1-x}Mn_xN$ layers. The PL results for epitaxially grown $Ga_{1-x}Mn_xN$ are shown in Figure 5.27. The figure includes room temperature measurements from thin (300nm) and thick (1 micron) layers grown on GaN templates, as well as samples which have been implanted with Mn. In the thick samples, the most prominent feature is the blue emission band around 3.0 eV which is also reported in both ion-implanted and MBE-grown $Ga_{1-x}Mn_xN$ [77, 188]. This blue emission band appears in samples with a Mn concentration >0.5 % ,resulting in two distinct peaks at 3.0 eV and 2.8 eV. The band at 3.0 eV is attributed to Mn-related or Mn-induced transitions for heavily Mn doped samples. Recently, the blue band emission was observed in MBE-grown $Ga_{1-x}Mn_xN$ and ion-implanted material [15]. These broad bands are actually a broad emission consisting of several bands (>7 distinct bands) ranging from 2.7eV to 3.1eV, has previously been assigned to transitions from conduction band electrons to Mn -related states and from shallow donor (e.g., N vacancy) to Mn acceptor [77, 114, 162, 188]. Peak energies reported for this emission band range from 2.90 eV [114] through 3.08 eV [118] at room temperature. These bands are also known to appear in GaN upon compensation of acceptors by doping-induced defect states as well as by the incorporation of hydrogen on interstitial sites. Accordingly, heavy Mn doping - in particular the band at 3.0 eV,- is attributed to Mn-induced transitions. Lifetime measurements suggest similarity to the correspond band observed for compensated GaN:Mg, where different defect bands involving spatially indirect transitions were foundd to contribute to the blue emission band [189].

In comparison, in the lightly Mn-doped $Ga_{1-x}Mn_xN$ samples (<0.5%) [190], annealed samples, and the samples co-doped with Si, almost no blue band emission but a pronounced yellow band attributed to intrinsic gallium defects was observed. In the first case, the behavior is assigned to the lower amount of Mn ion available to substitute on

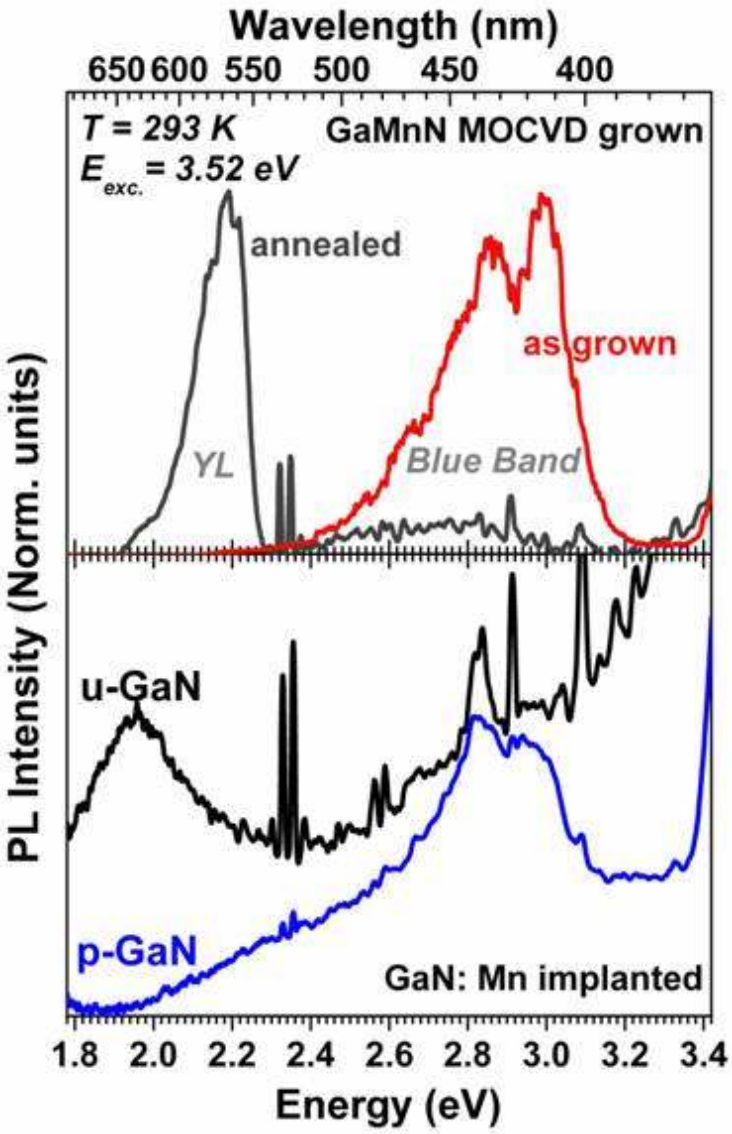

Figure 5.27 Photoluminescence spectra from MOCVD grown and implanted $Ga_{1-x}Mn_xN$. Samples. A Mn-related transition occurs at 3.0 eV, while the other transitions such as the yellow luminescence (YL) and the low-energy tail of the blue luminescence band (BL) can also be found in the template layer. The latter emissions are assigned either to crystalline defects (e.g., Ga vacancies) in the case of the YL or donor-acceptor transitions (BL) typically seen in compensated p-doped GaN.

lattice site which reduces the amount of Ga vacancies. In the latter two cases, intrinsic and extrinsic shallow donor states are introduced leading to a compensation mechanism of the Mn^{3+} acceptors. Following the annealing process, the dominant feature (yellow band emission) in these spectra is commonly attributed to defect centers (e.g., Ga vacancies [191]) in the GaN buffer layer and the epilayer. This is in agreement with the reduced intensity of the absorption band around 1.5 eV that was found to decrease also by decreasing the Mn concentration and as a result of annealing. A stronger compensation of Mn acceptors is seen for Si co-doping. Its PL is similar to that detected for $Ga_{1-x}Mn_xN$ with low Mn concentration, reinforcing that the origin of the particular blue bands observed here is assigned to (active) Mn acceptor related states as described above [[77, 114, 162, 188]. No emission around 3.0 eV was observed in compensated or partly compensated material.

For the implanted samples, the blue luminescence band is still visible in the implanted p-GaN sample, whereas the most prevalent feature in the implanted undoped sample is a broad emission band near the yellow, as seen in the annealed sample. As shown below, there is a correlation between the presence of these emission bands and the strength of the magnetic signal. It appears that the blue-band luminescence seen in these two samples is related to this state, which results in stronger ferromagnetic behavior in the $Ga_{1-x}Mn_xN$ system.

5.8.2 Optical Transmission

5.8.2.1 Si-codoping effects

Further investigations on the valence state of Mn in $Ga_{1-x}Mn_xN$ were performed using optical transmission studies. This method, described in more detail in Chapter 3, allows clarification of whether isolated Mn ions (as observed for bulk $Ga_{1-x}Mn_xN$ [192] and $Ga_{1-x}Mn_xAs$) or the formation of an Mn induced impurity energy, are the primary cause for the observed ferromagnetism. Fiugure 5.28 shows the room temperature

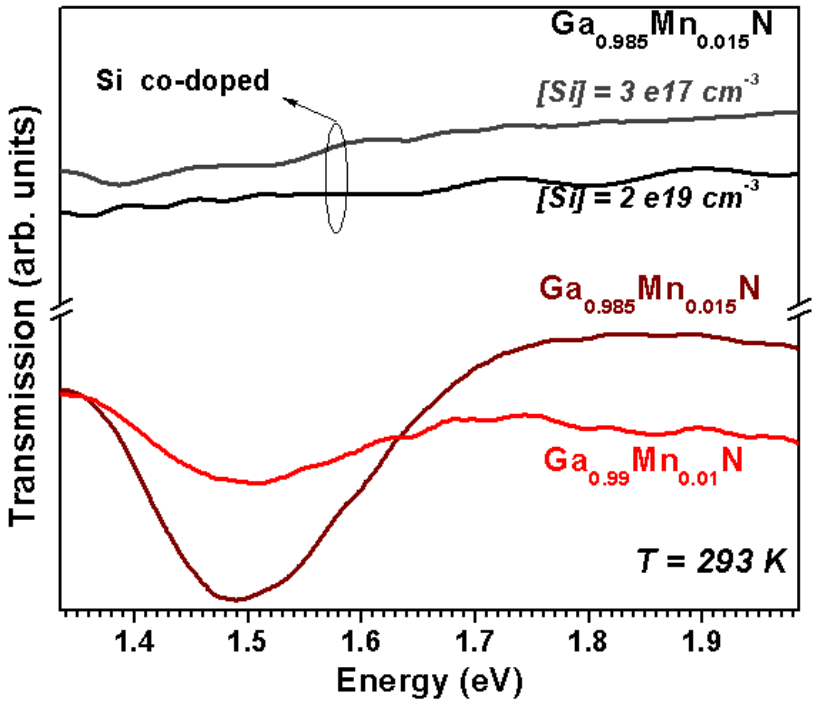

Figure 5.28 Optical transmission spectrum of $Ga_{1-x}Mn_xN$ with and without Si-codoping, showing an absorption near 1.5 eV due to d-d trnsitions

transmission spectra of four samples. The incorporation of Mn into GaN layers during MOCVD growth leads to a broad absorption band, a spectrally diffuse line around 1.5 eV with a larger full width at half of maximum (FWHM). These transitions have previously been reported in lightly-doped MBE-grown and implanted $Ga_{1-x}Mn_xN$ epilayers [169, 193], and identified as intra d-shell transitions in the Mn^{3+} atom. Optical analysis suggests that the incorporation of Mn into the GaN layers during growth leads to an absorption band and a resulting dip in transmission spectra around 1.5 eV. This energy is attributed to the transitions from the T_2 states to the E states of the ^5D level of the Mn^{3+} ion in the GaN environment. A relatively large FWHM of ~150 meV for this absorption band and an increase of its FWHM and its intensity with increasing Mn concentration

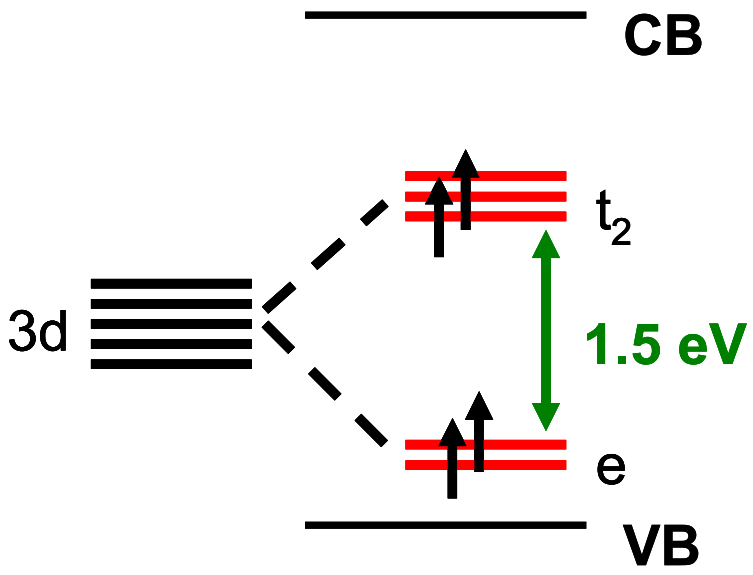

Figure 5.29 Expected splitting and location of Mn-d levels in the presence of the tetrahedral crystal field afforded by the GaN lattice

were observed. The intensity and linewidth of this band scale with Mn concentration; the absorption depth (FWHM of the absorption band near 1.4eV) is 1.8% (120meV) for the 1% Mn sample, and 6.0% (180meV) for the 1.5% Mn sample. The broadening of these states may be due to the high Mn concentration [53].

In contrast, no such absorption peak was observed in $Ga_{1-x}Mn_xN$ epilayers that were prepared to exhibit n-type behavior achieved by co-doping with Si during growth. The relatively large FWHM of 120 meV for this absorption band is much broader than previous reports of internal atomic transitions in isolated Mn ions [169]. This absorption peak is not observed in nominally undoped GaN grown on sapphire or $Ga_{1-x}Mn_xN$ layers co-doped with silicon, corresponding to a strong sensitivity to the position of the Fermi level. As mentioned above, silicon introduces shallow donor states in GaN, which leads to a partial or full compensation of the acceptor states introduced by the Mn ions. The absence of the absorption band around 1.5 eV in the $Ga_{1-x}Mn_xN$ layer co-doped with

silicon indicates the sensitivity of the E to T_2 transitions to the position of the Fermi level. The Fermi level is shifted towards the conduction band because electrons are trapped at the Mn levels and fill this T_2 band, eliminating this pathway for the internal absorption. Hence, electrons are trapped at deep defects and the position of the Fermi level shifts towards the conduction band.

No further absorption features were found in the infrared spectral range down to 0.5 eV. The transmission experiments did reveal an increase of detected light below 2.7 eV and a very weak absorption signal around 1.75 eV. The latter is attributed to the emission of holes from the neutral Mn^{3+} acceptor state [169]. The increase in the transmission signal below 2.7 eV is in good agreement with the observed PL band around 3.0 eV and suggests resonant absorption by Mn-related states [114].These findings indicate that the Fermi level in the investigated samples in the broad absorption band is located around 1.8 eV above the valence band energy or closer to the conduction band in the Si-codoped samples.

5.8.2.2 Low temperature transmission

Further information about the origin of the observed absorption band was derived from temperature dependent absorption measurements. Variations in the absorption position and linewidth of the band are expected if intratomic transitions of isolated Mn ions cause the absorption. Analysis of these effects is difficult due to Fabry-Perot (FP) interference oscillations superimposed on all of the background signals. This interference pattern was more pronounced in the case of the temperature-dependent measurement due to the measurement conditions. This effect can be somewhat eliminated through the use of liquid helium measurements at 2K and using bu not an external broadband source, but rather luminescence from Cr^{3+}impurities in the substrates. In this case, the 1.41 eV transmission shows up very sharply in these samples, with additional higher energy

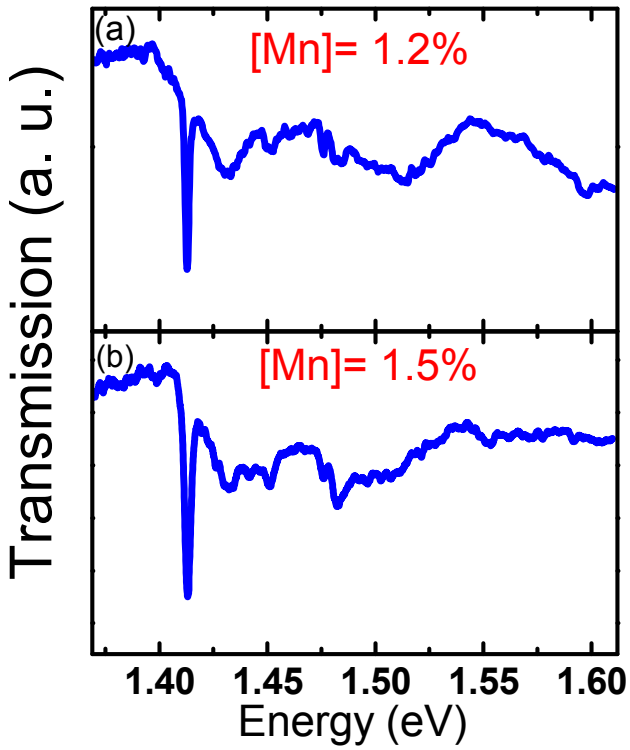

Figure 5.30 Transmission spectrum of $Ga_{1-x}Mn_xN$ from sapphire substrate luminescence at 2K, showing no indication of an impurity band at that temperature.

features. The sharp absorption line is attributable to the zero phonon line of the internal Mn^{3+} transition. The higher order features have been suggested to be phonon replicas. In addition, though II-VI compounds are known to have strong electron-phonon couplings, recent infrared transmission measurements performed on MBE-grown material suggest that the electron-phonon coupling in $Ga_{1-x}Mn_xN$ is relatively weak [194], though the superposition of phonon replicas in the absorption data presented here has not been eliminated. These findings suggest that disorder-induced broadening in the partially filled T_2 band can be seen at room temperature, but a closer analysis at low temperatures suggests that a broad impurity band capable of supporting long range hopping is not necessarily present. The narrow band may be consistent with the carrier freezeout which has been reported to occur [71].

5.9 Summary

In this chapter, it was demonstrated that metalorganic chemical vapor deposition is a suitable technique for the growth of $Ga_{1-x}Mn_xN$ thin films. The crystalline quality of $Ga_{1-x}Mn_xN$ and the absence of secondary phases in the layers were confirmed by XRD. Mn concentration was varied between 0.3 % and 1.5 % as confirmed by various techniques. Slight variations in Mn concentrations and thicknesses across the wafer were established based on the gas flow and the temperature gradients in the MOCVD growth. More importantly, Ga lattice site occupancy of substitutional Mn was confirmed. The valence state of the Mn could be varied through the incorporation of Si codoping and swapped from Mn^{3+} to Mn^{2+}. A significant number of compensating defects were incorporated with Mn alloying and confirmed via optical studies.

Ferromagnetic behavior, indicated by hysteresis in the magnetization spectra, was detected in the $Ga_{1-x}Mn_xN$ samples at alloy levels up to x=.015. Two significant results were obtained. First, the saturation magnetization (size of the hysteresis loop) scales with Mn concentration, confirming that Mn doping causes the observed ferromagnetic properties. Second, with increasing silicon concentration, the size of the hysteresis loop decreases significantly (by more than one order of magnitude). Curie temperature was not measured due to experimental limitations, but there is only a small drop-off in the observed magnetization between 5 K and 300 K indicating that T_C is well above room temperature. At high Si concentration ($[Si] > 10^{19}$ cm^{-3}), ferromagnetic behavior is suppressed and the magnetization spectra reveal an overall diamagnetic behavior for this sample due to the contribution from the sapphire substrate.

Table 5.1 Comparison of observed experimental data with expected results carrier mediated (Zener), double exchange, and clustering mode; Green up triangles indicate agreement, red down triangles disagreement, and square indicate inconclusive evidence.

Observation	**Zener Model**	**Double Exchange**	**Cluster Model**
RT ferromagnetism	▲	▲	▲
T_C> RT even at low concentration	▼	■	▲
No free carriers	▼	▲	▲
Fermi level dependent magnetization	▲	▲	▼
Irreversibility in ZFC/FC magnetization	■	■	▲
No second phases by XRD	▲	▲	■
No second phases in TEM	▲	▲	▼
Magnetic circular dichroism not observed	▼	▲	▲
Coercivity/Remnance ratio constant	■	■	▲
Anisotropic behavior	▼	▲	■

It is essential to compare these experimental results with the expected observations for the various theoretical models for ferromagnetism in these materials. Table 5.1 shows a list of the experimental observations, and compares them with expected behavior under the three prevailing theories of ferromagnetism in this system. According to the carrier model based theories, an increase in carrier concentration would also yield an increase of the magnetization. However, in these studies, the carrier and Mn concentration are not high enough to render the mean-field carrier mediated model applicable. The formation of transition metal-rich clusters is still a possibility. However, transmission electron microscopy does not see any indication of these secondary phases. The model that seems to have the best phenomenological correlation to the observed magnetization behavior of $Ga_{1-x}Mn_xN$ is the formation of a partially filled Mn-induced band. Ferromagnetism is stabilized by the double-exchange-like interaction of electrons in this band. In the case of low concentration Si co-doping, not every Mn acceptor state is compensated. Hence, holes are present in this band, and the magnetic ordering in optimally MOCVD-grown $Ga_{1-x}Mn_xN$ could be attributed to exchange between electrons localized on the levels lying deep in the forbidden energy gap. The reduction of available free states for the double-exchange-like interaction (holes) in the T_2 band holds for the observed smaller magnetization. Finally, although band-like features are seen in the optical transmission spectrum, it is unclear why a typically short ranged magnetic interaction can result in robust, above room temperature ferromagnetism in these alloys. The next chapter will focus on a method for elucidating the underlying physics behind this observed ferromagnetic ordering in the transition metal doped III-nitrides.

CHAPTER 6

COMPARISON OF GALLIUM IRON NITRIDE AND GALLIUM MANGANESE NITRIDE AND DEVICE INVESTIGATIONS

6.1 Introduction

In order to elucidate the true mechanism of ferromagnetism in $Ga_{1-x}TM_xN$, several possible methods can be used. One method is to perform extensive and sometimes esoteric additional characterization techniques on the already grown samples. Although this method should ultimately result in a clear understanding of the materials' properties, it can be extremely time-intensive and not feasible within the limitations of the characterization tools typically available. An alternate method which should provide the same information in a fraction of the time relies on a simple variation of the transition metal used in the study. The prevailing hypotheses on the magnetic ordering in these materials can be tested by varying the substitutional transition metal used in the GaN lattice rather than by a complete cataloging of a single materials system.

Figure 6.1 provides a schematic of several possible origins of the ferromagnetism in the nitrides and illustrates how this behavior can be further examined by varying the element. The empirical impurity band for ferromagnetism takes into account the fact that the majority of Mn atoms are in the d^4 configuration. Impurity band holes required for hopping that leads to ferromagnetic ordering, and the d^4 configurationis necessary to

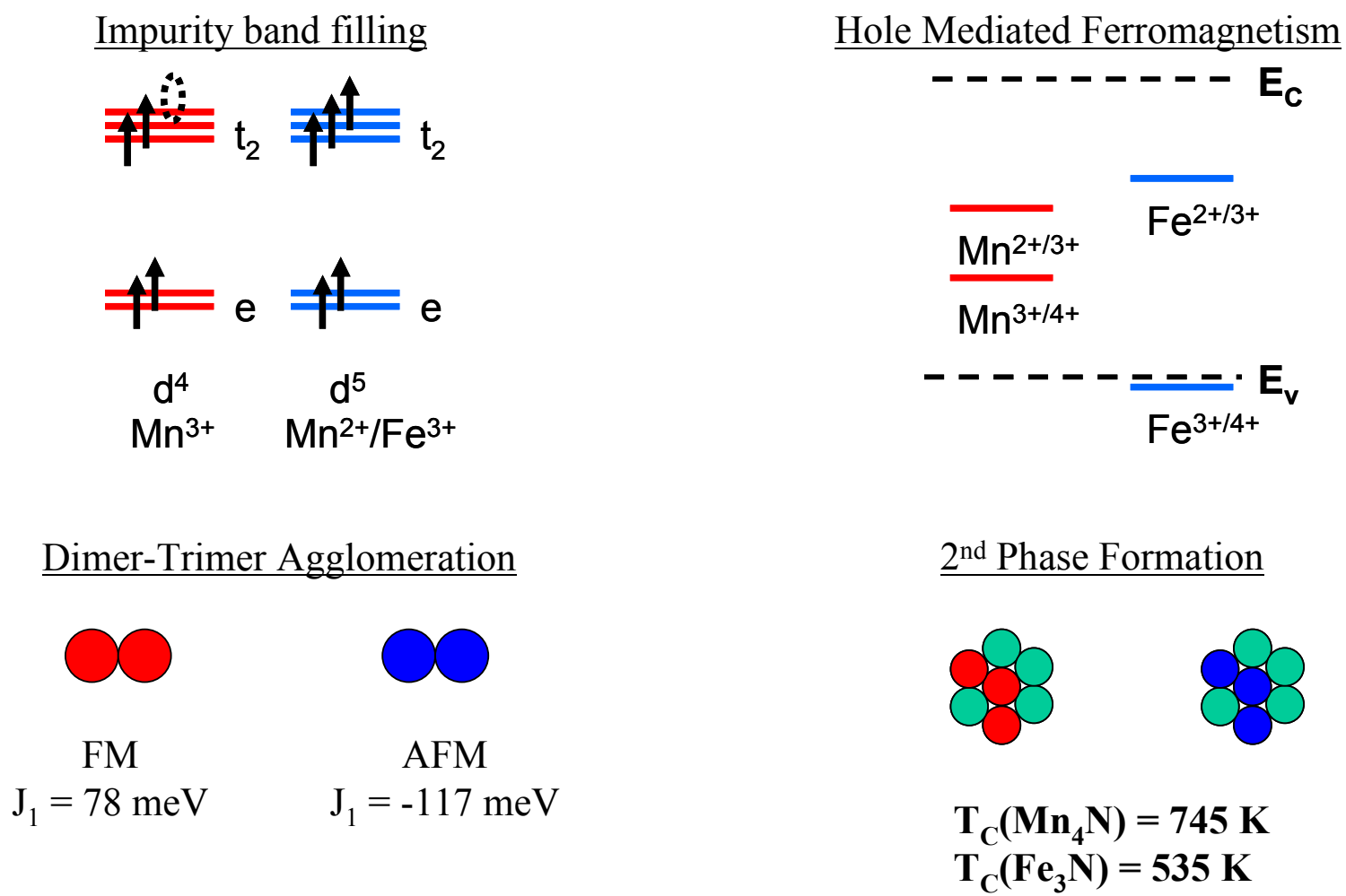

Figure 6.1 Comparison of the difference between Mn and Fe in various of the models for the origin of ferromagnetism in the transition metal-doped III-nitrides

ensure the presence of these holes. If Fe is used as the transition metal substituent and it remains in the trivalent state, the atom will be in the d^5 configuration. This would result in a completely half-filled shell, a full impurity band, and no hopping pathway for the electrons to stabilize the ferromagnetic ordering. Thus, if the impurity band model holds for all alloys, then the ferromagnetism should completely disappear. In addition, the substitutional Fe exhibits different behavior with respect to hole doping; this could potentially still enable the hole-mediated ferromagnetic model to be tested and explored in the nitride system. This is related to the positions of the various acceptor levels in the nitrides. For example, in the nitrides, the $Mn^{2+/3+}$ acceptor level is predicted to be 1.8 eV above the valence band edge. Optical measurements presented in the last chapter and by other researchers [169] support this analysis through both theoretical and experimental predictions. Upon attempting to introduce hole carriers into $Ga_{1-x}Mn_xN$ in an attempt to stabilize the ferromagnetism, only a conversion of Mn^{3+} to Mn^{4+} is observed [195], rather than an increase in carrier concentration. Optical measurements have confirmed a conversion through the optical transitions which places the position of this acceptor level at 1.1 eV above the valence band edge. Consequently, it is impossible to introduce any significant hole concentrations in $Ga_{1-x}Mn_xN$. The situation in $Ga_{1-x}Fe_xN$ is somewhat diffferent, since the $Fe^{3+/4+}$ acceptor transition is predicted to be near the valence band edge rather than near the middle of the gap [196]. This would make it possible, provided some of the other materials and crystalline quality issues can be resolved, to overcompensate the Fe traps and dope the material p-type. Whether sufficient hole concentrations could be obtained is a separate issue since the deep nature of the Mg acceptor (200 meV above the valence band edge) means that only about 1% of the

acceptors are activated at room temperature; carrier concentrations are typically on the order of 10^{17}, which is much less than the $3.5x10^{20}$ needed for room temperature ferromagnetism [22].

The use of both Fe and Mn in separate samples also allows for a comparison of the various cluster models for ferromagnetic ordering. In particular, Mn and Fe embedded clusters are expectted to behave very differently according to the dimer/trimer models for ferromagnetism [19]. Based on the first principles calculations used in the study, it was found that it is energetically favorable not only for Mn atoms to cluster, but also for ferromagnetic ordering by those atoms that do cluster to have a predelection to order ferromagnetically. The exchange integral J_1/k_B calculated for a dimer pair of Mn atoms in a GaN lattice is 78 meV. In contrast, the exchange integral for an Fe dimer is -117 meV. The change in sign indicates an antiferromagnetic coupling. The origin of this mechanism is similar to the impurity model and results from a competition between the superexchange and double exchange interactions. If small amounts of an incommensurate ferromagnetic phase instead of embedded clusters result in the hysterestic signal, then this should also be differentiable through a variation in the transition metal dopant. The various competing ferromagnetic phases should have distinct Curie temperatures based on the element used. For example, Mn_4N has a T_C of 745 K. Even in the arsenides, when phase separation occurs, the residual Curie temperatures of the embedded phases are still visible in the magnetization curves. These second phases might be somewhat affected by lattice parameter shifts since digression from the equilibttium value in the lattice spacings will result in a change in the strength of the magnetic exchange [197].

6.2 Growth of $Ga_{1-x}Fe_xN$

6.2.1 Background on $Ga_{1-x}Fe_xN$ growth

There has actually been interest in the use of MOCVD for the incorporation of Fe for a longer period than for incorporation of Mn. Specifically, the use of iron in semi-insulating templates for templates for high electron mobility transistors was reported as early as 2002 in the nitrides [198] and even further earlier in the phosphides [199]. More recent efforts have focused on producing $Ga_{1-x}Fe_xN$ at lattice concentrations suitable for spintronics, and there have been reports of MOCVD grown materials which exhibit room temperature ferromagnetism [200]. Other reports have seen ferromagnetism in implanted samples [201] although the observed T_C has been reported from less than room temperature to above room temperature. Moreover, the use of MOCVD as the growth technique has a number of challenges, such as selecting the suitable precursor and memory effects [198].

6.2.2 X-ray diffraction

High resolution x-ray diffraction (XRD) scans are shown in Figure 6.2. In these scans, the only visible reflections are the basal plane reflections of the GaN layer and the sapphire substrate. No significant angular deviation or peak splitting is observed in the GaN (0002) reflections; this indicates that the lattice parameter in the transition metal doped layer is close to that of the GaN template, as would be expected from the relative sizes of the Ga, Fe, and Mn ions and the relatively low alloying concentrations. The XRD linewidths varied slightly from sample to sample, but were about 200 arcsec for the (002) and 500 arcsec for the (102) reflections in all cases. Although no direct evidence of metallic Mn or Fe containing clusters was observed in high-resolution XRD, the presence of small ferromagnetic clusters or additional phases could not be eliminated based solely

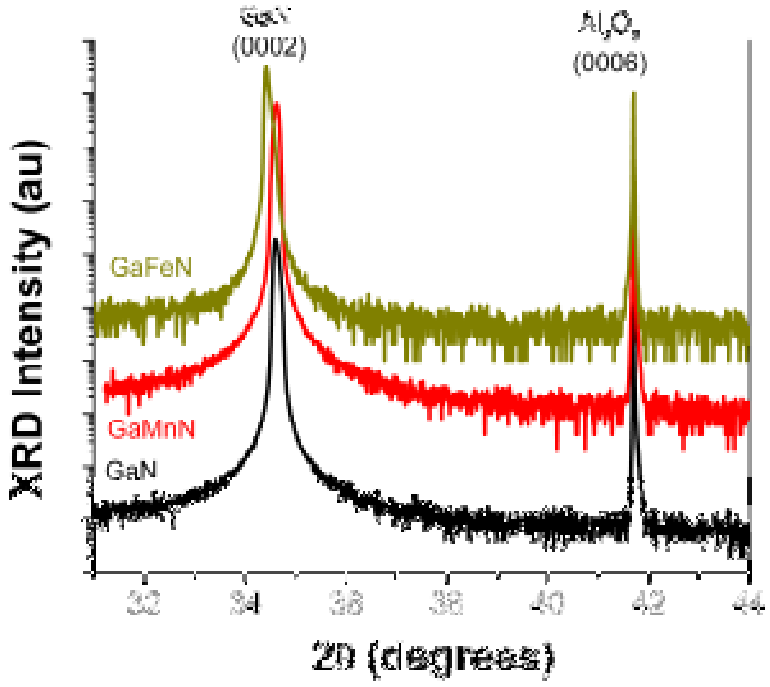

Figure 6.2 High resolution X-ray diffraction (2θ–θ) scans for $Ga_{1-x}Mn_xN$ and $Ga_{1-x}Fe_xN$ layers grown on sapphire templates. Note that over five orders of magnitude there is no indication of any secondary phase formation. The scans have been separated vertically for clarity

on the XRD data. Embedded nanocrystallites or an orientation along non-c-axis directions would not be measurable under the measurement configuration. The experimental findings do not fully preclude the existence of these second phases below the resolution limit of the XRD instrument.

6.2.3 Optical and Atomic Force Microscopy

The as-grown $Ga_{1-x}Fe_xN$ films are specular to the naked eye. Similar to the Mn-doped films which were reddish in color, the as-grown Fe-doped films are colorless except when co-doped with high levels of Si ($>10^{19}$ /cm^3); then the Fe-alloyed thin films turn yellow. This coloring can be attributed to the absorptions which result from d-d transitions in substitutional divalent transition metal atoms. In all cases, Hall Effect

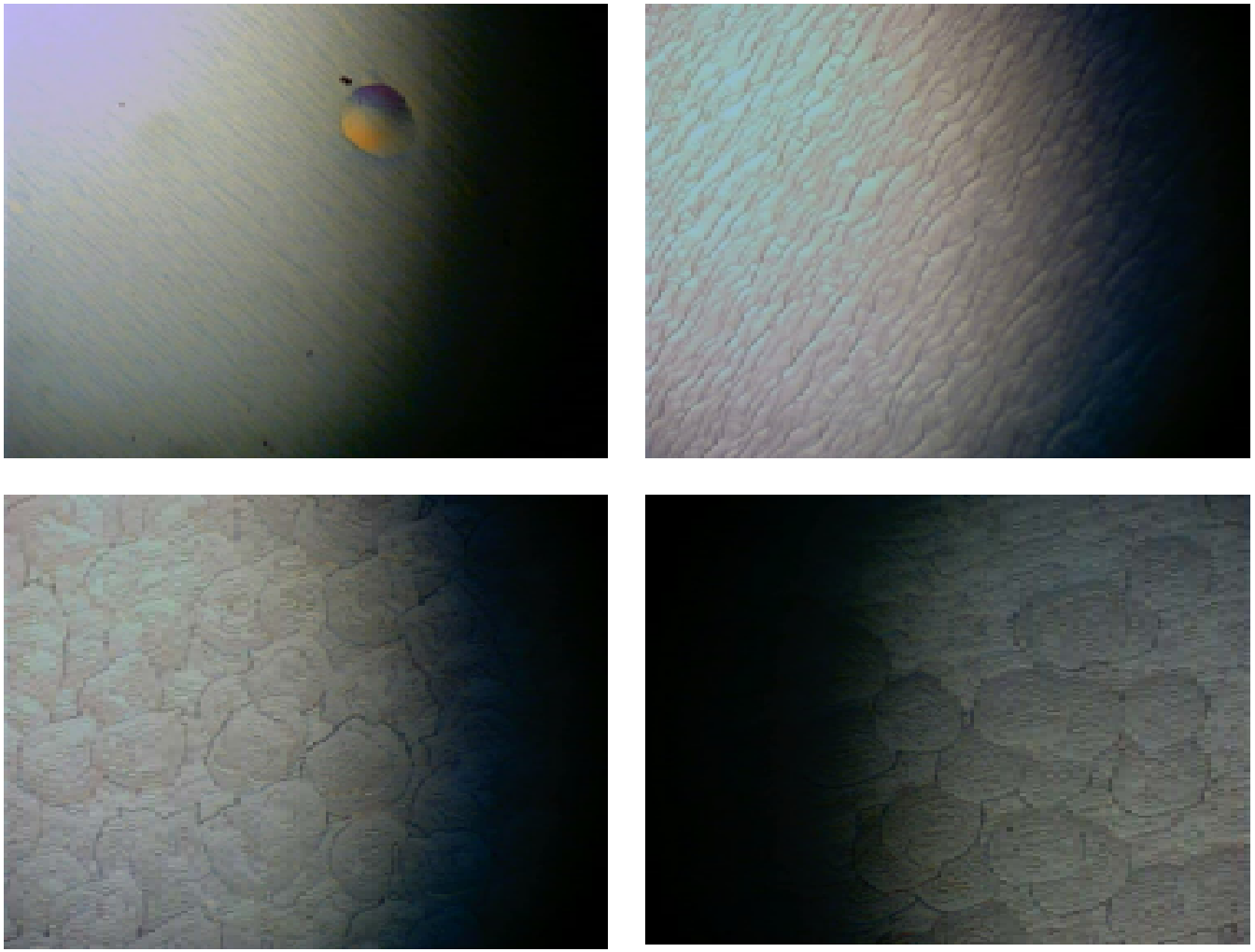

Figure 6.3 Nomarski images of as-grown GaMnN and GaFeN thin film surfaces; From the upper left a) $Ga_{1-x}Mn_xN$ (x=0.01) b) $Ga_{1-x}Fe_xN$ (x=0.001) c) $Ga_{1-x}Fe_xN$ (x=0.003) d) $Ga_{1-x}Fe_xN$ (x=0.005 The images represent an approximate area of 1.35 mm x 1 mm.

measurements indicated that the as-grown $Ga_{1-x}Fe_xN$ films are semi-insulating or weakly n-type, even in films which have been co-doped with Si-donors in an attempt to improve the carrier concentrations to induce carrier mediated magnetism.

Another important aspect of the as-grown films is the surface and structure quality. Although XRD does not reveal a large macroscopic effect, a considerable difference can be observed in the surface quality of the iron doped thin films when compared with undoped GaN thin films. Nomarski microscope images of the $Ga_{1-x}Mn_xN$ and $Ga_{1-x}Fe_xN$ thin films are shown in Figure 6.3. In the more heavily doped (~1%) $Ga_{1-x}Mn_xN$ thin films in Figure 6.3, the surface appears smooth and specular, even with the large intended doping levels. However, for the Fe-alloyed samples, there is a considerable change in the surface roughness with increasing Fe concentration. Memory effects which have been observed in $Ga_{1-x}Fe_xN$ [198] may play some role in $Ga_{1-x}Mn_xN$ as well. Nevertheless, samples grown at low doping levels after a series of high doping level runs can still exhibit a smoother surface in the Mn doped samples.

Results from atomic force microscopy (AFM) confirm the expected results of the optical microscopy. Figure 6.4 shows AFM scans for Fe-doped samples of increasing doping levels. In both of the lightly doped $Ga_{1-x}Fe_xN$ samples, clear step flow growth patterns typical of the 2-D step flow growth of GaN are clearly visible. The root-mean square (RMS) roughness values for these scans are less than 1nm, similar to that of the GaN template. However, as the Fe concentration is increased, the surface roughens considerably; it ranges from 3.7 nm to 28.4 nm RMS roughness for a 4 μm by 4 μm scan at 0.5% and 0.9% Fe molar flow ratios.

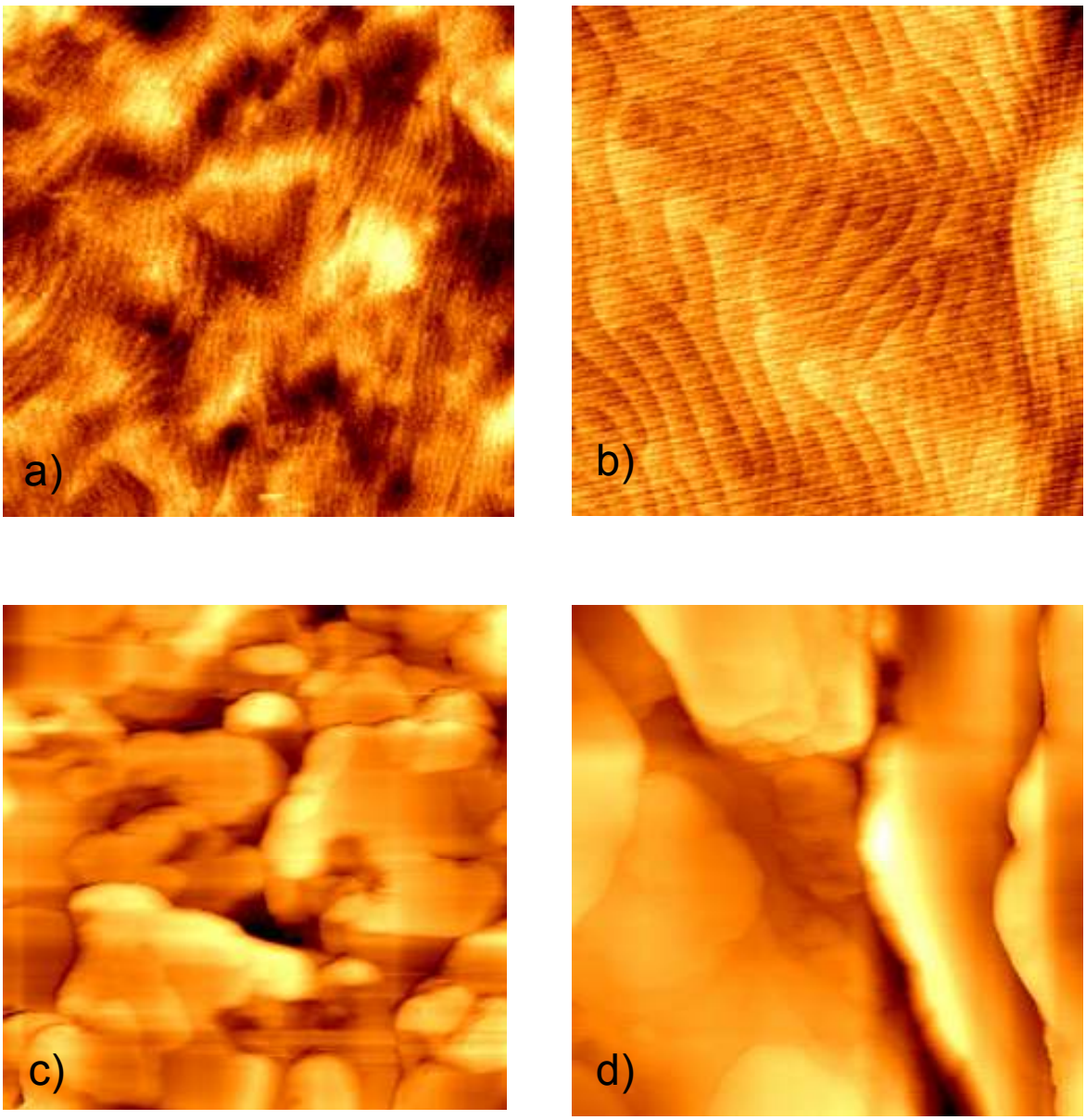

Figure 6.4 Atomic force microscopy scans of $Ga_{1-x}Mn_xN$ and $Ga_{1-x}Fe_xN$. The scans are of a) $Ga_{1-x}Mn_xN$ (x=0.015) 10 μm x 10 μm scan, RMS roughness = 0.32 nm. b) $Ga_{1-x}Fe_xN$ (x=0.001); 4 μm x 4 μm scan, RMS roughness = 0.4 nm. . c) $Ga_{1-x}Fe_xN$ (x=0.005); 4 μm x 4 μm scan, RMS roughness = 3.7 nm. . b) $Ga_{1-x}Fe_xN$ (x=0.009); 4 μm x 4 μm scan, RMS roughness = 28.4 nm

Iron, and its use in the MOCVD process, has a larger effect on the structural quality of the thin films than Mn-alloyed films grown by the same process. The reason for this may be related to an elevated growth rate used in the production of these samples. A new mass flow controller (MFC) allowed for a higher flow rate of the metallocene precursor and hence a higher overall growth rate in the $Ga_{1-x}Fe_xN$ runs as compared to the $Ga_{1-x}Mn_xN$ runs. If this affected the gas flow dynamics, it may prevent the formation of a good diffusion layer on the surface, and thus affects the incorporation and surface roughness of these films.

6.2.4 Raman Spectroscopy

Raman spectroscopy studies were performed to examine the effect of Fe incorporation on the vibrational modes of the GaN lattice. These studies were recorded at room temperature in back scattering geometry using a 488 nm laser. Figure 6.5 shows the Raman spectra between 525 cm^{-1} and 750 cm^{-1} for GaN epilayers without transition metal doping, a Mn concentration of 1.5%, and a Fe concentration of 0.7% as estimated from the growth conditions. The most prominent feature in all of these scans is the E_2(high) and A_1(LO) modes at 569 cm^{-1} and 735 cm^{-1} respectively. This indicates that there is not a significant degradation in crystalline quality with transition metal doping; the absence of a position shift of these Raman modes indicates that there is no significant strain induced by the transition metal incorporation. The A_1(LO) mode can be an indicator of free carrier concentration, as it is known to broaden and then wash out at heavy doping levels in GaN [179]. Moreover, there are no local phonon-plasmon coupled modes in the Raman spectra near the E_2(high) mode, which also points to a low carrier concentration. In contrast to Mn doping, which caused the appearance of modes at

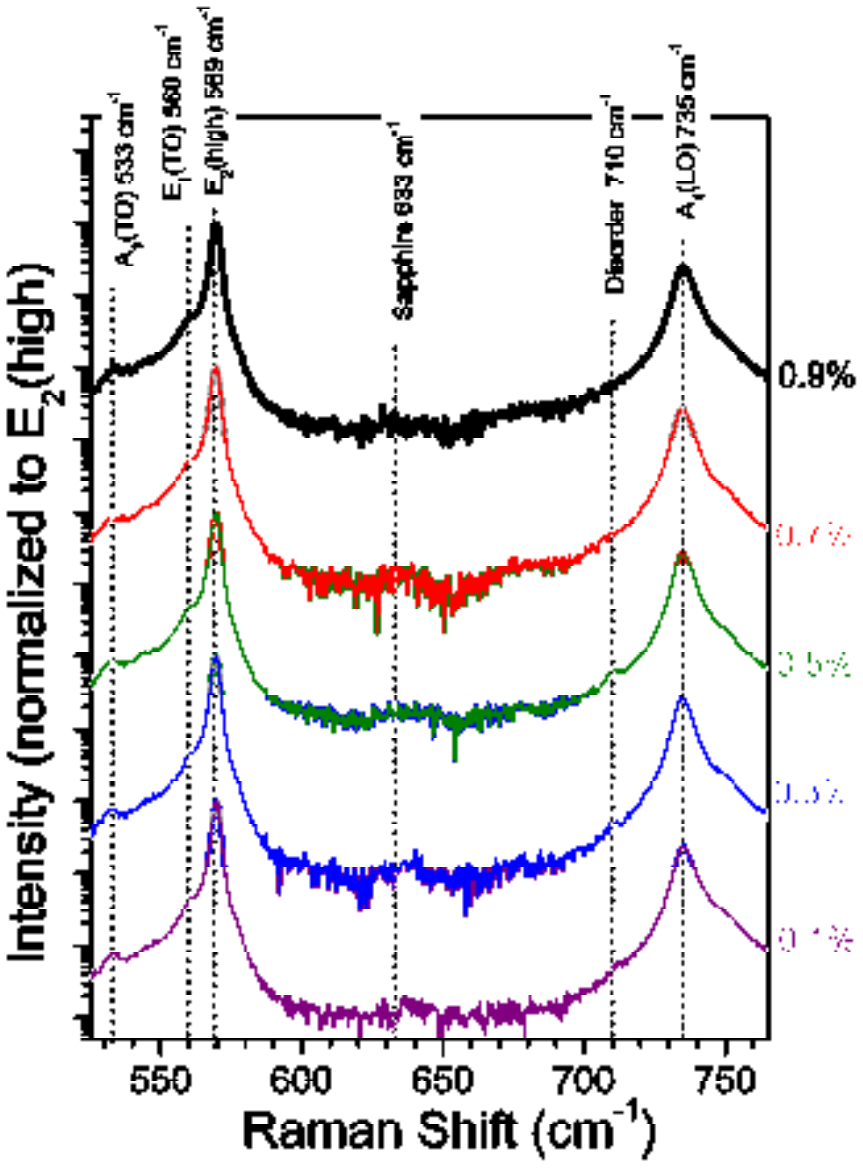

Figure 6.5 Raman spectroscopy measurements of GaN, $Ga_{0.985}Mn_{0.015}N$ and $Ga_{0.993}Fe_{0.007}N$ thin film taken with a 488 nm excitation wavelength. Note the similarity and crystalline quality with transition metal doping and the appearance of a vacancy related mode at 669 cm^{-1} in the $Ga_{1-x}Mn_xN$ sample and disorder related shoulder at 710 cm^{-1} in both materials.

669cm^{-1} and a shoulder at 664cm^{-1}, Fe doping showed no such mode at 669 cm^{-1}. Local vibrational modes (LVMs) of Fe ions on the Ga site based on the GaN E_2(high) LO mode with respect to the difference in the reduced masses might be expected around 580cm^{-1} [111]. However, no such mode was found in the $Ga_{1-x}Fe_xN$ epilayers; this again is most likely due to the dominance of the GaN E_2 (high) LO mode and a mode near 576cm^{-1} that was also seen in bare sapphire substrate, as well as the relatively low concentrations of transition metals in the Mn and Fe doped alloys.

In addition to a broad disorder related feature at 300 cm^{-1} (not shown), in both the Mn and Fe samples have an additional mode at 710 cm^{-1} which appears as a shoulder to the A_1(LO) mode. This mode increases in intensity with increased doping concentration. This mode has previously been reported in other Raman studies of transition metal doped GaN [164]. Due to its insensitivity to the nature of the dopant, it has been best attributed to a structurally induced disorder mode. In addition to the allowed c-plane GaN Raman modes, there appears an additional A_1(TO) mode and E_1(TO) mode in the $Ga_{1-x}Fe_xN$ scans. The modes are not expected for the backscattering geometry. The appearance of this mode is likely due to a relaxation of the Raman selection rules about the Fe-induced defects within the system and is consistent with the observed degradation of structural ordering in the system. Alternatively, this may be the result of some polycrystalline or disordered grains on the surface as a result of the high Mn incorporation.

6.2.5 Photoluminescence Spectroscopy

The effect of Fe incorporation was observed with photoluminescence spectroscopy (PL). Figure 6.6 shows a PL scan taken at room temperature for a moderately doped $Ga_{1-x}Fe_xN$ film; the scan is representative of other doping levels. The

a)

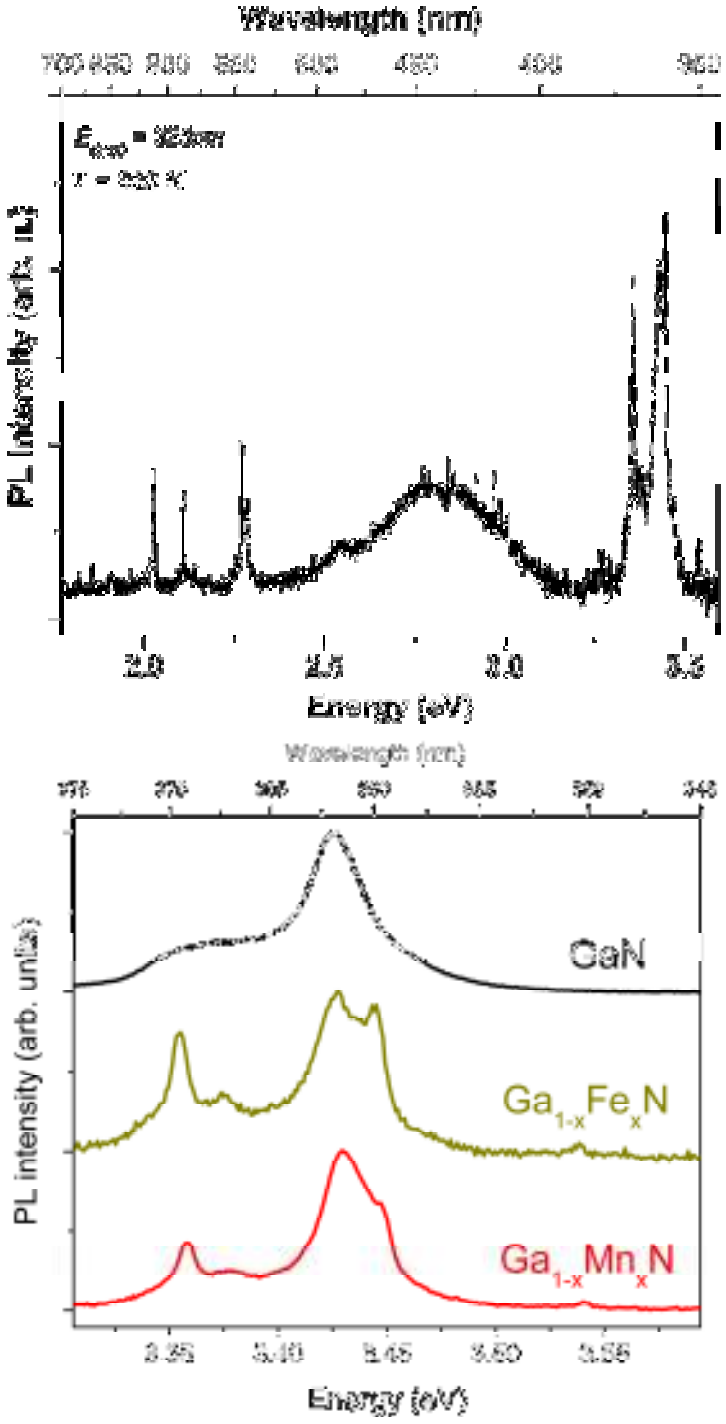

b)

Figure 6.6 PL measurement data for GaFeN layer at 0.3% doping b) Closeup of the room temperature band-edge photoluminescence response for GaN, $Ga_{1-x}Mn_xN$ (x=0.01) and $Ga_{1-x}Fe_xN$ (x=0.005).

major features in this scan are a near band edge luminescence peak and a broad blue band luminescence peak centered at 2.8 eV. The peak at 2.8 eV is outside the range of the yellow region of the visible spectra sometimes seen for intrinsic defects. This is slightly different than previous results reported for Mn where the most prominent feature is the blue emission band around 3.0 eV [112]. In some Fe doped samples, emission from a yellow band - likely due to defect centers in the GaN buffer layer - is also visible. Also present in the transition metal doped samples is a finer structure in the near band edge spectra, which is most prevalent in the Fe doped samples. Whereas the undoped GaN typically exhibits a single peak at 362 nm, the $Ga_{1-x}Fe_xN$ and $Ga_{1-x}Mn_xN$ show two distinct peaks – one at 362nm and one at approximately 360.5 nm. This may be due to either deviations in the alloying and bonding strength within the GaN layer or effects of the structural degradation caused by the incorporation of the transition metals. Note that this is not due to cubic GaN, whose formation has been previously observed by transition metal incorporation in radio frequency (RF) molecular beam epitaxy (MBE) grown $Ga_{1-x}Cr_xN$ [164].

6.2.6 Magnetization Studies

6.2.6.1 Hysteresis

Temperature-dependent SQUID magnetometry was performed on Fe-doped samples at temperatures ranging 5 K to 300 K. Figure 6.7 shows the magnetic hysteresis curves of a lightly alloyed Mn (1%) and Fe (0.7%) GaN as measured by molar flow ratio samples. All graphs have been normalized by the volume of the sample as estimated from *in situ* monitoring of the sample growth rate, time, and area. In both samples there is clear evidence of magnetic hysteresis and room temperature ferromagnetism of undetermined

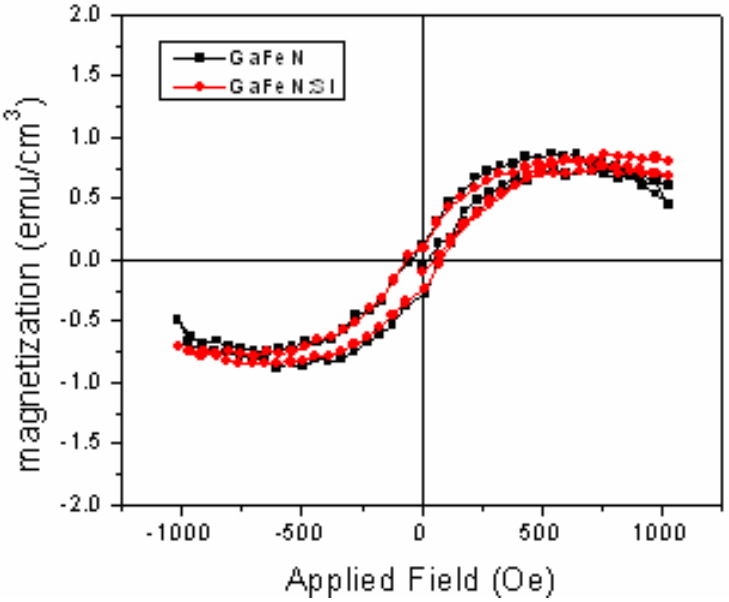

Figure 6.7 Magnetization as measured by SQUID of a) $Ga_{1-x}Mn_xN$ (x=0.01) and b) $Ga_{1-x}Fe_xN$ (x=0.003) taken at room temperature. A magnetic hysteresis is observed in both films, though the strength of the magnetization in considerably stronger in the Mn-containing films relative to the Fe containing films. Moreover, there is a strong dependence on the strength of the observed magnetization in the Mn-doped films with Si codoping at levels greater than 10^{19} cm^{-3}, which is not observed in the similarly doped Fe films.

origin. Note that ferromagnetism was achieved despite both the Fe and free hole concentration (as measured by Hall effect and Raman spectroscopy measurements) being far lower than that required by the free carrier mediated mean field theory [22]. Also shown in Figure 6.7 is the effect of high levels of Si co-doping on the magnetism as measured materials properties. With additional Si incorporation, there is no significant change in the carrier concentration in any of the samples likely due to parallel conduction through the template layer. In contrast to the structural properties, there is a large difference in the observed strength of the magnetization in these samples.

6.2.6.2 ZFC/FC Studies

The temperature dependence of the zero-field cooled and field cooled magnetization versus temperature curves (not shown) indicates that the T_C of the magnetic phase is well

above room temperature and higher is in the Mn doped samples than in the Fe doped samples. A comparison of the zero field cooled and field cooled magnetization plots at 100 Oe showed no evidence for superparamagnetic clusters as the source of the observed hysteresis. A close inspection of the zero-field cooled versus field-cooled temperature-dependent magnetization curves at the highest doping levels indeed shows a small irreversibility, which would suggest a minor contribution from ferromagnetic phase precipitates. Still, the observed strong magnetization could be a result of the improved crystalline quality of the $Ga_{1-x}Mn_xN$ films relative to the $Ga_{1-x}Fe_xN$ films, the interaction of the transition metal with the increased number of structural vacancies, or an enhanced clustering enabled by easier diffusion through the vacancy-rich Mn-alloyed materials.

6.2.6.3 Discussion and clustering analysis

The existence of ferromagnetism in the iron sample is problematic in light of the propoed double exchange-like impurity band hopping model, which fits well with the $Ga_{1-x}Mn_xN$ results presented in the last chapter. Provided that the impurity band was completely filled as would be expected from the doping conditions, there should be no pathway to stablize the ferromagnetism. It is possible that the ferromagnetic interaction therefore originates from extrinsic means. Further ZFC/FC analysis on the $Ga_{1-x}Mn_xN$ samples seems to support this observation.

An interesting behavior is observed in the films with increasing Si codoping, Figure 6.8. A pronounced superparamagnetic splitting, reminiscent of distributed sizes of magnetic nanoparticles, can be observed in the ZFC/FC curves with increasing silane molar flow rate. This observation can be understood by looking at the role of silane in both the charge state of the manganese ions and the expected behavior of a group of

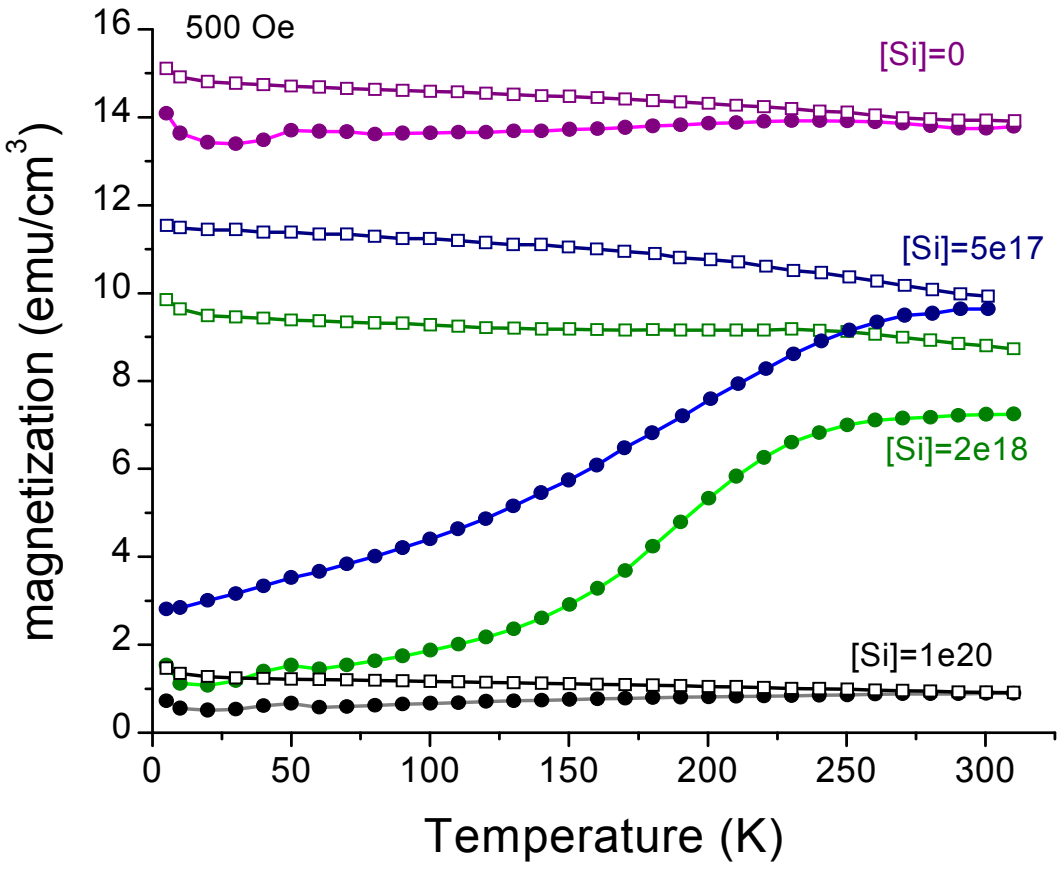

Figure 6.8 Zero field cool and field cooled magnetization versus temperature curves for $Ga_{1-x}Mn_xN$ samples with increasing silane molar flow rate. A drop in the observed magnetization and large ZFC/FC splitting is observed with intermediate codoping

magnetic nanoparticles of distributed size. The equation for the blocking temperature (T_b) of a magnetic cluster is given by equation (6.1):

$$T_b = \frac{KV}{k_b \ln\left(\tau_{\exp} / \tau_O\right)} \tag{6.1}$$

where V is particle volume, K is the anisotropy constant , τ_{exp} is the measurement time, and τ_o is the lifetime due to the natural gyromagnetic frequency of the particles. The two parameters of particular importance to the T_b of $Ga_{1-x}Mn_xN$ films are the magnetic anisotropy term and the volumetric term since the blocking temperature scales linearly with each. The magnetic anisotropy term can be particularly high for the embedded $Ga_xMn_yN_z$ particles due to the highly anisotropic nature of the polar wurtzite GaN films and 2-D surface diffusion during the growth. Combined with the volume of the particles, this could lead to blocking temperatures well above room temperature and an observed magnetic hysteresis in the films below the blocking temperature.

Silicon has two effects on the growth of MOCVD-grown films that could affect these samples. One effect is the aforementioned reduction of the Mn valence state which could result in an effective decrease in the order parameter and the inhibition of Mn-Mn interactions: this would then result in spinodal decomposition [202]. The second effect of silicon is that of an antisurfactant; it has been used as a nucleation center for the high temperature MOCVD growth of quantum dots [203]. Silicon on the GaN growth surface increases the local surface energy and acts as a nucleation site for islands; this lowers the effective diffusion length of these atoms, and hence lowers the number of Mn-Mn interactions which are necessary for the formation of the Mn-rich phase. This results in an overall decrease in the volume of the nanoparticles, which in turn leads to a greater fraction of this assembly with lower T_b. Hence, a more pronounced splitting in the ZFC/FC magnetization curves is observed.

6.2.6.4 ZFC/FC modeling for $Ga_{1-x}TM_xN$

Quantitative modeling of magnetic property curves is difficult because of fluctuations in wafer thickness, variations in doping level across the wafer, and limitations in sample size and shape measurement accuracy. Nevertheless, it is worthwhile to look qualitatively at how a modification in the various contributions to the magnetism affects the magnetic signature. In order to accomplish this, simulations were performed using a MATLAB program which plots the various contributions to the magnetic signature as a function of temperature and field. A temperature-independent, linear negative diamagnetic contribution is assumed for the substrate. The paramagnetic contribution was separated into a Curie (Mn^{2+}) and Van Vleck (Mn^{3+}) components, both of which will give a linear field response. The Curie paramagnetic component has a reciprocal temperature proportionality, whereas the Van Vleck paramagnetism was assumed to be completely temperature independent. For the ferromagnetic signal, a roughly square hysteresis loop shape was assumed with a coercivity of 70 Oe. Instead of performing a graphical solution for the molecular field theory ferromagnetic approximation, the temperature dependence of the ferromagnetism was fit to a sixth order polynomial. The influence of blocked nanoclusters was introduced by considering a linear zero field cooled temperature dependence below the blocking temperature. Three blocking temperatures (low, middle, and high) were used in these simulations.

Figure 6.9 shows a graph for what is assumed to be the atomic layout in an as-grown $Ga_{1-x}Mn_xN$ sample. The major input to the signal is the Mn^{3+} component, and lesser contributions from a ferromagnetic phase were incorporated into the model. This graph shows many of the prevailing features that are present in the observed graphs for

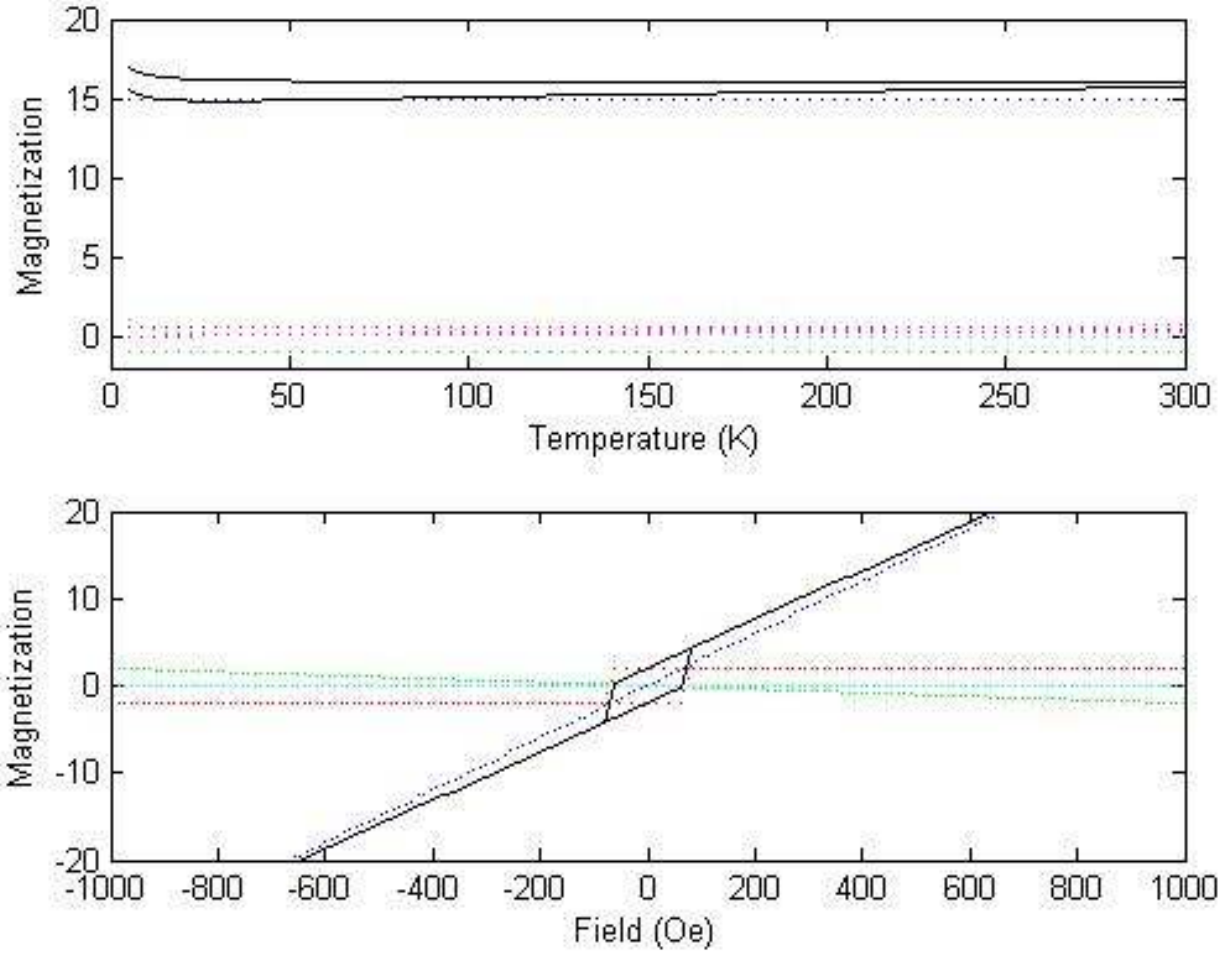

Figure 6.9 Simulated magnetization vs. temperature and field curves for $Ga_{1-x}Mn_xN$ with Mn primarily in the Mn^{3+} configuration and large or high anisotropic clusters.

the as-grown materials. The hysteresis curve exhibits a more parallelogram-shaped hysteresis curve than is typically present in magnetic materials. There is a long temperature-independent region which dominates the ZFC/FC spectrum, as well as a slight splitting in the ZFC/FC curves from the nanocluster contribution.

The effect with major silicon codoping (or alternately, changing the magnetic ion from Mn to iron) is shown in Figure 6.10. Instead of having a predominantly Van Vleck nature, the paramagnetic contribution has a Curie behavior and as such is much weaker at room temperature. This leads to a much smaller hysteresis loop, as is expected in the heavily codoped or Fe-doped samples. No change is the coercivity is observed; this is consistent with the reported magnetization data. A conversion of Mn^{3+} to Mn^{2+} (or Mn^{4+}) would result in an overall decrease in the size of the hysteretic signal, which could be interpreted as a change in the strength of the magnetization when it was really only a shift in the paramagnetic mechanism. Presumably, this would occur where it did through Si codoping; or, through attempts at carrier exchange through device layers as has been reported [69, 204].

The other predominant feature seen in the magnetization signature can also be simulated with the rudimentary approximation used in this study. Figure 6.11 shows a schematic of a simulation which demonstrates the enhanced splitting in the ZFC/FC plots, as was observed with intermediate Si codoping. In order to reproduce this signal, the Van Vleck contribution was reduced slightly. In addition, the contribution from nanocrystals with low blocking temperatures was enhanced to give a more pronounced splitting. This would be expected for smaller clusters that might form as a result of a Si-induced reduction in the surface carrier diffusion length.

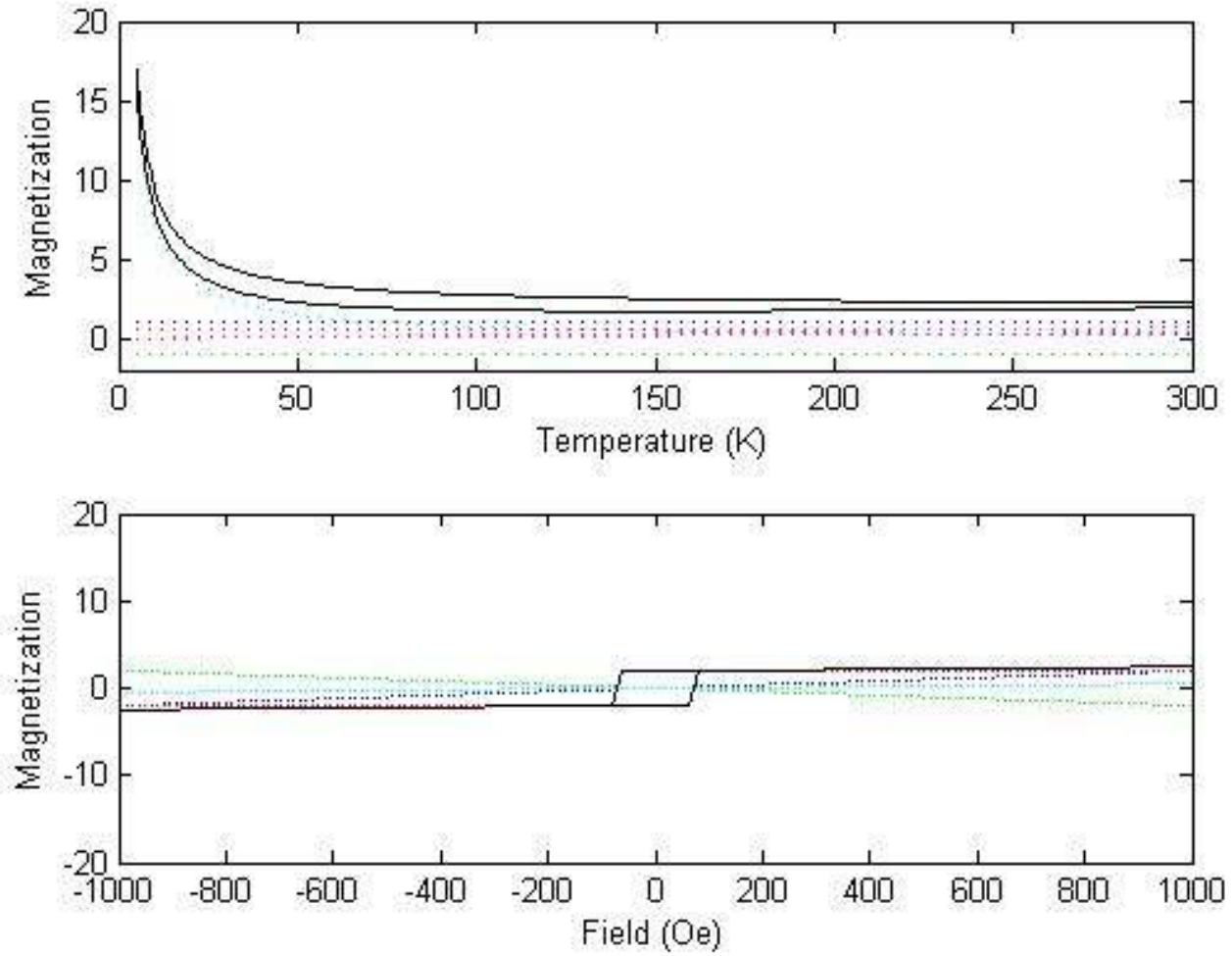

Figure 6.10 Simulated magnetization vs. temperature and field curves for $Ga_{1-x}Mn_xN$ with Mn primarily in the Mn^{2+} configuration.

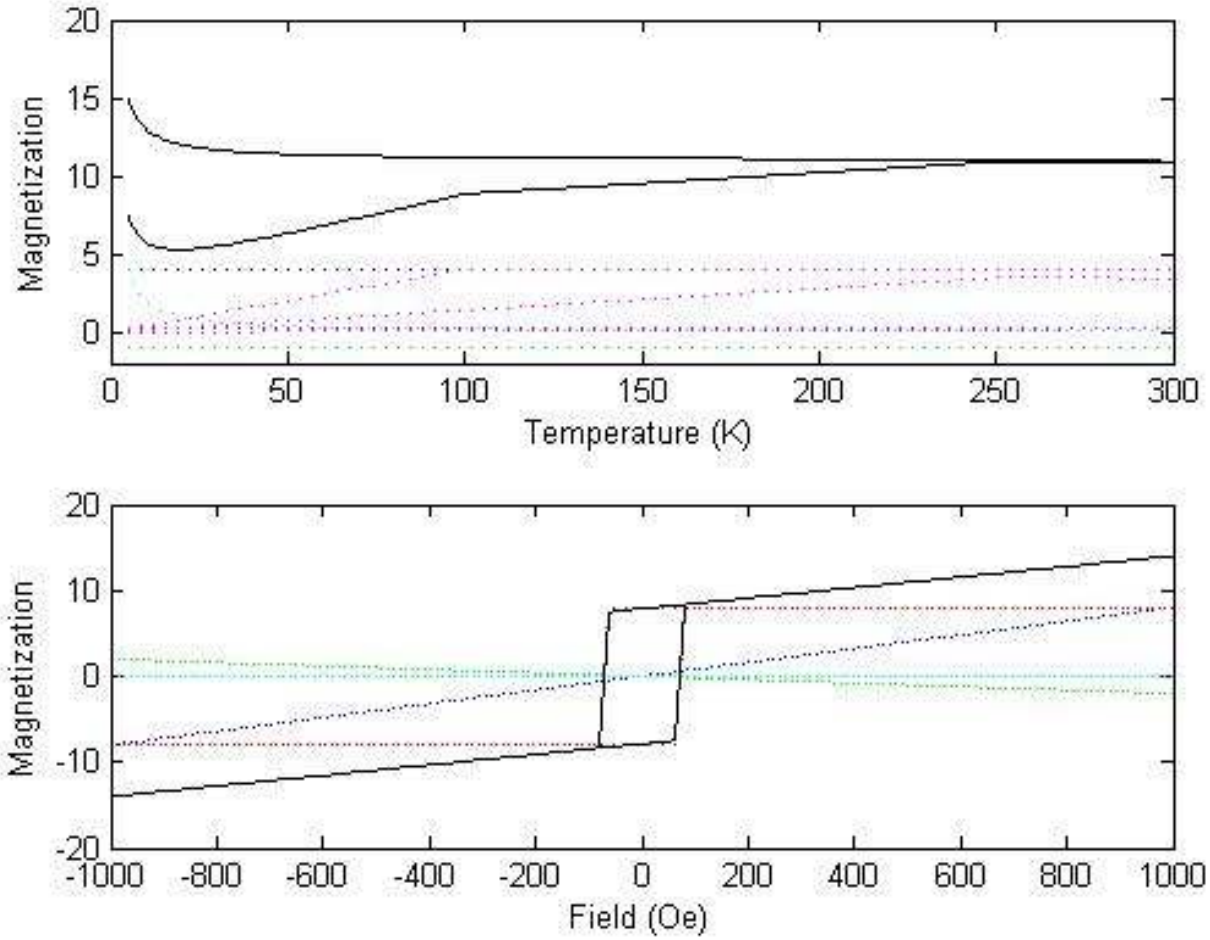

Figure 6.11 Simulated magnetization vs. temperature for $Ga_{1-x}Mn_xN$ with acontribution from smaller or less anisotropic clusters.

It is interesting to note that all of the major features seen in the magnetization studies can be replicated with this relatively simple analysis. It is apparent that the magnetization strength can be adjusted through a conversion between divalent and trivalent Mn states, which only affects the relative paramagnetic contributions to the signal. The large splitting in the ZFC/FC curves is indicative of a change in the nanocluster morphology that leads to a lower blocking temperature. Additionally, comparing the existing literature results for intentionally phase segregated samples, the large splitting is typical for intentionally overdoped and phase segregated samples [205]. On the other hand, $Ga_{1-x}Mn_xAs$ which has been grown via low temperature molecular beam epitaxy shows a more classical magnetization versus temperature curve. This classical magnetization versus temperature curve is also seen in $Ga_{1-x}Mn_xN$ when grown by low temperature MBE, with a Curie temperature of 8 K [58] as would predicted by Monte Carlo simulations to the double exchange model [206]. This provides further support for the idea that dilute $Ga_{1-x}Mn_xN$ is a low temperature ferromagnetic semiconductor, and that high temperature ferromagnetism can be realized through short-range ordering found in Mn rich regions.

6.2.6.5 Nanospinodal decomposition in $Ga_{1-x}TM_xN$

Efforts have been made via first principles studies to reconcile with theory the observed high temperature ferromagnetism that is often reported in these materials [207]. The pair interaction strength between substitutional Mn atoms was calculated using the same framework as the Curie temperature determination. The overall result is a tendency for Mn atoms to assemble together because adjacent Mn atoms in the crystal have an overall energy lower than that of dispersed Mn pairs. Because there is a similarity in metallic alloy solid solutions which possess a strength thermodynamic driving force for

like atoms to assemble together, this is termed a local "nanospinodal decomposition". The overall tendency towards phase separation in these materials is well-established: in $Ga_{1-x}Mn_xAs$ the formation of MnAs nanoparticles at elevated growth temperatures or beyond the solubility limit has been reported by numerous researchers [208, 209]. It is argued that through a series of 3-dimensional diffusion steps, the binary III-Mn-V alloys would segregate into interconnected networks of Mn-V and III-V regions. A calculation of the strength of the Mn-Mn interaction parameter in the III-V materials [207] shows that it is several times stronger in GaN than in GaAs (30 mRy versus 4 mRy at 5 at% Mn), whence the thermodynamic tendency towards local clustering should be even stronger in the wide-bandgap materials. If this is the case, then in order to minimize clustering, $Ga_{1-x}Mn_xN$ growth must proceed at conditions far from equilibrium – even moreso than for $Ga_{1-x}Mn_xAs$. Thus, at the near normal growth temperatures that are typically reported, it is probable that some degree of phase segregation cannot be avoided.

6.3 Initial device studies

The ultimate utility of this materials system will not be determined simply by its materials properties; eventually realization of new devices based on this new materials system must be achieved. Thus, it was essential in this study to explore preliminary devices as a building block for more complicated device structures. These results can further be expanded into future devices based on the transition metal doped nitrides.

6.3.1 Mn-containing light emitting diodes

GaN-based p-i-n structures with Mn integrated into the intrinsic region have been grown to investigate further the fundamental properties of $Ga_{1-x}Mn_xN$ layers within GaN-

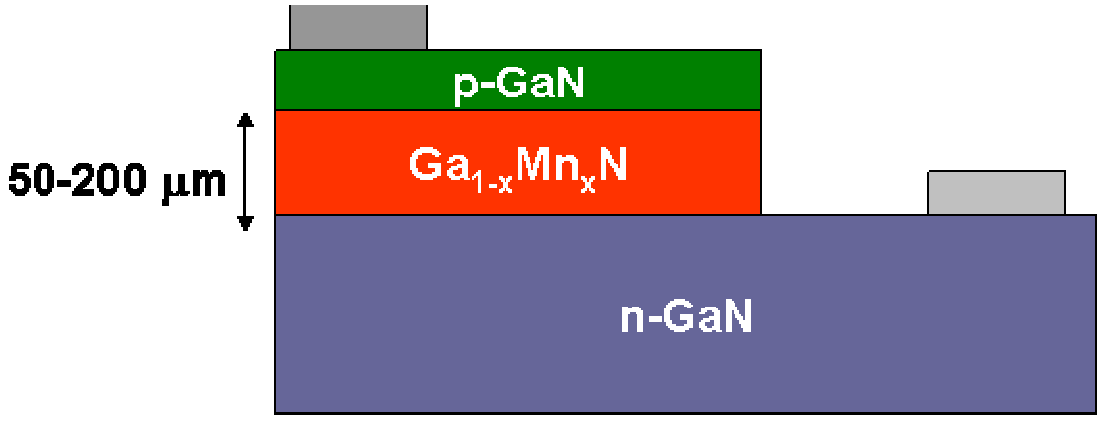

Figure 6.12 Schematic of $Ga_{1-x}Mn_xN$ p-i-n structures used to study the role of Mn incorporation into devices

based structures. $Ga_{1-x}Mn_xN$ layers at approximately 1% Mn doping level were grown on n-doped GaN layers and were subsequently capped p-type layers of approximately 200 nm. The Mn thickness was varied between 50nm and 200nm in order to investigate the effect of the thickness of the region on the behavior, as shown in Figure 6.12. The devices were then fabricated into diode structures using standard GaN LED processing techniques. I-V characteristics of the device structures clearly show rectifying behavior in the Mn p-i-n structures, as shown via the light and dark curves in Figure 6.13. With increasing Mn thickness, the turn-on voltage and resistance of the devices increases, as would be expected from the highly resistive nature of the centers. Figure 6.14 shows the electroluminescence (EL) behavior of a sample device. The EL spectrum is dominated by two peaks. The first one, at 3.4 eV, is due to the bandedge recombination; the second of approximately equal in magnitude, at around 2.1 eV, is due to Mn-induced defect-related emissions. A similar emission spectrum has recently been reported in $Al_{1-x}Mn_xN$ devices [210]. It is unclear whether this recombination is truly related to Mn recombination in the intrinsic region of the device, or whether it is due to recombination of electrons and holes

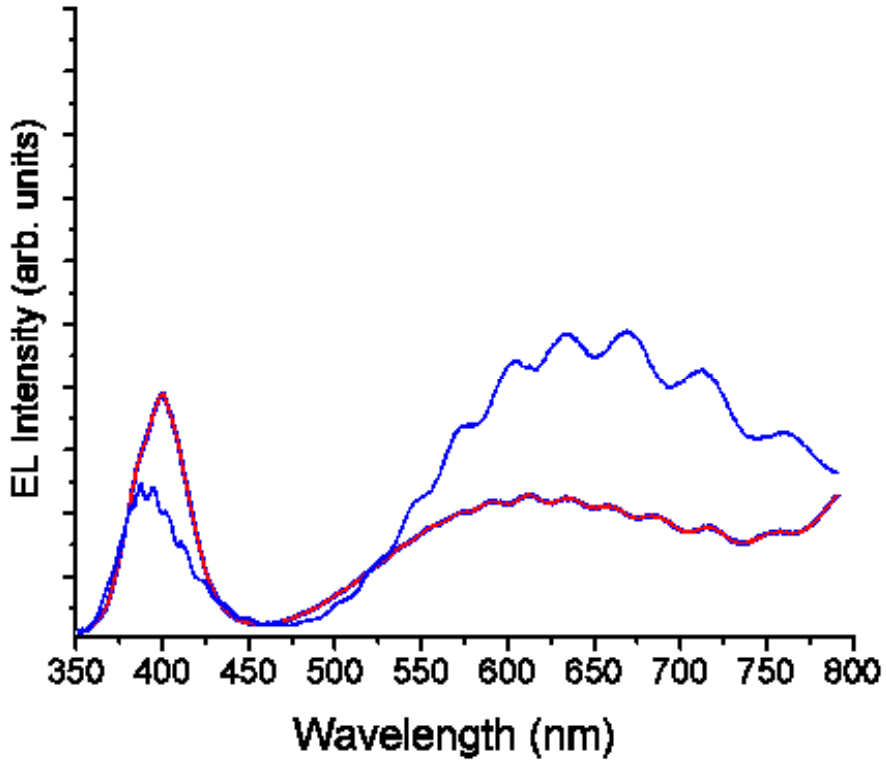

Figure 6.13 Electroluminesce behavior of GaN LED's with a Mn-containing active region

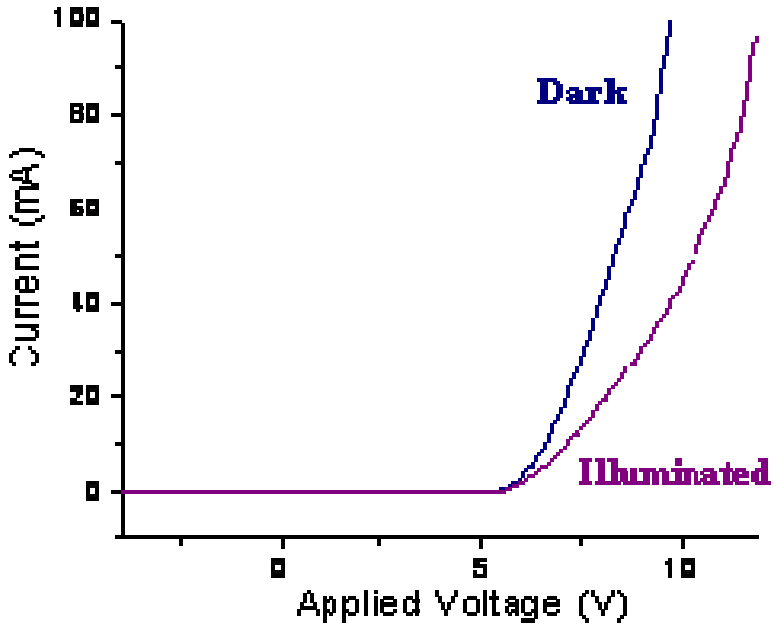

Figure 6.14 Illuminated and dark I-V characteristics of a sample p-i-n structure

with sufficient energy to transit the highly Mn-doped region that recombine in the GaN region. The intensity of the near-bandedge emission is several orders of magnitude lower in the transition metal doped p-i-n device than it would be in a GaN p-i-n LED structure, and visibly, the Mn-containing emitters are more of a yellow-orange rather than blue in color. With increasing thickness of the Mn, the area of light emission decreases consistent with a higher spreading resistance in the device with the thicker Mn layer. In fact, the lifetime of some of these devices was observed to be very short (on the order of a few seconds to a minutes), due to thermal management problems with the devices as-grown on sapphire substrates. No polarization was observed in the light output of these devices.

6.3.2 Magnetic Circular Dichroism

One method for determining the band structure of these dilute magnetic semiconductors is to use magnetic circular dichroism studies. By probing the difference between left- and right-circularly polarized absorption and through the use of optical selection rules, it is possible to analyze the spin split nature of the band structure in these materials system. It is also possible to analyze the exchange interactions via this method, and to determine if this interaction is ferromagnetic or paramagnetic through a field dependent measurement of the MCD. This differential absorption feature may also be important for device applications based on these materials.

Preliminary MCD measurements have been performed via the modulation method using a 50 KHz Hinds photoeleastic modulator (PEM). Figure 6.15 shows an (uncalibrated) MCD spectrum which compares the differential MCD signals for a $Ga_{1-x}Mn_xN$ sample taken at room temperature in a field of 0.1 T. In the region around

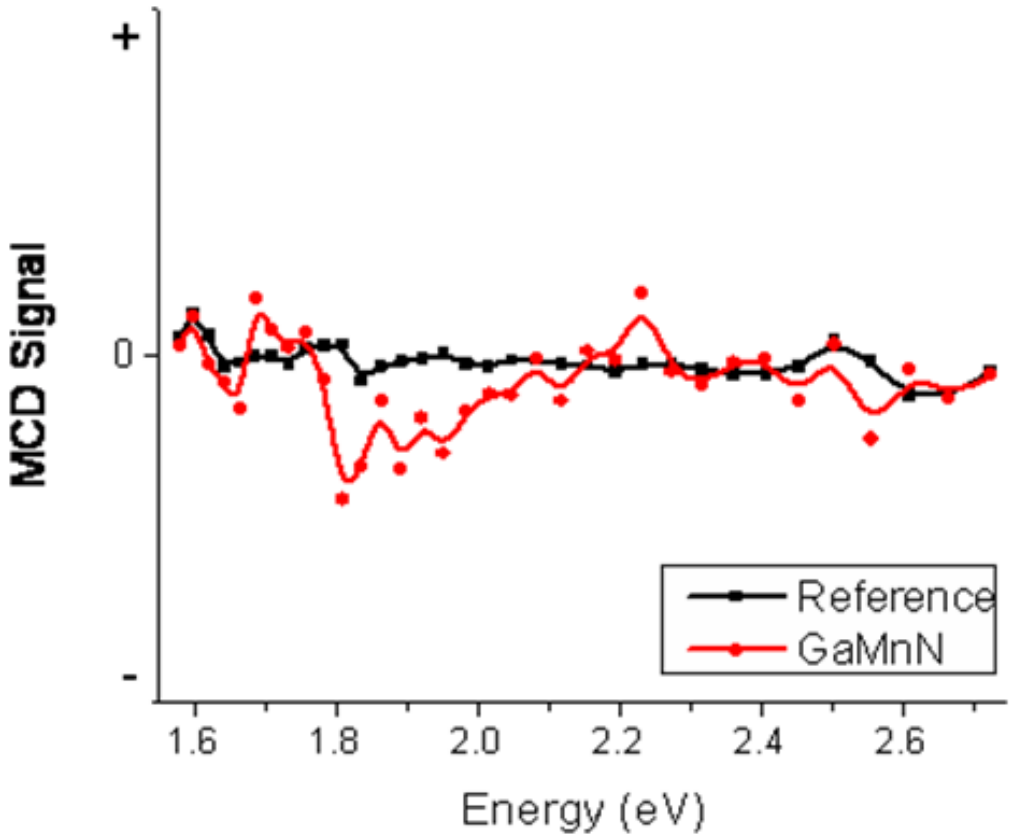

Figure 6.15 Magnetic circular dischroism signal at room temperature from a $Ga_{1-x}Mn_xN$ layer

1.8 eV, there appears to be a slight dip in the MCD spectrum, which could be an indication of a magnetic band-structure related contribution to the MCD signal. Note that this is not near the band edge as is typically observed for $Ga_{1-x}Mn_xAs$ [211]. Though this result is somewhat preliminary, these results are similar to MCD measurements reported in MBE-grown $Ga_{1-x}Mn_xN$ [116], where a MCD signature near 1.9 eV was attributed to an unknown secondary phase. More detailed and precise measurements, as well as a comparison with the MCD signals of known competing phases, will be essential to the future understanding of the physics of this materials system in the future and the development devices based on this magnetic circular dichroism behavior.

6.3.3 Optically induced magnetization

Another feature of $Ga_{1-x}Mn_xAs$ which has not been observed to date in $Ga_{1-x}Mn_xN$ is optically induced magnetization effects. By controlling the polarization of light near the band edge in $Ga_{1-x}Mn_xAs$, carriers can be excited in sufficient quantities to result in an observed FM signal [212]. Because of the deeper nature of the d-state related impurity band in $Ga_{1-x}Mn_xN$, optically induced magnetization will take on a different character. In order to study effects of a population of the band, VSM measurements were taken before and during excitation with the unfiltered, unpolarized light of an ultraviolet lamp, as shown in Figure 6.16. After illumination under the UV light, a rise in the measured magnetization can be seen. The effect is slight; less than 0.5% of the total

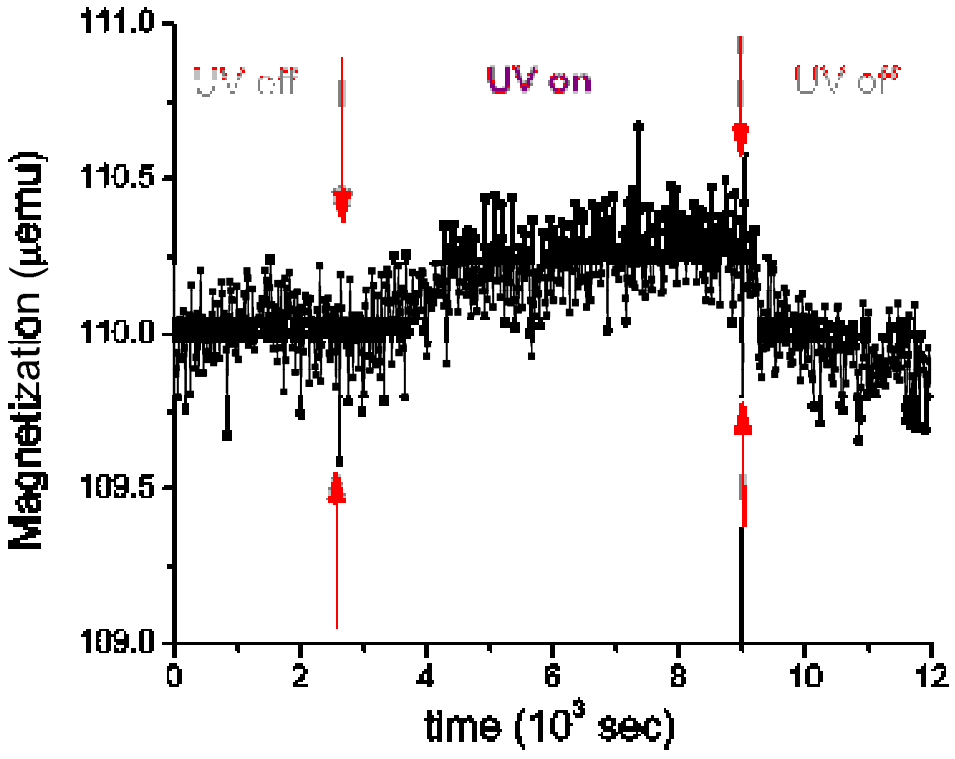

Figure 6.16 Measured VSM signal from a $Ga_{1-x}Mn_xN$ layer with and without ultraviolet illumination

magnetic signal (as would be expected from the relative intensity of the source relative to the population of the traps), but above the inherent noise of the measurement. Also, it is reversible with the illumination is removed. Further investigations should explore the spectral, radiant intensity, and polarization dependence of this phenomenon, and attempt to eliminate the possibility of any contribution from charging, heating, or other potential measurement-dependent effects. If a correlation between the polarization and strength of this signal can be understood, it might open up new avenues towards combined magneto-optical devices in the future.

CHAPTER 7

CONCLUSIONS AND FUTURE WORK

7.1 Conclusions

This work focused on the exploration of two materials systems, transition metal-doped ZnO and GaN, that theoretically showed promise towards the development of room temperature semiconductor spintronic applications. Through the development of growth techniques capable of producing high-quality material, numerous things were learned about these two materials systems. The results of this research demonstrate that the initial optimism over ferromagnetism in these materials may have been somewhat misguided, as many of the conditions needed to realize ferromagnetic ordering from the dilute semiconductor via the theoretical models are not achievable in these materials systems. Nevertheless, vital information was learned about these materials that may render them, or at least their derivatives, useful for future applications in the field of spintronics.

The initial studies focused on the characterization of bulk nominal-single crystals of ZnO. This bulk growth technique was particularly suitable for elucidating the true properties of this materials system because thermodynamics supports the alloy-level substitution of these elements on lattice sites. It can completely eliminate contributions from grain boundary effects and interfacial effects from the substrate. In this study, we have demonstrated that bulk melt-growth is a suitable technique for the introduction of transition metals on the lattice site in ZnO. X-ray diffraction reveals that, within limits,

the as-grown samples or oriented bulk single crystals have no gross indications of second phase formation up to an alloying concentration of 5%. The divalent substitution was revealed by the distinct color of the individual single crystals – red for Mn, yellow for Fe, and green for Co. UV visible transmission indicates the individual d-d transitions which cause the absorptions leading to these colors. Raman spectroscopy was performed on the sample and confirms the single-crystal nature of the bulk samples. The introduction of the alloying elements in these samples has a significant contribution to the appearance of silent modes in the Raman spectra due to local site disorder. Cobalt substitution has less of an effect on the overall crystalline quality, as evidenced by the XRD and Raman studies. Electron paramagnetic resonance also shows that substitutional divalent transition metals on the lattice site are present in both cases. Consistent with the Raman and XRD diffraction measurements, there is also the presence of a signal related to some imperfections in the material.

Magnetization revealed clearly and unequivocally that the ZnO based materials were not intrinsically ferromagnetic in the case of divalent substitution in the single crystal samples. All of the transition metals showed paramagnetic ordering at temperatures from 5 K to 300 K which scaled with the transition metal concentration. Through an analysis of the dependence of the magnetization on temperature, the predominant exchange mechanism was revealed to be antiferromagnetic superexchange. Magnetic hysteresis was observed in some single crystals; this phenomenon was limited to crystals produced via ion implantation or cases where the crystal was of reduced quality or possessed low-angle grain boundaries. These samples also showed evidence of small magnetic clusters in ZFC/FC magnetization scans. Thus, through the careful

development and analysis of this materials system, the true properties of the homogeneous alloy system were revealed. The observed ferromagnetism in these samples is likely due to a combination of impurity phases or an interaction with defects in the ZnO system that can stabilize the room temperature hysteretic signal.

GaN thin films doped with transition metals were also explored in this dissertation. Here, metalorganic chemical vapor deposition was demonstrated to be a suitable technique for the growth of these transition metal doped III-nitrides. Crystalline quality was observed to be similar to that for MOCVD-grown intrinsic GaN under the same conditions, as observed via atomic force microscopy and X-ray diffraction. Lattice site occupancy of the transition metal dopant was confirmed via electron paramagnetic resonance and optical transmission studies. In $Ga_{1-x}Mn_xN$, it was shown that Mn acts as a deep acceptor. Valence state control of the Mn atoms between the trivalent and divalent state was shown to be possible through the introduction of intentional codopants. A corresponding change in the optical, EPR, and magnetization signals was observed with silicon codoping. The introduction of alloying concentrations of Mn also introduced a significant amount of defect compensation into the material. Raman studies suggest that the formation of nitrogen vacancy related complexes increases with increasing Mn incorporation. This assignment is supported by an observed decrease in the thermal stability of the films.

In order to develop spintronic devices based on these materials systems, it is desirable to have an intrinsic origin for the room temperature ferromagnetism. Magnetization studies indicate the presence of a room temperature ferromagnetic contribution to the hysteresis curves. The strength of this magnetic signal, but not the

coercive field, appeared to be closely correlated to the presence of Mn^{3+} in the optical data, whereas a strong Mn^{2+} contribution leads to a much weaker ferromagnetism. This would be consistent with an impurity band model for ferromagnetism. To investigate this hypothesis, $Ga_{1-x}Fe_xN$ which do not have the same impurity band hopping pathway were grown. Nevertheless, room temperature ferromagnetism was also observed in the iron-doped samples. Additionally, the Mn-doped samples showed a strong irreversibility in the ZFC/FC curves with Si codoping, which is more consistent with a nanoclustering behavior as opposed to a homogeneous alloy behavior. Qualitative magnetization curve modeling suggests that the observed signal is consistent with a magnetic contribution from small TM-rich magnetic clustering regions, combined with a paramagnetic magnetization signal from isolated substitutional transition metal atoms. The apparent increase in the magnetization signal with codoping results from the conversion of transition metal ions from a Curie paramagnetic configuration to a temperature-independent Van Vleck parmagnetic configuration. These results are also consistent with homogeneous $Ga_{1-x}Mn_xN$ alloys grown by other methods exhibiting low temperature ferromagnetism (<30 K), as would be expected from the first principles calculations.

7.2 Future Directions

Though much had already been explored regarding the transition metal doped III-nitrides and zinc oxide, a considerable amount of scientific understanding and engineering capability can be gained from a further study of these materials. In particular, aspects related to role of defects in ZnO in the materials are not well understood. Further investigations might lead to a better understanding of these interfacial ferromagnetic interactions and see if it is possible to exploit this unusual scientific phenomenon for

spin-based devices. There have also been reports of unusual room temperature ferromagnetic behavior in Gd-doped GaN and ZnO samples. Though the ZFC/FC curves in these Gd samples is more consistent with clustered $Ga_{1-x}Mn_xAs$ and $Ga_{1-x}Mn_xN$ samples, the origin of the ferromagnetic interaction is not well understood. In addition, the theoretic predictions of spin-crossover, particularly optically-induced spin crossover, in the III-N might provide a new approach towards optically controlled magnetic devices. This work has also demonstrated that the MOCVVD growth route can be used to produce embedded magnetic phases within the GaN system. If the nature of these magnetic phases can be understood and control of these metstable embedded phases can be engineered within the growth process, it could enable the development of other novel device architectures as described below. Based on the nature of ferromagnetism that has been shown for the wide bandgap semiconductors, it is clear that different routes must be explored towards implementation than in traditional spin electronic devices.

7.2.1 Polarized emitters and detectors

One of the preliminary devices that previously been demonstrated in the GaAs system, and which has not been seen in the III-nitrides is that of the circular polarized light emitting diode. In $Ga_{1-x}Mn_xAs$, this is truly a spin-based device, where spin injection of polarized carriers from a semiconductor layer results in a polarized output. The case of the nitrides will not necessarily fit into this standard paradigm: the magnetic ordering mechanism in these materials appears to be considerably different, and likely has a strong contribution from Mn-rich clusters. In order to develop polarized emitters and spin polarized detectors from this materials systems, it may be possible to employ alternate routes for spin polarized emitters and detectors.

Figure 7.1 shows a diagram of some sample structures that can be used to test the feasibility of polarization-based devices. In these devices, the principle of operation is not to take advantage of the spin injection capabilities. The feature may not be observable in the III-nitride DMS materials based on the relatively large resistance mismatch between the two systems. However, there is a known magnetic circular dichroism signal in the $Ga_{1-x}Mn_xN$ system near the middle of the bandgap. If the source of this MCD signal can be identified, it may be possible to construct monolithic light emitting diode structures with emissions resonant with this MCD signal. By passing the unpolarized absorption through the $Ga_{1-x}Mn_xN$ layer, a circularly polarized output could be detected. Distributed Bragg reflectors can be embedded within this structure to increase the probability of a circularly polarized absorption and lead to an overall polarization in the output spectrum. In reverse bias, these devices might be used for polarization sensitive detectors for quantum information technology.

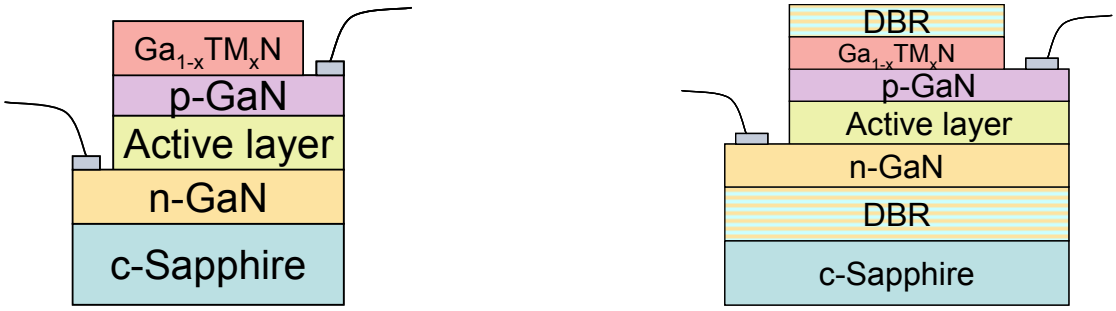

Figure 7.1 Schemating of light emitting diode or photodetector structures that take advantage of magnetic circular dichroism features observed in $Ga_{1-x}TM_xN$

7.2.2 Magnetic memory elements

The integration of magnetic and semiconductor functionality within a single package has long been a goal of the burgeoning field of spintronics. This research in dilute magnetic semiconductors has produced an exciting tangential result: a strong Mn-Mn self-interaction energy stabilizes Mn-rich atomic configurations, resulting in compositional fluctuations and phase segregation. This stabilization of commensurate metastable magnetic phases within the semiconductor lattice provides an avenue for the development of entirely new paradigms for multifunctional devices. This could be exploited for the MOCVD growth of regular arrays of high density embedded magnetic nanoparticle-semiconductor composites which are suitable for several applications, including ultra-

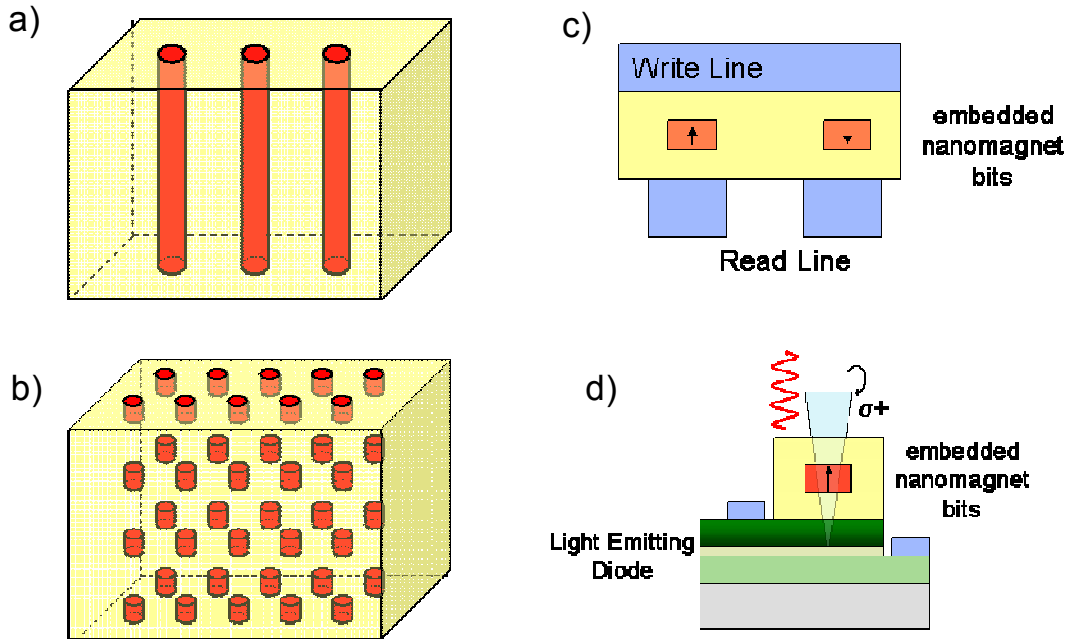

Figure 7.2: a) Nanopillar arrangement of embedded ferromagnetic MnN columns in GaN matrix b) Embedded dot-like array of MnN (red) in GaN (yellow) nanocomposite. These could be incorporated in the future into integrated high density data storage devices with c) electrical, d) optical, or magnetic force (not shown) readout

high-density data storage. Routes to explore the regular arrays of embedded magnetic nanostructures as the building block for memory elements could be developed through the seeding of substrates with ion implantation techniques. Figure 7.2 shows some conception embedded cluster arrangements and devices based on this materials system.

In epitaxial thin film growth processes, the bulk diffusion simulation and modeling approach does not work well, since growth proceeds by a layer-by-layer process. As such, three-dimensional diffusion is much slower - typically 3-4 orders of magnitude - than two-dimensional surface diffusion. In order to develop a more realistic model for what occurs during the growth process, another Monte Carlo simulation technique was developed, which accounts for layer-by-layer growth [213]. Randomly distributed Mn and Ga atomic fluxes are incident on the surface, which then diffuse to form two dimensional clusters before the next layer is added. Provided there is a strong enough interaction between the buried layers and the surface layers, the Monte Carlo simulation predicts the formation of a pillar-like "Konbu" phase, as shown in Figure 7.3.

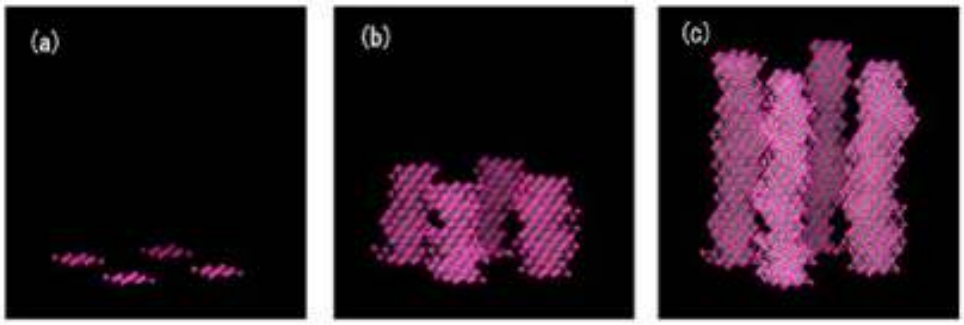

Figure 7.3: Predicted Mn-distribution via Monte Carlo simulations of the layer-by-layer growth of a III-Mn-V semiconductor. Note that if the appropriate Mn-rich patterned template is used (figure a), the Mn rich phases is predicted to align in vertical columns. From [215].

Such a periodic arrangement of embedded magnetic nanostructures would be useful for a number of applications, such as magnetic sensing elements, or by controlling the growth parameters to produce a 3-D array of structures that could be useful ultra-high density (>terabit/in^2) magnetic memories [213]. Moreover, similar nanopillar shapes in Si-Ge alloys have resulted in a strong magnetoelectric coupling between semiconductor carriers and the magnetic features [214]. This could form the basis of carrier-controlled spintronic devices.

7.3 Closing Statement

Wide bandgap dilute magnetic semiconductors were thought to be promising materials for next generation spin electronic devices. Through a careful study and development of $Zn_{1-x}Mn_xO$ and $Ga_{1-x}TM_xN$, this work has shown that the traditional paradigms available in more well-established DMS are not necessarily applicable and some of the assumptions used to predict room temperatre ferromagnetism in this system do not necessarily hold. New and exciting properties of this materials system were discovered, however, suggesting that these materials are still a promising resource for future materials science and engineering studies.

REFERENCES

[1] G. R. Moore, "Cramming more components onto integrated circuits," *Electronics*, vol. 38, 1965.

[2] G. K. Teal, "Single crystals of germanium and silicon-basic to the transistor and integrated circuit," *IEEE Transactions on Electron Devices*, vol. ED-23, pp. 621, 1976.

[3] H. Akinaga and H. Ohno, "Semiconductor Spintronics," *Nanotechnology, IEEE Transactions on*, vol. 1, pp. 19-31, 2002.

[4] J. Newey, "Spintronics holds promise for more efficient devices," *Compound Semiconductor*, vol. 10, pp. 23, 2004.

[5] S. A. Chambers and Y. K. Yoo, "New materials for spintronics," *MRS Bulletin*, vol. 28, pp. 706, 2003.

[6] J. Rudolph, D. Haegele, H. M. Gibbs, G. Khitrova, and M. Oestreich, "Laser threshold reduction in a spintonic device," *Applied Physics Letters*, vol. 82, pp. 4516-4518, 2003.

[7] R. G. Mani, W.B. Johnson, and V. Narayanamurti, "Nuclear spin based quantum information processing at high magnetic fields," *Nanotechnology*, vol. 14, pp. 515 - 522, 2003.

[8] R. G. Mani, W.B. Johnson, V. Narayanamurtia, V. Privmanc, Y-H. Zhang, "Nuclear spin based memory and logic in quantum Hall semiconductor nanostructures for quantum computing applications," *Physica*, vol. 12, pp. 152-156, 2002.

[9] C. H. Smith, "Commercial Applications of Spintronics Technology," presented at Nanomaterials 2004, 2004.

[10] Y. Ohno, D. K. Young, B. Beschoten, F. Matsukura, H. Ohno, and D. D. Awschalom, "Electrical spin injection in a ferromagnetic semiconductor heterostructure," *Nature*, vol. 402, pp. 790-792, 1999.

[11] B. L. Liu, M. Senes, S. Couderc, J. F. Bobo, X. Marie, T. Amand, C. Fontaine, and A. Arnoult, "Optical and electrical spin injection in spin-LED," *Physica E*, vol. 17, pp. 358-360, 2003.

[12] A. E. Turner, R. L. Gunshor, and S. Datta, "New class of materials for optical isolators," *Applied Optics*, vol. 22, pp. 3252, 1988.

[13] S. Datta and B. Das, "Electronic Analog of the Electro-optic Modulator," *Applied Physics Letters*, vol. 56, pp. 665-667, 1990.

[14] M. N. Baibich, J. M. Broto, A. Fert, F. Nguyen Van Dau, F. Petroff, P. Eitenne, G. Creuzet, A. Friedrich, and J. Chazelas, "Giant Magnetoresistance of (001)Fe/(001)Cr Magnetic Superlattices," *Phys. Rev. Lett.*, vol. 61, pp. 2472 - 2475, 1988.

[15] G. Binasch, P. Grunberg, F. Saurenbach, and W. Zinn, "Enhanced magnetoresistance in layered magnetic structures with antiferromagnetic interlayer exchange," *Phys. Rev. B*, vol. 39, pp. 4828 - 4830, 1989.

[16] G. Schmidt, D. Ferrand, L. W. Molenkamp, A. T. Filip, and B. J. van Wees, "Fundamental obstacle for electrical spin injection from a ferromagnetic metal into a diffusive semiconductor," *Physical Review B*, vol. 62, pp. R4790, 2000.

[17] M. Johnson and R. H. Silsbee, "Thermodynamic analysis of interfacial transport and of the thermomagnetoelectric system," *Physical Review B*, vol. 35, pp. 4959-4972, 1987.

[18] B. T. Jonker, S. C. Erwin, A. Petrou, and A. G. Petukhov, "Electrical spin injection and transport in semiconductor spintronic devices," *MRS Bulletin*, vol. 28, pp. 740, 2003.

[19] M. van Schilfgaarde and O. N. Myrasov, "Anomalous exchange interactions in III-V dilute magnetic semiconductors," *Physical Review B*, vol. 63, pp. 233205, 2001.

[20] T. Dietl and H. Ohno, "Ferromagnetic III-V and II-VI semiconductors," *MRS Bulletin*, vol. 28, pp. 714, 2003.

[21] S. von Molnar and D. Read, "Magneto-transport in magnetic compound semiconductors and metals," *Journal of Magnetism and Magnetic Materials*, vol. 242-245, pp. 13-20, 2002.

[22] T. Dietl, H. Ohno, F. Matsukura, J. Cibert, and D. Ferrand, "Zener Model Description of Ferromagnetism in Zinc-Blende Magnetic Semiconductors," *Science*, vol. 287, pp. 1019-1022, 2000.

[23] S. J. Pearton, C. R. Abernathy, M. E. Overberg, G. T. Thaler, and D. P. Norton, "Wide bandgap ferromagnetic semiconductors and oxides," *Journal of Applied Physics*, vol. 93, pp. 1-11, 2003.

[24] T. Dietl, "Nitrides as spintronic materials," *Physica Status Solidi B*, vol. 240, pp. 433-439, 2003.

[25] S. A. Wolf, D. D. Awschalom, R. A. Buhrman, J. M. Daughton, S. von Molnar, M. L. Roukes, A. Y. Chtchelkanova, and D. Treger, "Spintronics, A Spin-Based Electronics Vision for the Future," *Science*, vol. 294, pp. 1488-1495, 2001.

[26] D. Loss and D. P. DiVincenzo, "Quantum computation with quantum dots," *Physical Review A*, vol. 57, pp. 120, 1998.

[27] S. L. Chuang, *Physics of Optoelectronic Devices*: Wiley-Interscience, 1995.

[28] D. P. DiVincenzo, "Quantum Computation," *Science*, vol. 270, pp. 255-261, 1995.

[29] D. P. DiVincenzo, "Spins for Quantum Information Processing," in *Semiconductor Spintronics and Quantum Computation*, D. D. Awschalom, D. Loss, and N. Samarth, Eds. Berlin: Springer-Verlag, 2002, pp. 311.

[30] S. Ghosh and P. Bhattacharya, "Surface-emitting spin-polarized In0.4Ga0.6As/GaAs quantum-dot light-emitting diode," *Applied Physics Letters*, vol. 80, pp. 658-660, 2002.

[31] Y. Chye, M. E. White, E. Johnston-Halperin, B. D. Gerardot, D. D. Awschalom, and P. M. Petroff, "Spin injection from (Ga,Mn)As into InAs quantum dots," *Physical Review B*, vol. 66, pp. 201301, 2002.

[32] X. Y. Cui, B. Delley, A. J. Freeman, and C. Stampfl, "Magnetic metastability in tetrahedrally bonded magnetic III-nitride semiconductors," *Physical Review Letters*, vol. 97, pp. 016402, 2006.

[33] B. T. Jonker, A. T. Hanbicki, Y. D. Park, G. Itskos, M. Furis, G. Kioseoglou, A. Petrou, and X. Wei, "Quantifying electrical spin injection: component-resolved electroluminescence from spin-polarized light emitting diodes," *Applied Physics Letters*, vol. 79, pp. 3098-3100, 2001.

[34] A. Mauger and C. Godart, "The magnetic, optical, and transport properties of representatives of a class of magnetic semiconductors: the europium chalcogenides," *Physics Reports*, vol. 141, pp. 51, 1986.

[35] F. Holtzberg, S. Methfessel, J.C. Suits, and T.R. McGuire, " Effect of electron concentration on magnetic exchange interactions in rare earth chalcogenides," *Phys. Rev. Lett.*, vol. 13, pp. 18–21, 1964.

[36] K. C. Ku, S. J. Potashnik, R. F. Wang, S. H. Chun, P. Schiffer, N. Samarth, M. J. Seong, A. Mascarenhas, E. Johnston-Halperin, R. C. Myers, A. C. Gossard, and D. D. Awschalom, "Highly enhanced Curie temperature in low-temperature annealed [Ga,Mn]As epilayers," *Applied Physics Letters*, vol. 82, pp. 2302, 2003.

[37] H. Ohno, H. Munekata, T. Penney, S. von Molnar, and L. L. Chang, "Magnetotransport properties of p-type (In,Mn)As diluted magnetic III-V semicondcutors," *Physical Review Letters*, vol. 68, pp. 2664-2667, 1992.

[38] H. Ohno, A. Shen, F. Matsukura, A. Oiwa, A. Endo, S. Katsumoto, and Y. Iye, "(Ga,Mn)As: A new diluted magnetic semiconductor based GaAs," *Applied Physics Letters*, vol. 69, pp. 363-365, 1996.

[39] H. Ohno, "Making nonmagnetic semiconductors ferromagnetic," *Science*, vol. 281, pp. 951-956, 1998.

[40] A. J. Blattner, J. Lensch, and B. W. Wessels, "Growth and Characterization of OMVPE Grown (In, Mn)As Diluted Magnetic Semiconductor," *Journal of Electronic Materials*, vol. 30, pp. 1408-1411, 2001.

[41] M. Holub, S. Chakrabarti, S. Fathpour, P. Bhattacharya, Y. Lei, and K. Ghosh, "Mn-doped InAs self-organized diluted magnetic quantum-dot layers with Curie temperatures above 300 K," *Applied Physics Letters*, vol. 85, pp. 973-975, 2004.

[42] M. Yokoyama, H. Yamaguchi, T. Ogawa, and M. Tanaka, "Zinc-blende type MnAs Nanoclusters embedded in GaAs," presented at 49th Annual Conference on Magnetism and Magnetic Materials, Jacksonville, FL, 2004.

[43] A. W. Holleitner, H. Knotz, R. C. Myers, A. C. Gossard, and D. D. Awschalom, "Manipulating a domain wall in (Ga,Mn)As," *Journal of Applied Physics*, vol. 97, pp. 10D314, 2005.

[44] H. Munekata, T. Abe, S. Koshihara, A. Oiwa, M. Hirasawa, S. Katsumoto, Y. Iye, C. Urano, and H. Takigi, "Light-induced ferromagnetism in III-IV-based diluted magnetic semiconductor heterostructures," *Journal of Applied Physics*, vol. 81, pp. 4862-4864, 1997.

[45] Y. Ohno, D. K. Young, B. Beschoten, F. Matsukura, H. Ohno, and D. D. Awschalom, "Electrical spin injection in a ferromagnetic semiconductor heterostructure," *Nature*, vol. 402, pp. 790-2, 1999.

[46] B. T. Jonker, "Progress Toward Electrical Injection of Spin-Polarized Electrons into Semiconductors," *Proceedings of the IEEE*, vol. 91, pp. 727-740, 2003.

[47] M. Kohda, Y. Ohno, K. Takamura, F. Matsukura, and H. Ohno, "A Spin Esaki Diode," *Japanese Journal of Applied Physics*, vol. 40, pp. L1274-L1276, 2001.

[48] M. Kohda, Y. Ohno, K. Takamura, F. Matsukura, and H. Ohno, "Electrical electron spin injection with a p+-(Ga,Mn)As/n+-GaAs Tunnel Junction," *Journal of Superconductivity*, vol. 16, pp. 167-170, 2003.

[49] C. Zener, "Interaction between the d shells in the transition metals," *Physical Review*, vol. 81, pp. 440-444, 1950.

[50] L. Kronik, M. Jain, and J. R. Chelikowsky, "Electronic structure and spin polarization of $Mn_xGa_{1-x}N$," *Physical Review B*, vol. 66, pp. 041203, 2002.

[51] K. Sato and H. Katayama-Yoshida, "Ab initio study on the magnetism in ZnO-, ZnS-, ZnSe-, and ZnTe-based Diluted Magnetic Semiconductors," *Physica Status Solidi B*, vol. 229, pp. 673-680, 2002.

[52] H. Katayama-Yoshida and K. Sato, "Materials design for semiconductor spintronics by ab initio electronic structure calculation," *Physica B*, vol. 327, pp. 337-343, 2003.

[53] K. Sato, P. H. Dederichs, H. Katayama-Yoshida, and J. Kudrnovsky, "Magnetic impurities and materials design for semiconductor spintronics," *Physica B*, vol. 340-342, pp. 863–869, 2003.

[54] K. Sato and H. Katayama-Yoshida, "First principles materials design for semiconductor spintronics," *Semiconductor Science & Technology*, vol. 17, pp. 367-76, 2002.

[55] C. Zener, "Interaction between the d shells in transition metals. II. Ferromagnetic compounds of Manganese with Perovskite Structure," *Physical Review*, vol. 82, pp. 403 - 405, 1951.

[56] M. A. Scarpulla, B. L. Cardozo, R. Farshchi, W. M. H. Oo, M. D. McCluskey, K. M. Yu, and O. D. Dubon, "Ferromagnetism in $Ga_{1-x}Mn_xP$: evidence for inter-Mn exchange mediated by localized holes within a detached impurity band," *Physical Review Letters*, vol. 95, pp. 207204, 2005.

[57] P. Mahadevan and A. Zunger, "Trends in ferromagnetism, hole localization, and acceptor level depth for Mn substitution in GaN, GaP, GaAs, and GaSb," *Applied Physics Letters*, vol. 85, pp. 2860, 2004.

[58] E. Sarigiannidou, F. Wilhelm, E. Monroy, R. M. Galera, E. Bellet-Amalric, A. Rogalev, J. Goulon, J. Cibert, and H. Mariette, "Intrinsic ferromagnetism in wurtzite (Ga,Mn)N semiconductor," *Physical Review B (Condensed Matter and Materials Physics)*, vol. 74, pp. 041306, 2006.

[59] S. Marcet, D. Ferrand, S. Kuroda, E. Gheeraert, R. M. Galera, J. Cibert, and H. Mariette, "Magneto-optical spectroscopy of the wide band gap diluted magnetic semiconductor GaMnN," *Materials Science and Engineering: B*, vol. 126, pp. 240, 2006.

[60] V. Litvinov and V. Dugaev, "Ferromagnetism in Magnetically Doped III-V Semiconductors," *Physical Review Letters*, vol. 86, pp. 5593-5596, 2001.

[61] V. Litvinov, "Mixed valence, percolation, and ferromagnetism in transition-metal-doped GaN," *Physical Review B*, vol. 72, pp. 195209, 2005.

[62] M. Berciu and R. N. Bhatt, "Effects of disorder on ferromagnetism in diluted magnetic semiconductors," *Physical Review Letters*, vol. 87, pp. 107203, 2001.

[63] J. M. D. Coey, M. Venkatesan, and C. B. Fitzgerald, *Nature Materials*, vol. 4, pp. 173 - 179, 2005.

[64] J. M. D. Coey, "d^0 ferromagnetism," *Solid State Sciences*, vol. 7, pp. 660, 2005.

[65] D. Chakraborti, J. Narayan, and J. T. Prater, "Room temperature ferromagnetism in $Zn_{1-x}Cu_xO$ thin films," *Applied Physics Letters*, vol. 90, pp. 62504, 2007.

[66] K. R. Kittilstved, N. S. Norberg, and D. R. Gamelin, "Chemical Manipulation of High-T_C Ferromagnetism in ZnO Diluted Magnetic Semiconductors," *Physical Review Letters*, vol. 94, pp. 147209, 2005.

[67] B. K. Rao and P. Jena, "Giant Magnetic Moments of Nitrogen-Doped Mn Clusters and their Relevance to Ferromagnetism in Mn-Doped GaN," *Physical Review Letters*, vol. 89, pp. 185504, 2002.

[68] H. X. Liu, S. Y. Wu, R. K. Singh, and N. Newman, "Exchange biasing of ferromagnetic Cr-doped GaN using a MnO overlayer," *Journal of Applied Physics*, vol. 98, pp. 46106, 2005.

[69] M. J. Reed, F. E. Arkun, E. A. Berkman, N. A. Elmasry, J. Zavada, M. O. Luen, M. L. Reed, and S. M. Bedair, "Effect of doping on the magnetic properties of GaMnN: Fermi level engineering," *Applied Physics Letters*, vol. 86, pp. 102504, 2005.

[70] P. G. de Gennes, "Effects of Double Exchange in Magnetic Crystals," *Physical Review*, vol. 118, pp. 141, 1960.

[71] S. Sonoda, I. Tanaka, H. Ikeno, T. Yamamoto, F. Oba, T. Araki, Y. Yamamoto, K. Suga, Y. Nanishi, Y. Akasaka, K. Kindo, and H. Hori, "Coexistence of Mn^{2+} and Mn^{3+} in ferromagnetic GaMnN," *Journal of Physics Condensed Matter*, vol. 18, pp. 4615, 2006.

[72] S. Dhar, L. Perez, O. Brandt, A. Trampert, K. H. Ploog, J. Keller, and B. Beschoten, "Gd-doped GaN: A very dilute ferromagnetic semiconductor with a Curie temperature above 300 K," *Physical Review B (Condensed Matter and Materials Physics)*, vol. 72, pp. 245203, 2005.

[73] J. K. Hite, R. M. Frazier, R. Davies, G. T. Thaler, C. R. Abernathy, S. J. Pearton, and J. M. Zavada, "Effect of growth conditions on the magnetic characteristics of GaGdN," *Applied Physics Letters*, vol. 89, pp. 092119, 2006.

[74] A. Lewicki, J. Spalek, J. K. Furdyna, and R. R. Galazka, "Magnetic susceptibility of diluted magnetic (semimagnetic) semiconductors: further evidence for superexchange," *Physical Review B*, vol. 37, pp. 1860, 1988.

[75] M. Zajac, J. Gosk, M. Kaminska, A. Twardowski, T. Szyszko, and S. Podsiadlo, "Paramagnetism and antiferromagnetic d-d coupling in GaMnN magnetic semiconductor," *Applied Physics Letters*, vol. 79, pp. 2432-2434, 2001.

[76] G. T. Thaler, R. M. Frazier, J. Stapleton, C. R. Abernathy, S. J. Pearton, J. Kelly, R. Rairigh, A. F. Hebard, and J. M. Zavada, "Properties of GaMnN with and without detectable second phases," *Electrochemical and Solid-State Letters*, vol. 7, pp. G34-G36, 2004.

[77] Y. Shon, Y. H. Kwon, S. U. Yuldashev, J. H. Leem, C. S. Park, D. J. Fu, H. J. Kim, T. W. Kang, and X. J. Fan, "Optical and magnetic measurements of p-type GaN epilayers implanted with Mn+ ions," *Applied Physics Letters*, vol. 81, pp. 1845-1847, 2002.

[78] S. Dhar, O. Brandt, A. Trampert, L. Daweritz, K. J. Friedland, K. H. Ploog, J. Keller, B. Beschoten, and G. Guntherodt, "Origin of high-temperature ferromagnetism in (Ga,Mn)N layers grown on 4H-SiC(0001) by reactive MBE," *Applied Physics Letters*, vol. 82, pp. 2077-2079, 2003.

[79] S. Kuroda, E. Bellet-Amalric, X. Biquard, J. Cibert, R. Giraud, S. Marcet, and H. Mariette, "Optimization of the growth of GaMnN epilayers using plasma-assisted MBE," *Physica Status Solidi B*, vol. 240, pp. 443-446, 2003.

[80] M. H. Kane, A. Asghar, M. Strassburg, Q. Song, A. M. Payne, C. J. Summers, Z. J. Zhang, N. Dietz, and I. T. Ferguson, "Impact of Manganese incorporation on the structural and magnetic properties of MOCVD-grown $Ga_{1-x}Mn_xN$," *Materials Research Society Proceedings*, vol. 831, pp. E9.4.1, 2005.

[81] D. Fruchart, P. L'Heritier, and R. Fruchart, "Transformations de phases dans les nitrures et carbures du manganese de structure-type perovskite," *Materials Research Bulletin*, vol. 15, pp. 415-420, 1980.

[82] M. L. Reed, N. A. El-Masry, H. H. Stadelmaier, M. K. Ritums, M. J. Reed, C. A. Parker, J. C. Roberts, and S. M. Bedair, "Room temperature ferromagnetic properties of (Ga, Mn)N," *Applied Physics Letters*, vol. 79, pp. 3473-3475, 2001.

[83] Z. Jin, T. Fukumura, and M. Kawasaki, "High throughput fabrication of transition-metal-doped epitaxial ZnO thin films: a series of oxide-diluted magnetic semiconductors and their properties," *Applied Physics Letters*, vol. 78, pp. 3824-6, 2001.

[84] C. G. van de Walle and J. Neugebauer, "First-principles calculations for defects and impurities: applications to III-nitrides," *Journal of Applied Physics*, vol. 95, pp. 3851-3879, 2004.

[85] M. E. Overberg, C. R. Abernathy, S. J. Pearton, N. A. Theodoropoulou, K. T. McCarthy, and A. F. Hebard, "Indication of ferromagnetism in molecular-beam-

epitaxy-derived N-type GaMnN," *Applied Physics Letters*, vol. 79, pp. 1312-1314, 2001.

[86] K. Ueda, H. Tabata, and T. Kawai, "Magnetic and electric properties of transition-metal-doped ZnO films," *Applied Physics Letters*, vol. 79, pp. 988-990, 2001.

[87] K. Rode, A. Anane, R. Mattana, J. P. Contour, O. Durand, and R. LeBourgeois, "Magnetic semiconductors based on cobalt substituted ZnO," *Journal of Applied Physics*, vol. 93, pp. 7676-7678, 2003.

[88] J. H. Kim, J. B. Lee, H. Kim, D. Kim, Y. Ihm, and W. K. Choo, "Characteristics of Cobalt-doped Zinc Oxide thin films prepared by Pulsed Laser Deposition," *IEEE Transactions on Magnetics*, vol. 38, pp. 2880-2882, 2002.

[89] N. Theodoropoulou, A. F. Hebard, D. P. Norton, J. D. Budai, L. A. Boatner, J. S. Lee, Z. G. Khim, Y. D. Park, M. E. Overberg, S. J. Pearton, and R. G. Wilson, "Ferromagnetism in Co- and Mn-doped ZnO," *Solid State Communications*, 2003.

[90] D. P. Norton, S. J. Pearton, A. F. Hebard, N. Theodoropoulou, and L. A. Boatner, "Ferromagnetism in Mn-implanted ZnO:Sn single crystals," *Applied Physics Letters*, vol. 82, pp. 239-241, 2003.

[91] S. W. Jung, S. J. An, and G.-C. Yi, "Ferromagnetic properties of $Zn_{1-x}Mn_xO$ epitaxial thin films," *Applied Physics Letters*, vol. 80, pp. 4561-3, 2002.

[92] P. Sharma, A. Gupta, K. V. Rao, F. J. Owens, R. Sharma, R. Ahuja, J. M. Osorio Guillen, B. Johansson, and G. A. Gehring, "Ferromagnetism above room temperature in bulk and transparent thin films of Mn-doped ZnO," *Nature Materials*, vol. 2, pp. 673-677, 2003.

[93] S.-J. Han, T. H. Jang, Y. B. Kim, B.-G. Park, J.-H. Park, and Y. H. Jeong, "Magnetism in Mn-doped ZnO bulk samples prepared by solid state reaction," *Applied Physics Letters*, vol. 83, pp. 920-922, 2003.

[94] D. P. Norton, M. E. Overberg, S. J. Pearton, K. Pruessner, J. D. Budai, L. A. Boatner, M. F. Chisholm, J. S. Lee, Z. G. Khim, Y. D. Park, and R. G. Wilson, "Ferromagnetism in cobalt-implanted ZnO," *Applied Physics Letters*, vol. 83, pp. 5488-5490, 2003.

[95] S. J. Han, J. W. Song, C. H. Yang, S. H. Park, J. H. Park, Y. H. Jeong, and K. W. Rhie, "A key to room-temperature ferromagnetism in Fe-doped ZnO: Cu," *Applied Physics Letters*, vol. 81, pp. 4212, 2002.

[96] X. M. Cheng and C. L. Chien, "Magnetic properties of epitaxial Mn-doped ZnO thin films," *Journal of Applied Physics*, vol. 93, pp. 7876-7878, 2003.

[97] M. H. Kane, K. Shalini, C. J. Summers, R. Varatharajan, J. Nause, C. R. Vestal, Z. J. Zhang, and I. T. Ferguson, "Magnetic properties of bulk $Zn_{1-x}Mn_xO$ and $Zn_{1-x}Co_xO$ single crystals," *Journal of Applied Physics*, vol. 97, pp. 023906, 2005.

[98] T. Fukumura, Z. Jin, M. Kawasaki, T. Shono, T. Hasegawa, S. Koshihara, and H. Koinuma, "Magnetic properties on Mn-doped ZnO," *Applied Physics Letters*, vol. 78, pp. 958-960, 2001.

[99] S. W. Yoon, S.-B. Cho, S. C. We, S. Yoon, B. J. Suh, H. K. Song, and Y. J. Shin, "Magnetic properties of ZnO-based diluted magnetic semiconductors," *Journal of Applied Physics*, vol. 93, pp. 7879-7881, 2003.

[100] K. Doo Soo, K. Hwa-Mok, S. U. Yuldashev, L. Se Joon, K. Tae Won, and K. Deuk Young, "Characteristics of $Zn_{1-x}Mn_xO$ thin films prepared by RF magnetron sputtering," *Journal of the Korean Physical Society*, vol. 42, pp. 333, 2003.

[101] C. Young Mok, C. Woong Kil, K. Hyojin, K. Dojin, and Y. Ihm, "Effects of rapid thermal annealing on the ferromagnetic properties of sputtered $Zn_{1-x}(Co_{0.5}Fe_{0.5})_xO$ thin films," *Applied Physics Letters*, vol. 80, pp. 3358, 2002.

[102] J. H. Park, M. G. Kim, H. M. Jang, S. Ryu, and Y. M. Kim, "Co-metal clustering as the origin of ferromagnetism in Co-doped ZnO thin films," *Applied Physics Letters*, vol. 84, pp. 1338-1340, 2004.

[103] M. Zajac, R. Doradzinski, J. Gosk, J. Szczytko, M. Lefeld-Sosnowska, M. Kaminska, A. Twardowski, M. Palczewska, E. Grzanka, and W. Gebicki, "Magnetic and optical properties of GaMnN magnetic semiconductor," *Applied Physics Letters*, vol. 78, pp. 1276-1278, 2001.

[104] S. J. Pearton, M. E. Overberg, G. Thaler, C. R. Abernathy, N. Theodoropoulou, A. F. Hebard, S. N. G. Chu, R. G. Wilson, J. M. Zavada, A. Y. Polyakov, A. V. Osinsky, P. E. Norris, P. P. Chow, A. M. Wowchack, J. M. V. Hove, and Y. D. Park, "Characterization of High Dose Mn, Fe, and Ni implantation into p-GaN," *Journal of Vacuum Science and Technology*, vol. A20, pp. 721-724, 2002.

[105] M. E. Overberg, B. P. Gila, and R. Abernathy, "Magnetic properties of P-type GaMnP grown by molecular-beam epitaxy," *Applied Physics Letters*, vol. 79, pp. 3128-30, 2001.

[106] M. C. Park, K. S. Huh, J. M. Myounga, J. M. Lee, J. Y. Chang, K. I. Lee, S. H. Han, and W. Y. Lee, "Room temperature ferromagnetic (Ga,Mn)N epitaxial films with low Mn concentration grown by plasma-enhanced molecular beam epitaxy," *Solid State Communications*, vol. 124, pp. 11-14, 2002.

[107] K. Sardar, A. R. Raju, B. Bansal, V. Venkataraman, and C. N. R. Rao, "Magnetic, optical and transport properties of GaMnN films," *Solid State Communications*, vol. 125, pp. 55-57, 2003.

[108] H. Hori, S. Sonoda, T. Sasaki, Y. Yamamoto, S. Shimizu, K.-i. Suga, and K. Kindo, "High-TC ferromagnetism in diluted magnetic semiconducting GaN:Mn films," *Physica B*, vol. 324, pp. 142-150, 2002.

[109] S. Sonoda, H. Hori, Y. Yamamoto, T. Sasaki, M. Sato, S. Shimizu, K.-i. Suga, and K. Kindo, "Properties of Ferromagnetic $Ga_{1-x}Mn_xN$ Films Grown by Ammonia-MBE," *Magnetics, IEEE Transactions on*, vol. 38, pp. 2859-2862, 2002.

[110] E. A. Berkman, M. J. Reed, F. E. Arkun, N. A. El-Masry, J. M. Zavada, M. O. Luen, M. L. Reed, and S. M. Bedair, "The Effect of Mn Concentration on Curie Temperature and Magnetic Behavior of MOCVD Grown GaMnN Films," *Materials Research Society Proceedings*, vol. 834, pp. J7.3.1, 2005.

[111] H. Harima, "Raman studies on spintronics materials based on wide bandgap semiconductors," *Journal of Physics: Condensed Matter*, vol. 16, pp. S5653–S5660, 2004.

[112] M. H. Kane, A. Asghar, A. M. Payne, C. R. Vestal, M. Strassburg, J. Senawiratne, Z. J. Zhang, N. Dietz, C. R. Summers, and I. T. Ferguson, "Magnetic and optical properties of GaMnN grown by Metalorganic Chemical Vapor Deposition," *Semiconductor Science & Technology*, vol. 20, pp. L5-L9, 2005.

[113] Y. Shon, Y. H. Kwon, D. Y. Kim, D. Fu, and T. W. Kang, "Magnetic charcterization of Mn+ ion implanted layer," *Japanese Journal of Applied Physics*, vol. 40, pp. 5304-5305, 2001.

[114] A. Y. Polyakov, N. B. Smirnov, A. V. Govorkov, N. Y. Pashkova, J. Kim, F. Ren, M. E. Overberg, G. T. Thaler, C. R. Abernathy, S. J. Pearton, and R. G. Wilson, "Electrical and optical properties of GaN films implanted with Mn and Co," *Journal of Applied Physics*, vol. 92, pp. 3130-3135, 2002.

[115] R. Y. Korotkov, J. M. Gregie, and B. W. Wessels, "Optical Study of GaN doped with Mn grown by Metal Organic Vapor Phase Epitaxy," *Materials Research Society Proceedings*, vol. 639, pp. G3.7.1-G3.7.6, 2001.

[116] K. Ando, "Magneto-optical study of s,p-d exchange interations in GaN:Mn with room-temperature ferromagnetism," *Applied Physics Letters*, vol. 82, pp. 100-102, 2003.

[117] M. Strassburg, J. Senawirante, C. Hums, N. Dietz, M. H. Kane, A. Asghar, A. M. Payne, I. T. Ferguson, C. J. Summers, U. Haboeck, A. Hoffman, D. Azamat, and W. Gelhoff, "Optical and Structural Investigations on Mn-Ion States in MOCVD-grown $Ga_{1-x}Mn_xN$," *MRS Proceedings*, pp. submitted, 2004.

[118] I. T. Yoon, C. S. Park, H. J. Kim, Y. G. Kim, T. W. Kang, M. C. Jeong, M. H. Ham, and J. M. Myoung, "Characterization of ferromagnetic GaMn/N layers

grown on sapphire (0001) substrates," *Journal of Applied Physics*, vol. 95, pp. 591-596, 2004.

[119] R. K. Singh, S. Y. Wu, H. X. Liu, L. Gu, D. J. Smith, and N. Newman, "The role of Cr substitution on the ferromagnetic properties of $Ga_{1-x}Cr_xN$," *Applied Physics Letters*, vol. 86, pp. 012504, 2005.

[120] D. C. Reynolds, C. W. Litton, D. C. Look, J. E. Hoelscher, B. Claflin, T. C. Collins, B. Nemeth, and J. Nause, "High-quality, melt-grown ZnO single crystals," *Journal of Applied Physics*, vol. 95, pp. 4802-4805, 2004.

[121] M. W. Cho, C. Harada, H. Suzuki, T. Minegishi, T. Yao, H. Ko, K. Maeda, and I. Nikura, "Issues in ZnO homoepitaxy," *Superlattices and Microstructures*, vol. 38, pp. 349, 2005.

[122] X. A. Cao, H. Lu, E. B. Kaminsky, S. D. Arthur, J. R. Grandusky, and F. Shahedipour-Sandvik, "Homoepitaxial growth and electrical characterization of GaN-based Schottky and light-emitting diodes," *Journal of Crystal Growth*, vol. 300, pp. 382, 2007.

[123] T. Paskova, P. P. Paskov, E. Valcheva, V. Darakchieva, J. Birch, A. Kasic, B. Arnaudov, S. Tungasmita, and B. Monemar, "Polar and nonpolar GaN grown by HVPE: preferable substrates for nitride-based emitting devices," *Phys. Status Solidi*, vol. 9, pp. 2265, 2004.

[124] K. Maeda, M. Sato, I. Niikura, and T. Fukuda, "Growth of 2 inch ZnO bulk single crystal by the hydrothermal method," *Semiconductor Science and Technology*, vol. 20, pp. 49, 2005.

[125] E. Ohshima, H. Ogino, I. Niikura, K. Maeda, M. Sato, M. Ito, and T. Fukuda, "Growth of the 2-in-size bulk ZnO single crystals by the hydrothermal method," *Journal of Crystal Growth*, vol. 260, pp. 166, 2004.

[126] J. Nause and B. Nemeth, "Pressurized melt growth of ZnO boules," *Semiconductor Science and Technology*, vol. 20, pp. 45, 2005.

[127] A. Zunger, "Practical Doping Principles," *Applied Physics Letters*, vol. 83, pp. 57-59, 2003.

[128] H. Amano, N. Sawaki, I. Akasaki, and Y. Toyoda, "Metalorganic vapor phase epitaxial growth of a high quality GaN film using an AlN buffer layer," *Applied Physics Letters*, vol. 48, pp. 353, 1986.

[129] S. Nakamura and T. Mukai, "High-quality InGaN films grown on GaN films," *Japanese Journal of Applied Physics, Part 2 (Letters)*, vol. 31, pp. 1457, 1992.

[130] H. Amano, M. Kito, K. Hiramatsu, and I. Akasaki, "p-type conduction in Mg-doped GaN treated with low-energy electron beam irradiation (LEEBI)," *Japanese Journal of Applied Physics, Part 2 (Letters)*, vol. 28, pp. 2112, 1989.

[131] W. Gehlhoff: Technical University - Berlin, 2005.

[132] H. Harima, "Properties of GaN and related compounds studied by means of Raman scattering," *Journal of Physics: Condensed Matter*, vol. 14, pp. R967, 2002.

[133] A. Fouchet, W. Prellier, and B. Mercey, "Influence of the microstructure on the magnetism of Co-doped ZnO thin films," *Journal of Applied Physics*, vol. 100, pp. 013901, 2006.

[134] Z.-w. Jin, Y.-Z. Yoo, T. Sekiguchi, T. Chikyow, H. Ofuchi, H. Fujioka, M. Oshima, and H. Koinuma, "Blue and ultraviolet cathodoluminescence from Mn-doped epitaxial ZnO thin films," *Applied Physics Letters*, vol. 83, pp. 39-41, 2003.

[135] K. Samanta, P. Bhattacharya, and R. S. Katiyar, "Optical properties of $Zn_{1-x}Co_xO$ thin films grown on Al_2O_3 (0001) substrates," *Applied Physics Letters*, vol. 87, pp. 101903, 2005.

[136] C. H. Bates, W. B. White, and R. Roy, "The solubility of transition metal oxides in zinc oxide and the reflectance spectra of Mn^{2+} and Fe^{2+} in tetrahedral fields," *Journal of Inorganic and Nuclear Chemistry*, vol. 28, pp. 397-405, 1966.

[137] A. Hausmann and H. Huppertz, "Paramagnetic resonance of ZnO:Mn++ single crystals," *Journal of Physics and Chemistry of Solids*, vol. 29, pp. 1369, 1968.

[138] N. Jedrecy, H. J. von Bardeleben, Y. Zheng, and J. L. Cantin, "Electron paramagnetic resonance study of $Zn_{1-x}Co_xO$: A predicted high-temperature ferromagnetic semiconductor," *Physical Review B (Condensed Matter and Materials Physics)*, vol. 69, pp. 041308, 2004.

[139] J. M. Calleja and M. Cardona, "Resonant Raman Scattering in ZnO," *Physical Review B*, vol. 16, pp. 3753, 1977.

[140] F. J. Manjon, B. Mari, J. Serrano, and A. H. Romero, "Silent Raman modes in zinc oxide and related nitrides," *Journal of Applied Physics*, vol. 97, pp. 053516, 2005.

[141] N. Hasuike, H. Fukumura, H. Harima, K. Kisoda, H. Matsui, H. Saeki, and H. Tabata, "Raman scattering studies on ZnO doped with Ga and N (codoping) and magnetic impurities," *Journal of Physics: Condensed Matter*, vol. 16, pp. S5807-S5810, 2004.

[142] H. Zhou, L. Chen, V. Malik, C. Knies, D. M. Hofmann, K. P. Bhatti, S. Chaudhary, P. J. Klar, W. Heimbrodt, C. Klingshirn, and H. Kalt, "Raman studies of ZnO:Co thin films," *physica status solidi (a)*, vol. 204, pp. 112, 2007.

[143] A. Lewicki, J. Spalek, and A. Mycielski, "Magnetic susceptibility and specific heat of the semi-magnetic semiconductors CdFeSe and HgFeSe and their mixtures," *Journal of Physics C: Solid State Physics*, vol. 20, pp. 2005-2017, 1987.

[144] J. Spalek, A. Lewicki, Z. Tarnawski, J. K. Furdyna, R. R. Galazka, and Z. Obuszko, "Magnetic susceptibility of semimagnetic semiconductors: The high-temperature regime and the role of superexchange," *Physical Review B*, vol. 33, pp. 3407-3417, 1986.

[145] R. Laiho, K. G. Luisunov, E. Lahderanta, and V. S. Zakhvalinskii, "Magnetic MnAs nanoclusters in the diluted magnetic semiconductor $(Zn_{1-x}Mn_x)_3As_2$," *Journal of Physics: Condensed Matter*, vol. 11, pp. 8697-8706, 1999.

[146] A. Lewicki, A. I. Schindler, J. K. Furdyna, and T. M. Giebultowicz, "Magnetic Properties of Co-based diluted magnetic semiconductors," in *Diluted magnetic semiconductors*, M. Jain, Ed. Singapore: World Scientific, 1991.

[147] P. Sati, C. Deparis, C. Morhain, S. Schafer, and A. Stepanov, "Antiferromagnetic Interactions in Single Crystalline $Zn_{1-x}Co_xO$ Thin Films," *physical Review Letters*, vol. 98, pp. 137204, 2007.

[148] E.-C. Lee and K. J. Chang, "Ferromagnetic versus antiferromagnetic interaction in Co-doped ZnO," *Physical Review B*, vol. 69, pp. 085205, 2004.

[149] M. Venkatesan, C. B. Fitzgerald, J. G. Lunney, and J. M. D. Coey, "Anisotropic Ferromagnetism in Substituted Zinc Oxide," *Physical Review Letters*, vol. 93, pp. 177206, 2004.

[150] D.-L. Hou, X.-J. Ye, H.-J. Meng, H.-J. Zhou, X.-L. Li, C.-M. Zhen, and G.-D. Tang, "Magnetic properties of Mn-doped ZnO powder and thin films," *Materials Science and Engineering B: Solid-State Materials for Advanced Technology*, vol. 138, pp. 184, 2007.

[151] C. Sudakar, P. Kharel, G. Lawes, R. Suryanarayanan, R. Naik, and V. M. Naik, "Raman spectroscopic studies of oxygen defects in Co-doped ZnO films exhibiting room-temperature ferromagnetism," *Journal of Physics: Condensed Matter*, vol. 19, pp. 9 pp., 2007.

[152] U. Ozgur, Y. I. Alivov, C. Liu, A. Teke, M. A. Reshchikov, S. Dogan, V. Avrutin, S. J. Cho, and H. Morkoc, "A comprehensive review of ZnO materials and devices," *Journal of Applied Physics*, vol. 98, pp. 41301, 2005.

[153] K. R. Kittilstved, D. A. Schwartz, A. C. Tuan, S. M. Heald, S. A. Chambers, and D. R. Gamelin, "Direct Kinetic Correlation of Carriers and Ferromagnetism in Co^{2+}: ZnO," *Physical Review Letters*, vol. 97, pp. 037203, 2006.

[154] D. A. Schwartz, K. R. Kittilstved, and D. R. Gamelin, "Above-room-temperature ferromagnetic Ni^{2+}-doped ZnO thin films prepared from colloidal diluted magnetic semiconductor quantum dots," *Applied Physics Letters*, vol. 85, pp. 1395, 2004.

[155] A. B. Mahmoud, H. J. von Bardeleben, J. L. Cantin, A. Mauger, E. Chikoidze, and Y. Dumont, "From ferromagnetic to antiferromagnetic interactions in n-type $Zn_{1-x}Mn_xO$: An electron paramagnetic resonance study," *Physical Review B (Condensed Matter and Materials Physics)*, vol. 74, pp. 115203, 2006.

[156] C. Sudakar, J. S. Thakur, G. Lawes, R. Naik, and V. M. Naik, "Ferromagnetism induced by planar nanoscale CuO inclusions in Cu-doped ZnO thin films," *Physical Review B (Condensed Matter and Materials Physics)*, vol. 75, pp. 54423, 2007.

[157] D. Chakraborti, S. Ramachandran, G. Trichy, J. Narayan, and J. T. Prater, "Magnetic, electrical, and microstructural characterization of ZnO thin films codoped with Co and Cu," *Journal of Applied Physics*, vol. 101, pp. 53918, 2007.

[158] H. Saito, V. Zayets, S. Yamagata, and K. Ando, "Room-temperature ferromagnetism in highly Cr-doped II-VI diluted magnetic semiconductor $Zn_{1-x}Cr_xTe$," *Journal of Applied Physics*, vol. 93, pp. 6796, 2003.

[159] N. Theodoropoulou, A. F. Hebard, M. E. Overberg, C. R. Abernathy, S. J. Pearton, S. N. G. Chu, and R. G. Wilson, "Magnetic and structural properties of Mn-implanted GaN," *Applied Physics Letters*, vol. 78, pp. 3475-7, 2001.

[160] N. Theodoropoulou, A. F. Hebard, S. N. G. Chu, M. E. Overberg, C. R. Abernathy, S. J. Pearton, and R. G. Wilson, "Use of ion implantation to facilitate the discovery and characterization of ferromagnetic semiconductors," *Journal of Applied Physics*, vol. 91, pp. 7499-7501, 2002.

[161] Stopping Ranges of Ions in Materials, http://www.srim.org/, 2006.

[162] J. M. Baik, J.-L. Lee, Y. Shon, and T. W. Kang, "Microstructural, optical, and magnetic properties of Mn-implanted p-type GaN," *Journal of Applied Physics*, vol. 93, pp. 9024-9029, 2003.

[163] M. H. Kane, A. Asghar, A. M. Payne, C. R. Vestal, Z. J. Zhang, M. Strassburg, J. Senawirante, N. Dietz, C. J. Summers, and I. T. Ferguson, "Comparison of GaMnN epilayers prepared by ion implantation and metalorganic chemical vapor deposition," *Physica Status Solidi*, vol. C, pp. Submitted, 2004.

[164] S. Shanthi, M. Hashimoto, Y. K. Zhou, S. Kimura, M. S. Kim, S. Emura, N. Hasuike, H. Harima, S. Hasegawa, M. Ishimaru, Y. Hirotsu, and H. Asahi, "Polymorphism in the ferromagnetic GaCrN-diluted magnetic semiconductor: Luminescence and structural investigations," *Journal of Applied Physics*, vol. 98, pp. 013526, 2005.

[165] X. Y. Cui, J. E. Medvedeva, B. Delley, A. J. Freeman, N. Newman, and C. Stampfl, "Role of Embedded Clustering in Dilute Magnetic Semiconductors: Cr Doped GaN," *Physical Review Letters*, vol. 95, pp. 256404, 2005.

[166] M. Zajac, J. Gosk, E. Grzanka, M. Kaminska, A. Twardowski, B. Strojek, J. Szczytko, and S. Podsiadlo, "Possible origin of ferromagnetism in (Ga,Mn)N," *Journal of Applied Physics*, vol. 93, pp. 4715-4717, 2003.

[167] M. L. Reed, E. A. Berkman, M. J. Reed, F. E. Arkun, T. Chikyow, S. M. Bedair, J. M. Zavada, and N. A. El-Masry, "Magnetic properties of Mn-doped GaN, InGaN, And AlGaN," *Materials Research Society Proceedings*, vol. 798, pp. Y8.6.1, 2004.

[168] S. J. Potashnik, K. C. Ku, R. Mahendiran, S. H. Chun, R. F. Wang, N. Samarth, and P. Schiffer, "Saturated ferromagnetism and magnetization deficit in optimally annealed GaMnAs epilayers," *Physical Review B*, vol. 66, pp. 012408, 2002.

[169] T. Graf, M. Gjukic, M. S. Brandt, M. Stutzmann, and O. Ambacher, "The $Mn^{3+/2+}$ Acceptor level in Group III Nitrides," *Applied Physics Letters*, vol. 81, pp. 5159-5161, 2002.

[170] T. Hwang, J. H. Shim, and S. Lee, "Observation of MnP magnetic clusters in room-temperature ferromagnetic semiconductor $ZnMnGeP_2$ using nuclear magnetic resonance," *Applied Physics Letters*, vol. 83, pp. 1809-1811, 2003.

[171] S. Cho, S. Choi, G.-B. Cha, S. C. Hong, Y. Kim, Y.-J. Zhao, A. J. Freeman, J. B. Ketterson, B. J. Kim, Y. C. Kim, and B.-C. Choi, "Room Temperature Ferromagnetism in $(Zn_{1-x}Mn_x)GeP_2$ Semiconductors," *Physical Review Letters*, vol. 88, pp. 257203, 2002.

[172] R. S. Balmer, D. E. J. Soley, A. J. Simons, J. D. Mace, L. Koker, P. O. Jackson, D. J. Wallis, M. J. Uren, T. Martin, "On the incorporation mechanism of Fe in GaN grown by metal-organic vapour phase epitaxy," *physica status solidi (c)*, vol. 3, pp. 1429-1434, 2006.

[173] J. M. Baik, H. W. Jang, J. K. Kim, and J.-L. Lee, "Effect of microstructural change on magnetic property of Mn-implanted p-type GaN," *Applied Physics Letters*, vol. 82, pp. 583-585, 2003.

[174] H. Katayama-Yoshida and K. Sato, "Materials design for semiconductor spintronics by ab initio electronic-structure calculation," *Physica B*, vol. 327, pp. 337, 2003.

[175] K. H. Baik, R. M. Frazier, G. T. Thaler, C. R. Abernathy, S. J. Pearton, J. Kelly, R. Rairigh, A. F. Hebard, W. Tang, M. Stavola, and J. M. Zavada, "Effects of hydrogen incorporation in GaMnN," *Applied Physics Letters*, vol. 83, pp. 5458-5460, 2003.

[176] C. Thompson, G. B. Stephenson, J. A. Eastman, A. Munkholm, O. Auciello, M. V. Ramana-Murty, P. Fini, S. P. DenBaars, and J. S. Speck, "Investigations of Chemical Vapor Deposition of GaN using Synchrotron Radiation," *Journal of the Electrochemical Society*, vol. 148, pp. C390-C394, 2001.

[177] S. Gupta, H. Kang, M. Strassburg, A. Asghar, M. H. Kane, W. E. Fenwick, N. Dietz, and I. T. Ferguson, "A Nucleation Study of Group III-Nitride Multifunctional Nanostructures," *Journal of Crystal Growth*, pp. Submitted, 2005.

[178] W. Gehlhoff, D. Azamat, A. Hoffmann, N. Dietz, and O. V. Voevodina, "Transition metals in $ZnGeP_2$ and other II-IV-V_2 compounds," 2006.

[179] U. Haboeck, H. Siegle, A. Hoffmann, and C. Thomsen, "Lattice dynamics in GaN and AlN probed with first- and second-order Raman spectroscopy," *Physica Status Solidi C*, vol. 0, pp. 1710-1731, 2003.

[180] Z. G. Hu, M. Strassburg, N. Dietz, A. G. U. Perera, M. H. Kane, A. Asghar, and I. T. Ferguson, "Effect of Mn composition on E_1(TO) phonon mode in hexagonal GaMnN epitaxial films on c-plane sapphire substrates," *Applied Physics Letters*, pp. Submitted, 2005.

[181] J. Senawirante, M. Strassburg, A. M. Payne, A. Asghar, N. Dietz, and I. T. Ferguson, *unpublished data*.

[182] W. Limmer, W. Ritter, R. Sauer, B. Mensching, C. Liu, and R. Rauschenbach, "Raman Scattering in ion-implanted GaN," *Applied Physics Letters*, vol. 72, pp. 2589-2591, 1998.

[183] W. Gebicki, J. Strzeszewski, G. Kamler, T. Szyszko, and S. Podsiadlo, "Raman scattering study of $Ga_{1-x}Mn_xN$ crystals," *Applied Physics Letters*, vol. 76, pp. 3870-3872, 2000.

[184] B. He, X. Zhang, S. Wei, H. Oyanagi, S. V. Novikov, K. W. Edmonds, C. T. Foxon, G. e. Zhou, and Y. Jia, "Local structure around Mn atoms in cubic (Ga,Mn)N thin films probed by fluorescence extended x-ray absorption fine structure," *Applied Physics Letters*, vol. 88, pp. 051905, 2006.

[185] M. Strassburg, M. H. Kane, A. Asghar, Q. Song, Z. J. Zhang, J. Senawiratne, M. Alevli, N. Dietz, C. J. Summers, and I. T. Ferguson, "The Fermi Level Dependence of Optical and Magnetic Properties in MOCVD-grown GaMnN," *Journal of Physics: Condensed Matter*, vol. 18, pp. 2615, 2005.

[186] M. Strassburg, J. Senawirante, C. Hums, N. Dietz, M. H. Kane, A. Asghar, A. M. Payne, I. T. Ferguson, C. J. Summers, U. Haboeck, A. Hoffman, D. Azamat, and W. Gelhoff, "Optical and Structural Investigations on Mn-Ion States in MOCVD-grown $Ga_{1-x}Mn_xN$," *MRS Proceedings*, vol. 831, pp. E9.5.1, 2005.

[187] M. H. Kane, M. Strassburg, W. E. Fenwick, A. Asghar, and I. T. Ferguson, "The Growth and Characterization of Room Temperature Ferromagnetic Wideband-gap Materials for Spintronic Applications," *International Journal of High Speed Electronics*, in press, 2005.

[188] J. Xu, J. Li, R. Zhang, X. Q. Xiu, D. Q. Lu, S. L. Gu, B. Shen, Y. Shi, and Y. D. Zheng, *Materials Research Society Proceedings*, vol. 693, pp. 207, 2002.

[189] B. Han, J. M. Gregie, and B. W. Wessels, "Blue emission band in compensated GaN:Mg codoped with Si," *Physical Review B*, vol. 68, pp. 045205, 2003.

[190] T. Graf, M. Gjukic, M. Hermann, M. S. Brandt, M. Stutzmann, and O. Ambacher, "Spin resonance investigations of Mn^{2+} in wurtzite GaN and AlN films," *Physical Review B*, vol. 67, pp. 165215, 2003.

[191] B. Monemar, "Basic III-V research - Past, Present, and Future," *Journal of Crystal Growth*, vol. 189, pp. 1-7, 1998.

[192] A. Wolos, M. Palczewska, M. Zajac, J. Gosk, M. Kaminska, A. Twardowski, M. Bockowski, I. Grzegory, and S. Porowski, "Optical and magnetic properties of Mn in bulk GaN," *Physical Review B (Condensed Matter and Materials Physics)*, vol. 69, pp. 115210, 2004.

[193] O. Gelhausen, E. Malguth, M. R. Phillips, E. M. Goldys, M. Strassburg, A. Hoffmann, T. Graf, M. Gjukic, and M. Stutzmann, "Doping-level-dependent optical properties of GaN:Mn," *Applied Physics Letters*, vol. 84, pp. 4514-4516, 2004.

[194] T. Yamamoto, S. Marcet, E. Gheeraert, S. Kuroda, H. Mariette, D. Ferrand, and J. Cibert, *Journal of Crystal Growth*, vol. 275, pp. e2233, 2005.

[195] B. Han, R. Y. Korotkov, B. W. Wessels, and M. P. Ulmer, "Optical propertis of Mn^{4+} ions in GaNMn codoped with Mg acceptors," *Applied Physics Letters*, vol. 84, pp. 5320-5322, 2004.

[196] T. Graf, T. B. Goennenwein, and M. S. Brandt, "Prospects for carrier-mediated ferromagnetism in GaN," *Physica status solidi (b)*, vol. 239, pp. 277-290, 2003.

[197] M. S. Miao, A. Herwadkar, and W. R. L. Lambrecht, "Electronic structure and magnetic properties of Mn_3GaN precipitates in $Ga_{1-x}Mn_xN$," *Physical Review B (Condensed Matter and Materials Physics)*, vol. 72, pp. 33204, 2005.

[198] S. Heikman, S. Keller, S. P. DenBaars, and U. K. Mishra, "Growth of Fe doped semi-insulating GaN by metalorganic chemical vapor deposition," *Applied Physics Letters*, vol. 81, pp. 439-441, 2002.

[199] P. K. Khowash, V. A. Singh, and D. C. Khan, "A theoretical study of the semiinsulating behaviour of Fe in InP," *Physica Status Solidi B*, vol. 136, pp. 715, 1986.

[200] H. Przybylinska, A. Bonanni, A. Wolos, M. Kiecana, M. Sawicki, T. Dietl, H. Malissa, C. Simbrunner, M. Wegscheider, and H. Sitter, "Magnetic properties of a new spintronic material--GaN:Fe," *Materials Science and Engineering: B*, vol. 126, pp. 222, 2006.

[201] N. Theodoropoulou, A. F. Hebard, S. N. G. Chu, M. E. Overberg, C. R. Abernathy, S. J. Pearton, R. G. Wilson, and J. M. Zavada, "Characterization of high dose Fe implantation into p-GaN," *Applied Physics Letters*, vol. 79, pp. 3452-3454, 2001.

[202] T. Dietl, "Self-organized growth controlled by charge states of magnetic impurities," *Nature Materials*, vol. 9, pp. 673, 2006.

[203] S. Tanaka, M. Takeuchi, and Y. Aoyagi, "Anti-surfactant in III-nitride epitaxy - quantum dot formation and dislocation termination," *Japanese Journal of Applied Physics, Part 2: Letters*, vol. 39, pp. 831-834, 2000.

[204] F. E. Arkun, M. J. Reed, E. A. Berkman, N. A. El-Masry, J. M. Zavada, M. L. Reed, and S. M. Bedair, "Dependence of ferromagnetic properties on carrier transfer at GaMnN/GaN:Mg interface," *Applied Physics Letters*, vol. 85, pp. 3809, 2004.

[205] M. Ramsteiner, H. Y. Hao, A. Kawaharazuka, H. J. Zhu, M. Kastner, R. Hey, L. Daweritz, H. T. Grahn, and K. H. Ploog, "Electrical spin injection from ferromagnetic MnAs layers into GaAs," *Physical Review B*, vol. 66, pp. 081304, 2002.

[206] K. Sato, P. H. Dederichs, and H. Katayama-Yoshida, "Is high T_C possible in (Ga,Mn)N? Monte Carlo Simulation vs. mean field approximation," *Journal of Superconductivity*, vol. 18, pp. 33, 2005.

[207] H. Katayama-Yoshida, K. Sato, T. Fukushima, M. Toyoda, H. Kizaki, V. A. Dinh, and P. H. Dederichs, "Theory of ferromagnetic semiconductors," *physica status solidi (a)*, vol. 204, pp. 3, 2007.

[208] M. Moreno, B. Jenichen, L. Daweritz, and K. H. Ploog, "Lattice distortion of MnAs nanocrystals embedded in GaAs: Effect on the magnetic properties," *Applied Physics Letters*, vol. 86, pp. 161903, 2005.

[209] M. Yokoyama, H. Yamaguchi, T. Ogawa, and M. Tanaka, "Zinc-blende-type MnAs nanoclusters embedded in GaAs," *Journal of Applied Physics*, vol. 97, pp. 10D317, 2005.

[210] A. Sato, K. Azumada, T. Atsumori, and K. Hara, "Low-temperature metalorganic chemical vapor deposition of luminescent manganese-doped aluminum nitride films," *Applied Physics Letters*, vol. 87, pp. 21907, 2005.

[211] K. Ando, H. Saito, V. Zayets, and M. C. Debnath, "Optical properties and functions of dilute magnetic semiconductors," *Journal of Physics: Condensed Matter*, vol. 16, pp. 5541, 2004.

[212] H. Munekata, "Photomagnetic effects in III-V based semiconductors," *Physica E*, vol. 25, pp. 160, 2004.

[213] T. Fukushima, K. Sato, H. Katayama-Yoshida, and P. H. Dederichs, "Spinodal decomposition under layer by layer growth condition and high curie temperature quasi-one-dimensional nano-structure in dilute magnetic semiconductors," *Japanese Journal of Applied Physics, Part 2: Letters*, vol. 45, pp. 416-418, 2006.

[214] T. Devillers, M. Jamet, A. Barski, V. Poydenot, R. Dujardi, P. Bayle-Guillemaud, J. Rothman, E. Bellet-Amalric, J. Cibert, R. Mattana, and S. Tatarenko, "Structural and magnetic properties of GeMn layers; High Curie temperature ferromagnetism induced by self organized GeMn nano-columns," *physica status solidi (a)*, vol. 204, pp. 130-135, 2007.

VITA

Matthew Hartmann Kane was born March 1, 1974, in Tulsa, Oklahoma. He graduated magna cum laude with a B. S. in Materials Science and Engineering from Rice University in 1996. In 1997, he completed his M.S. in Materials Science in Engineering at Northwestern University. His thesis was directed by Prof. Thomas O. Mason and focused on the defect analysis of layered cuprate compounds. After receiving his master's degree, Kane served for five years in the United States Navy as a submarine warfare officer aboard the USS Springfield (SSN-761). He joined the School of Materials Science and Engineering at Georgia Tech in December of 2002, focusing on the development of novel wide bandgap magnetic semiconductors for potential applications in the field of spintronics.